Capping of Very Weak Dredged Materials in Confined Aquatic Disposal: Modeling of Strength and Transport Behavior

by

Sanjay Pahuja

Submitted to the Department of Civil and Environmental Engineering in partial fulfillment of the requirements for the degree of

Doctor of Philosophy in Civil and Environmental Engineering

at the

MASSACHUSETTS INSTITUTE OF TECHNOLOGY

June 2001

Author .....
Department of Civil and Environmental Engineering
May 1, 2001

Certified by .....
Ole S. Madsen
Professor, Civil and Environmental Engineering
Thesis Supervisor

Certified by .....
John T. Germaine
Principal Research Associate, Civil and Environmental Engineering
Thesis Supervisor

Accepted by .....
Oral Buyukozturk
Chairman, Departmental Committee on Graduate Studies

Capping of Very Weak Dredged Materials in Confined Aquatic Disposal: Modeling of Strength and Transport Behavior

by

Sanjay Pahuja

Submitted to the Department of Civil and Environmental Engineering
on May 1, 2001, in partial fulfillment of the
requirements for the degree of
Doctor of Philosophy in Civil and Environmental Engineering

Abstract

The technique of Confined Aquatic Disposal (CAD) capping is often utilized for sequestering contaminated marine sediments. It involves excavation of subaqueous borrow pits which are subsequently filled with the contaminated material and then capped with a clean sediment. This thesis applies to two different problems that have been identified as major issues of concern in capping projects: The lack of adequate knowledge of shear strength development in very weak sediments, and, an absence of sediment transport models that can incorporate non-equilibrium effects in suspended sediment concentration.

Experiments were conducted to measure the undrained shear strength in specimens of sediment from Boston harbor. Tests were performed at different times and for different values of initial specimen height and initial water content. The results show that there exist two distinct regimes of shear strength variation with effective stress, and that the low-effective stress behavior can not be modeled by the classical cohesion-friction angle formulation based on standard geotechnical testing. At low effective stresses, we parameterize the undrained shear strength as an exponential function of effective stress, while retaining dependence on the initial water content and deposit height.

A simple model is developed for the temporal response of suspended sediment concentration in a water column, based on a Lagrangian analysis of water columns oscillating in a region of linearly varying bottom sediment concentration. By considering the difference in suspended sediment transport past a fixed point when a water column passes in the up-gradient and down-gradient directions, the model predicts the net sediment transported during a period of oscillation. The net sediment transport rate is proportional to the reference bottom sediment concentration gradient. Application of the model to different scenarios shows that the non-equilibrium effect can cause appreciable sediment transport in certain physical systems.

Thesis Supervisor: Ole S. Madsen
Title: Professor, Civil and Environmental Engineering

Thesis Supervisor: John T. Germaine
Title: Principal Research Associate, Civil and Environmental Engineering

Acknowledgments

"This frail vessel thou emptiest again and again, and fillest it ever with fresh life. This little flute of a reed thou hast carried over hills and dales, and hast breathed through it melodies eternally new ... Thy infinite gifts come to me only on these very small hands of mine. Ages pass, and still thou pourest, and still there is room to fill."

The lovingkindness of God shows in the people around me. Lest this note should become the longest chapter of the book, I will only briefly mention their good names and kind deeds.

I commence with my advisors: Ole Madsen and John Germaine. I am most fortunate in having these two exceptional men as my mentors, who have trained me in my metier and much else. Their support and friendship have amply sustained me through the years of doctoral work. In addition to what I have learnt at their feet, I am very grateful to them for their kindness and good humor.

My thanks are also due to the members of my doctoral research committee: Eric Adams and Thomas Fredette, whose feedback and guidance have greatly benefited this work.

A number of people have lit up my life during these years: Emmanuelle St. Claire, Payman Kassaei, Philippe May, Rebecca Frank, Bassam Kassab, Miguel-Angel Hernando Cupido, Behrang Noohi, Jorge Gonzalez, Sarah Bush, Catalina Marulanda, Rachel Adams, Ioanid Rosu, Ramkumar, Greg Da Re, Jesse Hong, Guoping Zhang, Kurt Sjoblom, Soosan Beheshti, Susan Brown, Robert Meyer, Karim Karam, Jean Fitzmaurice, Munish Sawhney, Carl Chen, Analia Barrantes, Row Selman, Amy Germaine, Jingfeng Wang, and Feng Ye. My special thanks are due to Jesse Hong, Greg Da Re, and Catalina Marulanda for their gracious help during the final days of this work, and to Rachel Adams, Diane Jarrah, and Josh Carter for the post-defense celebration.

I owe a lot to Alice Kalemkiarian, for nourishing me with her good cheer, bagels, and a permanent readiness to help. Cynthia Stewart, Vicky Murphy, Pat Dixon, and

Sheila Frankel owe my gratitude for being excellent trouble-shooters and for giving me a smooth passage through the system. And many thanks to Joe Melo of Ashdown House, who happily repaired me and my gadgets with his smile and skills.

My heart is eternally grateful to Catherine Eileen Kelly, for her generous love and friendship. Her innumerable kindnesses defy my words and constrain me to silence.

And finally, *ab imo pectore*, I thank my parents, for literally starting it all. They have been with me all along, with their encouragement for my endeavors and their patience with my follies. They have inspired in my heart a love large and limitless, and I am grateful that I was put in their hands.

This thesis is dedicated to my beloved grandfathers, Bodh Raj and Brahm Dutt, men of exceptional grace and kindness, who both checked out of this world while I was away from home. I aspire to live like them.

Contents

List of Figures

List of Tables

Chapter 1

Introduction

Dredging techniques have been employed for centuries for the development and routine maintenance of ports and harbors. Dredging of waterways is required in the interests of efficiency, economy, and navigational safety. Approximately 300 million cubic yards of material are now dredged in the United States every year (National Research Council, 1997). This dredged material must be managed and disposed of in accordance with the stipulations of various environmental statutes such as the Clean Water Act and the Marine Protection, Research, and Sanctuaries Act.

Various options have historically been available for dredged material disposal. Material with low or undetectable levels of contaminants has been used for beneficial projects like island or marsh creation and beach nourishment. More contaminated dredgings have been used as landfill for industrial development and municipal projects. Dredged material has also been stored in diked, upland containment areas. The use of aquatic disposal sites has been the most common means of dredged material disposal. Uncontaminated material can be safely disposed of in the open waters, but ocean disposal is prohibited if the material is assessed as harmful under the testing required by the Public Law 92-532. Since the remediation of contaminated dredged material proves to be very expensive, the "capping" technique is utilized to minimize the adverse effects on the environment when contaminated dredged material must be disposed of at sea. This technique involves covering the contaminated material with clean sediment (the "cap") in order to isolate the contaminants and to prevent their

resuspension.

The technical and operational feasibility of the capping concept has been demonstrated by laboratory research and practical field applications since the late 1970s. It is recognized as an effective technique for chemical and biological isolation of contaminants (Palermo, 1991) and a number of capping projects have been executed by the U.S. Army Corps of Engineers (USACOE), which is the responsible agency for maintaining and improving the nation's waterways. Fredette (1994) provides a summary of some of the recent projects undertaken by the New England Division of USACOE. The interest in capping techniques was reinforced in 1984, when the convention on the Prevention of Marine Pollution by Dumping of Wastes and Other Matter (the London Dumping Convention) accepted the capping concept, subject to monitoring, as an appropriate technology for rapidly rendering harmless the contaminants of concern in dredged material.

There are basically two types of capping project designs: level-bottom capping and Confined Aquatic Disposal (CAD) capping. The level-bottom capping projects create a discrete mound of dredged material on an existing flat or very gently sloping bottom (Figure 1.1), and then assure coverage of this mound with a layer of clean sediment. CAD projects, on the other hand, require excavation of subaqueous borrow pits which are subsequently filled with dredged material and then capped with clean sediment (Figure 1.2).

A cap is an engineered structure with design and construction requirements that must be met, verified, and maintained over the design life (Brannon *et al.*, 1984). Many design parameters must be considered in a capping project, making each design highly site-specific. The main design considerations include, but are not limited to contaminated and capping sediment properties, disposal site water depth, bottom contours, current and wave conditions, ship prop scour, etc. The multitude of factors affecting the cap design makes each design highly site-specific.

Although extensive experience has been gained from the capping projects of the last two decades, most of the experience is limited to level-bottom capping. CAD capping is a relatively new technique, and the capping of a pilot cell in the inner Boston

Harbor provided the first extensively monitored study of this technique (ENSR, 1997; Murray, 1999). This pilot project involved excavation, filling, and capping of a CAD cell 500 ft long by 200 ft wide by 40 ft deep in a water depth of approximately 40 ft. This trial effort constituted Phase I of the Boston Harbor Navigation Improvement Project (BHNIP), a $66 million project that generated 3 million cubic yards of dredged material from Boston's Inner Harbor (Massport and USACOE, 1995).

The extensive monitoring of the sand cap and an investigation of its performance in this trial project emphasized the need for better understanding of some critical aspects of the capping process. The issues of concern include inadequate knowledge of the geotechnical properties of the dredged material, absence of guidelines regarding the choice of the capping material placement technique, lack of accurate models to predict the short- and long-term fates of the deposited material, and the need for development of better cap monitoring techniques (SAIC, 1997). Research is also needed to understand the impact of cap load on the soft dredged material and to develop methods for analyzing cap stability.

Figure 1.3 shows a schematic diagram of a capped CAD cell. A successful capping operation requires that the underlying material have enough shear strength to support the load of the overlying cap. Since the processes of dredging, transport, and deposition effectively remold the dredged material, its strength in the freshly-deposited state in a CAD cell is lower than its in-situ strength prior to dredging. With the passage of time, the shear strength of this material increases. If a cap is placed before it has developed the strength required to support the load, the cap will penetrate through the weak material, leaving the contaminants exposed to the water column. On the other hand, the polluted dredged material continues to release contaminants into the water column during the time it stays uncapped. The cap, therefore, should be placed as soon as the dredged material is strong enough to support it, but no sooner. A related issue is the mode of cap placement, i.e., whether the cap is placed in one operation or in incremental layers. To ascertain the proper cap-placement mode and timing from the properties of a given dredged material, a methodology is required that is based on the knowledge of shear strength development in dredged

sediments.

Once the cap is placed, it is susceptible to erosion due to waves and currents. Storm conditions at the site can lead to the loss of especially large amounts of capping material. For a given cap thickness, the design life of the cap is based on an estimate of the amount of cap material lost due to erosion. Although a number of models are available for the long-term fate prediction of materials deposited in water, all these models treat the suspended sediment transport in a steady-state manner. It is assumed that the concentration profile of suspended sediment in the water column is in equilibrium with the concentration of available sediment at the bottom of the column. It has, however, been acknowledged by many researchers (Freeland *et al.*, 1983) that the non-equilibrium effects may be important, and that neglecting these effects may lead to considerable error in transport calculations (Nadaoka *et al.*, 1991).

Figure 1.4 illustrates a common problem that arises with the sediment transport models when the non-equilibrium effect in suspended sediment is ignored. The figure shows a water column traversing a region of a sharp interface between two different types of sediments. This situation is representative of the region around the edges of a cap comprised of non-native materials. Initially, the suspended concentration profile of the native material in the water column is in equilibrium with the bottom availability of the sediment. When this water column enters the region of non-native cap material, the assumption of the equilibrium condition forces it to instantaneously release all the native sediment in suspension. Equivalently, it is required to instantaneously pick up an amount of the non-native material that corresponds to its equilibrium suspended concentration profile. As the grid size of the model decreases, the equilibrium assumption in this case leads to a prediction of increasingly unreasonable scour and deposition patterns at the cap edges. Incorporation of the temporal response of suspended sediment concentration can alleviate this problem and provide a better picture of bed evolution in time, and hence, of the long-term fate of the cap.

The research effort presented here aims to study the two issues described above: strength development in consolidating dredged material, and improvements in the methods for long-term fate prediction of cap material. The former problem lies in

the domain of geotechnical engineering while the latter belongs to the realm of sediment transport. The choice of these two problems from rather disjointed areas of environmental engineering merely serves to illustrate the multi-disciplinary nature of the research needs of present-day environmental projects. The rest of this thesis is divided into two parts that are devoted to separate treatment of each problem.

1.1 Organization of thesis

The next four chapters (Chapters 2-5) present the research on shear strength development in consolidating dredged material. Chapter 2 provides a theoretical background and a survey of the extant literature on the subject. The structure of the experimental program is described in Chapter 3, along with the different test methods employed in the experiments. Chapter 4 is devoted to presentation and discussion of results. In Chapter 5, the applicability of the research results is illustrated with a simple example. Conclusions and suggestions for future research are also presented in this chapter.

Chapters 6 though 9 present the research on the non-equilibrium effect in suspended sediment concentration. Chapter 6 introduces the subject. In Chapter 7, theory is developed for the temporal response of suspended sediment concentration. A Lagrangian model is presented for estimating the net sediment transport rate due to the non-equilibrium effect in certain physical systems. Chapter 8 provides examples of applications of this model, along with a discussion of the results obtained. Chapter 9 concludes with a summary of the findings of this research and recommendations for future work.

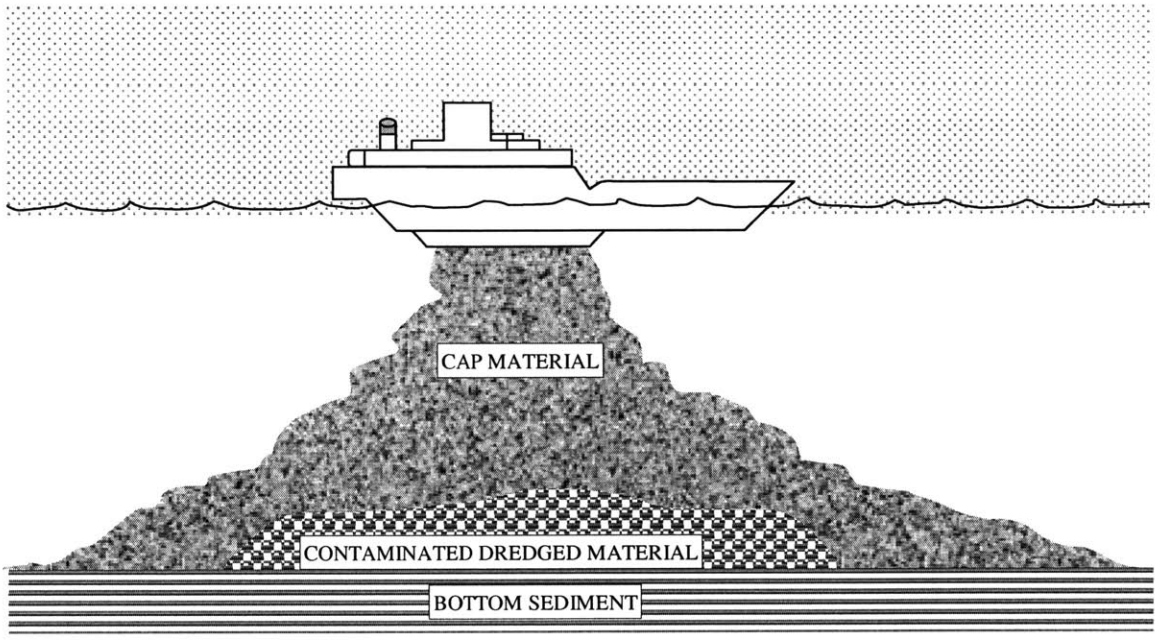

Figure 1-1: Level Bottom Capping Operation

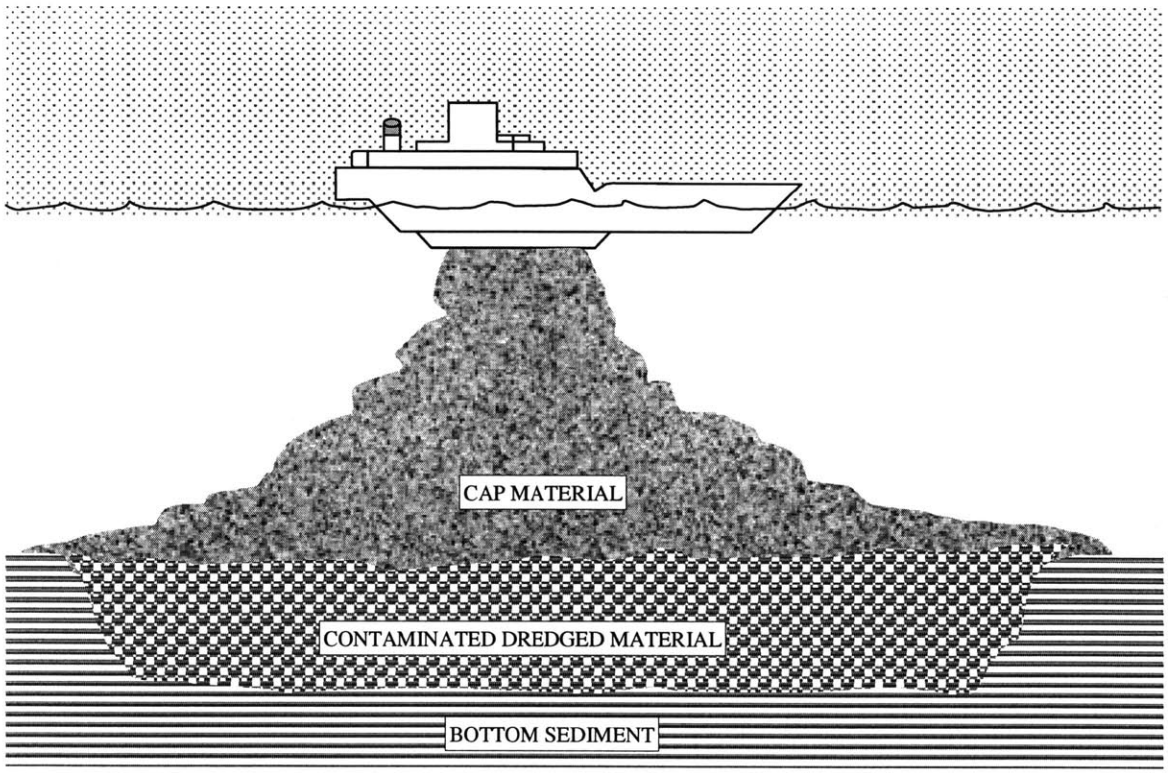

Figure 1-2: Confined Aquatic Disposal (CAD) Capping Operation

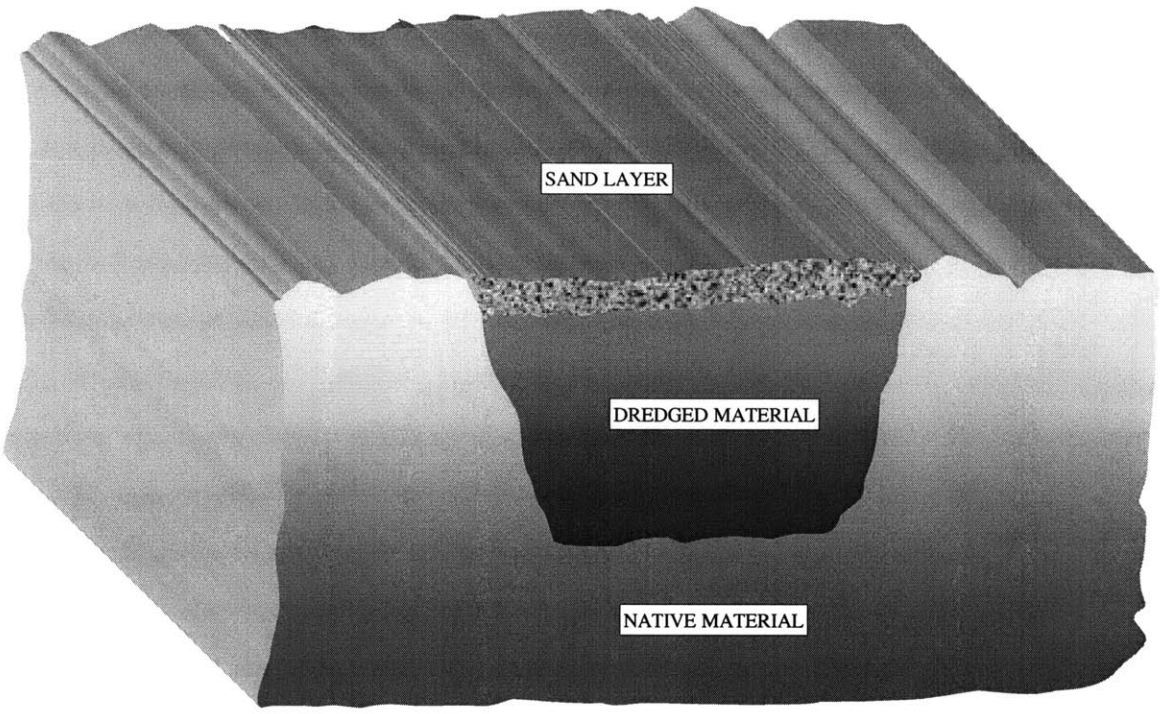

Figure 1-3: Schematic Diagram of a CAD Cell

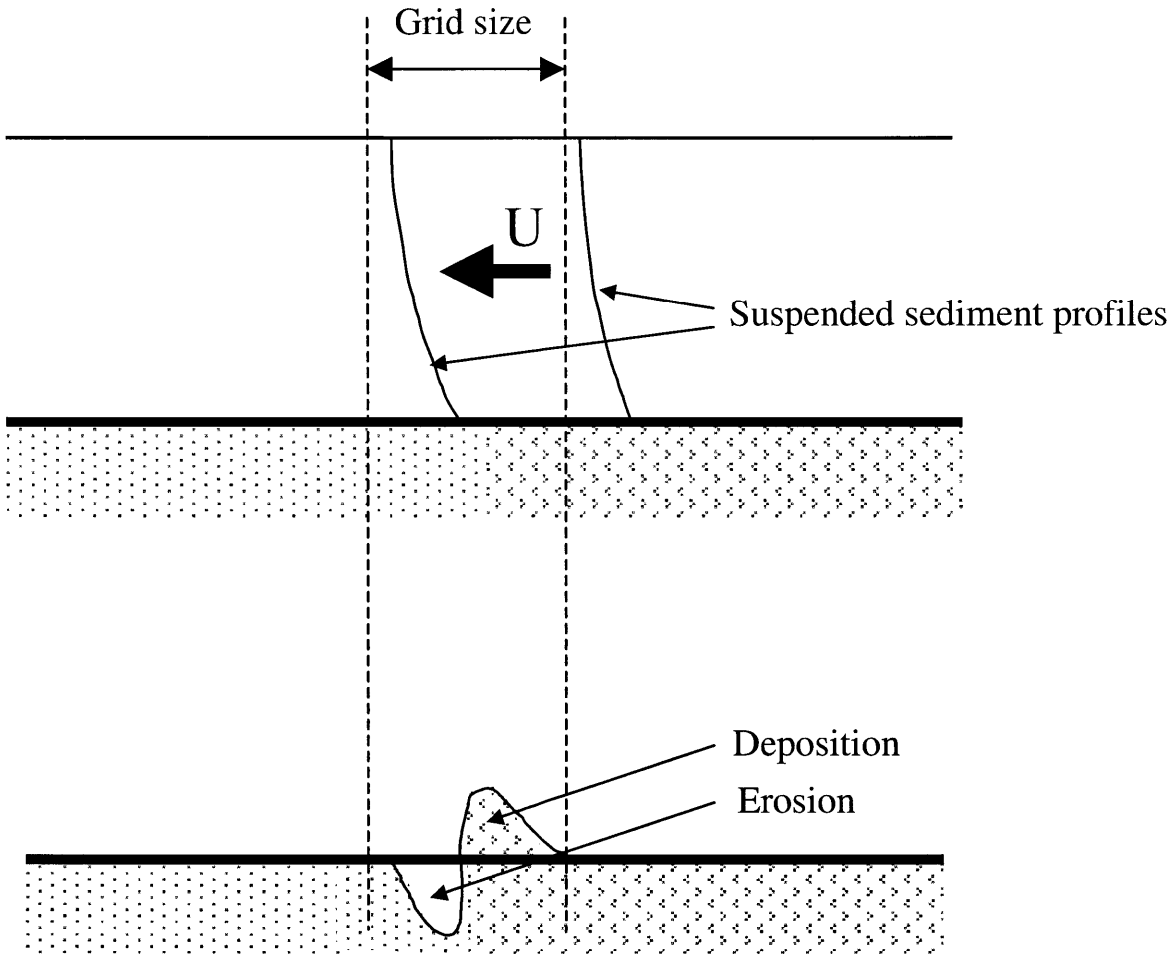

Figure 1-4: Scour and deposition patterns predicted near the cap edges by equilibrium-based sediment transport models

Chapter 2

Part I: Background

The process of shear strength development in dredged materials is of direct relevance to capping projects because a certain amount of time is required before the dredged material develops the strength required to support the cap. Successful capping of dredged marine sediments in CAD cells, therefore, requires an ability to estimate the shear strength as it varies with time. Also of concern in capping design is the consolidation behavior of the dredged material, because estimating the decrease in volume due to consolidation is critical to proper sizing of the CAD cells.

Freshly-deposited dredgings are a fluid-mud mixture at high water content, with strength characteristics that are known to be markedly different from those of the compact soils. The undrained shear strength of these materials does not exceed 50 g/cm^2 (1 $g/cm^2 = 98\ N/m^2$), which classifies them as soft sediments.

Due to their prevalence in both natural and anthropogenic environments, soft sediments have been the subject of a number of investigations. Various aspects of the work presented here have been studied in different contexts and to different degrees. Knowledge of these previous efforts provides a background for the present research, and highlights both the motivation as well as the significance of the work presented in the following chapters. To this end, the scope and results of previously published studies, arranged by topic, are discussed in the following sections.

2.1 Large Strain Consolidation

Consolidation is the process of time-dependent densification of the soil under a load. For soft sediments, the self-weight of the matrix is sufficient to cause large deformations in a deposit. The process of self-weight consolidation is of interest in many different engineering disciplines, which include geotechnical, environmental, coastal and chemical engineering. Some examples from the wide range of applications of consolidation include designing the capacity of disposal sites for dredged material (Umehara and Zen, 1982), prediction of surface settlement due to self-weight subsidence of soft soils in aquifers (Corapcioglu, 1984), and estimating suspended sediment transport of cohesive marine sediments (Alexis *et al.*, 1992).

Consolidation is distinguished from sedimentation, which is the process of particles settling from a suspension. The interest in research on consolidation has historically come from the area of geotechnical engineering and soil mechanics whereas sedimentation from suspensions and slurries has been investigated mainly by chemical and materials scientists (Buscall, 1990). The theories for these two closely linked processes have developed independently of each other until relatively recent research efforts of Been and Sills (1981), Pane and Schiffman (1985), Partheniades (1986), Schiffman *et al.*, (1988), and Toorman (1996, 1999).

A suspension is characterized by zero effective stress and behaves as a non-Newtonian fluid. The weight of sediment in this phase is completely borne by water. As particle flocs come together and begin to settle, physical contact between them forms a structure that can support a fraction of the total vertical stress. This point of inception of effective stress identifies the transition from suspension to soil. The process of self-weight consolidation begins at this point, as more material settles on top of this highly compressible skeleton structure and squeezes out the pore water from it. Under a constant load, the excess pore pressure that develops as a result of loading dissipates as consolidation proceeds, and the end of consolidation is marked by zero excess pore pressure.

Reviews of different approaches to self-weight consolidation can be found in Schiff-

man *et al.*, (1988) and Alexis *et al.*, (1992). The following paragraphs present a discussion of the important contributions in this field.

The first theory of consolidation was proposed by Terzaghi (1943), based on the assumptions of infinitesimal strain and constant compressibility and permeability of the material. Starting with mass conservation and force equilibrium, Terzaghi derived the consolidation equation:

$$c_v \frac{\partial^2 u_e}{\partial z^2} = \frac{\partial u_e}{\partial t} \tag{2.1}$$

where u_e is the excess pore pressure, z is the coordinate in vertical direction, and t is time. The coefficient of consolidation, c_v, is given by:

$$c_v = \frac{k(1+e)}{\gamma_w a_v} \tag{2.2}$$

where k is coefficient of permeability (also called hydraulic conductivity), e is void ratio (ratio of volume of voids to volume of solids), γ_w is unit weight of water and a_v is the coefficient of compressibility (measured as the slope of the void ratio-effective stress curve for the soil).

Figure 2.1 is a graphical presentation of the non-dimensionalized solution for a simple case of one-dimensional constant loading. The curves show the evolution of consolidation ratio, U_z, which is defined as:

$$U_z = 1 - \frac{u_e}{u_0} \tag{2.3}$$

where u_0 is the value of initial uniform excess pore pressure. The non-dimensional variables are:

$$Z = \frac{z}{H} \tag{2.4}$$

and

$$T = \frac{c_v t}{H^2} \tag{2.5}$$

where H is the length of drainage path. Both z and Z are measured from the top of the consolidating deposit. The rate of settlement is assumed to be the same as the

rate of pore pressure dissipation, and therefore the same curves are used to compute the volume change due to consolidation.

Terzaghi's theory is widely used in conventional soil mechanics applications. A notable difference between experimental consolidation results and the predictions of Terzaghi's theory is the phenomenon of secondary compression, illustrated in Figure 2.2, which shows settlement on a log-time scale. The initial high-slope part of the curve corresponds to primary compression regime, where pore pressures are dissipating in accordance with Terzaghi's equation. The latter part of the curve has a very low settlement rate and almost zero excess pore pressure. This regime is termed secondary compression, and the settlement in this regime may be appreciable for organic and highly plastic soils.

Terzaghi's consolidation equation is known to give erroneous results (Cargill, 1984; Papanicolaou and Diplas, 1999) when applied to self-weight consolidation of soft sediments. This is because the consolidation in soft sediments is characterized by large deformations and variable compressibility and permeability.

Davis and Raymond (1965) developed a non-linear settlement model based on a logarithmic relationship between void ratio and effective stress. The first complete finite strain formulation of consolidation was presented by Gibson *et al.* (1967) in a Lagrangian coordinate system. The non-linear governing equation presented therein forms the basis for most of the present-day consolidation models.

In a pioneering study, Been and Sills (1981) conducted sedimentation and consolidation experiments on an estuarine mud. The authors used the large strain consolidation theory with the assumption of a linear void ratio-effective stress relationship and a constant coefficient of consolidation. The model results indicated a good ability to predict the settling and consolidation of soft soil beds deposited from suspension. The same approach was utilized by Lee and Sills (1981), who obtained analytical expressions for self-weight settlement behavior of soft soils.

Most advances in self-weight consolidation have been made with numerical techniques based on the theoretical model of Gibson *et al.* (1967). Both Lagrangian and Eulerian forms of the governing equation have been numerically solved, using finite

difference, finite element or combined approaches. A short list of numerical research efforts includes the following works: Carrier *et al.* (1983), Cargill (1984), Mesri and Choi (1985), Huerta *et al.* (1988), Feldkamp (1989), Townsend and McVay (1990), Liu and Znidarcic (1991), Fahey and Toh (1992), Huerta and Rodriguez (1992), Shodja and Feldkamp (1993), Seneviratne *et al.* (1996), Fox and Berles (1997), Tuncay *et al.* (1998), Fox (1999), Toorman (1999), Papanicolaou and Diplas (1999), Lee *et al.* (2000), and Consoli and Sills (2000).

There is general agreement on the fact that the state of today's modeling techniques is sophisticated enough to capture the consolidation process, and that the accuracy of results is limited by the quality of constitutive relationships that are used as input for modeling. The conventional geotechnical procedure of oedometer testing is not appropriate for very soft sediments due to both theoretical and testing constraints. For the determination of consolidation characteristics of very soft marine sediments, Umehara and Zen (1980) advised on a test method based on a modified constant rate of strain (CRS) consolidation and also on the interpretation of these CRS results. In a subsequent paper (Umehara and Zen, 1982) the authors used the procedure to obtain the consolidation characteristics of soft bottom sediments from seven Japanese harbors. Slurries were preloaded in consolidation rings prior to testing in the CRS apparatus. Sedimentation tests were carried out on slurries with initial void ratio ranging from 4 to 79, to evaluate the characteristics in the low pressure range. The authors reported a dependence of compressibility on initial water content in the low effective stress regime. The coefficient of consolidation was found to increase with effective stress, with the stress dependence being different for each sediment type.

Another technique for determination of consolidation characteristics of soft sediments was developed by Imai (1979), who proposed a consolidation test in which a constant head difference is maintained across the sample while imposing a downward seepage force. Liu and Znidarcic (1991) have adopted a version of this seepage-induced consolidation test whereby flow rate instead of head difference is maintained constant. Measurements are made of final (consolidated) sample height and bottom

effective stress as the sample achieves steady state conditions. These two values in conjunction with the measurement of zero effective stress void ratio ascertain the low pressure consolidation behavior of the material. The consolidation characteristics in high pressure regime are obtained by consolidating the seepage-induced test sample to a high value of vertical effective stress and then measuring its permeability and void ratio. The constitutive relationships are parameterized in accordance with the inverse solution approach developed by Znidarcic (1982) and adopted by Huerta *et al.* (1988). The void ratio, e, is expressed as an extended power function of effective stress, σ'_v:

$$e = A(\sigma'_v + Z)^B \tag{2.6}$$

whereas the coefficient of permeability, k, is related to void ratio by the conventional power function:

$$k = Ce^D \tag{2.7}$$

Based on the governing equation for large strain consolidation (Gibson *et al.*, 1967), the empirical factors A, B, C, D, and Z are determined from the steady state test data obtained from the seepage-induced consolidation test. The use of steady state as the measurement basis differentiates the technique from those based on transient state measurements (e.g., Been and Sills, 1981). The constitutive relationships derived from this parameterization procedure were employed in numerical modeling of consolidation of soft phosphatic waste clays (Abu-Hejleh *et al.*, 1996) and the results were found to be in good agreement with field data.

Some researchers have adopted the approach of using universal constitutive relationships derived on the basis of data aggregated from many different materials. Papanicolaou and Diplas (1999) numerically solved the general self-weight consolidation equation by reducing it to a transient non-linear partial differential equation of parabolic type. This Eulerian form of the governing equation was solved by using finite element method in space and finite difference method in time. For constitutive relationships the authors relied on the best-fit equation for 59 consolidation test data points from 39 different materials. A linear distribution was assumed as the initial

condition for effective stress distribution. The model predictions were compared with data from an attapulgite slurry settlement experiment of Tiller and Khatib (1984) and from a self-weight consolidation experiment on kaolinite-bentonite mixture, conducted by Been (1980). A good agreement was found for settlement rates as well as for density profiles. Since the constitutive relationships are based on the best-fit analysis of data from many different materials, the authors claimed that the model can be run for a wide range of materials with satisfactory results. It was also shown that the error due to the assumption of linear effective stress distribution in the column at the beginning of consolidation decreases with simulation time and is negligible at long times. The data used in the study were drawn from the low effective stress range and would need to be extended for the model results to be valid for large strains.

In a similar study, Alexis *et al.* (1992) attempted to compute universal constitutive relationships by conglomerating data from numerous other research efforts (Imai, 1981; Umehara and Zen, 1982; Pane *et al.*, 1982; Yong *et al.*, 1983; Tan *et al.*, 1988; Tan *et al.* , 1990; and Toorman, 1992). The constitutive equations derived from the best fit to these data were successfully employed in a numerical model to reproduce the laboratory settling column results of Been and Sills (1981). The authors also reported field measurements on the muds from Elorn Estuary in Brittany to illustrate the difficult task of modeling the in situ behavior of soft marine sediments.

Centrifuge modeling has also been advantageously employed to simulate the consolidation process. This technique has the advantage that the actual consolidation time scale, which can be of the order of a few years for very soft materials, is reduced by the square of the scaling factor, hence permitting long-term simulations. Centrifuge modeling of a mine tailings deposit is described by Stone *et al.* (1994). Data obtained from centrifuge tests were combined with results from Rowe cell oedometer tests on the tailings to compute the consolidation parameters for the material. A Lagrangian finite difference model developed by Fahey and Toh (1992) used these parameters along with the initial conditions to predict the settlement in the deposit for up to 12 years from the time of deposit.

A common theoretical framework is emerging for unified treatment of sedimenta-

tion and consolidation processes. Toorman (1996) proposed a general theory, starting from two-phase conservation equations. It was demonstrated that this general theory contained the seemingly different governing equations employed in chemical and geotechnical engineering, including the well-known equation of Gibson *et al.* (1967). Although this theory can be applied over the whole range of concentrations from zero to maximum consolidation, a big obstacle remains in the formulation of constitutive relationships required for numerical modeling of consolidation. All forms for these relationships assume the permeability and effective stress to be functions of void ratio alone (A review of various constitutive equations is given by Krizek and Somogyi, 1984). The dependence of effective stress on concentration alone, which is correct in the regime of consolidation, is an impediment in the development of a single theory for sedimentation-consolidation, because it predicts a finite effective stress in a suspension where effective stress is actually zero. Toorman and Huysentruyt (1997) investigated this problem and also some alternative solutions for it. In a subsequent publication, Toorman (1999) proposed new semi-empirical relationships for modeling, including the suggestion to split the effective stress contribution into two terms: the first arising from the support of particles and the second representing the structural resistance to deformation of the floc network. The author reported that the consolidation rates predicted by the models for late stages of primary consolidation were higher than the values measured in experiments (Figure 2.3). For cohesive sediments, the internal structural changes that are purely time-dependent are likely to affect the permeability of sediment bed. This phenomenon is not accounted for in the closure equations and is a possible explanation for over-prediction of consolidation rates by numerical models. These observations point out the need for more detailed experimental work that can provide the high-quality data required for modeling.

2.2 Undrained Shear Strength of Soft Sediments

Placement of a cap imposes impact and static loads on the underlying dredged material. A successful capping design needs to ensure that the underlying material can

support these loads. The bearing capacity for a sediment foundation is defined as the mean total stress on its load-bearing surface when this surface is on the point of collapse. A cap is expected to be stable when the loads imposed by it on the underlying material are smaller than the bearing capacity of this material.

In subaqueous capping projects where the underlying dredged material consists mainly of silt and clay fractions, the consolidation time for the underlying deposit is much greater than the cap loading time. The situation, therefore, corresponds to undrained loading and the sediment strength in this case depends mainly on pre-load conditions. Furthermore, the cap material is often dispersed on the dredged sediment (with the use of a split-bottom barge, for example) and does not penetrate the underlying material. The bearing capacity, q_u, in this case is given as a direct function of the undrained shear strength of the underlying material:

$$q_u = c_u N_c \tag{2.8}$$

if the undrained shear strength, c_u, is assumed to be constant in the underlying deposit. N_c is a dimensionless bearing capacity factor (Lambe and Whitman, 1969). For the case of infinitely long strip loading that does not penetrate the substrate, Terzaghi and Peck (1967) give a value of 5.14 for N_c. Chen (1975) has reported on values of N_c estimated by researchers for various load configurations.

A more realistic formulation is to assume that the undrained shear strength varies linearly with depth. In a bearing capacity analysis of soft seabed sediments, Hu *et al.* (1999) used this approximation:

$$c_u = c_{um} + kz \tag{2.9}$$

where c_{um} is the soil strength at the seabed (the mudline), k is the strength gradient and z is soil depth. Although this formulation permits a simple analysis, it leaves out many important features of shear strength variation. Figure 2.4 shows the variation of shear strength in an actual deposit of gold mine tailings (Stone *et al.*, 1994). The deposit was placed in multiple stages. The depth profile of strength is seen to change

with time, and this time-related increase in strength is known to be a complicated process that depends upon, among other things, water content as well as the magnitude of effective stress (Zreik, 1994). It is acknowledged that two different mechanisms contribute to the gain in shear strength of sediments. The first is the consolidation-related strength gain, which is the result of solid particles coming closer as the pore water is squeezed out of the deposit. The second contribution comes from thixotropy, which is defined as the reversible time-dependent increase in strength of the material occurring under conditions of constant composition and volume (Mitchell, 1960).

Silva *et al.* (1994) have discussed in detail the geotechnical aspects of a level-bottom capping project. An example of bearing capacity calculation for contaminated submarine sediments is provided in Ling *et al.* (1996).

The concept of capping is not limited to underwater isolation of contaminated sediments. The method of choice for sequestering mine tailings is to impound them under a cover of cleaner material in specially designed dams (Williams *et al.*, 1997; Rassam and Williams, 1999), and the undrained shear strength of tailings is a critical required input for dam design. Other examples of capping applications are crusted coal-mine tailings (Williams, 1992), soft fine phosphatic clays (Carrier *et al.*, 1983), and mixtures of landfill ash and wastewater sludge (Benoit *et al.*, 1999).

In addition to capping, the importance of sediment shear strength is obvious in many other projects, which include land reclamation (Kurumada *et al.*, 1992), construction on super soft clays (Yano *et al.*, 1985; Fakher and Jones, 1996), drilling projects (Rabia, 1989), seabed pipeline design (Murff *et al.*, 1989; Pastor *et al.*, 1989), skirted shallow foundations (Hu *et al.*, 1999) and suction anchor piles for permanent mooring of large structures (Rao *et al.*, 1997; Colliat *et al.*, 1998).

Interest in shear strength of sediments stems also from its correlation to various other material properties. The erosion potential of contaminated sediments has been related to the undrained shear strength (Tsuruya *et al.*, 1986; Zreik, 1994). This relationship is used for prediction of sediment transport under currents and wave action in riparian and marine environments. Soil scientists have also used the undrained shear strength of soils as a measure of their resistance to detachment by raindrops

(Sharma *et al.*, 1991; Becher *et al.*, 1997). Another strength-dependent phenomenon of interest is the formation of mud waves when a sudden load is placed upon weak sediments (Broms, 1987).

Notwithstanding a wide range of situations where the shear strength of soft sediments is an important parameter, literature concerning this subject is scant. In comparison, the state-of-art in understanding and predicting the strength behavior in classical soils is quite well developed (Ladd and Foott, 1974; Sheahan *et al.*, 1996). The discrepancy is explained by the difficulties encountered in measurement of very low values of strength.

2.3 Measurement of Strength in Soft Sediments

Zreik (1991) and Fakher *et al.* (1999) have summarized various methods that have been used for strength measurements in very weak sediments. The devices employed most commonly are viscometers and penetrometers. In a viscometer, the yield strength of soils is quantitatively determined by carrying out a stress-strain rate test. The shear stress at zero rate of shear is taken as the yield stress of the material. Since viscometer measurements are conducted at finite shear strain rates, the stress-shear rate data are extrapolated to zero shear rate to ascertain the yield stress. The penetrometer principle, on the other hand, is based on relating the penetration of the device into the sediment matrix to the undrained shear strength of the matrix.

Various types of viscometers are used in practice. Prominent in use are the coaxial viscometer (consisting of concentric rotating cylinders with the sample material in the annular space) and the shear vane device (consisting of a vane with four blades). Examples of penetrometers are the Swedish fall cone, the Automated Fall Cone Device (Zreik, 1994), the falling ball device (Zakaria, 1994), the thin plate device (Inoue *et al.*, 1990), and the T-penetrometer (Stewart and Randolph, 1991).

A number of research efforts have employed viscometers or the fall cone for measurement of sediment shear strength. Selected examples include Nguyen and Boger (1983), Bentley (1979), Dzuy and Boger (1985), Torrance (1987), and Locat and

Demers (1988).

The fall cone and the shear vane are able to measure shear strength of either undisturbed or remolded sediments, whereas the rotary viscometer device by its very method of operation is limited to remolded soils. The methods of choice, therefore, are the shear vane and the fall cone penetrometer, both of which are simple strength index tests. These tests are simple and quick, and can be performed on samples that are still in the coring tubes or barrels, thus preserving to a large extent the in situ water content. The lowest measurable strength for both these devices is in the range of 1-5 g/cm^2 (98-490 N/m^2). The laboratory shear vane device has been used to develop empirical cone factors for the fall cone device (Karlsson, 1961; Wood, 1985), and remains the more commonly used device of the two for strength measurements in the field. The requirements of the present research program, however, favor the choice of a fall cone-type device. This is because it is difficult to adapt a lab vane to measure very low values of strength since it would require an ability to measure very small torques (Zreik *et al.*, 2000). Furthermore, a modification of the traditional fall cone device is available that was developed by Zreik (1991) for the measurement of ultra-low values of shear strength. This device, discussed later in this section, is able to provide both the low-strength measurement capability and the depth resolution required for obtaining the shear strength profiles in very soft sediment.

A historical account of research and development of the fall cone is given in Zreik (1991). The fall cone was originally developed by the Swedish Railways to measure the strength of soft clays. The device consisted of a cone whose depth of penetration under free fall in a clay sample was taken as an indicator of the shear strength of the sample. Hansbo (1957) performed a theoretical analysis of cone motion dynamics, and verified his results with high-speed photography. He proposed the semi-empirical relationship between the shear strength, c_u, cone weight, W, and cone penetration, d:

$$c_u = k\frac{W}{d^2} \tag{2.10}$$

where k is a constant depending on the cone shape.

Houlsby (1982) presented a detailed analysis of the motion of a cone penetrating a horizontal surface of a material, along with an investigation of the effects of various phenomena (viscous effects, soil self-weight, etc.) on the motion of the cone. Based on these studies, he suggested the theoretical values of k to be used for different cone angles. A finite element numerical simulation of cone penetration was also carried out.

Karlsson (1961) and Wood (1985) carried out a comparison of shear strength measurements using fall cone and vane shear devices, and obtained "experimental" k values, which were found to be lower than the theoretical ones. According to Zreik (1991), this may be due to the difference in strain rates between the shear vane and the fall cone tests.

The fall cone has been extensively used to empirically correlate various characteristic properties of soils. The relationship between liquid limit and fall cone penetration has been extensively studied, for example, in the research efforts of Clayton and Jukes (1978), Nagaraj and Jayadeva (1981), Wood (1982), Nagaraj *et al.* (1987), Wasti (1987), Koester (1992), and Farrell *et al.* (1997). Fall-cone shear strength has been correlated with the plastic limit of the material by Wroth and Wood (1978), Lerouil *et al.* (1983), Harison (1988), and Feng (2000), and with water content by Wood (1985), and Kumar and Wood (1999), among others. Zreik (1994) reports that the fall cone has also been extensively used by agriculture scientists (Al-Durrah and Bradford, 1981; Sharma *et al.*, 1991) to estimate various properties of farm soils.

Kravitz (1970) used both the fall cone and the shear vane devices to measure the strength of weak soils, but found that the devices suffered from poor repeatability for strength values below 5 g/cm^2.

Numerous studies (for example, Krizek and Salem, 1977; Lu *et al.*, 1991; Ockenden and Delo, 1991; Christian *et al.*, 1991; Suthaker and Scott, 1997) have reported the undrained shear strength measurements carried out in the course of research on soft sediments. Nevertheless, there is no published research documenting a systematic investigation of the process of shear strength development in soft sediments, with the exception of Krizek and Salem (1977) and Zreik *et al.* (1998).

The first authors conducted laboratory and field strength measurements on dredged materials placed in upland disposal sites, which exhibited strengths above 5 g/cm^2. They reported an increase with time in the undisturbed strength profile over a depth of 5 meters, indicating the importance of thixotropic behavior in dredgings. It was also found that the shear strength values determined in laboratory by unconfined compression test were significantly lower compared to the fall cone measurements. The strength loss was attributed to sampling and trimming disturbances.

Zreik (1991) developed a more sensitive version of the conventional fall cone, called the Automated Fall Cone Device (AFCD), which is capable of measuring strengths as low as 0.03 g/cm^2. The depth resolution in measurements is in the range 5-10 mm, compared to 13 to 33 mm for the lab shear vane. The author sedimented beds of Boston blue clay from the slurry state and carried out experiments to investigate the effects of depth, age, initial water content and deposit height on the undrained shear strength of the material. The strength at a given depth was found to increase with decreasing bed thickness for beds of same age and initial water content. At early times, the strength was mainly a function of water content, with a secondary positive dependence on effective stress (Figure 2.5). At later times, the effective stress dependence was dominant, with a secondary water content effect (Figure 2.6). Furthermore, the author found the magnitude of thixotropic strength gain to be significant and increasing with increasing effective stress. It was hypothesized that the bed structure after the end of primary consolidation continued to undergo the process of floc rearrangement. This redistribution of internal stresses at constant volume is responsible for the strength increase with time.

The authors did not perform long term tests to determine the end of thixotropic strength gain. There is also a need for data to investigate the scaling effect of deposit height on shear strength development. This information is very relevant in the context of capping design, which requires an accurate estimate of sediment shear strength profile as a function of consolidation time. While the consolidation of soft sediments has been extensively studied in recent years, there is not sufficient data on the shear strength behavior of these sediments.

2.4 Objectives

The goal of the present research effort is to advance our understanding of the process of shear strength development in soft sediments. Specifically, this research strives to answer the following questions:

- Does the classical shear strength formulation, based on cohesion and friction angle, hold at low effective stresses?
- Relative to primary consolidation, what is the contribution of thixotropy to undrained shear strength?
- Is the thixotropic strength gain concurrent with primary consolidation, or only subsequent to it?
- What is the effect of initial water content and specimen height on undrained shear strength? In what effective stress range are these effects important?
- Is it possible to parameterize shear strength as a function of effective stress? Given the advanced state of consolidation modeling, can the results of numerical consolidation models be empirically extended to obtain estimates of undrained shear strength?

The knowledge of the undrained shear strength profile and its variation with time in the consolidating dredged material is a critical prerequisite for cap design as well as cap placement timing. Therefore, the answers to the above questions will form the basis for the development of a useful predictive procedure for capping project managers.

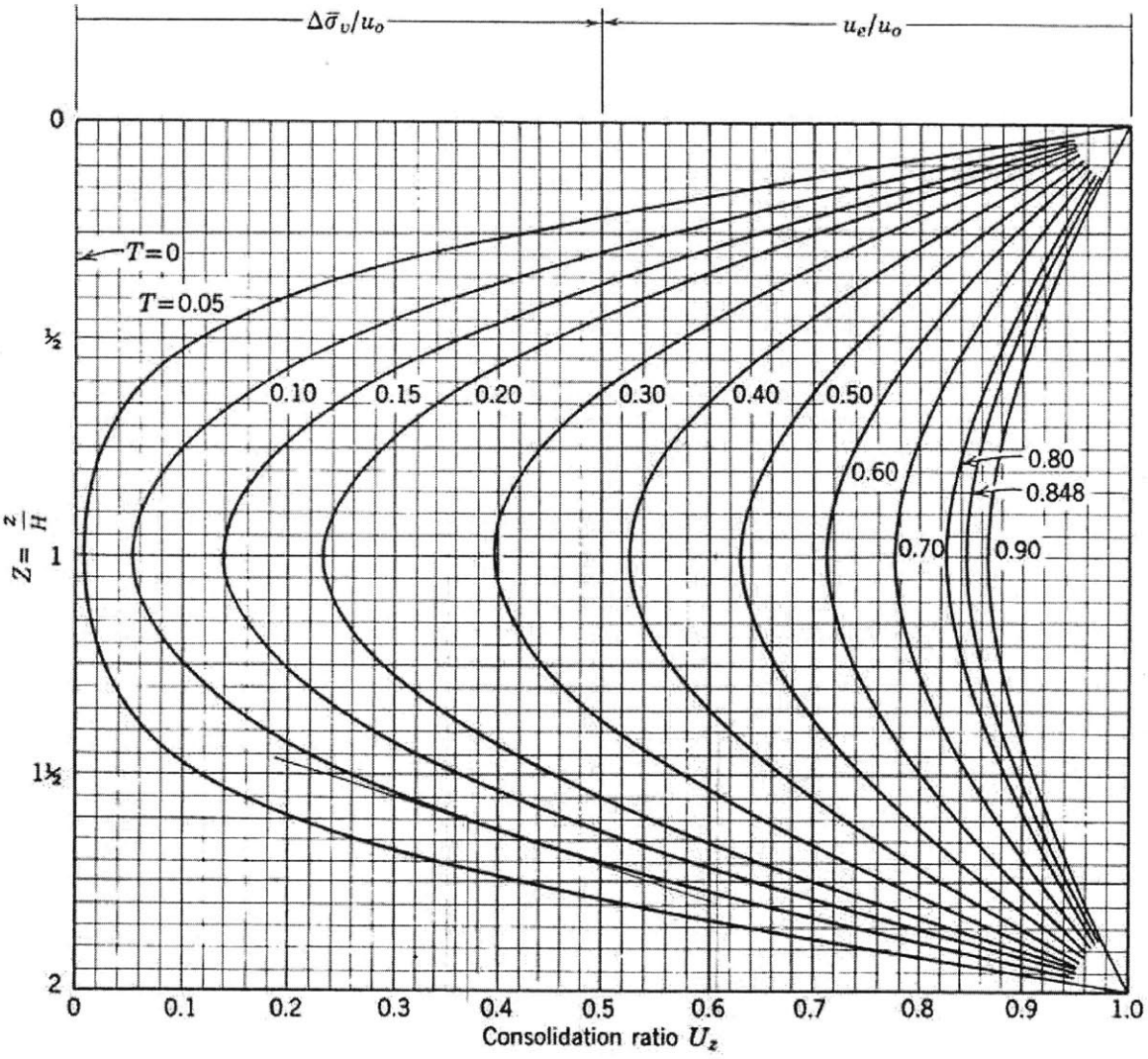

Figure 2-1: Consolidation ratio as a function of depth and time factor (Lambe and Whitman, 1969)

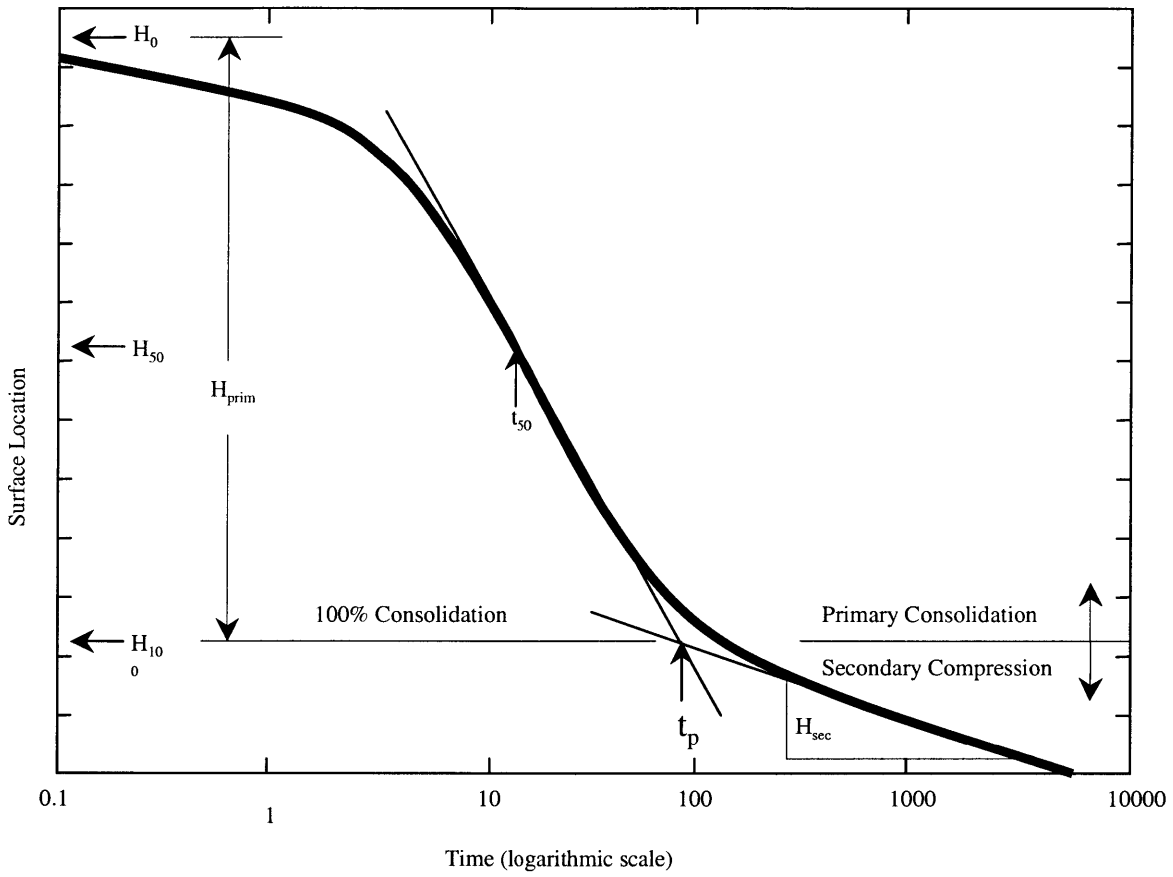

Figure 2-2: Settlement corresponding to primary consolidation and secondary compression in a sediment deposit

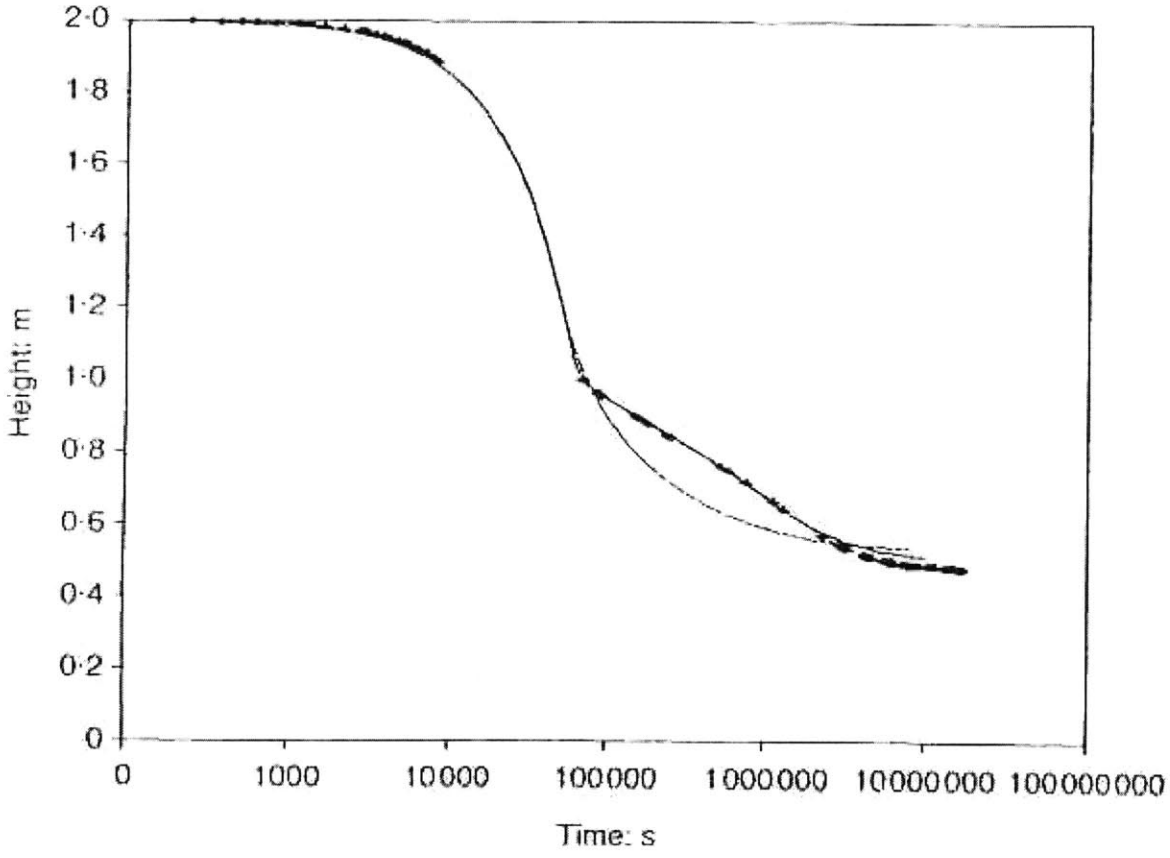

Figure 2-3: Comparison between experimental (+) and computed (lines) settling curves for China clay (Toorman, 1999): Finite element solution without (dashed line) and with (full line) taking into account the additional decrease of permeability

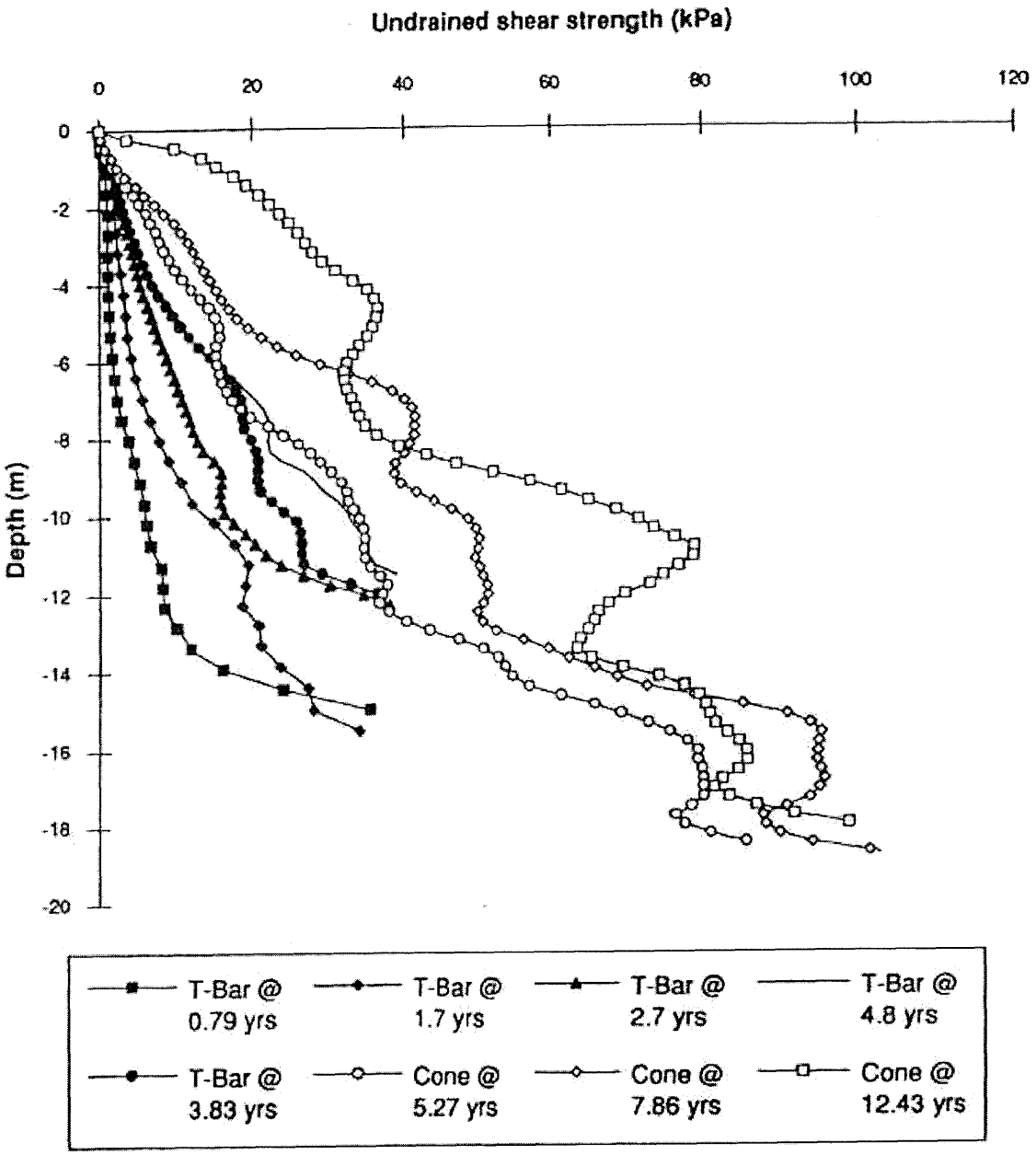

Figure 2-4: Variation of undrained shear strength with depth and time in a deposit of gold tailings (Stone *et al.*, 1994)

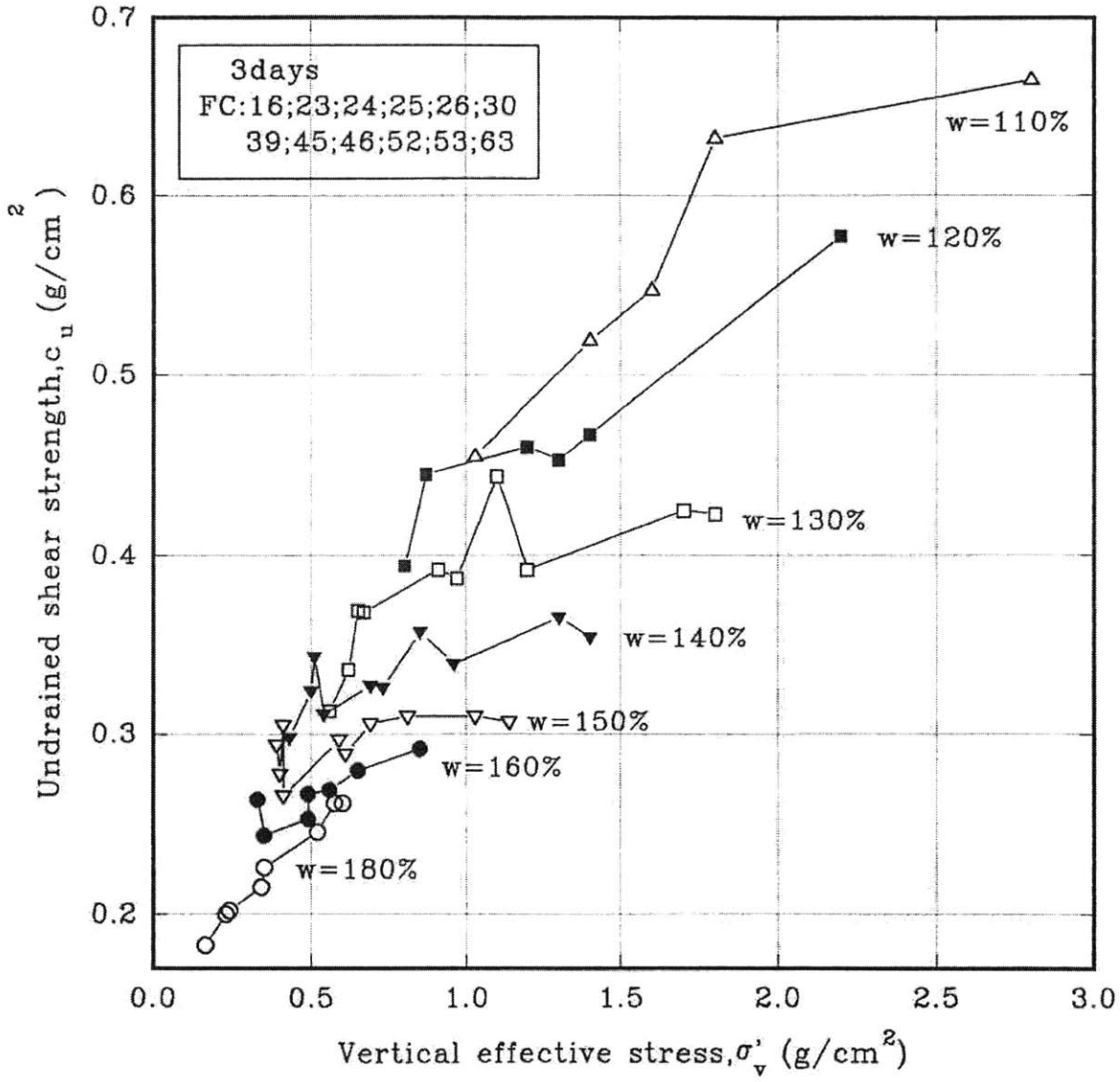

Figure 2-5: Variation of undrained shear strength with vertical effective stress in Boston Blue Clay (Zreik, 1994)

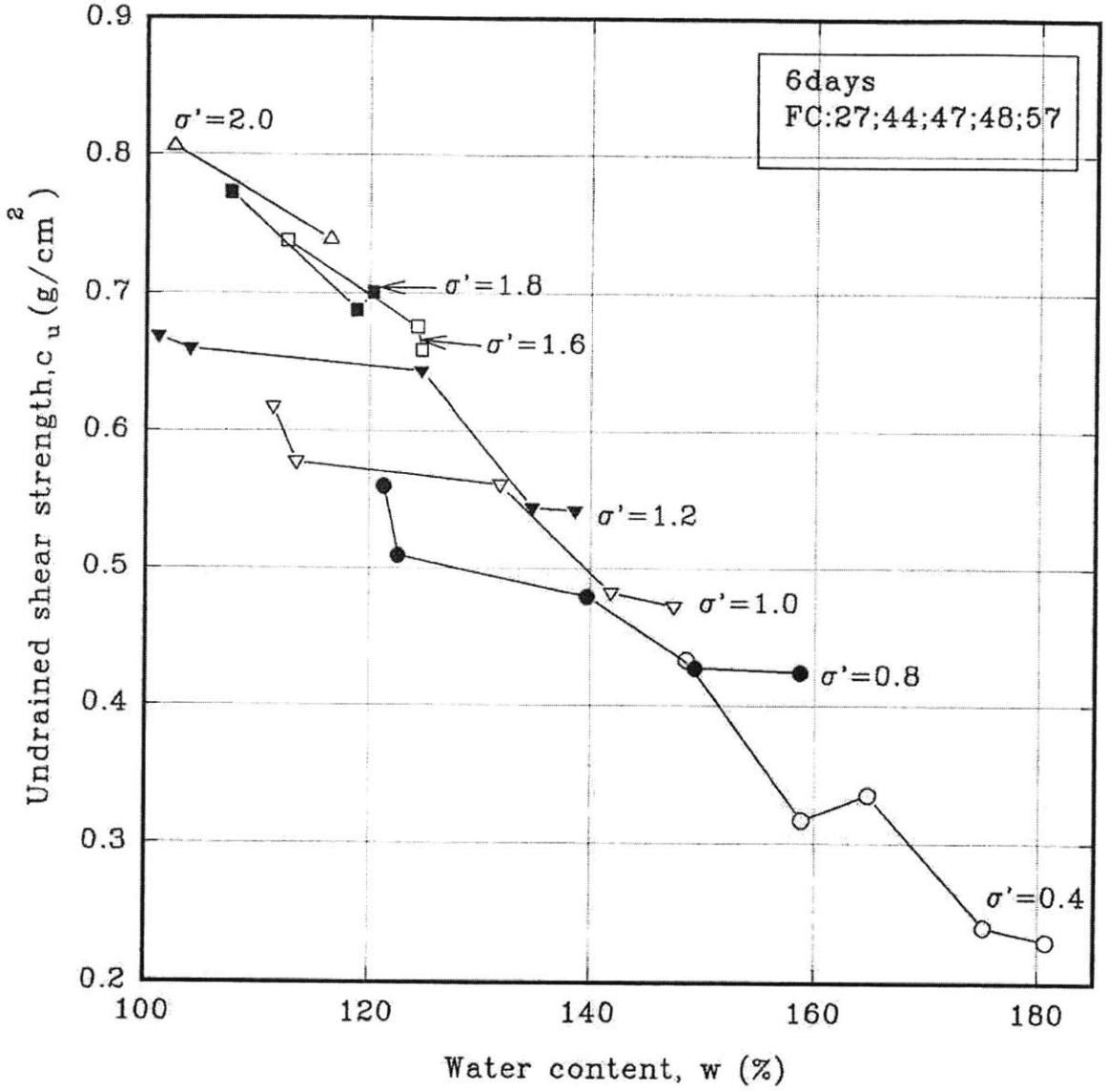

Figure 2-6: Variation of undrained shear strength with water content in Boston Blue Clay (Zreik, 1994)

Chapter 3

Experimental Methods

The experimental program was designed with emphasis on obtaining the depth profiles of undrained shear strength and void ratio in laboratory deposits of dredged sediment, consolidating under self-weight in different conditions of initial concentration, initial deposit height, and age of deposit. Experiments were also conducted to determine undrained shear-strength and void-ratio in sediment specimens undergoing consolidation under different surcharge loads, and to determine the high-stress consolidation behavior of the material.

The various experiments conducted in this program can be categorized as follows:

1. Surface Settlement Experiments for Consolidation Characteristics
2. Self-weight Consolidation Experiments
3. Surcharge Consolidation Experiments
4. Constant Rate of Strain Testing

Each category of these experiments is explained in a separate section in this chapter. The next section describes the dredged material on which these experiments were conducted.

3.1 Sediment Procurement, Processing, Storage, and Characterization

3.1.1 Sediment Retrieval and Processing

This research project was designed to provide capping guidelines for the Boston Harbor Navigation Improvement Project (BHNIP), described in Chapter 2. A site in the Inner Boston Harbor was, therefore, chosen to provide the material for experimental investigation in this study. Sediment was retrieved from the Reserved Channel, an area designated for dredging under BHNIP. The site location is shown in Figure 3.1, and has the GPS coordinates of N $42^o20.575'$, W $71^o01.671'$.

Sediment was retrieved in April 1998, before the channel was dredged. A feasibility report for BHNIP found that the sediment samples from Reserved Channel were fairly representative of the harbor sediments in physical and chemical composition, a notable difference being higher levels of PCBs in Reserved Channel sediments. (Massport and USACOE, 1995).

An Ekman dredge was used to collect the sediment. This device is widely used for sampling of bottom macrofauna (Blomqvist, 1990) and consists of a square-crossection sampler enclosed at the bottom by two spring-loaded jaws (Figure 3.2). The dredge is lowered on a line in free-fall into the surficial sediment. A messenger weight sent down along the line to the device causes the spring-loaded bottom plates to close, trapping the sediment in the process. The supernatant water collected in the dredge during the trapping process leaks out during the withdrawal of the device, because the device permits free water passage. The device was able to penetrate between 10-15 cm into the Boston Harbor sediments. About 25 gallons of the Reserved Channel Sediment (RCS) was retrieved in this manner, in five buckets of 5 gallons capacity. The sediment was first sieved with a Number 10 sieve (opening size: 2 mm) to remove debris. It was then homogenized in a commercial dough mixer. The objective was to break down any existing clods of clay and to ensure a uniform consistency. Each bucket-load was homogenized separately and then divided into five equal parts by

pouring it in five new buckets.

When full, the contents of each new bucket were again homogenized separately in the mixer. It was thus ensured that :

1. The sediment is well mixed in each bucket.

2. There is no variation of sediment properties between different buckets.

3.1.2 Sediment Storage

The experimental program involved testing of multiple sediment specimens prepared and consolidated at different times. In order to ensure that all experiments were performed on essentially the same sediment, it was imperative to maintain a homogeneous stock of sediment under stable conditions.

A sediment removed from its natural environment and stored in the laboratory is subject to the following processes:

1. Evaporation, which results in a decrease in the water content of the sediment.

2. Segregation of different grain sizes, with coarser fractions settling near the bottom of the sediment container.

3. Self-weight consolidation: This causes the sediment to settle, and the concomitant density changes are responsible for an increase in sediment strength. However, the strength gain due to consolidation during the storage period can be reversed by mechanically remixing the sediment to its original consistency.

4. Thixotropic hardening, which refers to the phenomenon of increase in sediment strength with the passage of time, under conditions of constant water content. Remolding the sediment again reverses this strength gain.

5. The chemical balance shifts to a new equilibrium corresponding to storage conditions in the laboratory.

6. A shift in the biological species balance in response to the new storage conditions.

The effects of evaporation, segregation, consolidation, and thixotropy can be measured and reversed easily. The chemical and biological processes, on the other hand, are more difficult to monitor and therefore, need to be arrested. The option of sterilizing the sediment prior to storage was considered. This could be achieved by either irradiating the sediment with Gamma rays, or by autoclaving, which involves heating the sediment at high temperature and pressure. These options were rejected because the treated sediment would then need to be stored and experimented upon in a sterilized environment, for which adequate facilities were not available in the Geotechnical Engineering Laboratory at MIT. Instead, it was decided to store the sediment in opaque airtight buckets kept in a cold room permanently maintained at 4^{o}C. The sediment was brought up to room temperature over a period of a few days prior to specimen preparation.

3.1.3 Sediment Characterization

Before starting a detailed experimental study of the consolidation of the dredged sediment, it was necessary to establish its index properties as an engineering material. This section describes the various classification tests performed on the Reserved Channel Sediment (RCS) and their results. The tests were performed on RCS after it was sieved, homogenized and stabilized, as described in the previous section. The following is a brief description of the test procedures. The results are presented in Table 3.1, which shows the values of the measured parameters as well as the coefficient of variation, defined as the ratio of standard deviation to the mean value of the measured parameter.

Water content:

The moisture content of RCS was measured by direct heating method, in accordance with ASTM standard D 4959.

Atterberg limits:

Liquid limit and plastic limit of RCS were determined in accordance with ASTM standard D 4318. This standard employs the Casagrande cup method for determination of liquid limit, and the hand rolling method for plastic limit.

Specific gravity:

The pycnometer technique, as described in ASTM standard D5550, was employed to measure the specific gravity of RCS.

Particle size distribution:

The hydrometer test was adopted for grain size analysis. ASTM standard D 422 was followed, with the exception that additional readings were taken at early times to better ascertain the coarse fractions of the sediment. Since the high salinity levels in RCS are liable to affect the hydrometer analysis, the RCS sample was washed repeatedly to remove the soluble salts. The electrical conductivity of the sediment sample finally used for the hydrometer analysis was less than 400 $mho[micro(1/ohm)]$. The particle size distribution for RCS is presented in Figure 3.3.

Organic content:

Estimates of organic content were obtained by the two different techniques commonly employed for this purpose. ASTM standard D 2974 was followed for the ash method, which is based on the measurement of sediment mass lost on ignition from a dry sample at 400^o C.

A second estimate of the organic content is provided by oxidizing and removing it from the sediment sample with hydrogen peroxide solution. This organic content of RCS estimated by this technique is higher than the percentage loss on ignition determined by the ash method. This is most probably due to inadvertent loss of material during the process of rinsing the oxidized sediment sample.

Salinity:

The electrical conductivity of RCS was measured at dilution corresponding to the hydrometer suspension concentration (1 g dry sediment : 20 ml of distilled water). The molality of equivalent potassium chloride solution is also presented in Table 1.

Element Concentrations:

X-ray fluorescence assays were performed to determine concentrations of different elements in the Reserved Channel Sediment. A Spectro X-Lab 2000 energy-dispersive x-ray fluorescence spectrometer was used for this purpose. This technique involves focusing an x-ray beam on a sediment pellet and measuring the energy spectrum of the

resultant x-ray fluorescence. The elemental concentrations are determined from the energy content corresponding to the characteristic x-ray radiations of each element. The results are shown in Table 3.2. Concentrations are indicated for elements with atomic number greater than ten, because the spectrometer facility does not have sufficient energy level to excite fluorescence in the atoms of the first ten elements of the periodic table. The sum of concentrations in Table 3.2, therefore, does not equal 100%.

3.2 Choice of Parameters for Specimen Preparation

All specimens were prepared from the homogenized Reserved Channel Sediment. For ease of production and handling, it was decided to use cylindrical containers fabricated from transparent polycarbonate material. Tube stock of 4-inch outer diameter with 1/8-inch wall thickness was selected for the containers, giving an internal diameter of 3-3/4 inches (9.5 cm). Three deposit heights were selected: 3, 6 and 12 inches. The tallest specimen was limited to 12 inches in height, because precise strength measurements could not be made on a sediment layer in deeper containers. The minimum diameter-height ratio for the specimens in this research program was thus limited to 0.34. This value is higher than the minimum ratio of 0.25 that is recommended by most consolidation researchers (Elder and Sills, 1985), in order to avoid sidewall effects.

Three different values of initial water content were selected: 150%, 200%, and 250%, to cover the range around the natural water content of 160%. This range covered the scenarios of drying and consolidation of dredged material in the barges, as well as dilution of dredged material during the descent phase of the placement in the CAD cells.

Sediment specimens were tested at five different values of consolidation time: 1 hour, 12 hours, 3 days, 15 days, and 30 days after pouring. As a first approxima-

tion, a c_v (coefficient of consolidation) value of 3 x $10^{-3} cm^2/s$ was used to compute approximate times for the end of primary consolidation. This value corresponds to the coefficient of consolidation for Boston Blue Clay at effective stress of 20 g/cm^2 (Seah, 1990). Using Terzaghi's linear theory (Eqs. [2.1-2.5]), the longest time required for the end of primary consolidation was determined to be 10 days. Therefore, the initially selected range of consolidation times was expected to ensure end of primary consolidation for all specimen heights. However, values of c_v measured from surface settlement experiments on the Reserved Channel Sediment were found to be 3 x $10^{-4} cm^2/s$. The 12-inch specimens, therefore, could not be tested in the fully consolidated state.

The measurement schedule was leapfrogged. The sediment specimens requiring longer consolidation times were started first, and the intervening time was utilized for consolidation and testing of specimens with shorter consolidation times.

3.3 Surface Settlement Experiments for Consolidation Characteristics

The aim of these preliminary experiments was to establish the consolidation characteristics of the Reserved Channel Sediment. Nine different specimens were prepared, corresponding to three values each of initial height and initial water content. After pouring the sediment in containers, the movement of sediment-supernatant interface was monitored. The location of the interface was measured from the bottom of the sediment deposit, using a scale with 0.5 mm graduations. Four different measurements were taken along the circumference of the deposit. The measurement times were spread out in order to obtain a well-distributed settlement curve on logarithmic time scale.

3.4 Self-Weight Consolidation Experiments

The aim of these experiments was to obtain shear strength and water content profiles for sediment deposits that are up to 12 inches tall and consolidating under self-weight. For a deposit of Reserved Channel Sediment (with specific gravity of 2.683) undergoing subaqueous self-weight consolidation, this corresponds to the vertical effective stress range of 0-10 g/cm^2. Forty-five sediment specimens were prepared, corresponding to three different values each of initial deposit height and initial water content, and five different values of consolidation times.

At the time of testing, the shear strength and water content profiles of each column were obtained by successive testing and removal of sediment layers from the deposit. Strength measurements were obtained by the Automated Fall Cone Device (AFCD), and the water content was measured by direct heating method (ASTM standard D 4959). Depending upon the water content of the sediment, a mechanical or vacuum-aided sediment removal device was used in order to expose underlying layers for testing.

3.4.1 Automated Fall Cone Device

The Automated Fall Cone Device (AFCD) was developed by Zreik *et al.* (1998) to measure soil strength values as low as 0.03 g/cm^2 (1 g/cm^2 = 98.1 Pa). Figure 3.4 shows a schematic representation of this device. It consists of a precisely machined and weighted cone that is initially positioned such that its tip just touches the sediment surface. The cone is allowed to fall and penetrate the sediment specimen under its own weight for a specified amount of time (5 seconds). The soil shear strength is inversely proportional to the square of the penetration depth. According to Hansbo (1957), the undrained shear strength, c_u, is given by:

$$c_u = k\frac{W}{d^2} \tag{3.1}$$

where W is cone weight, d is cone penetration, and k is a constant depending on the cone shape. Only 60^o cone angles were used in this experimental program, for which k equals 0.69 (Houlsby, 1982).

The measurement system of AFCD is based on a direct-current Linear Voltage Displacement Transducer (LVDT). The cone is threaded to the transducer core and this arrangement allows the measurement of cone displacement as a voltage output readable on a voltmeter. The release and clamping of the cone are controlled by an electronic timer. A pulley with a counterweight system allows the use of cones with a very small effective weight, thus enabling measurement of low values of undrained shear strength. For use in this experimental program, the displacement transducer of the AFCD was re-calibrated, the cones and counterweights were cleaned and weighed, and a special extension rod was machined to enable strength measurements in sediment layers located at the depth of up to 12 inches (31 cm) from the top of the container. Furthermore, strength measurements were performed on kaolinite at different water contents, and were compared to those performed by Zreik (1994). The resulting comparison, shown in Figure 3.5, indicates excellent repeatability of AFCD measurements. In this program, six to eight strength measurements were taken with the AFCD on each exposed sediment layer.

3.4.2 Direct Heating Method for Water Content Measurement

Guidelines in ASTM D 4959 were followed for obtaining the water content of sediment specimens. From each sediment layer tested, about 25 g of material was placed in a clean Aluminum tare. The tare was weighed to 0.01g and then placed in a temperature-controlled oven at 105°C for overnight drying. The dried sample was cooled in a dessicator for a few minutes prior to obtaining the dry weight of tare. The water content, w, is given by:

$$w = \frac{W_1 - W_2}{W_2 - W_c} \tag{3.2}$$

where W_c is the weight of the tare, W_1 is the weight of the tare plus moist sediment, and W_2 is the weight of tare plus oven-dried sediment. Provided a resolution of 0.01 g in weight measurement, this method provided a repeatability of $\pm$ 1% in water content for sediment water contents in the range of 150-300%.

3.4.3 Profiling Technique

Once the strength and water content measurements were performed on a sediment layer in a deposit, a vacuum scraping device was used for exposing a fresh underlying layer. The device, shown in Figure 3.6, essentially consists of a sharp metal scraper mounted on a graduated support, which enables lowering of the scraping edge to a precise depth in the sediment deposit. A channel running through the scraper assembly can be connected to a vaccum pump which aids in removal of very soft sediments. For sediment specimens with low water contents, a different version of this device was used. Since dense sediments were found to block the suction channel, the modified device relied on manual removal of scraped material from the cutting edge. A schematic of this device is shown in Figure 3.7.

The strength and density profiles were obtained in the following manner. Once the sediment specimen was ready for testing, the supernatant was drained and the container was placed on the base platform of the AFCD. The cone tip was lowered and brought into contact with the surface sediment layer. After the required number of strength measurements were performed at different points on this layer, a spoon-shaped tool was used to withdraw a sample for water content measurement. Only one sample was taken from each layer for water content measurements, as the excellent repeatability of oven-drying method obviated the need for multiple measurements. The layer of sediment thus tested was subsequently removed to the desired depth by the scraping device, to expose a deeper layer of sediment. Strength and water content measurements were performed on the new layer, and this procedure was repeated to provide an adequate number of points for establishing the depth profile of strength and water content.

The distance between successive sediment layers was decided by the extent of

cone penetration in the sediment and the total height of the specimen at the time of testing. Since the cone weights were chosen to always limit the penetration in the sediment layer to about 5 mm, two successive sediment layers were always separated by a minimum distance of 1 cm to ensure that the underlying layer was not disturbed by the testing of the overlying layer. The actual distance between the layers was not kept constant but increased with depth, so as to obtain a representative profile along the height of the deposit without testing an inordinately large number of sediment layers. In general, the number of sediment layers chosen for testing was kept between five and seven, irrespective of the specimen height. This resulted in the distance between the successive sediment layers being larger in the case of taller sediment deposits.

3.5 Surcharge Consolidation Experiments

The objective of the surcharge experiments was to obtain shear strength and water content values for sediment conditions corresponding to the depth range of 12 inches to 10 feet below the surface of the consolidating sediment deposit. Surcharge experiments were conducted because it was impractical to test sediment deposits of this height undergoing self-weight consolidation. The vertical effective stress at these values of depth is in the range of 10-100 g/cm^2. The experiments were performed in the following manner:

Sediment specimens with different initial water contents were prepared in the 4-inch diameter containers. One important feature of the specimens prepared for surcharge consolidation was that double-drainage conditions were simulated for these experiments. Since double-drainage reduces the drainage path of the sediment deposit by half, it leads to four-fold decrease in consolidation time (Equation [2.5]) and hence expedites the experiment schedule. The double-drainage conditions were achieved by creating a porous boundary at the top and the bottom of the cylindrical container, as shown in Figure 3.8. The top and bottom of the sediment were in contact with a nylon 5-μ filter paper and cotton fabric supported on a perforated plastic plate. This

arrangement permitted lateral and axial movement of water at the boundaries. Additionally, the bottom perforated plate supported a tube that discharged the bottom efflux from the sediment deposit into the supernatant layer on top of the deposit.

Once the sediment was poured into a container with the bottom drainage assembly in place, it was allowed to gain some strength (for about 8 hours) before the top perforated plate was placed on it. After the placement of the perforated plate, weights were incrementally added using a load increment ratio of 1 (that is, the weight was doubled in every increment).

For surcharge levels higher than 10 g/cm^2, the sediment containers were transferred to a soil-testing load frame. This apparatus, shown in Figure 3.9, was used for a manual and continuous adjustment of surcharge up to 100 g/cm^2.

Four different values of final surcharge were selected: 10 g/cm^2, 30 g/cm^2, 60 g/cm^2, and 100 g/cm^2. With three different values of initial water content (150%, 200%, and 250%), a total number of twelve specimens were prepared.

For testing of surcharged sediment specimens, strength measurements were carried out with AFCD at two different layers in the specimen, along with the water content measurements. Due to high surcharge loading, the depth effect in these deposits was found to be negligible, and consequently a single value of undrained shear strength and water content was obtained for each of the surcharge consolidation tests.

3.6 Constant Rate of Strain (CRS) Testing

These tests were performed to obtain the stress-strain and consolidation characteristics of the Reserved Channel Sediment in the high effective stress range (> 100 g/cm^2, corresponding to depths greater than 10 feet).

A general-purpose consolidometer developed by Wissa *et al.* (1971) was used to perform the CRS tests. A schematic of the device is shown in Figure 3.10. The sediment specimen is laterally confined in a metal ring, while the base of the specimen maintains contact with a ceramic porous stone. The excess pore pressure during consolidation is measured by a pressure transducer connected to the ceramic stone.

The top of the specimen is in contact with a piston through a porous stone. Continuous loading of the sediment specimen is achieved by a gear-driven load frame that moves the piston at a constant velocity. The axial load is measured by a pressure transducer in the piston shaft, and the deformation of the specimen is measured by a displacement transducer. The sediment specimen is contained in a pressure chamber which can maintain a constant confining stress to ensure complete saturation. The instrumentation in the CRS test provides for continuous measurement of axial stress, pore pressure, confining cell pressure, and deformation, and this test is widely used to achieve continuous stress-strain characteristics for soils, as well as continuous data for variation of hydraulic conductivity and coefficient of consolidation with effective stress.

The cross-sectional area of the specimen remains constant during the test. The net vertical effective stress is determined from the measurements of net axial load applied by the piston and the excess pore water pressure at the base of the specimen. The strain is similarly determined from the measurement of vertical deformation in the specimen. Hence, the measurements provide the necessary data for calculating the coefficient of compressibility, the coefficient of consolidation, and vertical hydraulic conductivity for continuous increments in loading. Gonzalez (2000) provides the detailed data interpretation scheme in CRS tests.

Three CRS tests were performed on the Reserved Channel Sediment, corresponding to three different values of initial water content. Since the sediment specimen needs to have sufficient strength in order to support the load of piston at the start of the CRS test, sediment specimens were first consolidated under surcharge of approximately 100 g/cm^2 before they could be subjected to CRS testing. After a sediment specimen reached the end of primary consolidation under this value of surcharge, the surcharge load was removed and the specimen was taken out from the container by injecting compressed air at its base. This cylindrical specimen was used to trim a specimen into a thin-walled stainless steel ring for CRS testing, by employing a trimming device with a knife-edge cutting shoe.

The results of these tests provided continuous data on variation of axial strain,

coefficient of consolidation, average void ratio, excess pore pressure, and hydraulic conductivity with vertical effective stress. It should be noted that the tests did not provide any information on the behavior of undrained shear strength of the material.

3.7 Summary

The self-weight and surcharge experiments covered the effective stress range up to 100 g/cm^2, corresponding to the top one inch to 10 feet of depth in sediment deposits. Coupled with the CRS tests, which spanned the effective stress range from 100 to 2000 g/cm^2, the experimental program was tailored to provide exhaustive information on the consolidation and strength behavior of the Reserved Channel Sediment.

Table 3.1: Index properties of the Reserved Channel Sediment (RCS)

Parameter	Value	Number of tests	Coeff. of variation
Water Content	161.6 %	8	0.1 %
Liquid Limit (LL)	91.4 %	5	4.8 %
Plastic Limit (PL)	39.0 %	5	6.1 %
Plasticity Index (PI =LL-PL)	52.4		
Specific Gravity	2.683	2	
Organic Content (Ash method)	6.3 %	5	2.8 %
Organic Content (H_2O_2 method)	6.9 %	5	4.4 %
Clay Percentage (d <0.002 mm)	34 %		
Silt Percentage (0.002 mm<d<0.075 mm)	47 %		
Activity (=PI/Clay Percentage)	1.5		
Conductivity (1 g : 20 ml dilution)	4196 μmho	2	0.5 %
Equivalent KCl	0.031 M (2.3 g/l of pore fluid)		

Table 3.2: Elemental composition of RCS, from x-ray fluorescence tests

Atomic number	Element symbol	Element	Concentration, ppm
11	Na	Sodium	1.6e4
12	Mg	Magnesium	1.35e4
13	Al	Aluminum	6.72e4
14	Si	Silicon	24.84e4
15	P	Phosphorus	0.12e4
16	S	Sulphur	0.73e4
17	Cl	Chlorine	1.76e4
19	K	Potassium	2.26e4
20	Ca	Calcium	1.18e4
22	Ti	Titanium	0.47e4
23	V	Vanadium	0.02e4
24	Cr	Chromium	0.01e4
25	Mn	Manganese	0.04e4
26	Fe	Iron	3.69e4
27	Co	Cobalt	32
28	Ni	Nickel	22.2
29	Cu	Copper	69.2
30	Zn	Zinc	145.2
31	Ga	Gallium	11.4
32	Ge	Germanium	1.1
33	As	Arsenic	10.1
34	Se	Selenium	0.7
35	Br	Bromine	158.1
37	Rb	Rubidium	101.7
38	Sr	Strontium	146.6
39	Y	Yttrium	19.9
40	Zr	Zirconium	207.9
41	Nb	Niobium	15.8
42	Mo	Molybdenum	2.5
47	Ag	Silver	3.0
48	Cd	Cadmium	1.3
49	In	Indium	0.6
50	Sn	Tin	17.8
51	Sb	Antimony	2.5
52	Te	Tellurium	2.3
53	I	Iodine	89.2
55	Cs	Cesium	4.3
56	Ba	Barium	589.5
57	La	Lanthanum	14.7
74	W	Tungsten	51.9
80	Hg	Mercury	1.8
81	Tl	Thallium	1.4
82	Pb	Lead	87.8
83	Bi	Bismuth	1.2

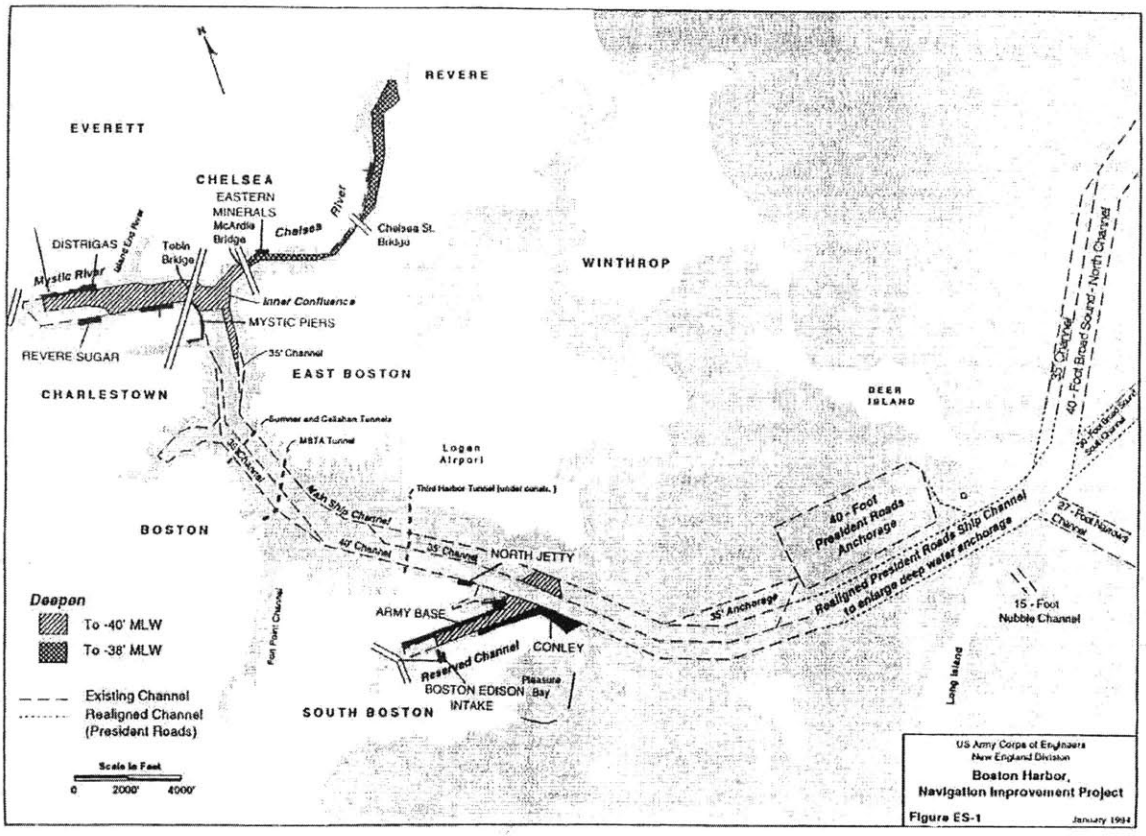

Figure 3-1: Map of Boston Harbor, showing areas designated for dredging under BHNIP (Massport and USACOE, 1995)

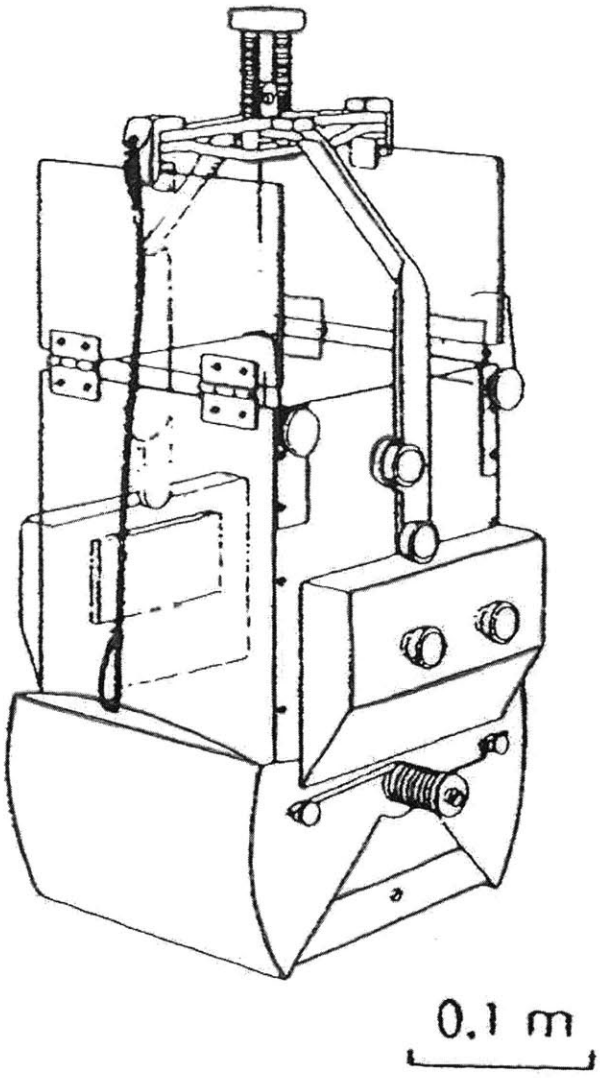

Figure 3-2: Ekman dredge, in cocked configuration (Blomqvist, 1985)

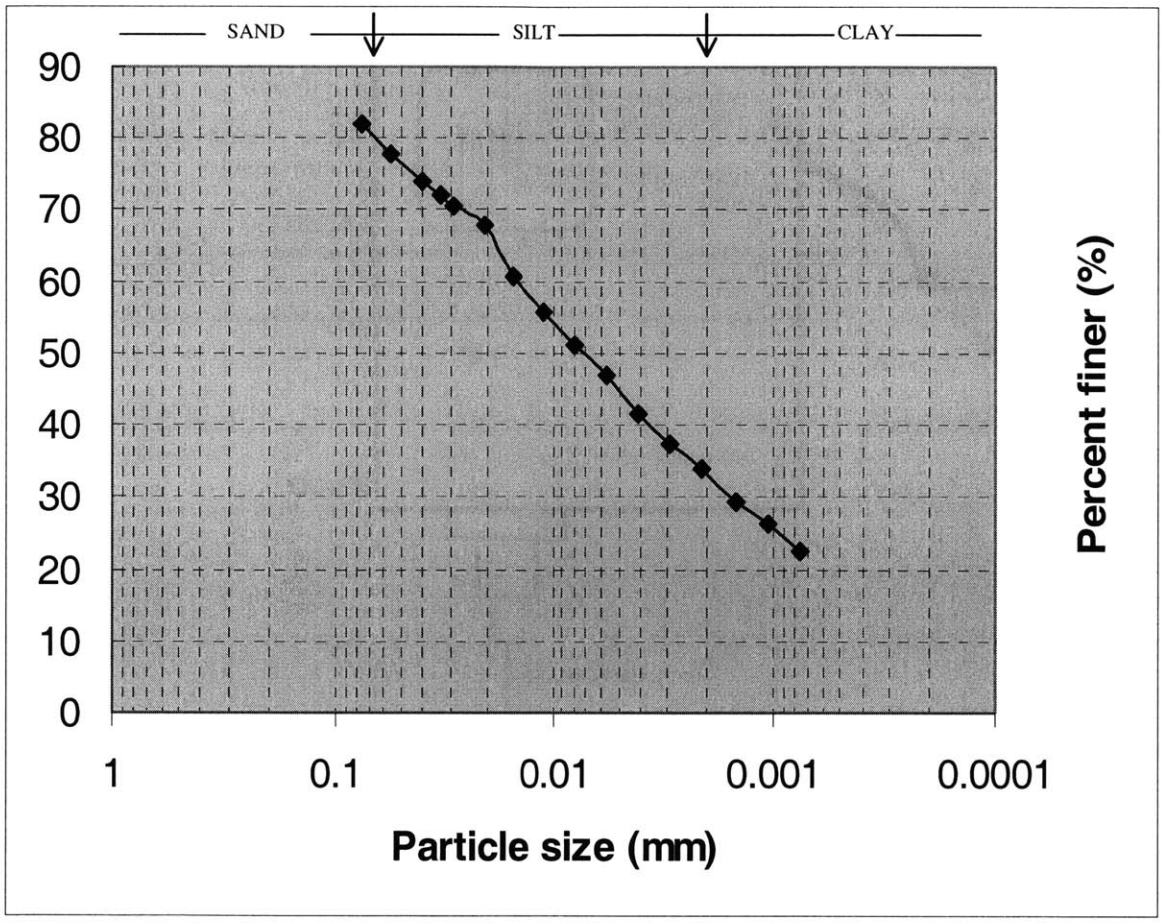

Figure 3-3: Particle size distribution of Reserved Channel Sediment

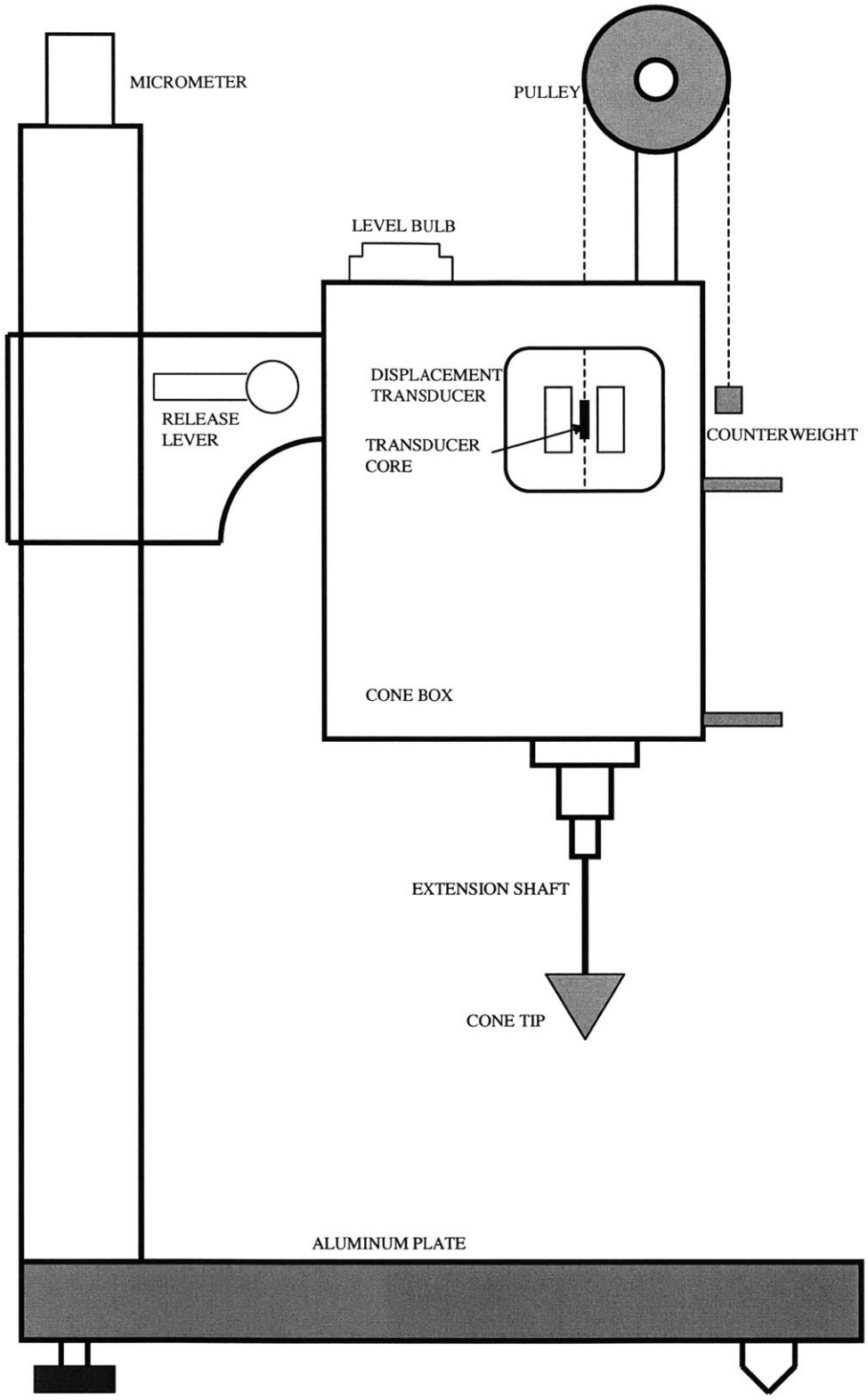

FIGURE 5: Schematic of the Automated Fall Cone Device

Figure 3-4: Schematic diagram of the Automated Fall Cone Device (AFCD)

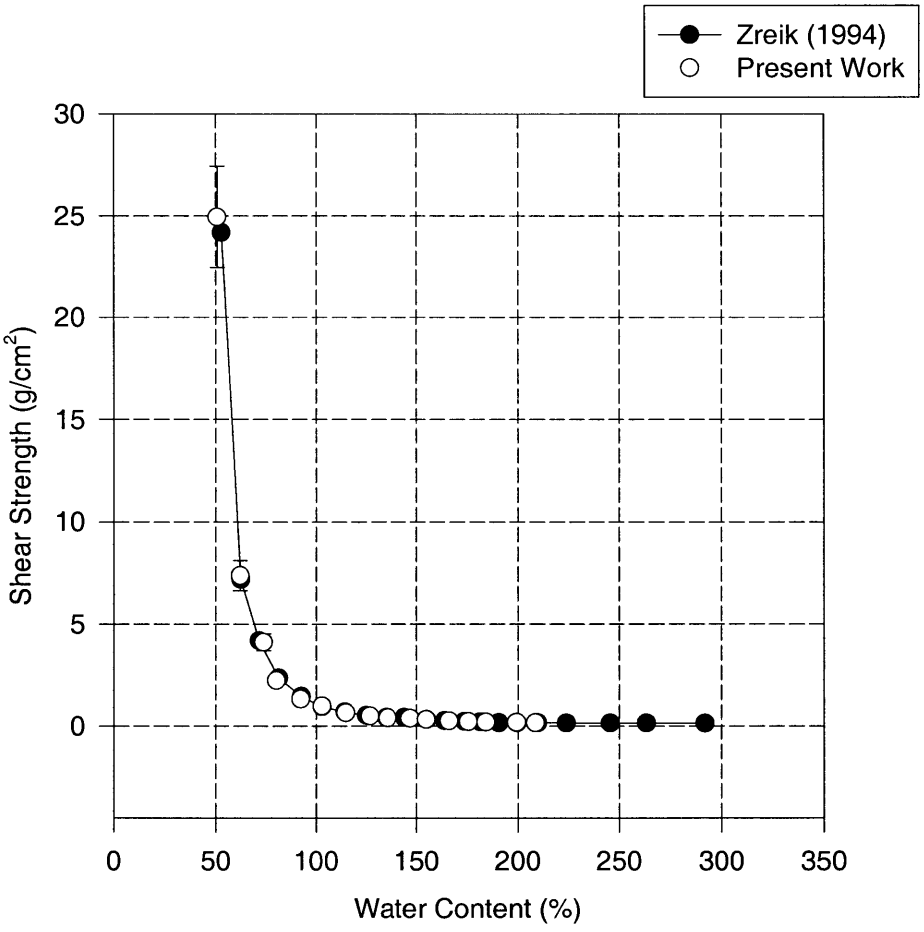

Figure 3-5: Shear strength of remolded kaolinite at different water contents, measured by AFCD

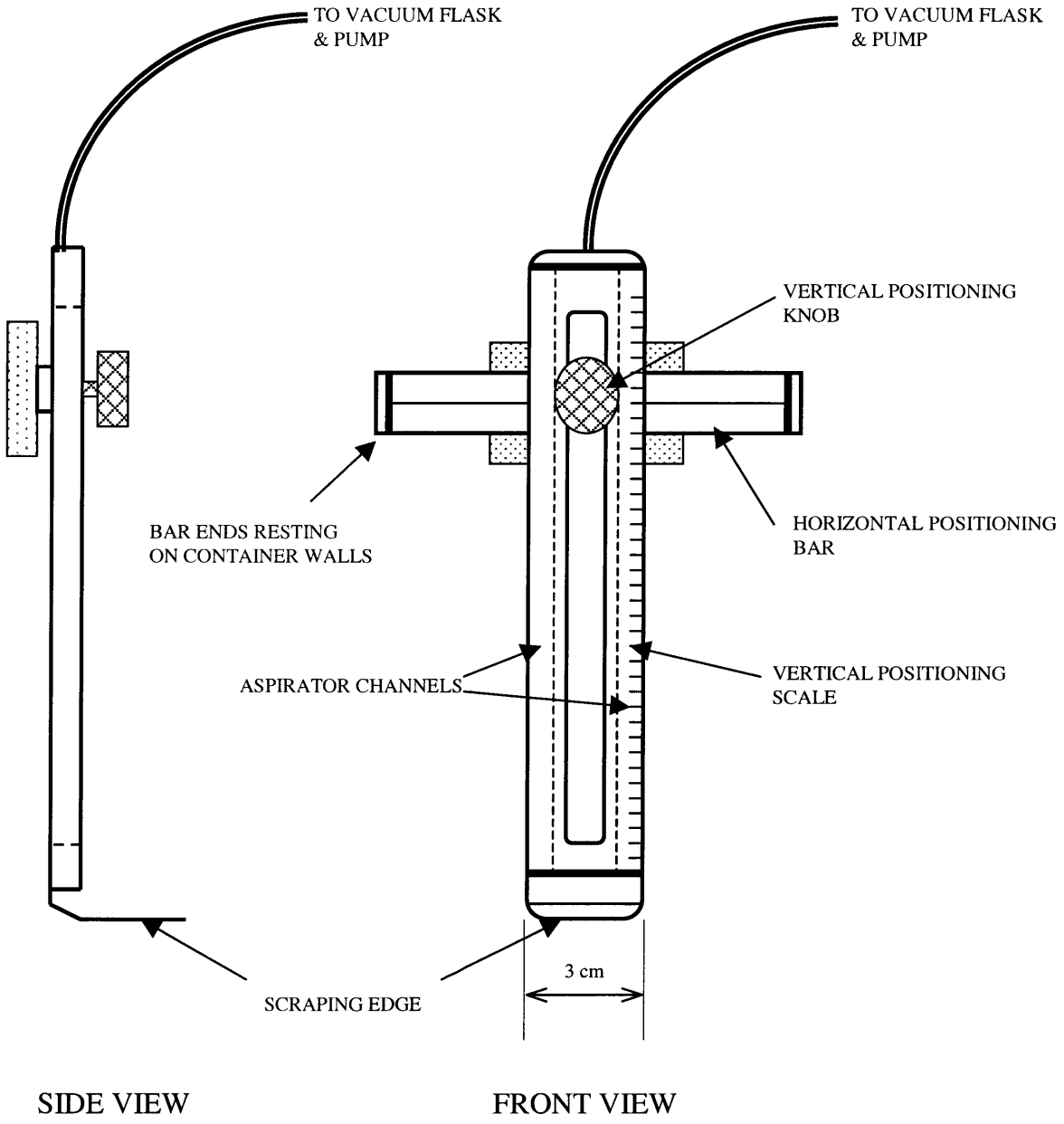

Figure 3-6: Schematic diagram of the vacuum scraping device

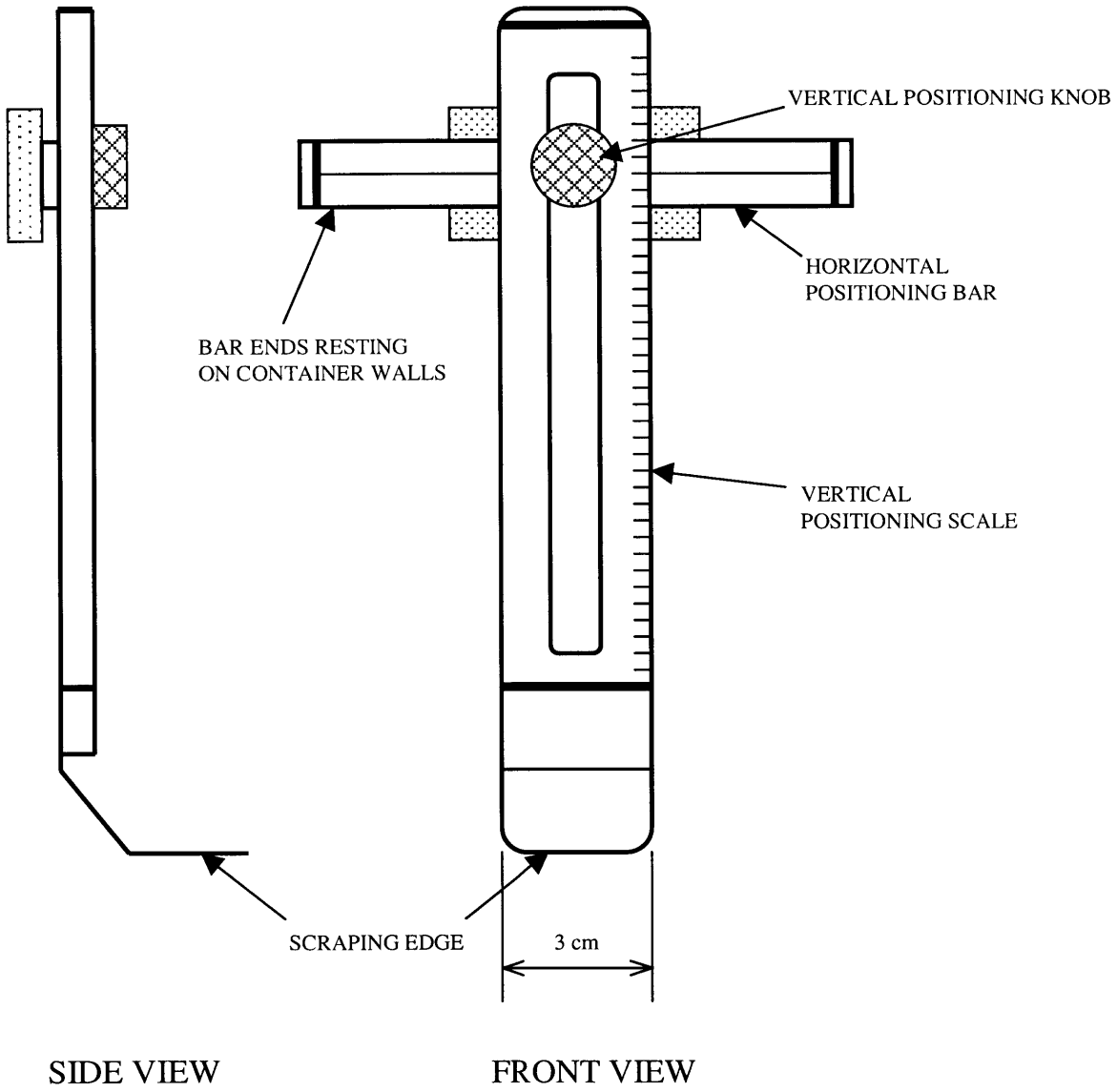

Figure 3-7: Schematic diagram of the sediment removal device (without vacuum)

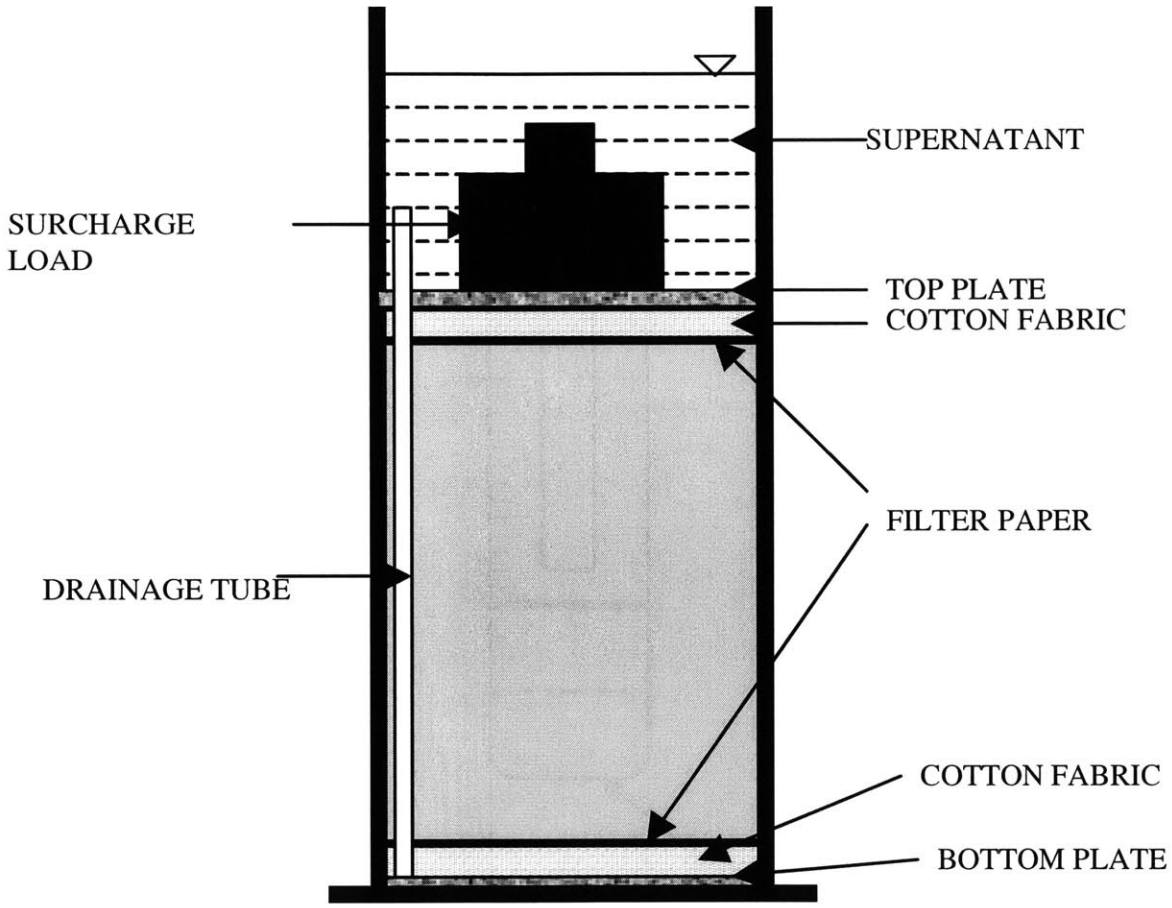

Figure 3-8: Double-drainage arrangement for surcharge specimens

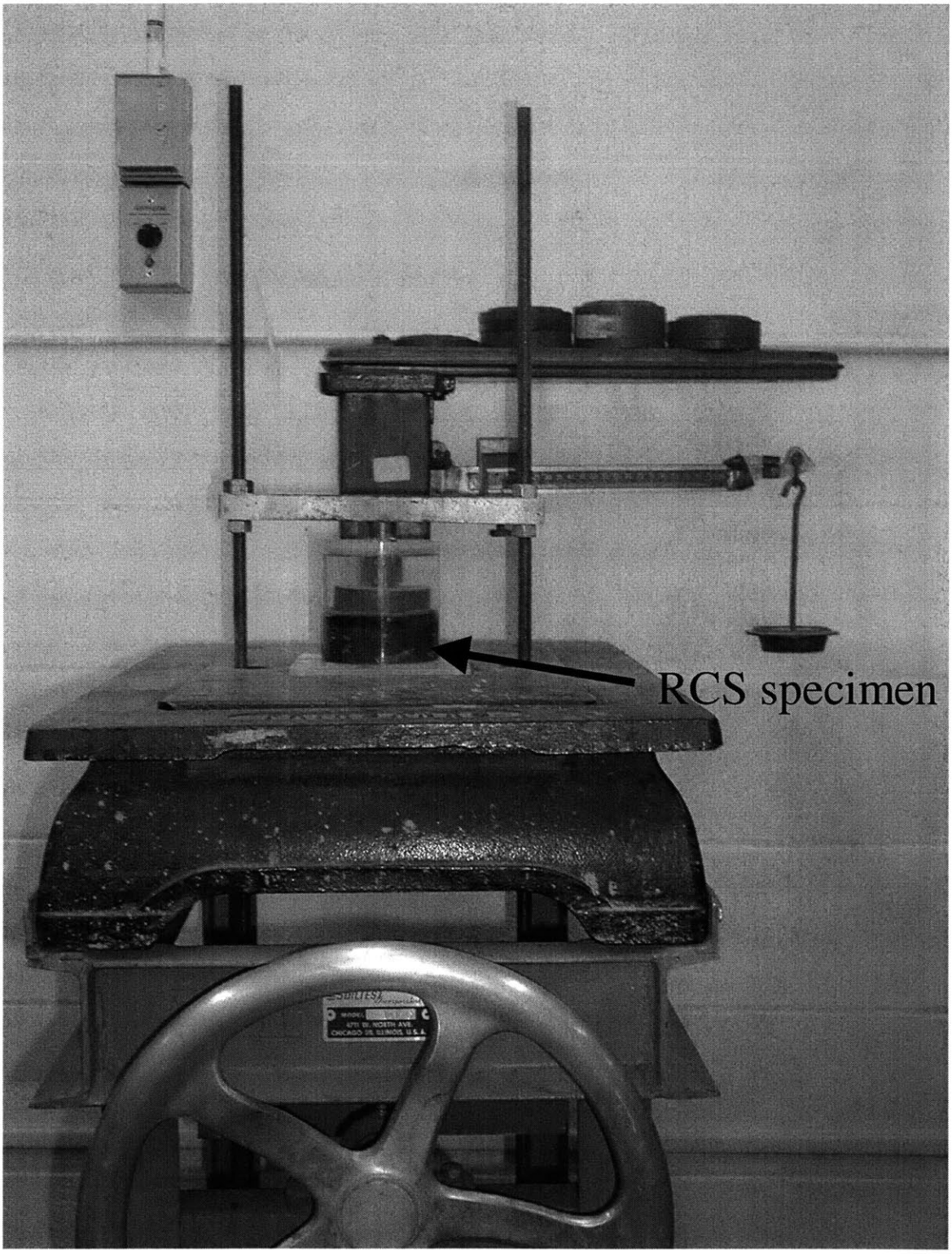

Figure 3-9: Manual continuous-loading load-frame apparatus

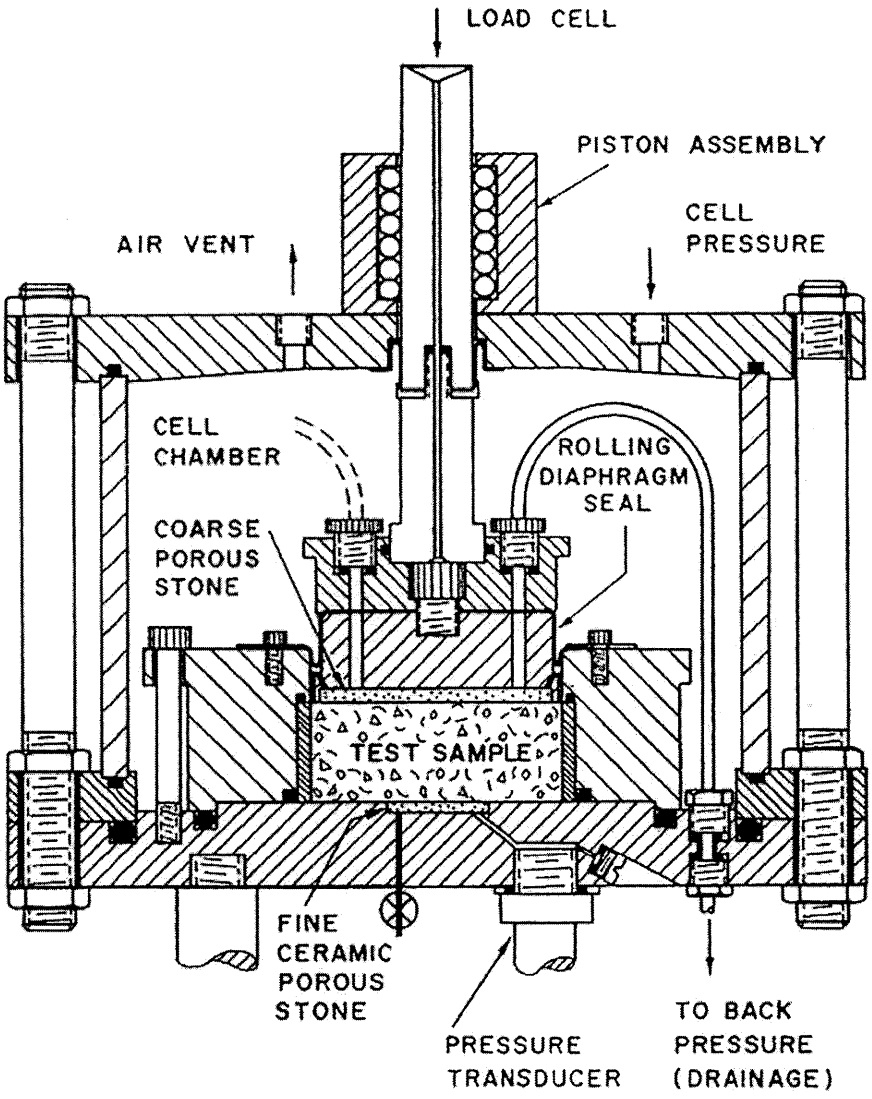

Figure 3-10: Schematic diagram of Constant Rate of Strain (CRS) consolidometer (Wissa *et al.*, 1977)

Chapter 4

Results and Discussion

This chapter is devoted to the presentation, processing, and analysis of experimental data. The results are divided into three main sections as follows. Section 4.1 discusses the data from settlement experiments and establishes key consolidation parameters. Section 4.2 is devoted to presentation and processing of density profiles. In Section 4.3, the shear strength data are presented and analyzed in order to establish shear strength-effective stress correlations .

4.1 Surface-settlement experiments

Settlement is defined as the total vertical deformation at the surface resulting from loading. In self-weight consolidation, the load for a given sediment layer arises from the weight of the sediment layers overlying it, and it squeezes the pore fluid out of the soil matrix. This results in an increase in the density of the sediment layer, which causes a decrease in the total volume of the specimen and the settlement of the specimen surface.

The flow of pore fluid is not instantaneous, but depends on the permeability of the sediment. Clayey sediments have low permeability. Hence, as the pore fluid is slowly squeezed out of the sediment matrix, the increase in density and decrease in volume are manifested as the time-dependent process of consolidation.

The results of surface settlement experiments are presented in Figures 4.1-4.3.

These plots show the location of the sediment surface on a logarithmic time axis, for RCS specimens with different values of initial water content (IWC) and initial specimen height. Logarithmic time scale was chosen because it facilitates graphical determination of various consolidation parameters. The plots are grouped by specimen height. Figure 4.1, for example, shows the location of the surface with time for specimens with 3-inch initial height, and for 150%, 200%, and 250% IWC (The 250% IWC specimen was inadvertently filled to an initial height slightly greater than 3 inches). Surface location was determined as the average of four measurements taken at different points along the circumference of the specimen container. It is shown in the units of centimeters above bottom.

The settlement curves show two distinct regimes of consolidation: primary consolidation and secondary consolidation (also called creep). Figure 4.4 shows the settlement curve plotted on logarithmic time scale. Primary consolidation refers to the steep region of the settlement curve, where settlement occurs as a result of the dissipation of excess pore pressures and the resulting change in water content. In contrast, secondary compression is the slower process of consolidation that continues after the excess pore pressures have effectively dissipated. This phenomenon is responsible for the partial time-dependence of the void ratio-effective stress relationship of the material, and significantly affects the magnitude of long-term settlement in sediment deposits.

Although Terzhaghi's theory [Eqs 2.1-2.5] is applicable only for infinitesimal strain conditions, the concept is employed in the following sections for estimating material properties during the large-strain consolidation of the sediment under self-weight.

4.1.1 End of primary consolidation

The time to end of primary consolidation (t_p) is defined as the intersection of the tangents to the primary and secondary regions of the settlement curve plotted on logarithmic time axis. The graphically determined values of t_p are presented in Table 4.1.

The primary consolidation of 3-inch and 6-inch specimens for all values of initial

water contents is completed in times less than 30 days, which is the longest time interval for which the RCS specimens were systematically tested. It is important to note that t_p is a rough and lower-bound indicator of the time to the end of primary consolidation, and appreciable settlement occurs after t_p. This means that the 12-inch specimens can not be assumed to be completely consolidated at the end of 30 days. Furthermore, the consolidation times (as indicated by t_p) do not scale by the square of the specimen height. This indicates that the behavior of RCS at low effective stresses corresponding to self-weight consolidation can not be accurately modeled by Terzaghi's linear theory of consolidation. [Eqs. 2.1-2.5].

4.1.2 Coefficient of consolidation

The coefficient of consolidation, c_v, is determined from Casagrande's logarithmic time method, which graphically ascertains the time for 50% (primary) consolidation from the time settlement curve (see Figure 4.4). The value of c_v is estimated by Terzaghi's linear theory, for the average height of specimen during the settlement:

$$c_v = \frac{0.19 {H_{dr}}^2}{t_{50}} \tag{4.1}$$

where H_{dr} is the length of drainage path and t_{50} is the time for 50% consolidation. Table 4.2 shows the values of c_v (in cm^2/s) determined in this manner.

During the design phase of the experiments, a value of 3 x $10^{-3} cm^2/s$ was chosen, as a first estimate of c_v for RCS. This value corresponds to c_v of Boston Blue Clay at effective stress of 20 g/cm^2 (Seah, 1990). The actual values of c_v estimated from the settlement curves are 1-2 orders of magnitude lower, which is why the times to end of primary consolidation are higher than the values anticipated during the design phase of these experiments.

Table 4.2 shows the variation of c_v with specimen height, which indicates the dependence of c_v on effective stress. Also, c_v increases with increasing initial water content, which is in agreement with the expectation that specimens with higher water content would settle at a faster rate, due to higher permeability.

The values of c_v are consistent with the extant literature. Lowe *et al.* (1964) reported the c_v to be in the range of 2-10 x $10^{-4} cm^2/s$ for organic silty sediments. The US Navy Foundations Design Manual (US Navy, 1971) suggests a c_v value of 1 x $10^{-4} cm^2/s$ for remolded sediments with liquid limit around 100.

It is important to note that estimation of c_v by the method adopted here can produce results that might vary significantly even between specimens of the same soil (Lambe and Whitman, 1969). Hence the c_v calculated here provides only an approximate value of this consolidation parameter for RCS.

4.1.3 Rate of secondary compression

The secondary compression ratio, c_α, also called the rate of secondary compression, is defined as the ratio of incremental strain in secondary compression to the incremental change in corresponding logarithmic time.

$$c_\alpha = \frac{\frac{\triangle H_{sec}}{H}}{\triangle log_{10} t} \tag{4.2}$$

where $\triangle H_{sec}$ is the settlement due to secondary compression over a time t, as shown in Figure 4.4. The secondary compression ratio is graphically determined as the slope of the secondary consolidation curve on the logarithmic time axis. The values of c_α, as calculated graphically from logarithmic time settlement curves are presented in Table 4.3. It is generally recommended that incremental strain be measured over a period no smaller than one logarithmic cycle of secondary compression. Although this condition is satisfied only for 3-inch specimens, estimates of c_α are presented in Table 4.3 for all the specimens.

The values for c_α are in the range of 0.02-0.06, which denotes a fairly high rate of secondary compression. Organic and highly plastic soils typically have high values of c_α, in contrast to normally consolidated clays, which have a c_α range of 0.005-0.02 (Ladd, 1967).

The simultaneous nature of the two processes makes it difficult to separate the effects of secondary compression from those of primary consolidation. For thick sed-

iment deposits, the layers near the drainage surface get fully consolidated and are undergoing secondary effects while the deeper layers are still in primary consolidation. Due to the complicated nature of the consolidation process, the calculated values of c_α can only be considered approximate.

4.1.4 Hydraulic conductivity

Approximate calculations for hydraulic conductivity can be made from settlement curves in the following manner:

The strain, ϵ, corresponding to primary consolidation is:

$$\epsilon = \frac{\triangle H_{prim}}{H} \tag{4.3}$$

where $\triangle H_{prim}$ is the settlement during primary consolidation in a sediment deposit of initial height H, as shown in Figure 4.4.

The change in average void ratio, $\triangle e$, is then calculated as:

$$\triangle e = \epsilon(1 + e_0) \tag{4.4}$$

where e_0 is the initial void ratio. For this change in average void ratio, the change in effective stress, $\triangle \sigma'_v$, is calculated from the void ratio-effective stress relationship for the material. This relationship is obtained in the later course of experiments, from the water content profiles of the consolidated specimens. The procedure for establishing the void ratio-effective stress relationship is detailed in Section 4.2.

The coefficient of compressibility, a_v, can now be calculated as:

$$a_v = \frac{\triangle e}{\triangle \sigma'_v} \tag{4.5}$$

and the hydraulic conductivity, k, is estimated based on Terzaghi's theory as :

$$k = \frac{a_v \rho_w c_v}{(1 + e_0)} \tag{4.6}$$

where ρ_w is the density of water and c_v is the coefficient of consolidation.

This value of k corresponds to the average void ratio during the consolidation, e_f, given by:

$$e_f = e_0 - \frac{\triangle e}{2} \tag{4.7}$$

The values of hydraulic conductivity thus estimated are presented in Table 4.4. The numbers tabulated in parentheses are the average void ratios, e_f, at which these hydraulic conductivity values are applicable. These values of hydraulic conductivity classify RCS as a low permeability material (Lambe and Whitman, 1969).

It should again be noted that these values are only approximations, since the process of consolidation over a range of void ratios is being represented by one average value.

4.2 Water content profiles

4.2.1 Void ratio-depth curves

The preliminary results of water content measurements are presented as variation of void ratio with depth. The depth is measured from the surface of the consolidating specimen, which moves downward with time. The absolute magnitude of error in water content measurements is $\pm 1\%$. This translates into an uncertainty of ± 0.03 in void ratio. Figures 4.5-4.13 show the void ratio profiles for test specimens with different initial water contents and different initial heights.

The first location in measurement of density profiles is the surface layer. The density profiles show an abrupt increase in void ratio very near to the surface layer. This increase is clearly pronounced in taller specimens, for instance in Figures 4.7 and 4.10, which show the void ratio profiles for 12-inch specimens with 150% and 200% IWC. Accurate measurements of water content in the surface layer could not be obtained because of the difficulty in draining the supernatant completely at the time of water content measurement. Furthermore, in the course of shear strength measurements, it was found that the surface layer consistently displayed a high and

anomalous value of shear strength. This anomalous behavior of the surface layer is due to a biological oxidation process that leads to changes in the soil structure of the layer. Since the present research effort is limited to the study of the physical aspects of consolidation and strength development in weak dredged materials, investigation of this biological oxidation process was limited to a simple experiment for comparing the shear strength of sterilized and unsterilized (standard) RCS specimens. In order to concentrate on the consolidation behavior, it was decided to exclude the surface layer measurements from the subsequent analysis of the void ratio profiles.

Figure 4.14 presents the void ratio profiles at 30 days for 12-inch specimens with different initial water contents. It is evident from the figure that the void ratio-depth relationship is not independent of the initial water content of the specimens. It can be seen that the specimens with higher initial water content consolidate with a steeper density gradient. This is due to greater segregation of sediment solids that is facilitated at higher initial water contents. Research efforts of Been and Sills (1981) and Zreik (1994) report similar observations. Sedimentation experiments performed by Imai (1981) on natural muds also resulted in the finding that the compression curve depends on the initial slurry water content.

It can also be observed that in a sediment deposit with given initial water content, the density during consolidation does not depend only on the depth of layer below the surface but also on the total height of the specimen. Hence the void ratio-depth relationship is a function of specimen height, too. This effect is illustrated in Figure 4.15, which shows void ratio profiles at 3 days for RCS specimens with 200% IWC and different initial specimen heights. The water content at a certain depth is higher for a taller bed. Hence a sediment layer at a certain void ratio can exist at different depths inside a bed, i.e. under different effective stresses, in sediment deposits of different height.

Imai (1981) provided an explanation for non-uniqueness of density profiles during consolidation. According to him, the upward seepage force that results from ongoing consolidation of underlying layers decreases the vertical effective stress on a sediment layer. For a sediment layer at a given depth from the surface, this seepage force is

larger in a taller bed, due to higher amount of sediment undergoing consolidation in underlying layers. This sediment layer would consequently be under a lower net effective stress at any given time during consolidation in a taller bed. Due to smaller net effective stress, the structure is looser, resulting in higher water content. This effect of deposit height on density profiles is present in consolidated beds as well, as can be seen in a comparison of 30-day void ratio profiles for RCS specimens with 200% IWC (Figure 4.16). It should be noted that the 12-inch specimen is not fully consolidated at the end of 30 days. The void ratio profile in a fully consolidated 12-inch specimen, therefore, would be closer to the void ratio profiles of 6-inch and 3-inch specimens than what is indicated in Figure 4.16. The non-uniqueness of compression curves is further discussed in the context of void ratio-effective stress profiles, since it has important implications for parameterization of consolidation characteristics.

4.2.2 Void ratio-effective stress curves

For purpose of quantifying the consolidation characteristics of the RCS, the depth coordinate is converted to the effective stress coordinate by

$$\sigma_v^{'} = \sum_i \gamma_{b,i} h_i \tag{4.8}$$

where $\gamma_{b,i}$ and h_i are the unit buoyant weight and thickness of layer i, respectively. The summation is over all the layers overlying the point where the effective stress is being calculated.

If 100% saturation is assumed, the unit buoyant weight, $\gamma_{b,i}$, can be calculated by using the phase relationship:

$$\gamma_{b,i} = \gamma_w \frac{(G-1)}{(1+Gw_i)} \tag{4.9}$$

where G is the specific gravity of sediment solids, γ_w is unit weight of water, and w_i is the water content of the sediment layer.

The above equation implies that the effective stress at a given depth in the sed-

iment specimen is equal to the submerged weight of the sediment layers overlying it. This formulation is correct only after the end of primary consolidation, when the excess pore pressures have dissipated and the entire load of overlying columns is supported by the intergranular effective stress. During the period that consolidation is proceeding, the upward seepage force due to consolidation of underlying sediment layers decreases the effective stress, and the above equation consequently overestimates the magnitude of effective vertical stress.

In Figures 4.17-4.25, which show the variation of void ratio with effective stress, the empty symbols denote the experimental points obtained during the consolidation process. These points, although plotted as void ratio-effective stress measurements, do not represent the true value of effective stress in the specimen at the time of measurement, but rather an overestimated value as explained above. The solid symbols, in contrast, represent measurements taken at or after the end of primary consolidation, and hence, the true value of vertical effective stress at the time of measurement. The true magnitude of vertical effective stress during the consolidation process could not be measured directly because the experiments in the present effort were not instrumented for measurement of excess pore pressures.

In Figures 4.19, 4.22, and 4.25, which show the void ratio-effective stress profiles for 12-inch specimens, all measurements are shown in empty symbols. This is because these specimens have not completed primary consolidation at 30 days, as discussed earlier. The 3-inch and 6-inch specimens, however, have fully consolidated by 30 days, and therefore the 30-day density profiles for these specimens are the true void ratio-effective stress curves for RCS. These compression curves are presented in Figures 4.26, 4.27, and 4.28, which show the variations in 30-day compression curve with specimen height for 150%, 200%, and 250% IWC, respectively. It is clear that the void ratio-effective stress relationship is a function of specimen height in this range of effective stress. This phenomenon is a strong departure from high effective stress behavior of sediments, where there exists a unique void ratio-effective stress relationship (often called the virgin compression curve) independent of initial water content and specimen height.

In geotechnical engineering practice, compression curves are conventionally plotted with effective stress on semi-log scale. This allows for admitting the large range of effective stresses that soils are normally subjected to. In the present case, the adoption of semi-log scale is advantageous for showing the results from self-weight experiments, surcharge experiments, and the Constant Rate of Strain (CRS) testing on the same plot. In Figure 4.29, the progression of the compression curve in time is shown on logarithmic stress scale for 3-inch specimens with 150% IWC. The solid dots in the effective stress range of 10-100 g/cm^2 are the density measurements from the four surcharge experiments conducted on specimens with 150% IWC. Also appearing as a continuous line is the void ratio-effective stress curve obtained from a CRS test. The CRS testing was carried out on RCS material that was consolidated from an initial remolded state at 150% water content to an effective stress of approximately 100 g/cm^2. The combination of data points from self-weight experiments, surcharge experiments, and CRS testing, as shown in this figure, exhibits a high degree of continuity and thus provides the extension of the virgin compression curve in the low effective stress region ($\sigma_v^{'} < 100\ g/cm^2$). Figure 4.30 shows the result of the same exercise for the 6-inch-150% IWC self-weight consolidation specimen. Note that the data for surcharge and CRS tests in this figure are the same as for 3-inch-150% IWC specimen. This is because the effect of specimen height is negligible in the effective stress range corresponding to the surcharge and CRS tests. Figure 4.30 has more density measurements in the self-weight consolidation region and, therefore, approaches even more closely the low-end of data from surcharge experiments. The data from self-weight consolidation of 12-inch specimens are not presented in this analysis because of the failure to obtain fully consolidated compression curves for these specimens within 30 days. The combined void ratio-effective stress profiles for RCS specimens with 200% and 250% IWC are shown in Figures 4.31-4.34. These plots define the shape of compression curves in low effective stress ranges under different conditions of initial water content and specimen height.

In order to obtain the void ratio-effective stress relationship for self-weight consolidation of RCS at different water contents and under different specimen heights, the

data presented so far are fitted on a log-log linear curve. For example, Figure 4.35 shows the fit to e-$\sigma_v^{'}$ data for 6-inch-150% IWC specimen at 30 days. The equation for the fit is:

$$e = A(\sigma_v^{'})^B \tag{4.10}$$

where A = 3.52, B = -0.046, and for 95% confidence interval, 3.47 < A < 3.58 and -0.062 < B < -0.030. Fitting of consolidation data for other specimens provides the A and B values for void ratio-effective stress relationships that are presented in Table 4.5. These relationships are needed as input for modeling of large-strain consolidation of the sediment under self-weight, as explained in the next section. For 95% confidence level, the relationships are non-distinct for the 150% IWC 3-inch and 6-inch specimens. For the other two values of initial water contents, the slopes of the log-log linear line for 3-inch and 6-inch are statistically the same, whereas the intercepts are statistically different.

In Figure 4.36, the consolidated e-$\sigma_v^{'}$ data for 6-inch RCS specimens with different initial water contents have been collated. This illustrates the nature of compression curve for RCS. As effective stress increases, the effects of initial water content and specimen height become negligible, giving a compression behavior where the void ratio is almost uniquely determined by the vertical effective stress. The compression curve begins to fan out in the low effective stress range. The effect of initial water content on the compression curve starts showing in the intermediate effective stress range ($10\ g/cm^2 < \sigma_v^{'} < 100\ g/cm^2$), and the compression curves are distinctly non-unique below $10\ g/cm^2$.

Before proceeding to the shear strength-effective stress behavior of the sediment, a description and results of the consolidation model CONDES0 are provided in the following section.

4.2.3 Consolidation model CONDES0

CONDES0 (CONDES-Zero) is a finite difference consolidation model developed by Yao and Znidarcic (1997), and is available free-of-cost upon request from the authors.

Based on non-linear governing equations, this model is adapted for analysis of large strain one-dimensional consolidation and dessication of soft soils. The input information required by the model includes all the parameters in the constitutive relationships along with the information on geometry and boundary conditions. Specifically, the program needs the material characteristics in the following form:

Void ratio-effective stress relationship:

$$e = A(\sigma_v^{'} + Z)^B \tag{4.11}$$

Hydraulic conductivity-void ratio relationship:

$$k = Ce^D \tag{4.12}$$

where A, B, C, D, and Z are empirical constants. C and Z have the same units as the hydraulic conductivity and vertical effective stress units employed in the analysis.

The values of A and B were obtained from void ratio-effective stress profiles discussed in the previous section. A value of 0.005 g/cm^2 was used for Z, which is equivalent to the effective stress for an RCS layer less than 1 mm thick. This small value of Z has no discernible effect on the model output, but a small positive value of Z is required in order to ensure a well-defined void ratio in the slurry stage (where effective stress is assumed to be zero). The material constants C and D were ascertained from the estimates of hydraulic conductivity in Table 4.4.

Void ratio and surface settlement profiles were generated by CONDES0 for RCS specimens with different initial water contents and initial deposit heights. For a given initial water content, the same void ratio-effective stress relationship (obtained from the 6-inch specimen measurements) was used as input for model runs with all specimen heights. The values of different input parameters are summarized in Table 4.6.

The comparisons of model results with experimental void ratio measurements are presented in Figures 4.37-4.45, at different consolidation times for each sediment specimen.

The model performs fairly well in predicting the density profiles of consolidating specimens, given the scarcity of data that are used to estimate the material properties, especially the data for hydraulic conductivity-void ratio relationship. A general trend, which is clearly evident in high initial water content specimens, is that the model over-predicts the extent of consolidation at early times and under-predicts it at later times. The deviation from experimental measurements exists mainly in the upper layers of the consolidating specimens. The maximum percentage difference, defined as the ratio of difference to the experimentally measured value of void ratio, is 6.6% for specimens with 150% IWC. For specimens with 200% IWC, comparisons for which are shown in Figures 4.40-4.42, the maximum percentage difference is 10.5% in top layers of the specimens and 5.5% in deeper layers. The maximum difference for specimens with 250% IWC, shown in Figures 4.43-4.45, is also around 10% in top layers and around 5% in deeper layers.

The CONDES0 model can also give the time profiles of surface settlement. These results are compared with the measured settlement profiles in Figures 4.46-4.48. The profiles compare well, with the maximum error in predicted settlement being less than 10%. Since the deposit height is a function of void ratio distribution over depth, only the accumulated (over depth) error in void ratio reflects in the surface settlement profiles.

4.3 Shear Strength Measurements

This section presents the measurements and analysis of undrained shear strength behavior in RCS specimens. For self-weight and surcharge consolidation experiments, the measurements were obtained with the Automated Fall Cone Device (AFCD). The shear strength value for a particular layer in self-weight consolidation experiments was obtained from the average of 6-8 tests performed on that layer. The maximum value of the coefficient of variation (ratio of standard deviation to the average value) in these measurements was about 10%. For surcharge experiments, the shear strength measurements were obtained at different points on two layers in the middle of the

consolidated specimen. The coefficient of variation for these measurements for a given specimen was less than 10%. The error bars corresponding to 95% confidence level are plotted along with the shear strength values in the figures presented in this section. No shear strength measurements could be performed at the effective stresses greater than 100 g/cm^2, due to the limitations of CRS testing method.

For self-weight experiments, the depth coordinate associated with each shear strength measurement corresponds to the depth (below the surface) of the sediment layer being tested, and takes into account the depth of cone penetration into the layer. Similar to the methodology adopted for void ratio-effective stress curves, the depth coordinate is converted to an effective stress value in accordance with Eqs. [4.8] and [4.9]. As discussed earlier, the values of effective stress calculated in this manner overestimate the true effective stress in sediment specimens during the consolidation period, and represent the true effective stress only for fully consolidated specimens. In the following figures, the empty and solid symbols are used respectively to denote the overestimated and true values of effective stress, unless otherwise noted. For surcharge experiments, the value of effective stress is directly calculated from the amount of surcharge applied to the specimen.

Figure 4.49 shows the variation of shear strength-effective stress curve with time for 3-inch specimen with 150% IWC. The solid circular symbols represent the measurements from surcharge experiments. Figures 4.50-4.54 show the similar data for other specimens with different initial heights and initial water content. The trend of solid symbols on these plots indicates the possibility of a correlation between undrained shear strength and effective stress in consolidated specimens, but the data are not sufficient enough to explore this possibility. The following section discusses the technique that was adopted to utilize the shear strength data obtained during consolidation.

4.3.1 Estimation of vertical effective stress during consolidation

For specimens undergoing self-weight consolidation, it may be assumed that the material can be characterized by the compression curve obtained at the end of consolidation. In other words, the material behavior during consolidation is assumed to be governed by the void ratio-effective stress characteristic obtained from its consolidated state. Hence, an extrapolation of this characteristic relationship to effective stresses lower than the consolidated state can be used to correlate effective stresses during consolidation to extant void ratios and vice versa. This assumption also forms the basis of numerical consolidation models like CONDES0.

In the present case, this technique is used to estimate true values of effective stress corresponding to void ratio measurements performed during consolidation. The calculations are performed as follows. For a specimen with given initial height and initial water content, its void ratio-effective stress relationship is extracted from the density profile measurements in the consolidated state. (These characteristic relationships were summarized in Table 4.5 for 3-inch and 6-inch specimens). For every void ratio measurement performed during the consolidation process, the effective stress is found from the void ratio-effective stress relationship. Figure 4.55 illustrates this procedure for the 3-inch-150% IWC specimen. This value of effective stress is then paired with the corresponding shear strength measurement performed on the same sediment layer during the consolidation process, and in this manner the corrected shear strength-effective stress curves are obtained for times during the consolidation period.

4.3.2 Shear strength- corrected effective stress curves

Figure 4.56 shows the shear strength-corrected effective stress variation for 3-inch-150% IWC sediment specimen. The plot shows a linear dependence on logarithmic scales. In contrast, the conventional soil mechanics formulation for shear strength is

a linear function of effective stress:

$$c_u = c + \sigma_v^{'} tan\phi \tag{4.13}$$

where c is the cohesion-intercept and ϕ is the friction angle for the material. In order to examine the applicability of the conventional strength formulation, the shear strength-corrected effective stress variation for the same specimen is plotted on linear scale in Figure 4.57.

A comparison with Figure 4.56 indicates that the shear strength-effective stress relationship is exponential in low effective stress range, but approaches linear behavior at high effective stresses. An examination of data shows that the two trends predict the same value of shear strength at the effective stress of 5 g/cm^2 (Figure 4.57). The transition region, therefore, is around the effective stress value of 5 g/cm^2. Hence, two equations would be required to provide an accurate predictive relationship for shear strength: one equation for the log-log linear effective stress dependence in the low effective stress range, and the other for linear effective stress dependence. A common transition point would ensure the continuity of shear strength variation between the two regimes.

In order to determine the parameters for the classical cohesion-friction angle formulation of shear strength (Eq. [4.12]), the data from surcharge experiments alone are subjected to linear regression, as shown. The best-fit line is indicated in Figure 4.57, and it yields a cohesion intercept of 7.7 g/cm^2 and a friction angle of 30^o.

The upper and lower bounds for 95% confidence level upper and lower bounds on the fit parameters are presented in Table 4.7.

Figure 4.58 shows the result of extending this classical cohesion-friction angle formulation to low effective stress range. The thick solid line indicates the shear strengths predicted by this relationship. It can be seen that the classical model increasingly over-predicts the strength as the effective stress decreases.

An examination of the data on Figure 4.57 indicates that the transition point, below which the linear strength relationship derived from the high-stress (surcharge)

experiments may not be assumed to be valid, is around ($\sigma_v^{'}$ = 5 g/cm^2, c_u = 10 g/cm^2).

The 3-inch self-weight consolidation data are now regressed for the best log-log linear fit. In order to ensure the continuity of strength variation between the exponential and linear dependence regimes, this fit is constrained to pass through the transition point. The constrained fit to the 3-inch specimen data is presented in Figure 4.58, and is given by the equation :

$$c_u = 4.79\sigma_v^{'\,0.46} \tag{4.14}$$

The units of $\sigma_v^{'}$ and c_u are in g/cm^2. The exponent lies in the range 0.40-0.51 for 95% confidence intervals. The range of the multiplier (4.79) is a direct function of range in the exponent, due to the forcing of the fit.

Figure 4.58 also shows the fit for 6-inch data, similarly constrained to pass through the pivot point of($\sigma_v^{'}$ = 5 g/cm^2, c_u = 10 g/cm^2). The regression equation is:

$$c_u = 3.89\sigma_v^{'\,0.58} \tag{4.15}$$

with the 95% confidence interval range for the exponent being 0.53-0.64.

The shear strength for 6-inch specimens at a given effective stress value is lower than its corresponding value in the 3-inch specimen. This difference is due to the difference in void ratio-effective stress relationship for the two specimens. At a certain effective stress, the 6-inch specimen has higher void ratio than the 3-inch specimen, as shown in Figure 4.26. The variation of shear strength-effective stress relationship with specimen height was also observed by Zreik (1994) for Boston Blue Clay (BBC) beds deposited from slurry. Figure 4.59 is a reproduction of Zreik's results for strength variation in 3-day old beds with initial slurry water content of 550%. A comparison of BBC results with the Reserved Channel Sediment (RCS) measurements shows that RCS is a much stronger material than BBC. For effective stress values below 1 g/cm^2, the undrained strength ratio (defined as the ratio of undrained shear strength to vertical effective stress) for RCS is almost an order of magnitude higher than the value for BBC. The undrained strength ratio decreases with increasing effective stress

and is around unity at and above 10 g/cm^2.

The 95% confidence ranges for the exponents in Equations 4.13 and 4.14 are presented in Table 4.7, and can be seen to be statistically distinct. The difference is important to note because there is no statistical difference in the void ratio-effective stress relationships for the two specimens, as discussed earlier. This difference in the shear strength relationships for 3-inch and 6-inch specimens indicates that the effect of specimen height is important in the low effective stress region for small specimen heights. As specimen height increases, the shear strength-effective stress lines are expected to move downward. In order to test this hypothesis, it was decided to utilize the measurements from 12-inch 150% IWC specimen. It should be noted that since the 12-inch specimens could not be tested in consolidated state, the void ratio-effective relationship from the 12-inch specimen is not known. Instead, the relationship for the 6-inch 150% IWC specimen was used to correct the shear strength-effective stress profiles of the 12-inch specimen. The 12-inch measurements are shown as empty symbols in Figure 4.58. The regression line for these points does lie below the line for 6-inch specimen measurements. The 95% confidence range for the exponent, however, overlaps with the exponent range for the 6-inch specimen relationship (Table 4.7). The effect of doubling the specimen height from 6 inches to 12 inches is smaller than the effect of doubling it from 3 inches to 6 inches. The difference could, therefore, be expected to diminish with increasing deposit heights. Hence, the log-log fit to 3-inch specimen measurements may be taken as the upper-bound estimator of shear strength for a certain effective stress in a sediment deposit of any height.

The lowest strength possible for a sediment layer in a deposit of any height is the remolded strength of the sediment at its initial water content. For a deposit with initial water content of 150%, this is shown in Figure 4.58 by the horizontal line at $c_{u(rm)} = 0.45\ g/cm^2$. The thin solid line in the figure is the best log-log linear fit to the surcharge measurements alone. It may be assumed that in the low effective stress range (where the classical shear strength relationship is not valid), the lower-bound estimate of shear strength is given by the intersection of the (constant) remolded strength line with the line for the log-log linear fit to the surcharge data alone.

With these estimators of upper and lower bounds, the strength in the low effective stress region in a deposit of any size is constrained to lie in the triangular region formed by the following three lines: the constant (remolded) strength line, the log-log regression line for 3-inch specimen measurements (0 to pass through a chosen transition point), and the log-log regression line for the surcharge data alone. Figures 4.60 and 4.61 show this region for specimens with 200% and 250% IWC. The fit of surcharge data for these specimens to the classical cohesion-friction angle formulation is shown in Figures 4.62 and 4.63. All the fit parameters are provided in the legends, and the 95% confidence level upper and lower bounds on these parameters are given in Table 4.7. The transition values of the effective stress for each initial water content are also provided in the table.

The classical cohesion-friction angle formulation should be used to predict shear strength for effective stresses above the transition point, whereas the exponential strength relationships should be used for accurate estimation of strength below the transition point.

To conclude, the shear strength-effective stress relationship for RCS specimens can be adequately characterized by employing two different strength formulations. This ability to correlate undrained shear strength with effective stress at all times during consolidation can be used to predict in situ shear strength of sediment deposits, as is discussed in the next chapter.

4.4 Summary

The results of surface settlement experiments on RCS specimens were analyzed to estimate important consolidation parameters like coefficient of consolidation and hydraulic conductivity. The values of these parameters were found to be typical of organic silty sediments. RCS specimens with 3-inch and 6-inch initial heights were found to be completely consolidated within 30 days.

The data on water content profiles were converted to void ratio-depth and void ratio-effective stress profiles. The void ratio-effective stress profiles obtained from the

specimens in consolidated state were used to establish the characteristic compression curves for the specimens. These compression curves were used as input material characteristics for a numerical simulation of consolidation using the numerical model CONDES0. The void ratio-depth profiles predicted by the model were within 10% of the measured values.

The compression curves established from the density profiles of consolidated specimens were also used to predict the true value of effective stress for measurements taken on the specimens during consolidation. The corrected values of effective stress were paired with shear strength measurements performed during consolidation to establish shear strength-effective strength relationships. These relationships can be employed to devise methods for estimation of in situ strength in consolidating dredged material deposits.

Table 4.1: Time to end of primary consolidation, t_p, for RCS self-weight specimens

IWC	3-inch specimen	6-inch specimen	12-inch specimen
150 %	150 hrs (6.2 days)	380 hrs (15.8 days)	910 hrs (38 days)
200 %	140 hrs (5.8 days)	300 hrs (12.5 days)	710 hrs (29.6 days)
250 %	135 hrs (5.6 days)	270 hrs (11.2 days)	660 hrs (27.5 days)

Table 4.2: Coefficient of consolidation, c_v (in cm^2/s), for RCS self-weight specimens

IWC	3-inch specimen	6-inch specimen	12-inch specimen
150 %	0.48e-4	0.84e-4	1.5e-4
200 %	0.63e-4	0.94e-4	2.1e-4
250 %	0.83e-4	1.28e-4	2.37e-4

Table 4.3: Rate of secondary compression, c_α, for RCS self-weight specimens

IWC	3-inch specimen	6-inch specimen	12-inch specimen
150 %	0.020	0.033	0.047
200 %	0.025	0.045	0.058
250 %	0.035	0.045	0.061

Table 4.4: Hydraulic conductivity, k (in cm/s) and corresponding void ratios for RCS

IWC	3-inch specimen	6-inch specimen	12-inch specimen
150 %	3.47e-6 (3.79)	2.37e-6 (3.74)	0.97e-6 (3.64)
200 %	6.02e-6 (4.74)	5.40e-6 (4.64)	2.62e-6 (4.48)
250 %	30.5e-6 (5.46)	25.0e-6 (5.44)	13.3e-6 (5.24)

Table 4.5: Void ratio - effective stress relationships for RCS

Specimen	$e = A\sigma_v'^{B}$	95% confidence limits
150% 3-inch	A=3.51, B=-0.045	3.47 < A < 3.55 -0.067 < B < -0.024
150% 6-inch	A=3.52, B=-0.046	3.47 < A < 3.55 -0.062 < B < -0.003
200% 3-inch	A=3.96, B=-0.096	3.90 < A < 4.01 -0.118 < B < -0.074
200% 6-inch	A=4.05, B=-0.086	4.01 < A < 4.10 -0.099 < B < -0.074
250% 3-inch	A=4.14, B=-0.092	4.07 < A < 4.21 -0.116 < B < -0.067
250% 6-inch	A=4.29, B=-0.098	4.21 < A < 4.37 -0.121 < B < -0.075

Table 4.6: Choice of input parameters for CONDES0, based on 6-inch specimens (RCS self-weight consolidation)

IWC	A	B	C	D	Z
150 %	3.52	-0.046	0.5e-24	32.42	0.005
200 %	4.05	-0.086	0.4e-15	15.26	0.005
250 %	4.29	-0.098	0.4e-18	18.83	0.005

Table 4.7: Shear strength- effective stress relationships for RCS

IWC	$c_u = c + \sigma_v' tan\phi$ surcharge	Transition eff. stress	$c_u = F\sigma_v'^{G}$ 3-inch	6-inch	surcharge
150 %	c=7.69 g/cm^2	5 g/cm^2	F=4.79	F=3.89	F=2.68
	tan ϕ=0.58		G=0.46	G=0.58	G=0.68
	-7.24 < c < 22.63				0.93 < F < 7.76
	0.33 < tan ϕ < 0.82		0.40 < G < 0.51	0.53 < G < 0.64	0.39 < G < 0.96
200 %	c=6.42 g/cm^2	4 g/cm^2	F=3.26	F=3.18	F=1.68
	tan ϕ=0.61		G=0.80	G=0.83	G=0.80
	-12.84 < c < 25.69				0.41 < F < 6.91
	0.29 < tan ϕ < 0.92		0.72 < G < 0.89	0.78 < G < 0.88	0.42 < G < 1.18
250 %	c=3.48 g/cm^2	3 g/cm^2	F=2.24	F=1.83	F=1.09
	tan ϕ=0.62		G=0.72	G=0.86	G=0.89
	-12.44 < c < 19.41				0.28 < F < 4.11
	0.36 < tan ϕ < 0.88		0.66 < G < 0.78	0.81 < G < 0.92	0.53 < G < 1.25

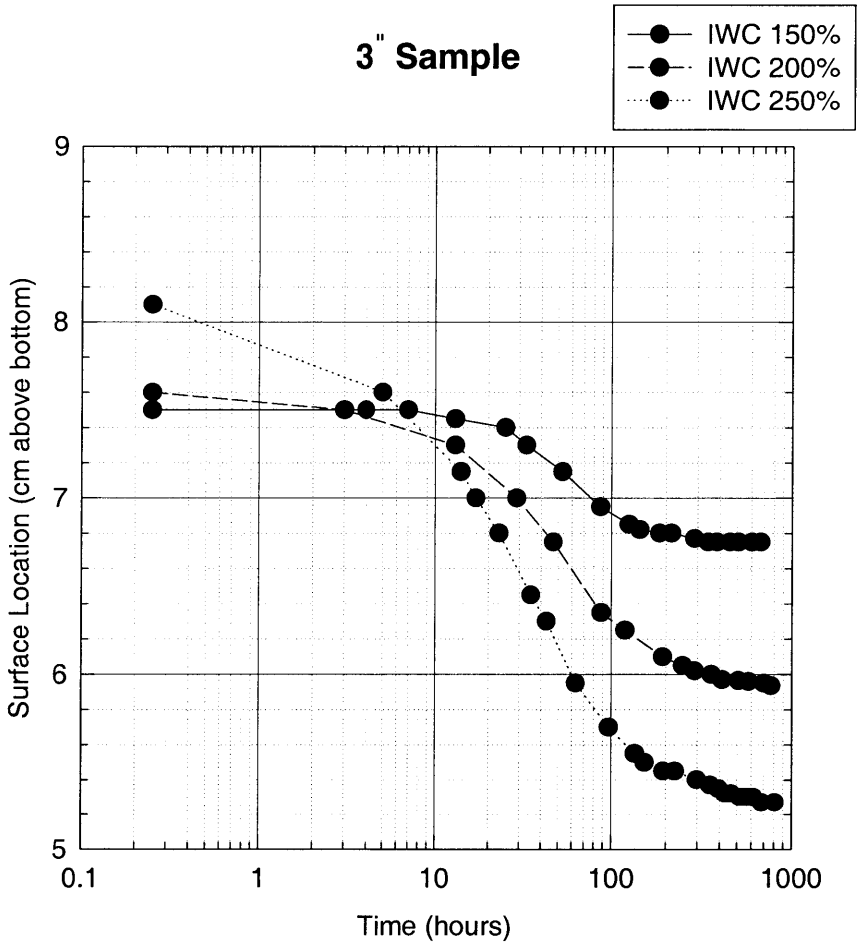

Figure 4-1: Settlement in RCS deposits: Self weight consolidation of 3-inch specimens with different initial water contents

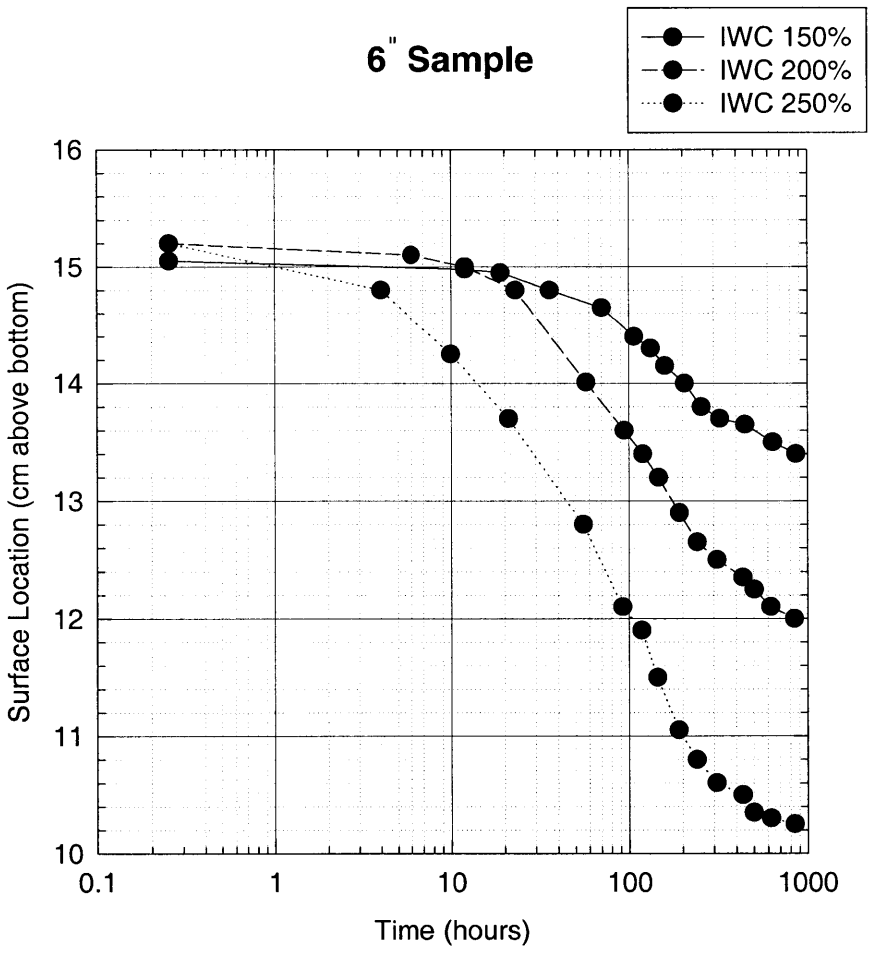

Figure 4-2: Settlement in RCS deposits: Self weight consolidation of 6-inch specimens with different initial water contents

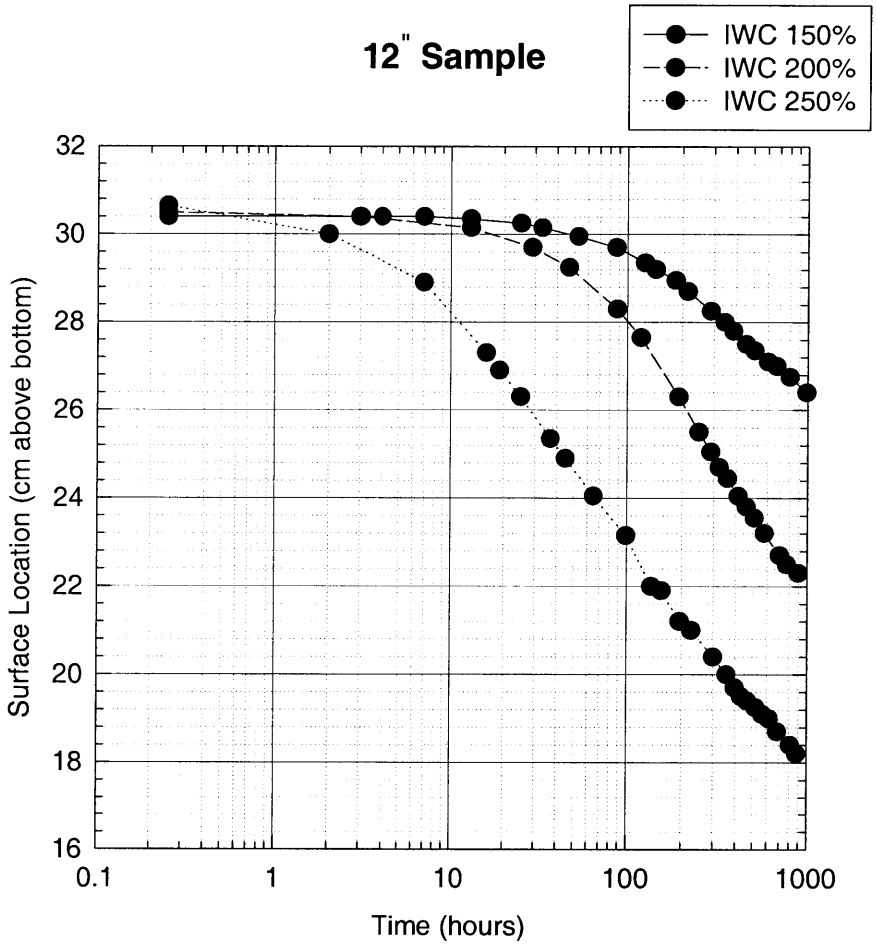

Figure 4-3: Settlement in RCS deposits: Self weight consolidation of 12-inch specimens with different initial water contents

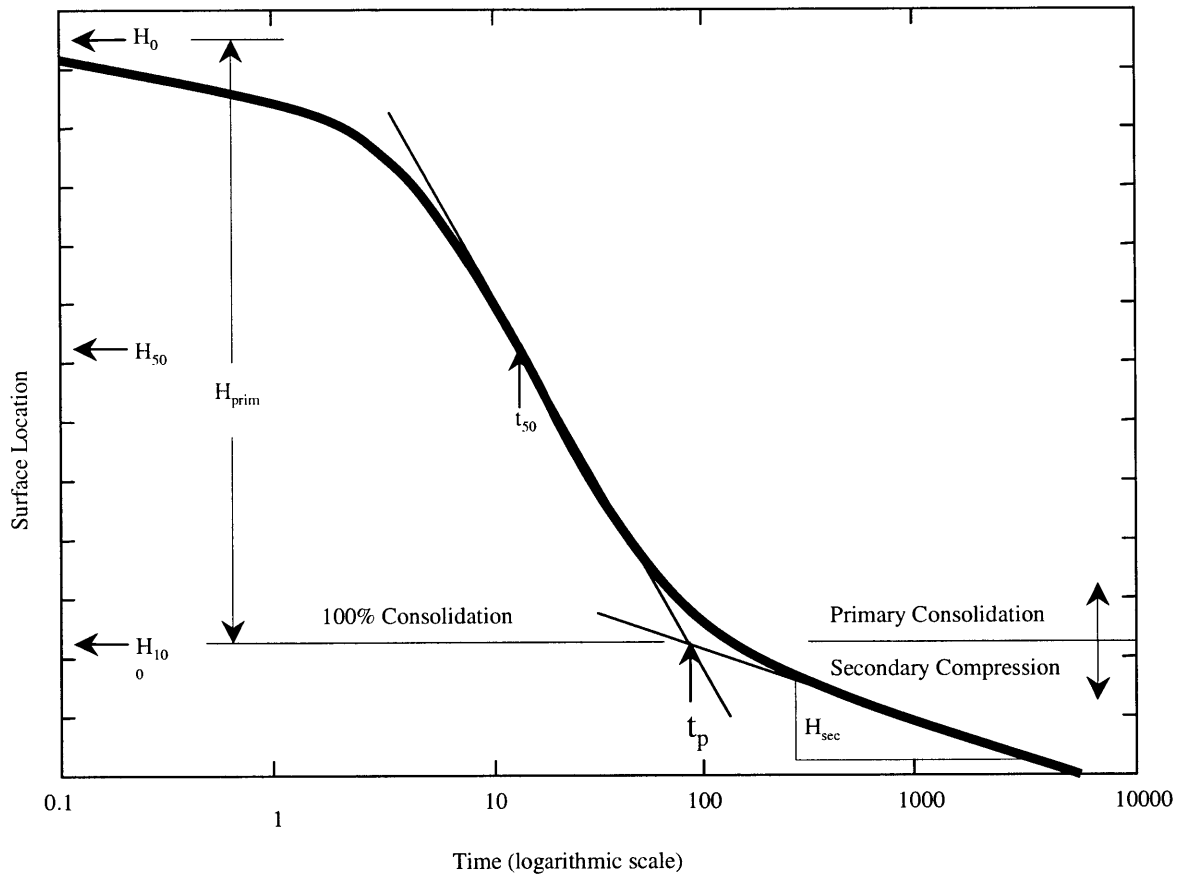

Figure 4-4: Settlement corresponding to primary consolidation and secondary compression in a sediment deposit

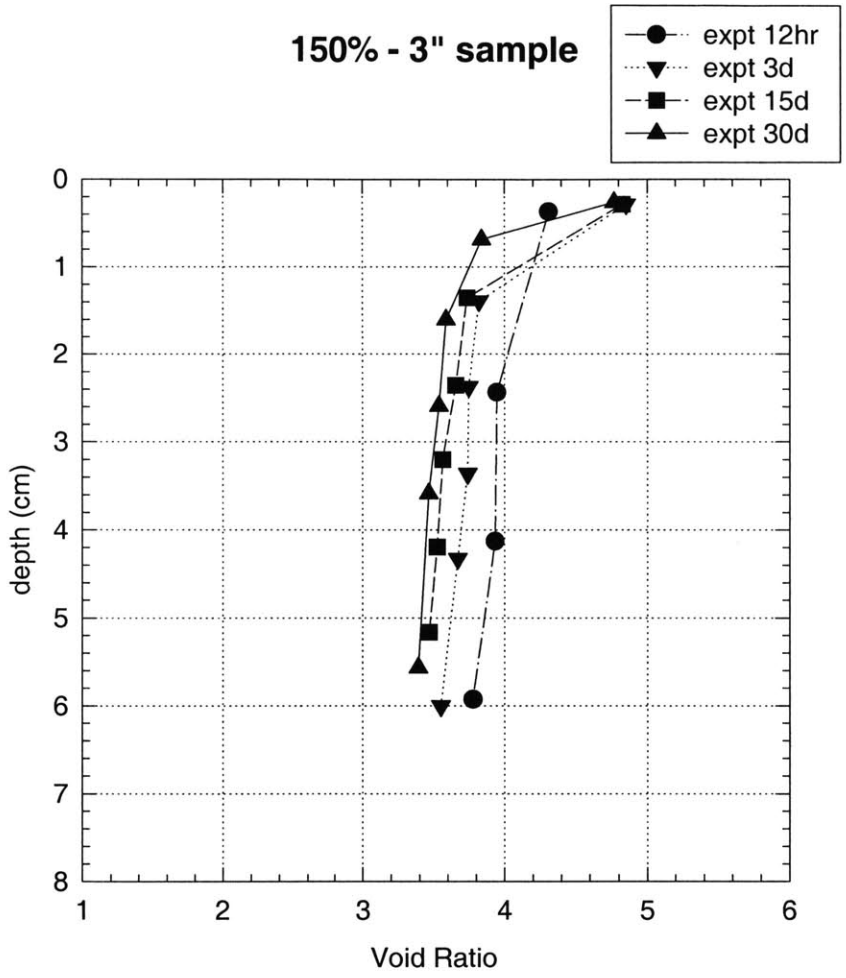

Figure 4-5: Void ratio - depth profiles for RCS 150% IWC 3-inch specimen

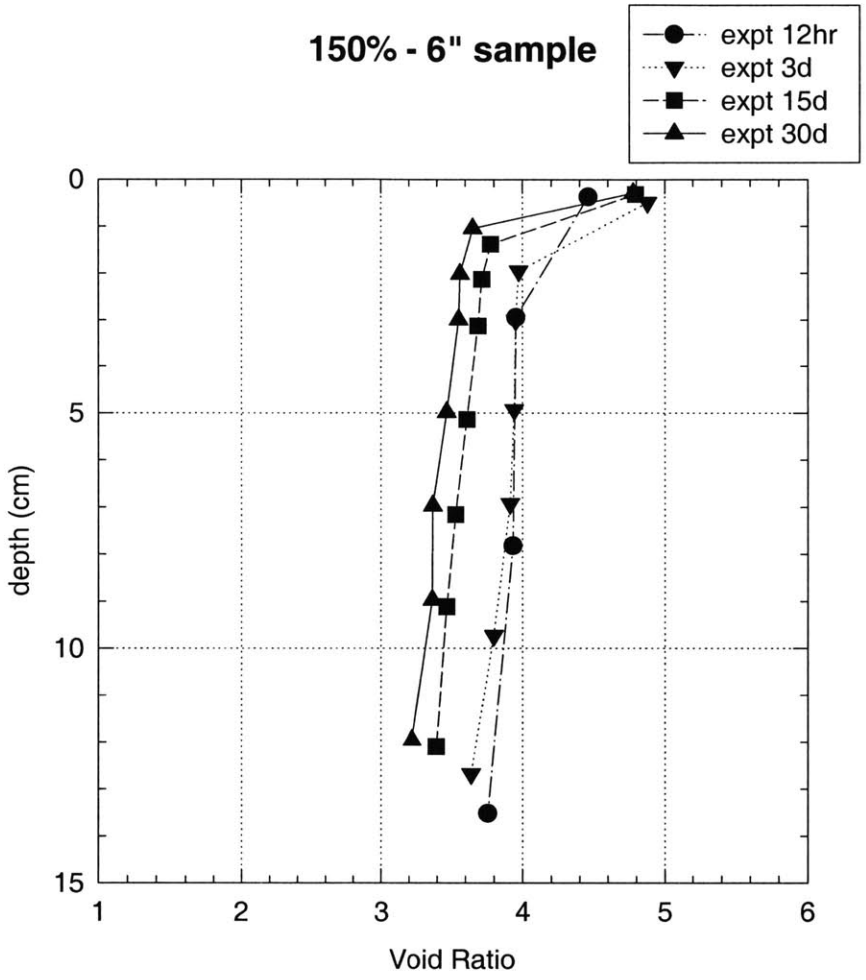

Figure 4-6: Void ratio - depth profiles for RCS 150% IWC 6-inch specimen

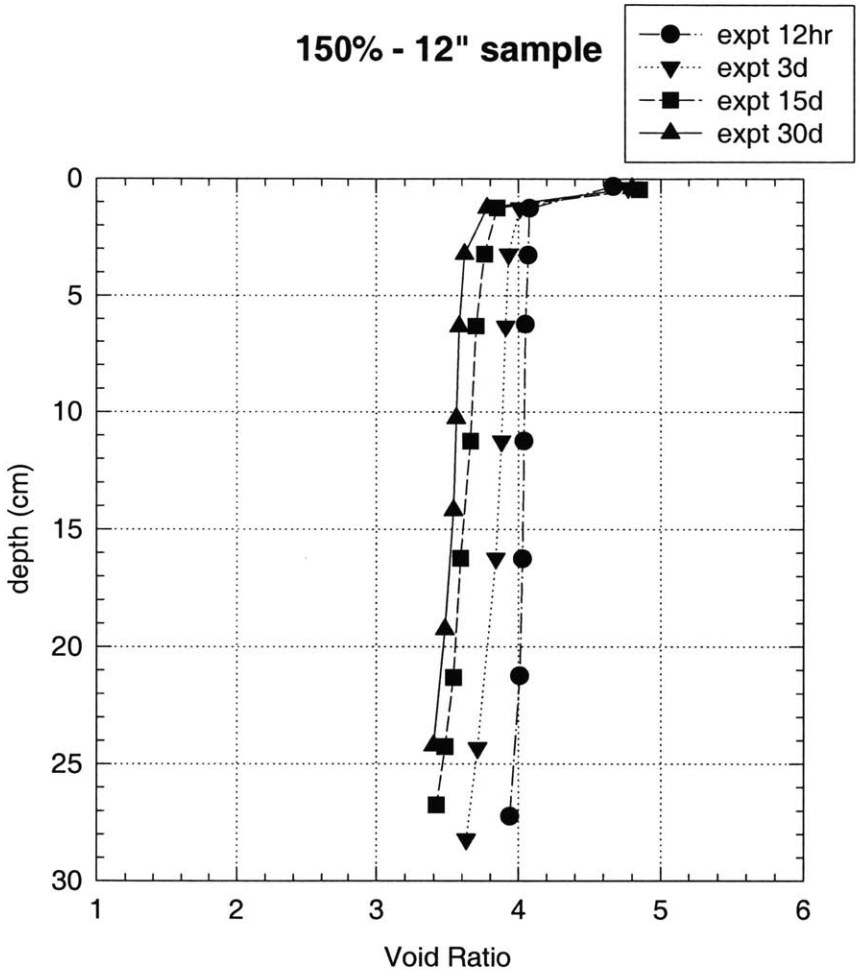

Figure 4-7: Void ratio - depth profiles for RCS 150% IWC 12-inch specimen

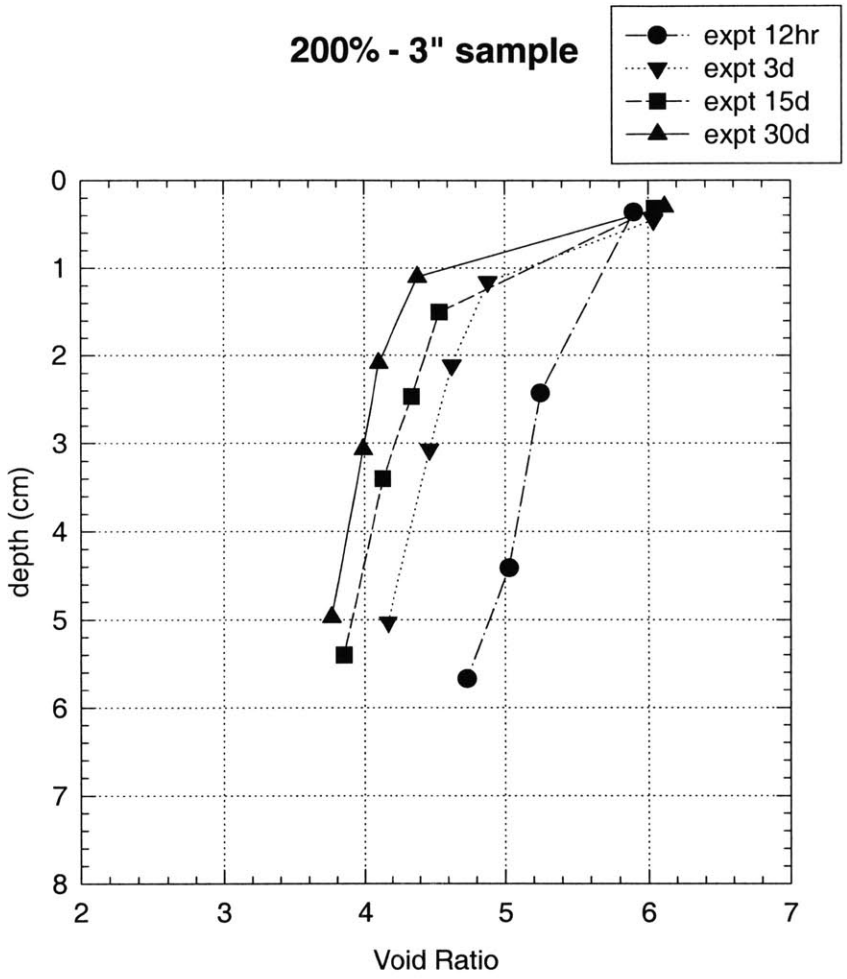

Figure 4-8: Void ratio - depth profiles for RCS 200% IWC 3-inch specimen

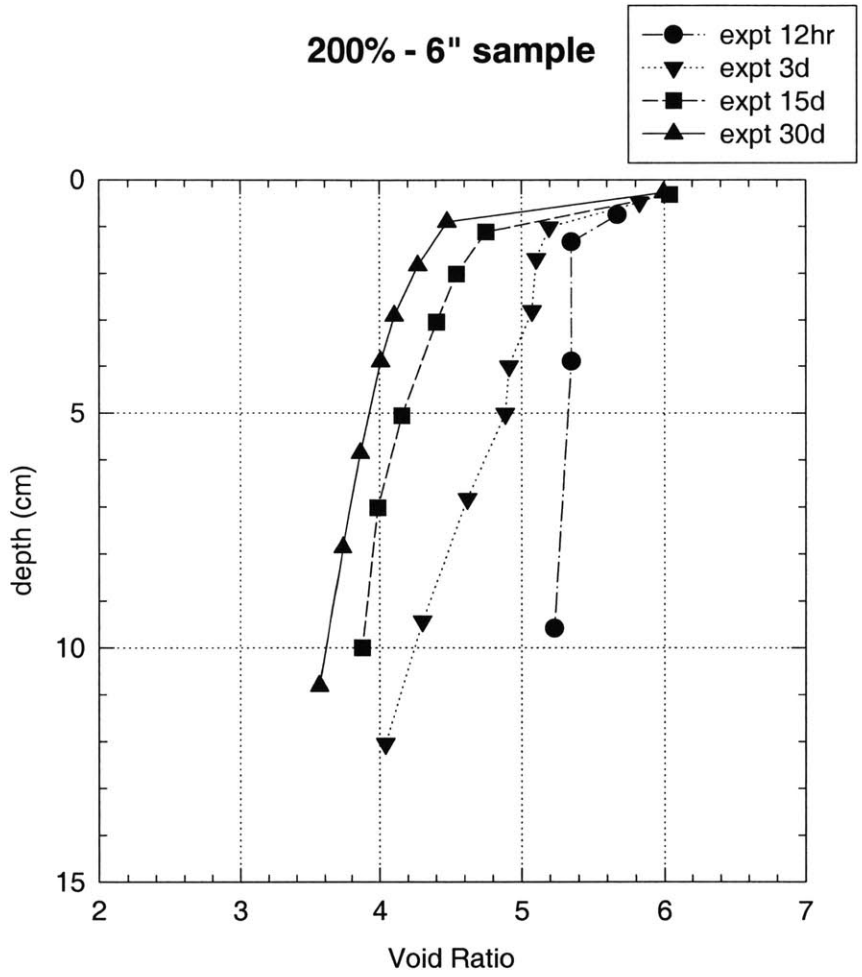

Figure 4-9: Void ratio - depth profiles for RCS 200% IWC 6-inch specimen

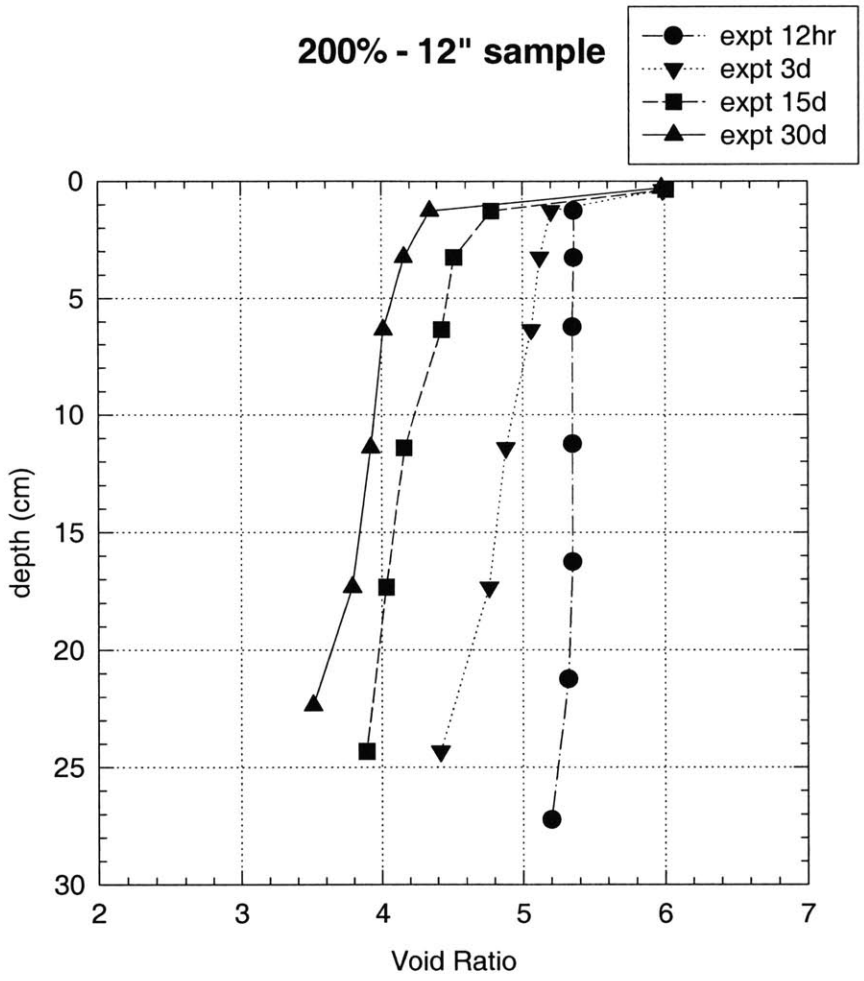

Figure 4-10: Void ratio - depth profiles for RCS 200% IWC 12-inch specimen

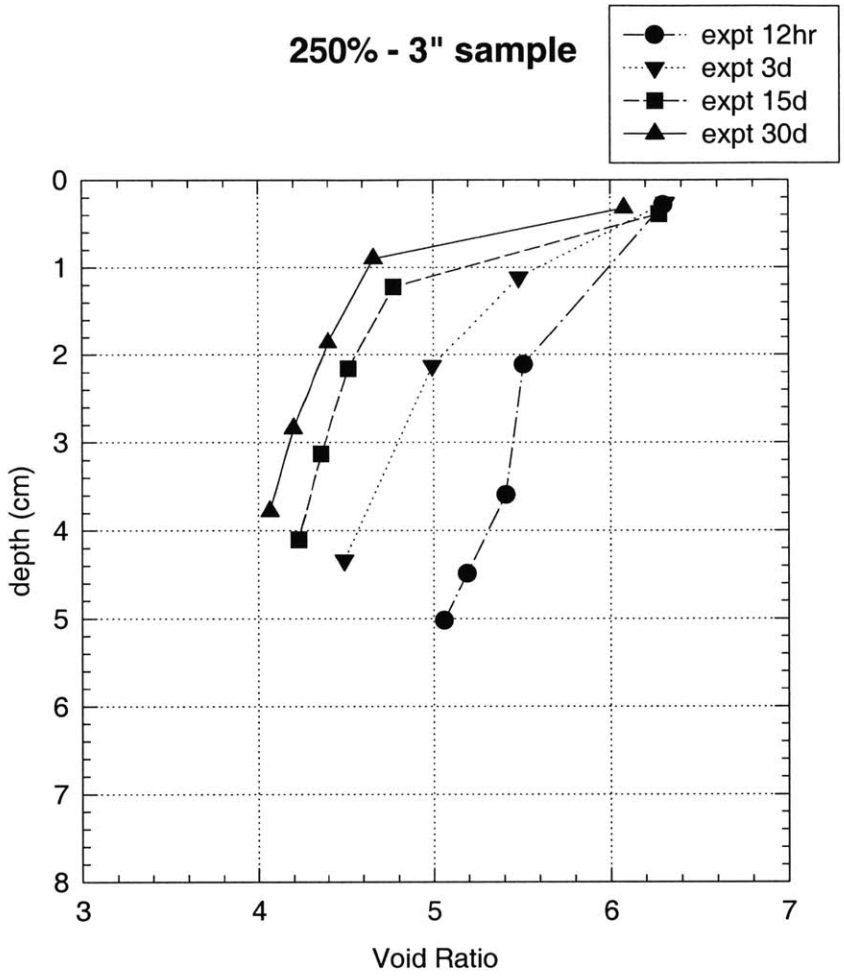

Figure 4-11: Void ratio - depth profiles for RCS 250% IWC 3-inch specimen

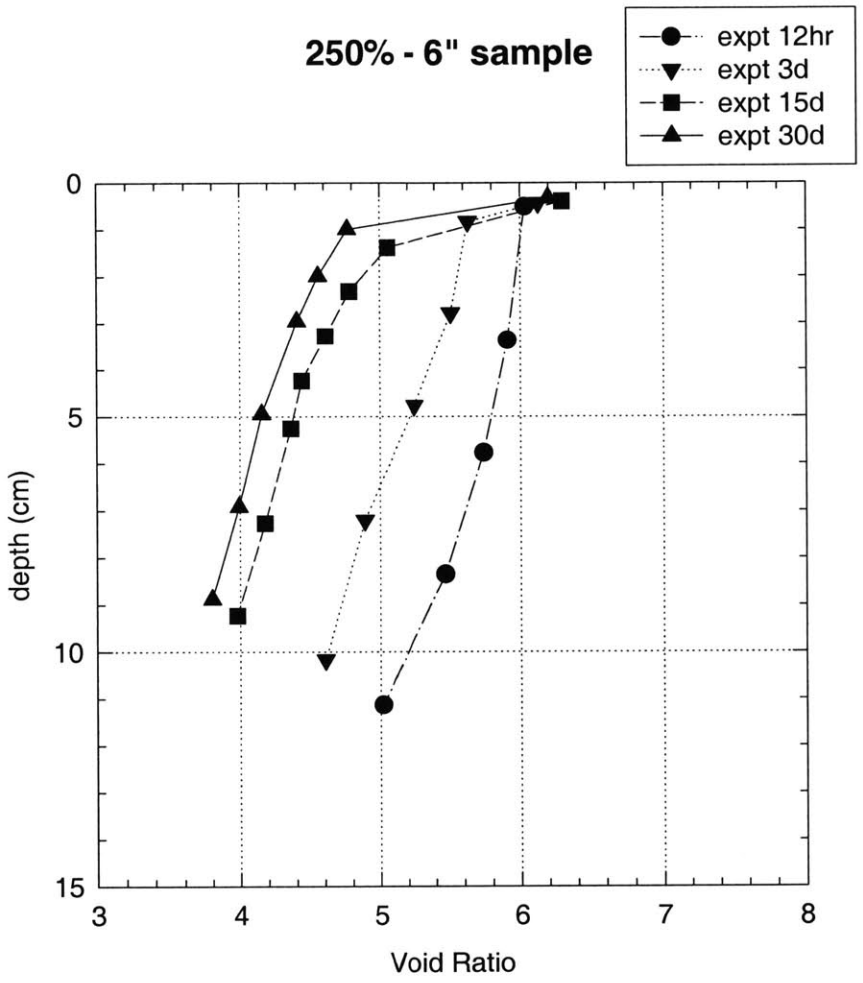

Figure 4-12: Void ratio - depth profiles for RCS 250% IWC 6-inch specimen

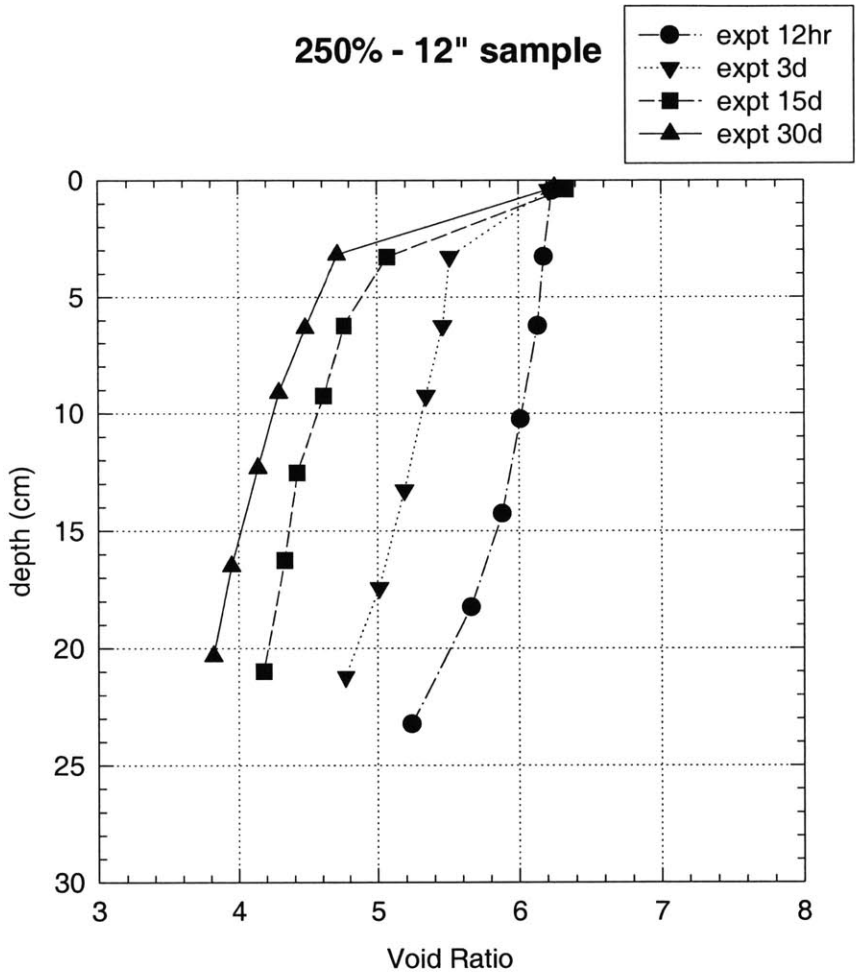

Figure 4-13: Void ratio - depth profiles for RCS 250% IWC 12-inch specimen

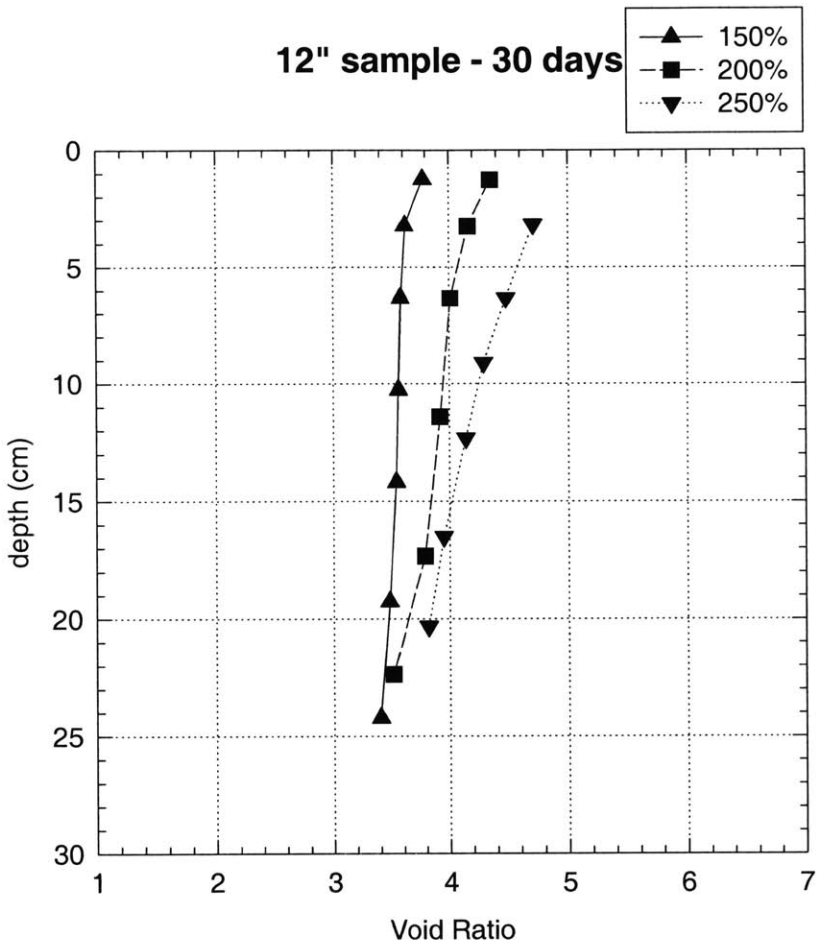

Figure 4-14: Void ratio - depth profiles for RCS 12-inch specimens at 30 days

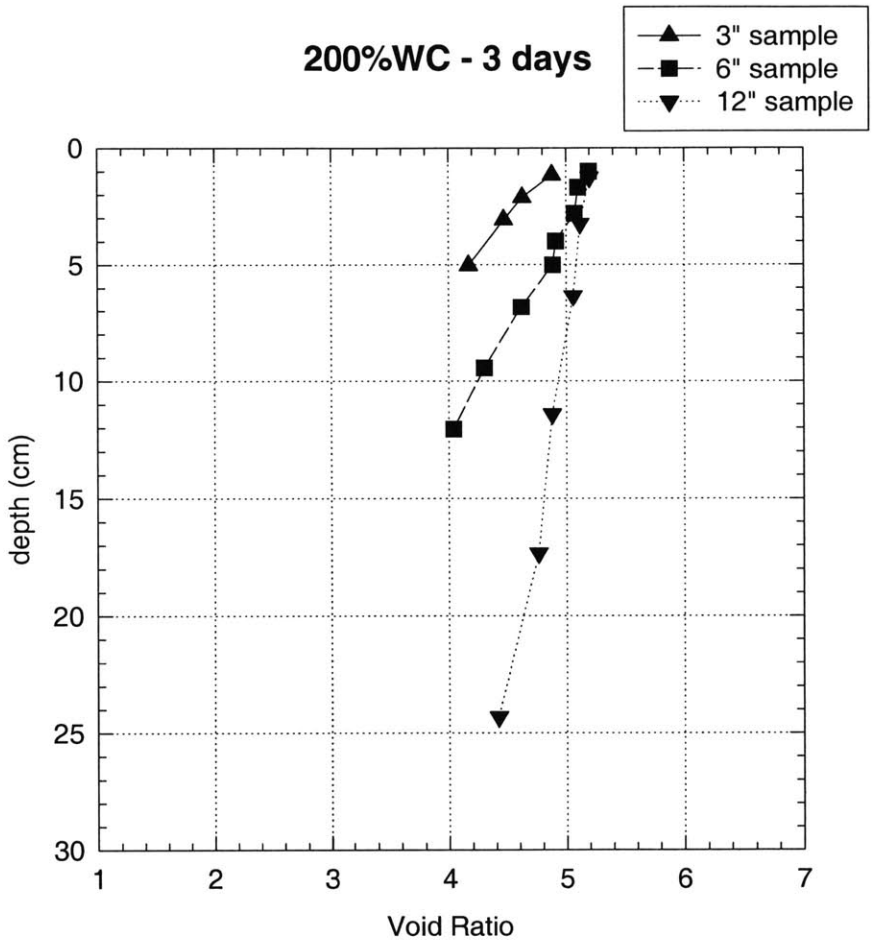

Figure 4-15: Void ratio - depth profiles for RCS 200% IWC specimens at 3 days

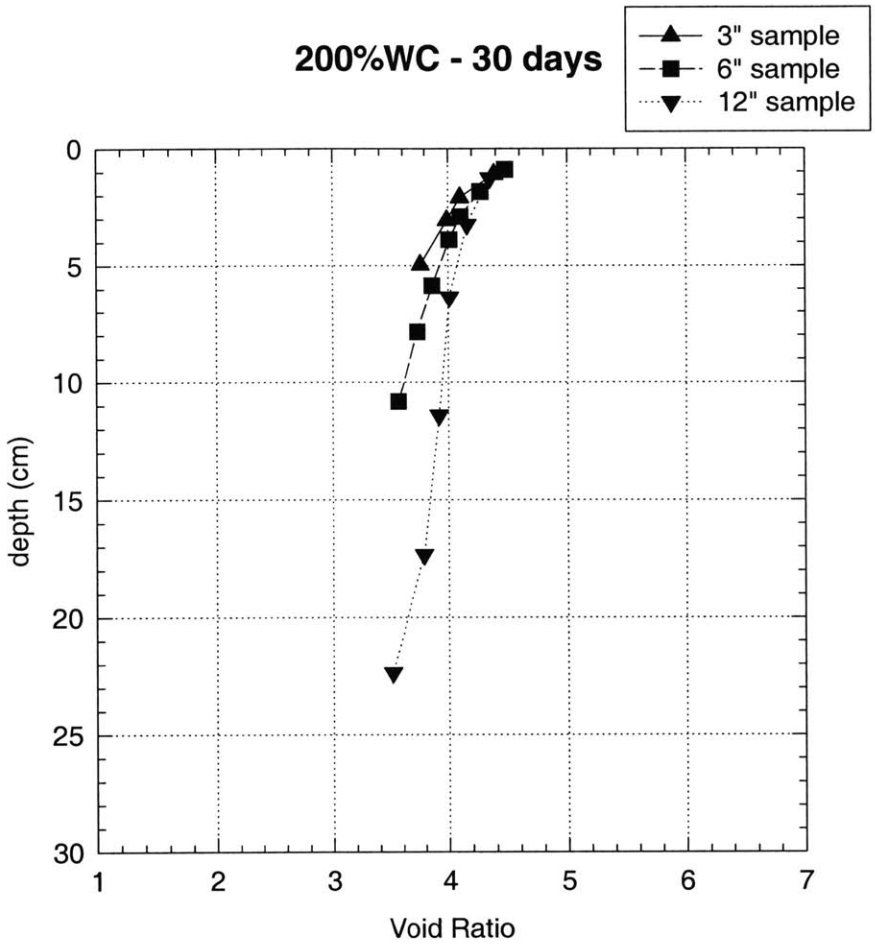

Figure 4-16: Void ratio - depth profiles for RCS 200% IWC specimens at 30 days

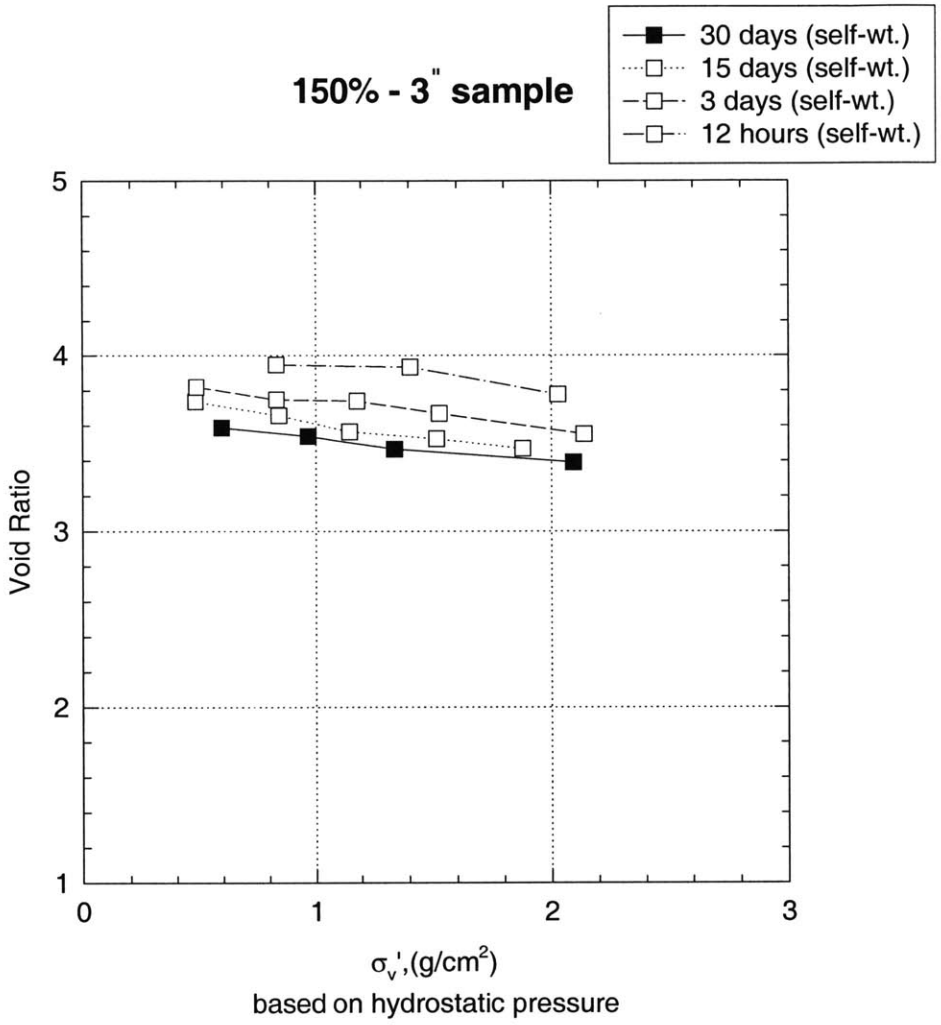

Figure 4-17: Void ratio - effective stress profiles for RCS 150% IWC 3-inch specimen

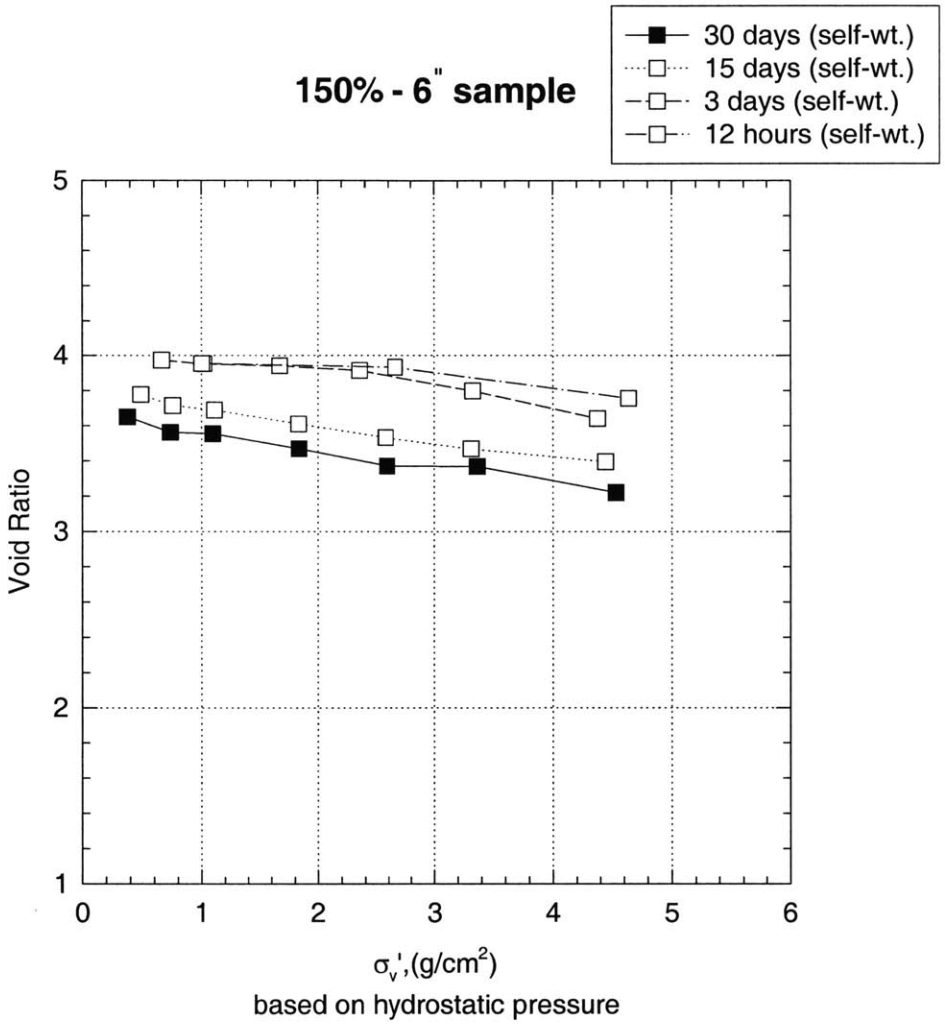

Figure 4-18: Void ratio - effective stress profiles for RCS 150% IWC 6-inch specimen

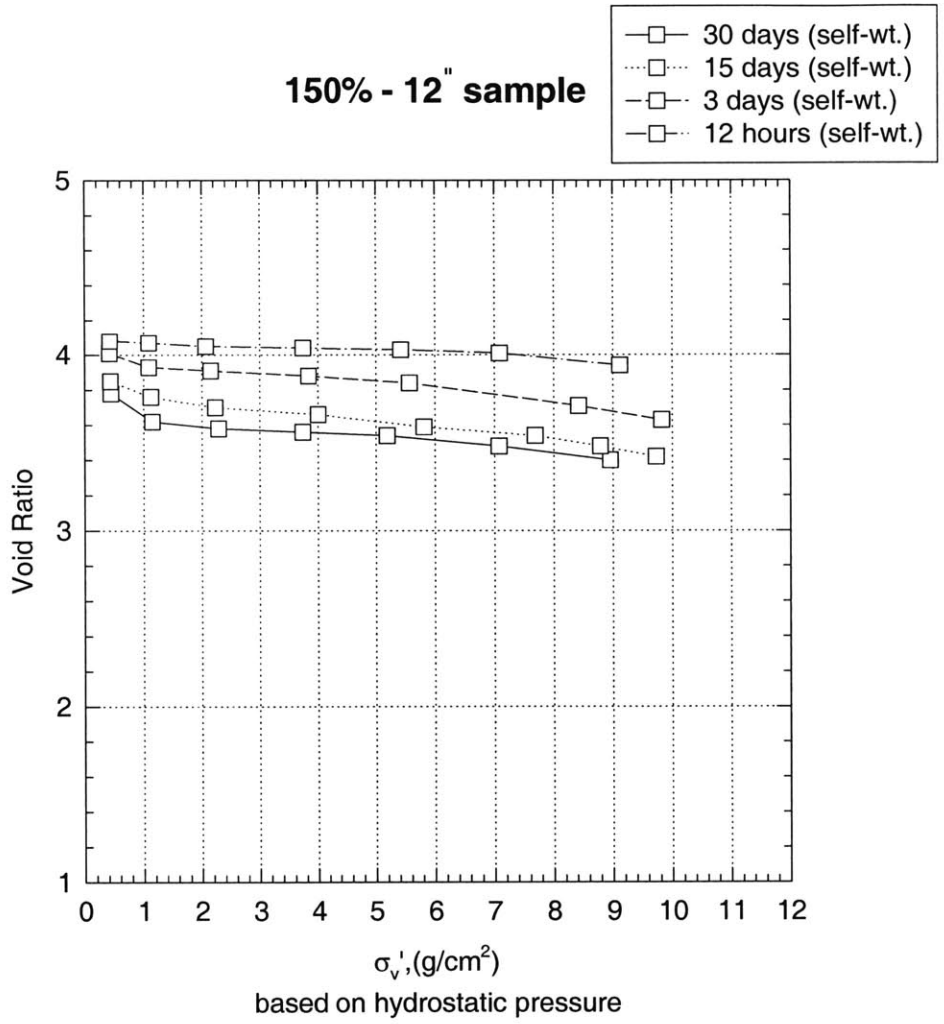

Figure 4-19: Void ratio - effective stress profiles for RCS 150% IWC 12-inch specimen

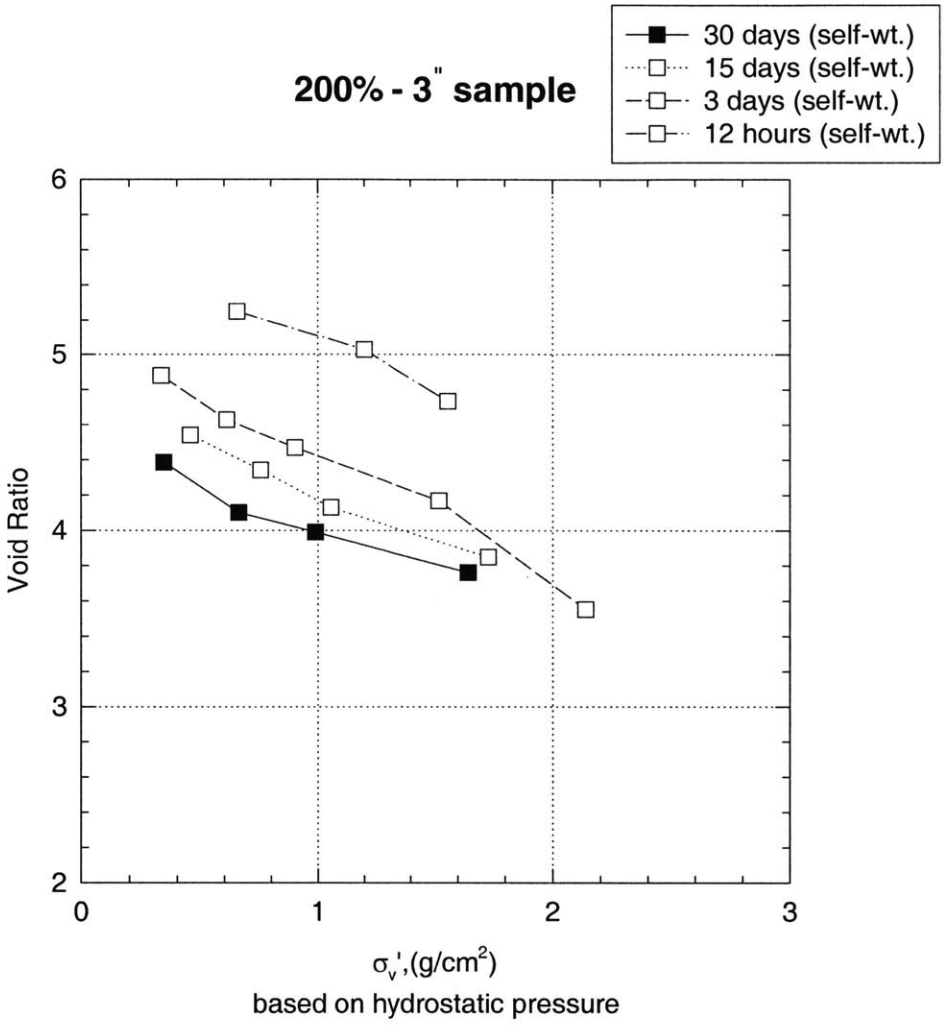

Figure 4-20: Void ratio - effective stress profiles for RCS 200% IWC 3-inch specimen

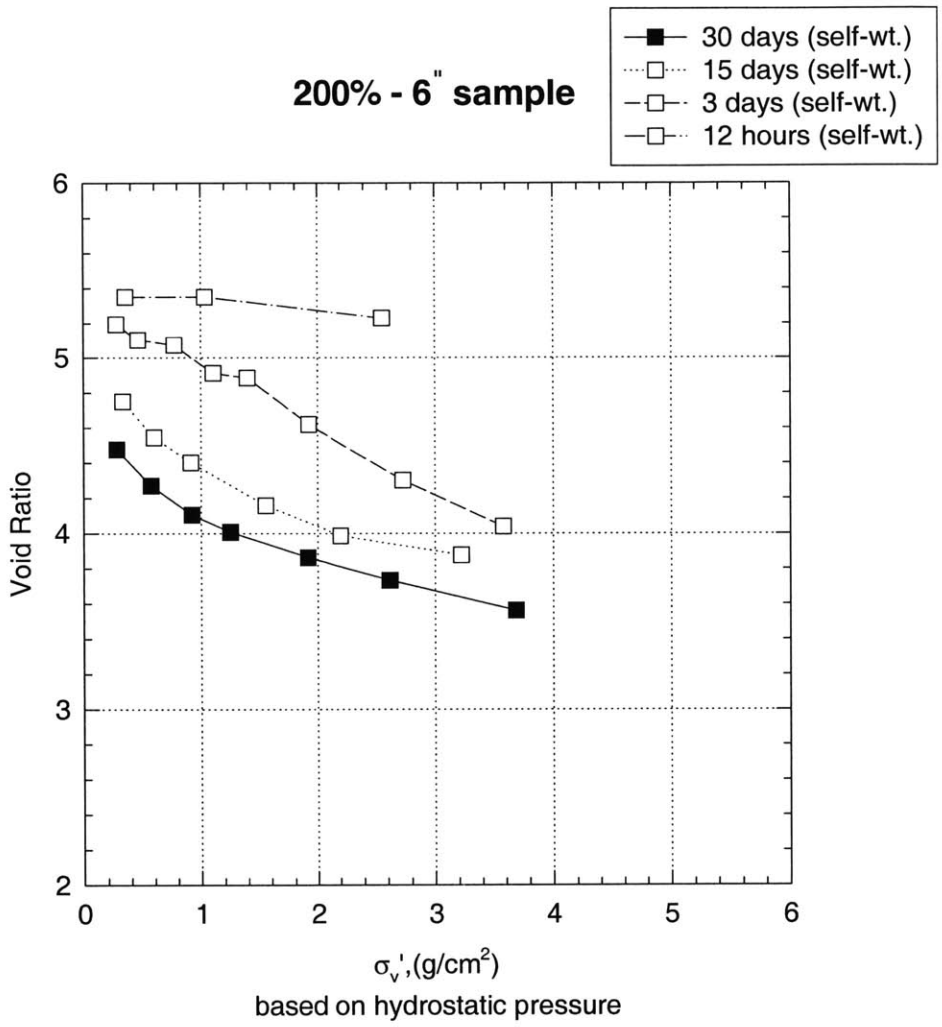

Figure 4-21: Void ratio - effective stress profiles for RCS 200% IWC 6-inch specimen

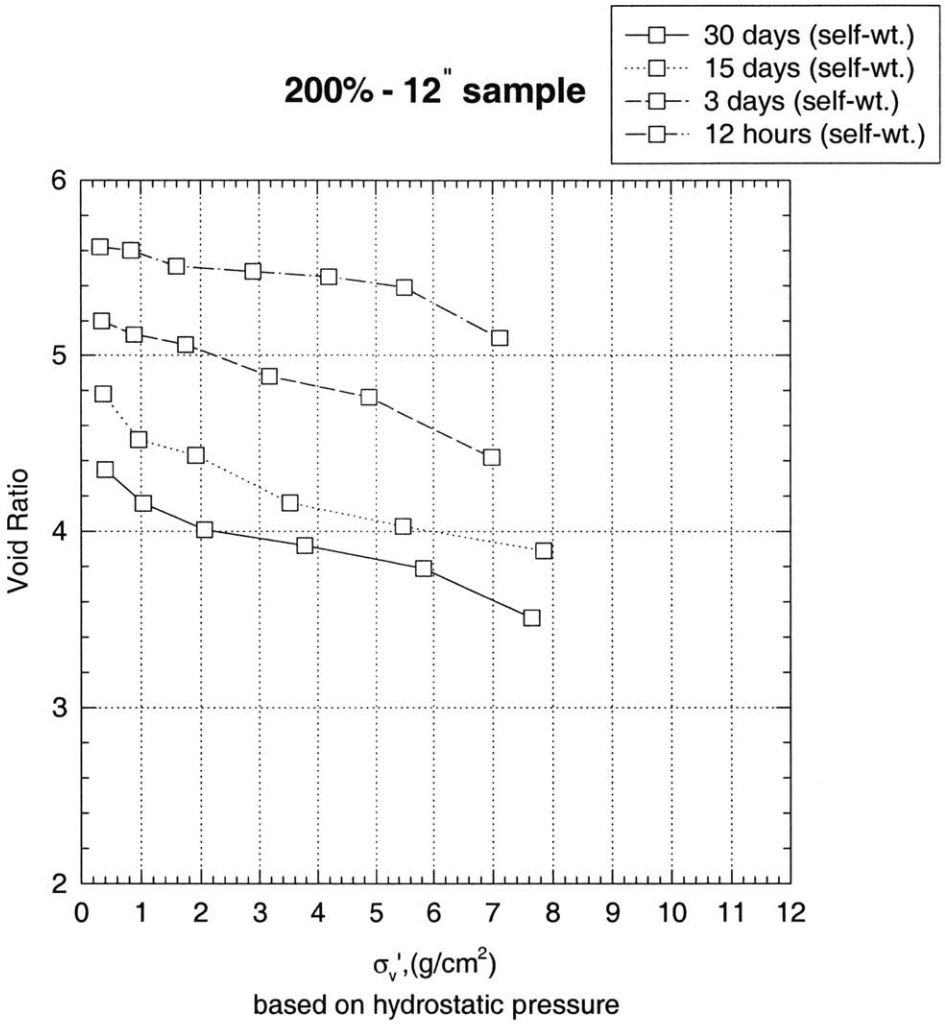

Figure 4-22: Void ratio - effective stress profiles for RCS 200% IWC 12-inch specimen

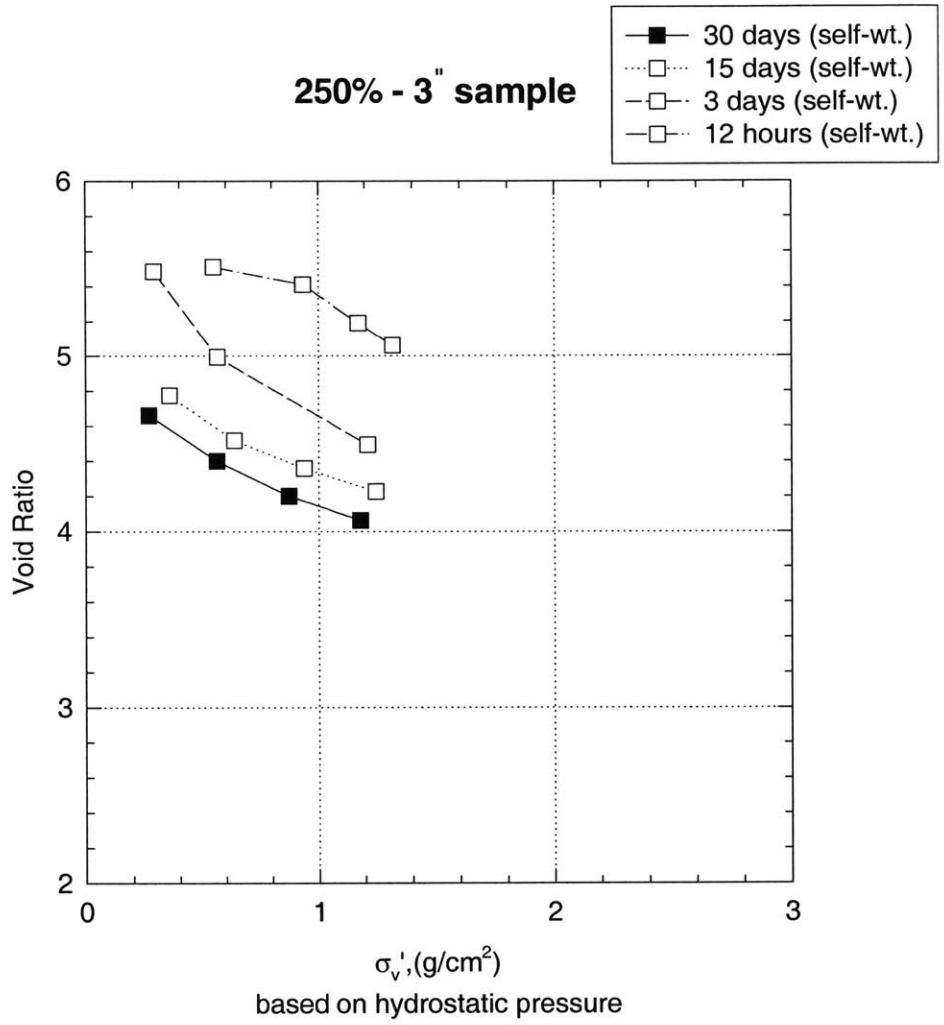

Figure 4-23: Void ratio - effective stress profiles for RCS 250% IWC 3-inch specimen

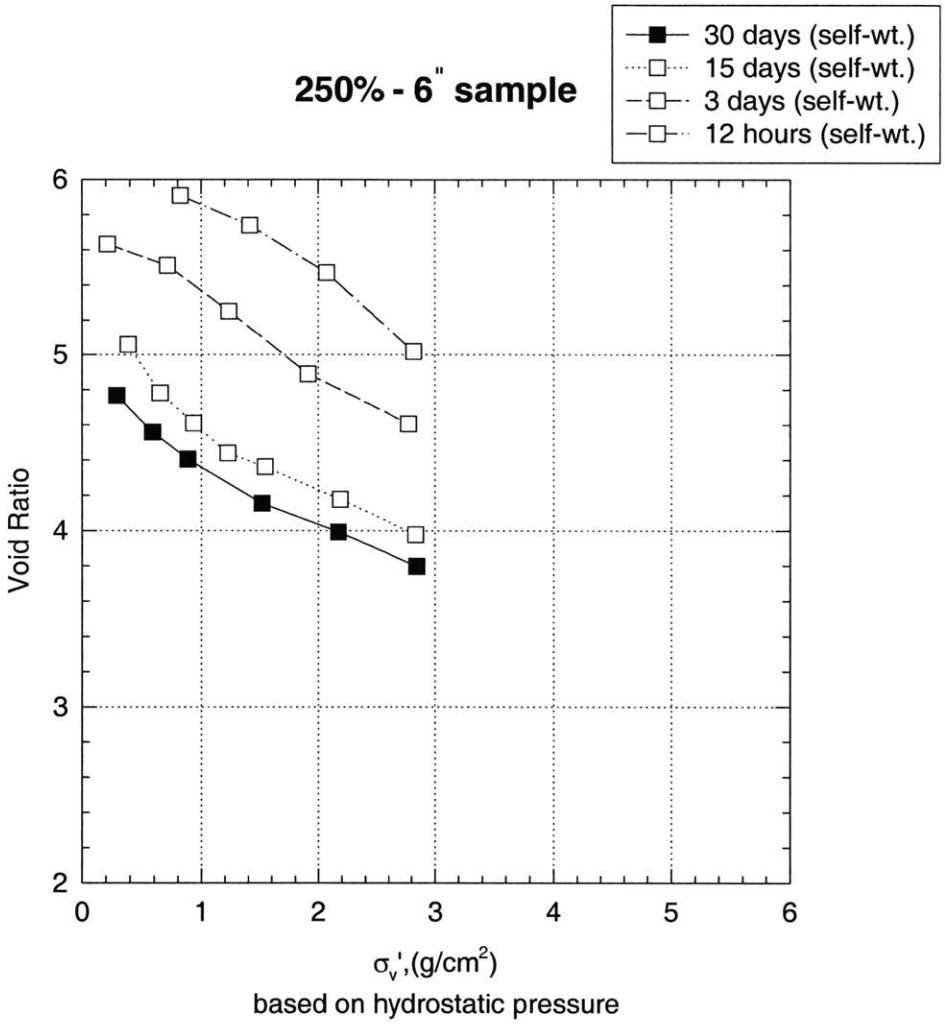

Figure 4-24: Void ratio - effective stress profiles for RCS 250% IWC 6-inch specimen

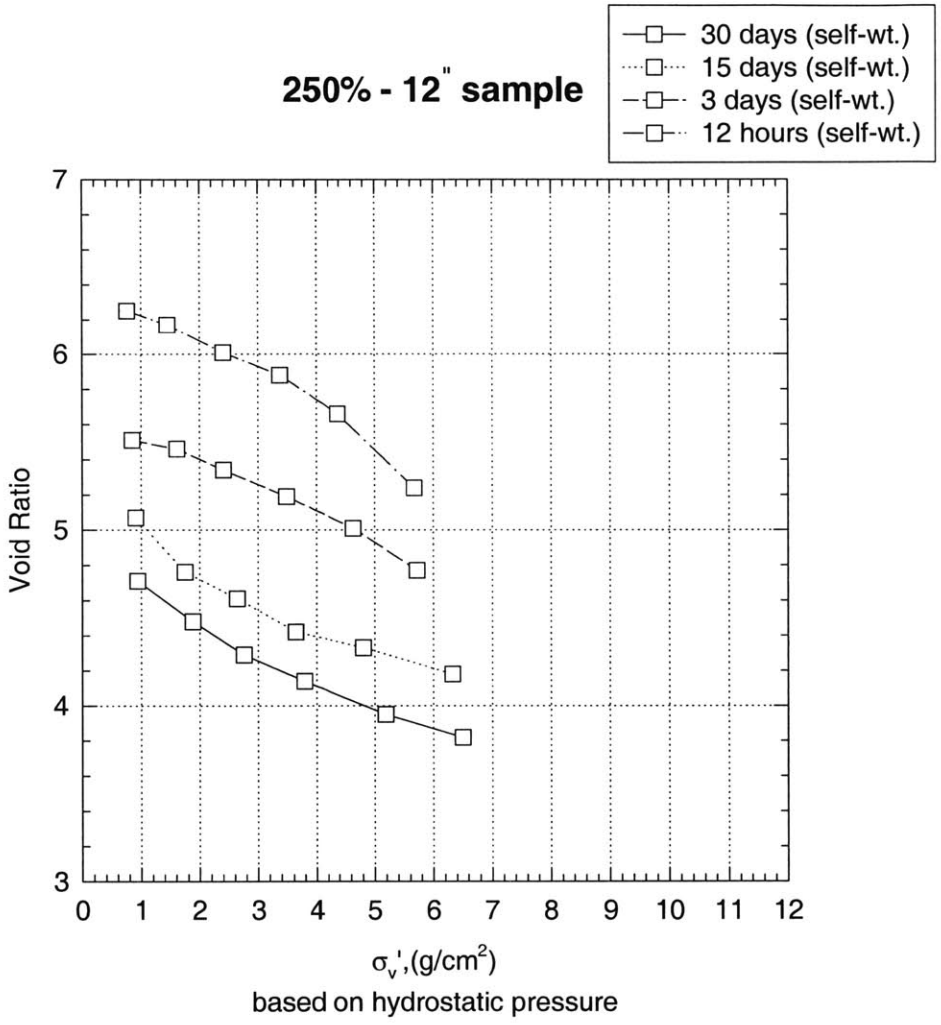

Figure 4-25: Void ratio - effective stress profiles for RCS 250% IWC 12-inch specimen

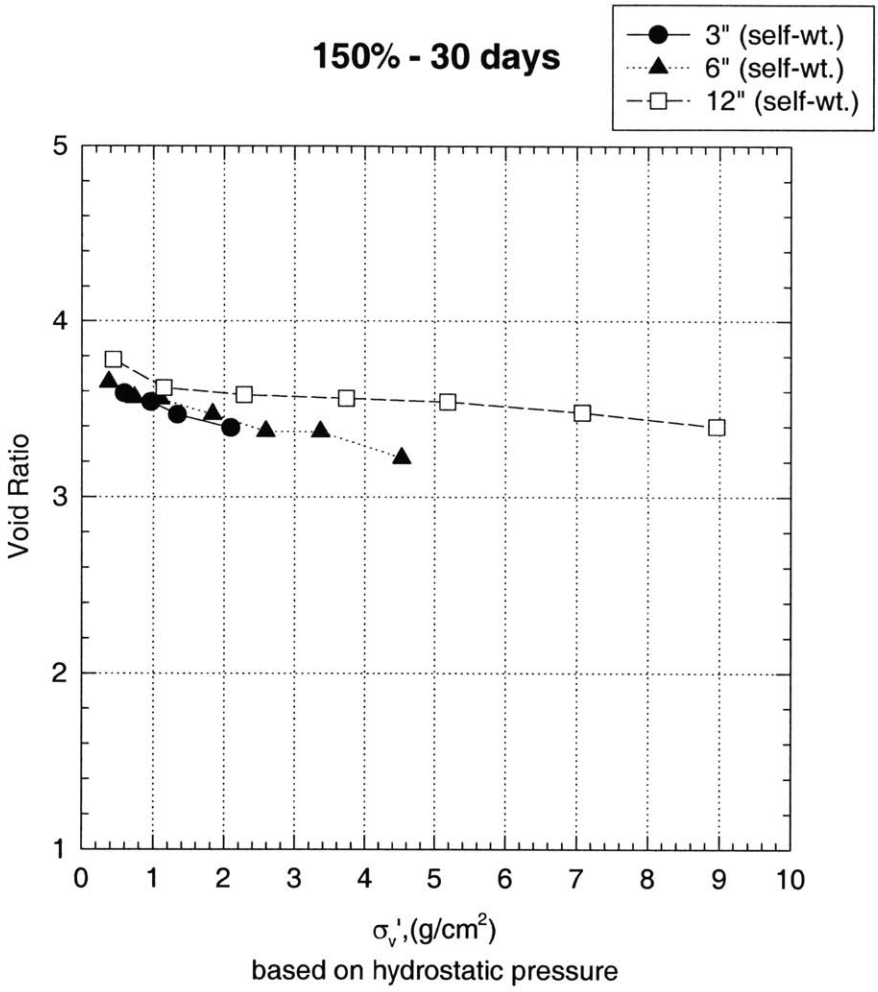

Figure 4-26: Void ratio - effective stress profiles for RCS 150% IWC specimens at 30 days

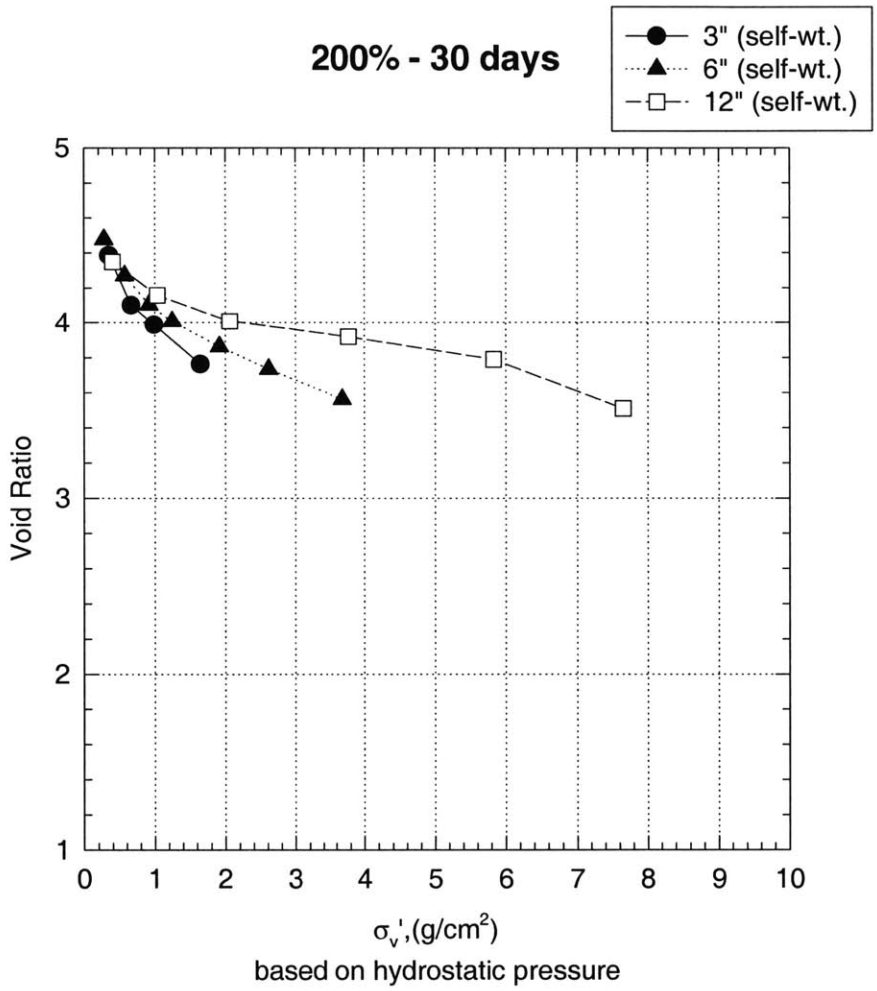

Figure 4-27: Void ratio - effective stress profiles for RCS 200% IWC specimens at 30 days

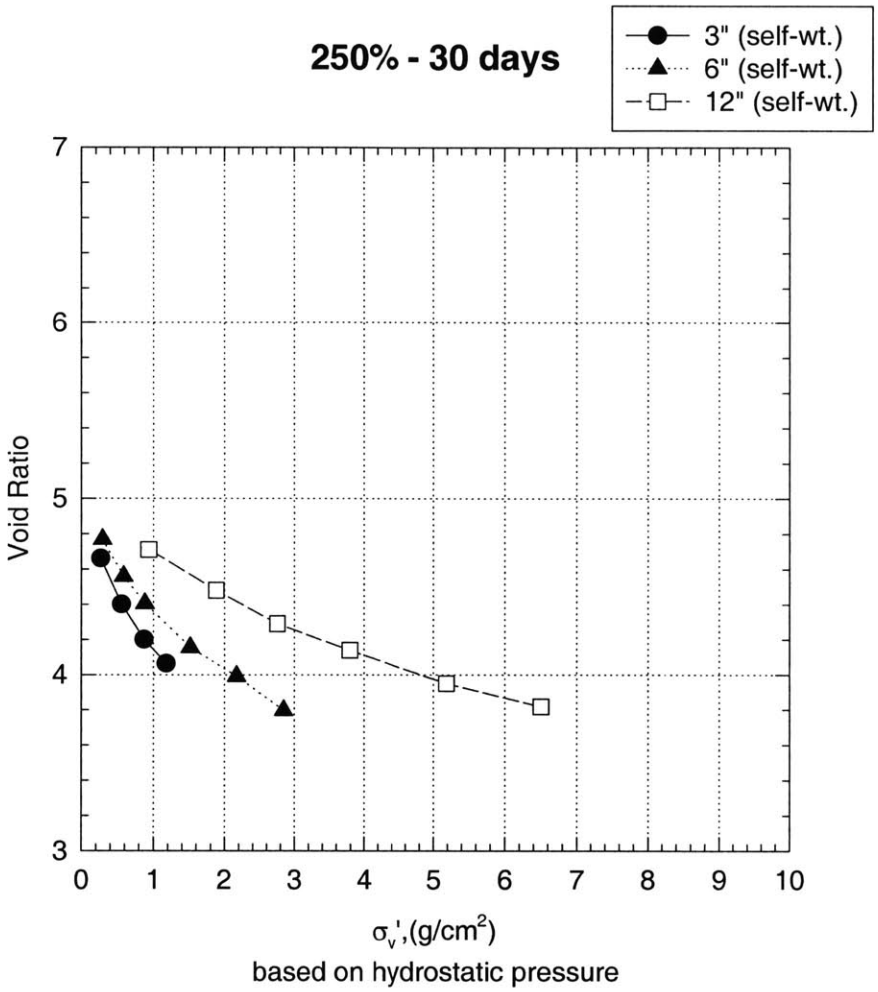

Figure 4-28: Void ratio - effective stress profiles for RCS 250% IWC specimens at 30 days

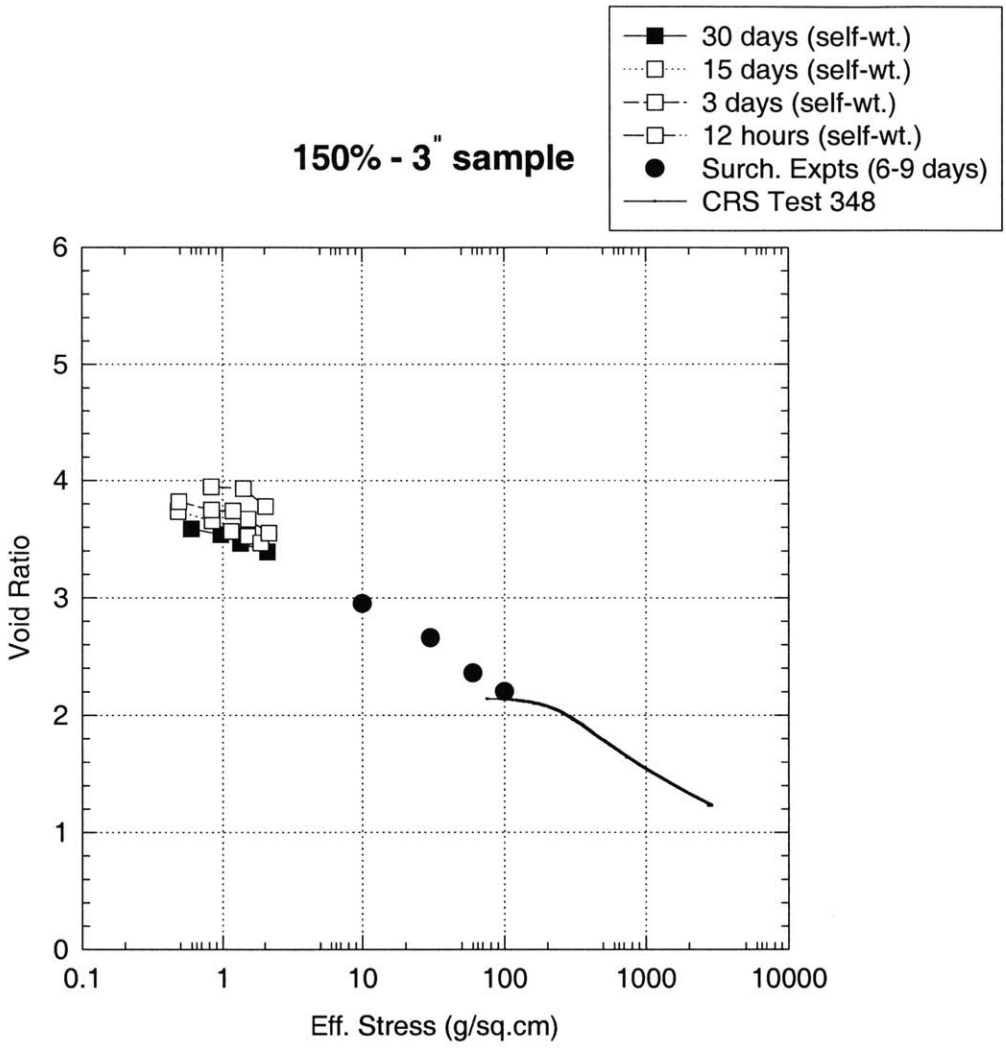

Figure 4-29: Void ratio v/s log effective stress for RCS 150% IWC specimens: 3-inch self-weight consolidation, surcharge, and CRS data

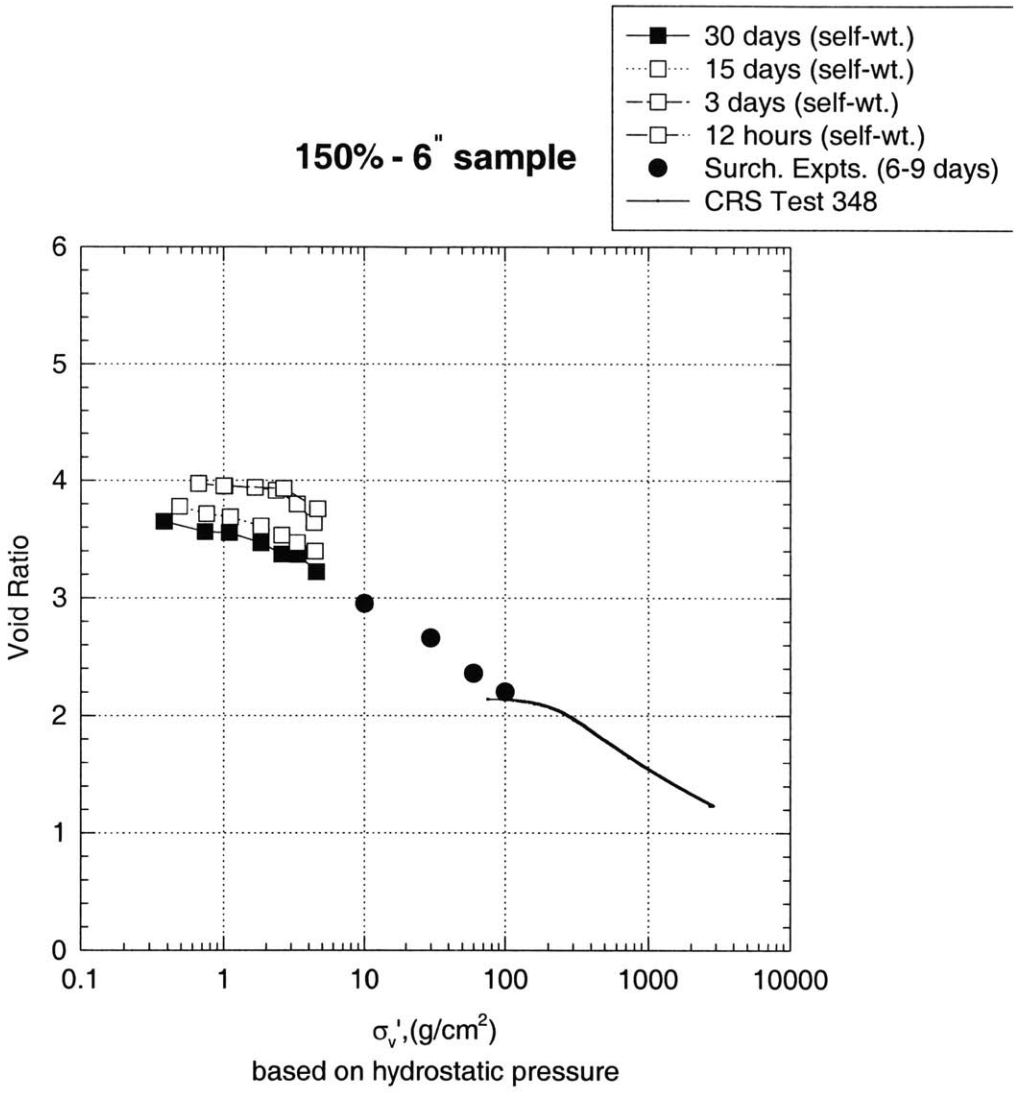

Figure 4-30: Void ratio v/s log effective stress for RCS 150% IWC specimens: 6-inch self-weight consolidation, surcharge, and CRS data

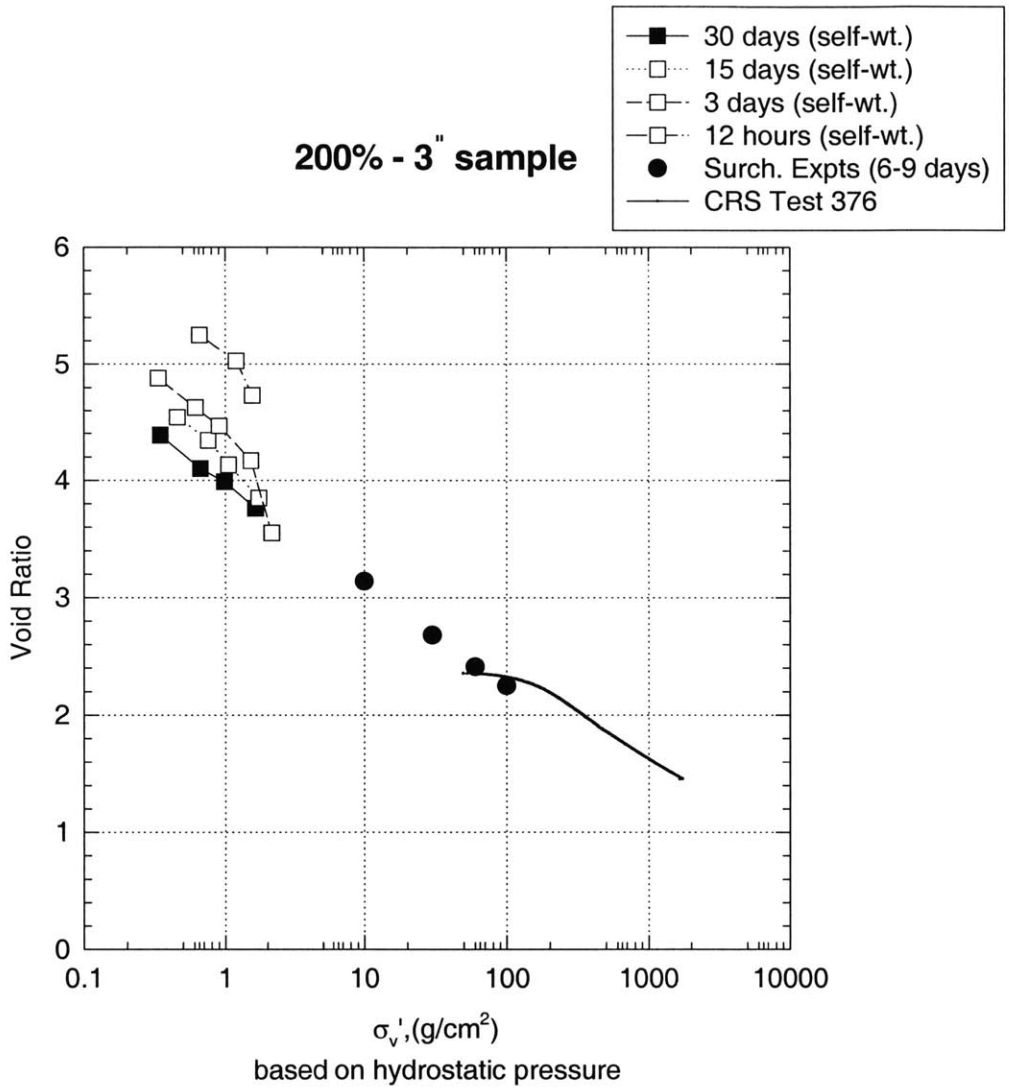

Figure 4-31: Void ratio v/s log effective stress for RCS 200% IWC specimens: 3-inch self-weight consolidation, surcharge, and CRS data

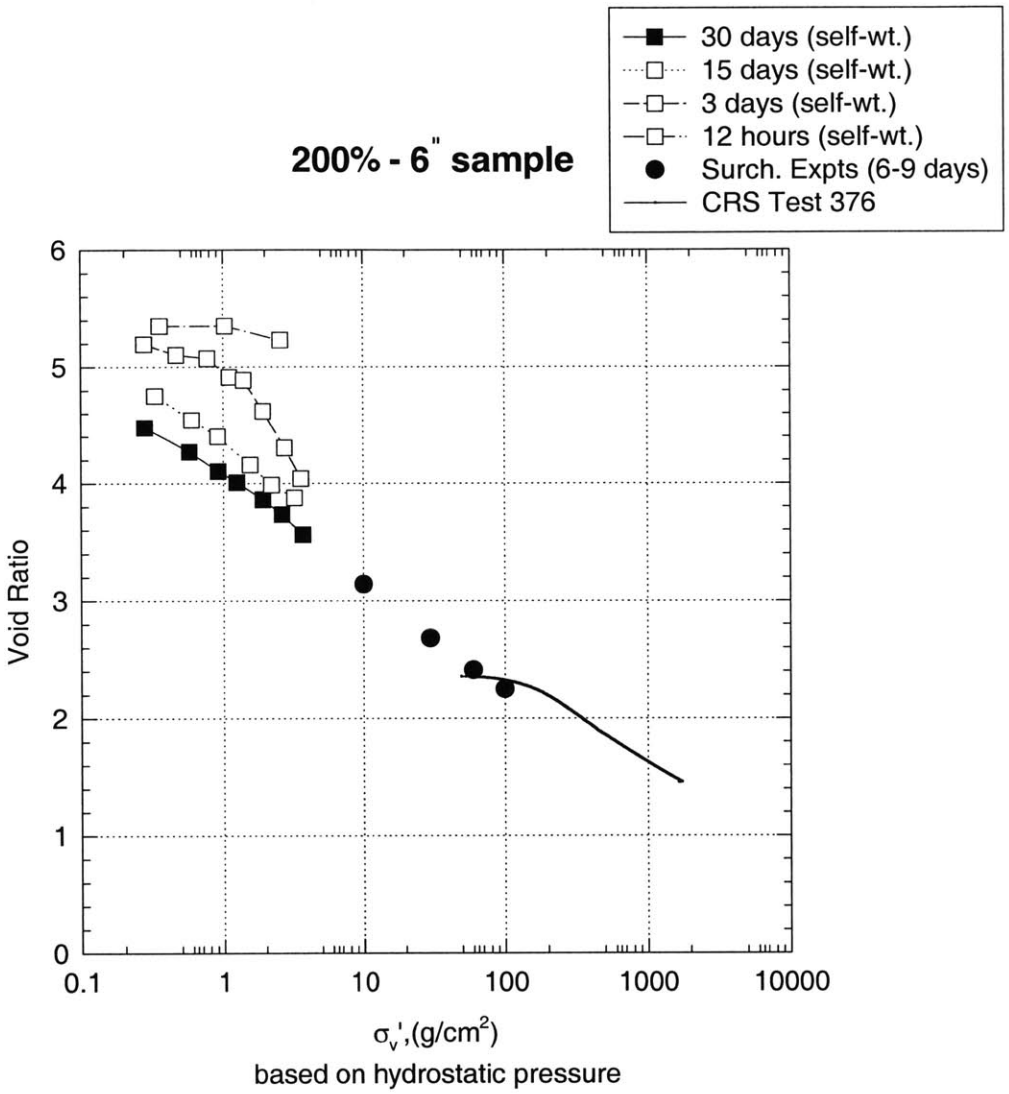

Figure 4-32: Void ratio v/s log effective stress for RCS 200% IWC specimens: 6-inch self-weight consolidation, surcharge, and CRS data

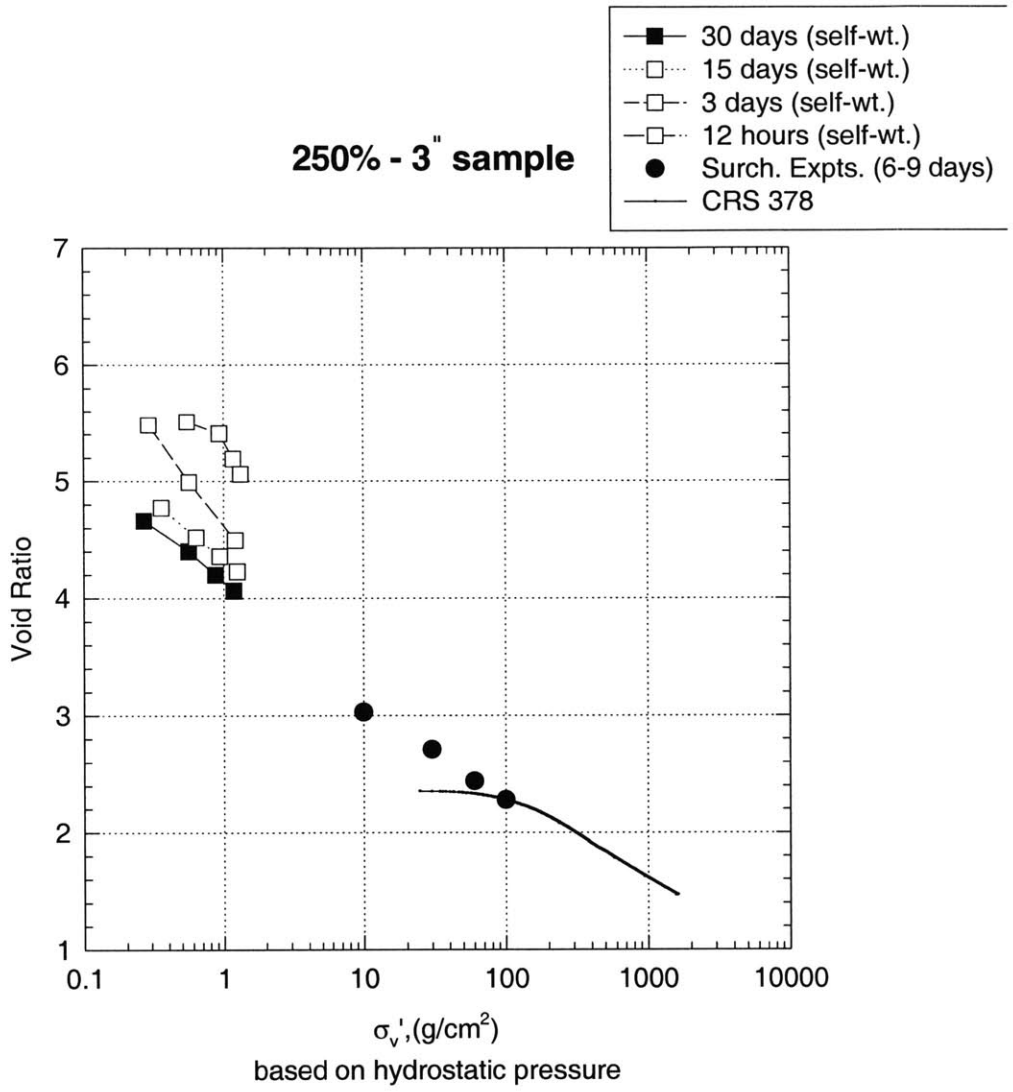

Figure 4-33: Void ratio v/s log effective stress for RCS 250% IWC specimens: 3-inch self-weight consolidation, surcharge, and CRS data

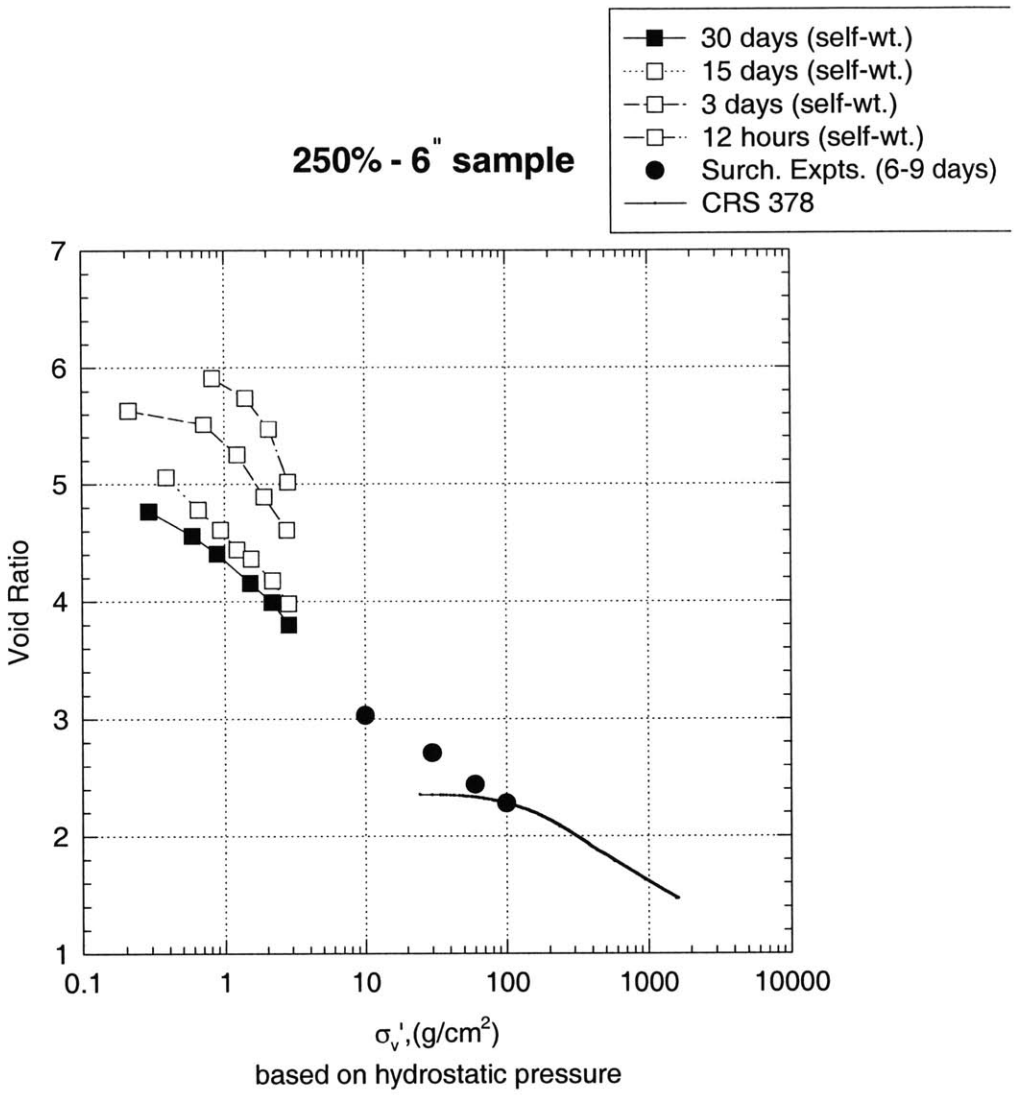

Figure 4-34: Void ratio v/s log effective stress for RCS 250% IWC specimens: 6-inch self-weight consolidation, surcharge, and CRS data

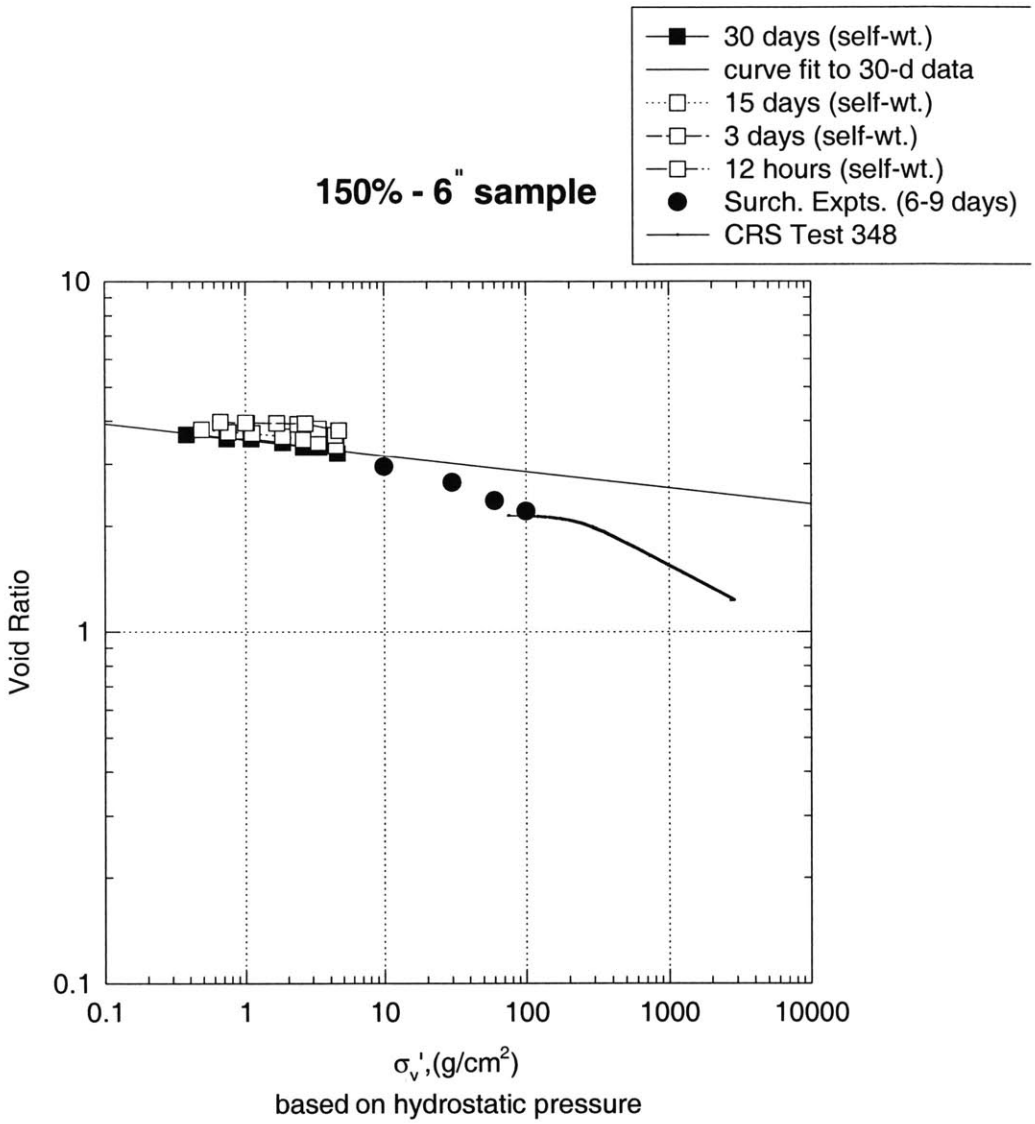

Figure 4-35: Best log-log linear fit for void ratio - effective stress relationship: RCS 150% IWC 3-inch self-weight consolidation specimen

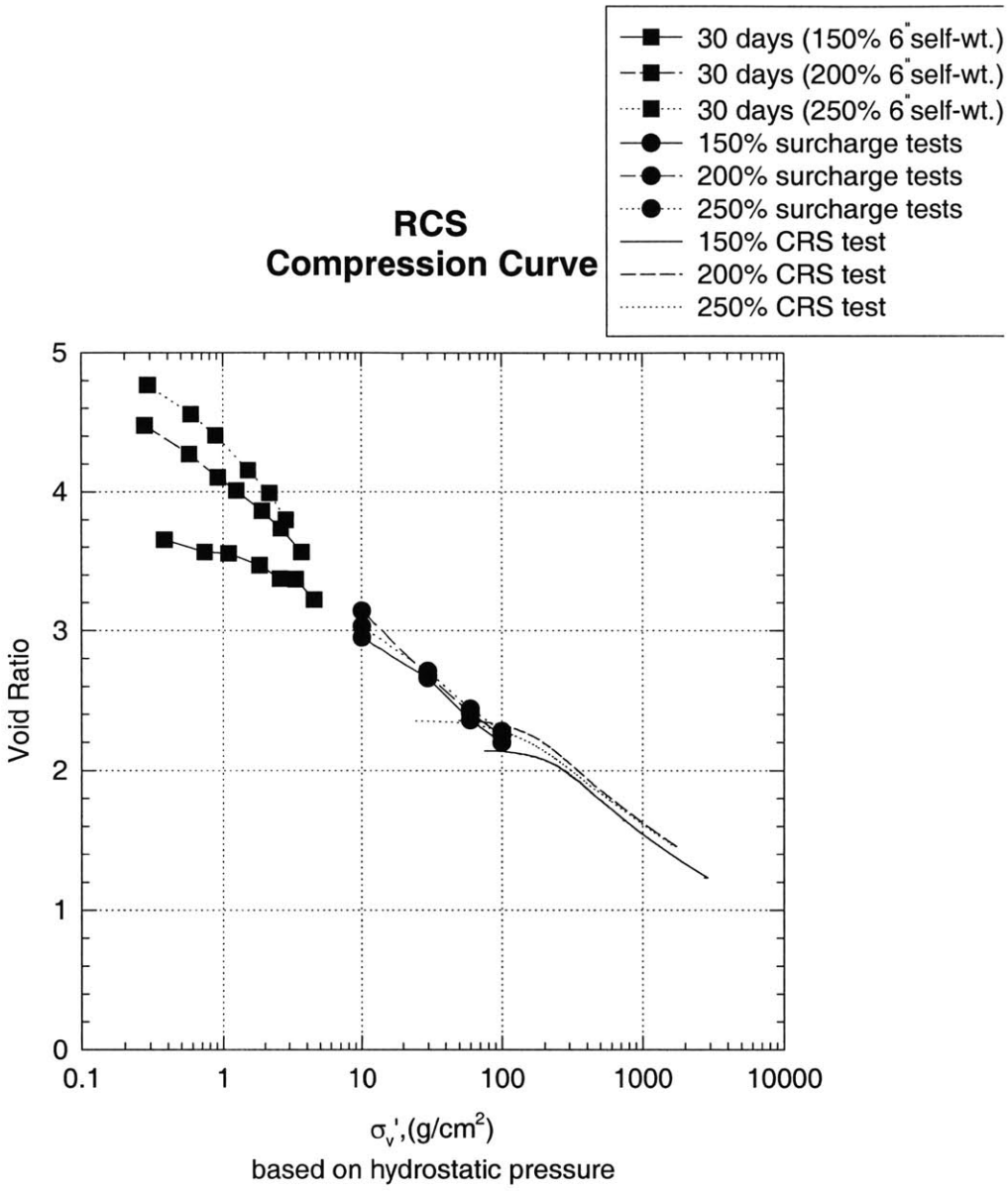

Figure 4-36: RCS compression curve: Void ratio - effective stress for RCS specimens with different initial water contents: 6-inch self-weight consolidation, surcharge, and CRS data

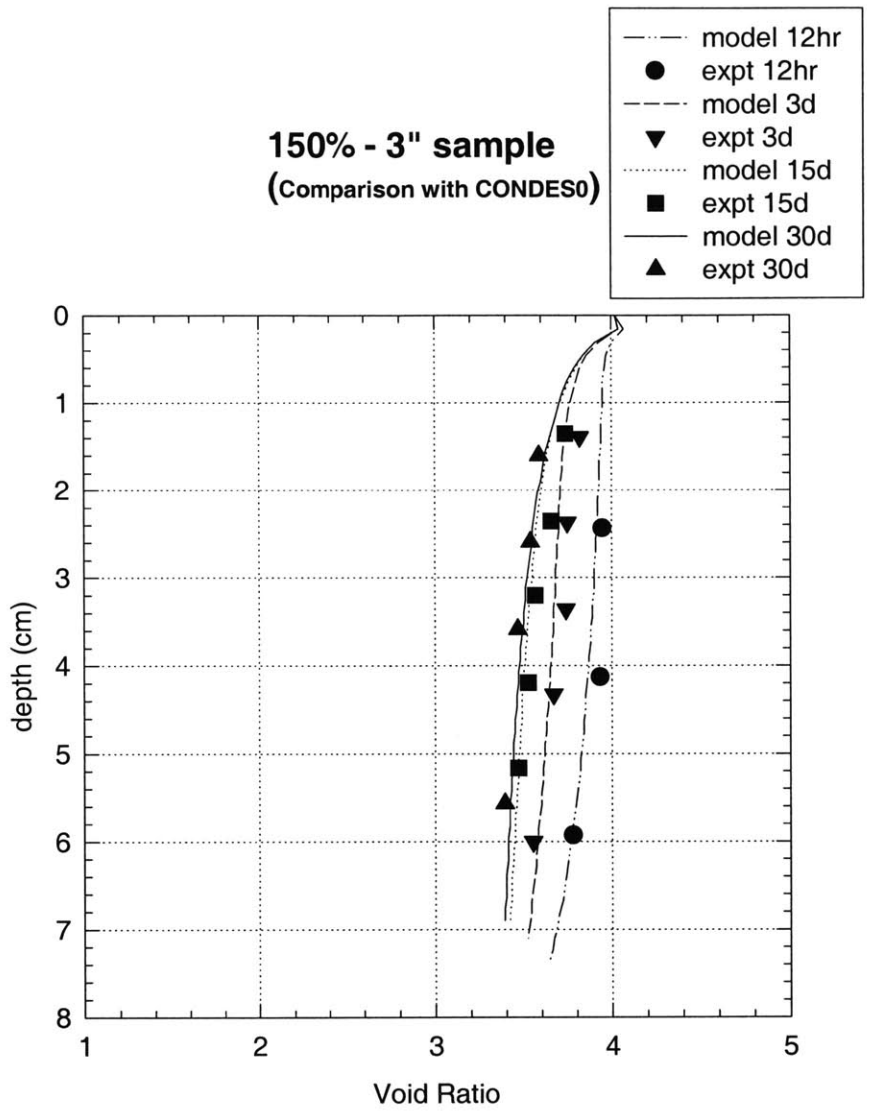

Figure 4-37: Comparison of void ratio - depth profiles for RCS 150% IWC 3-inch specimen

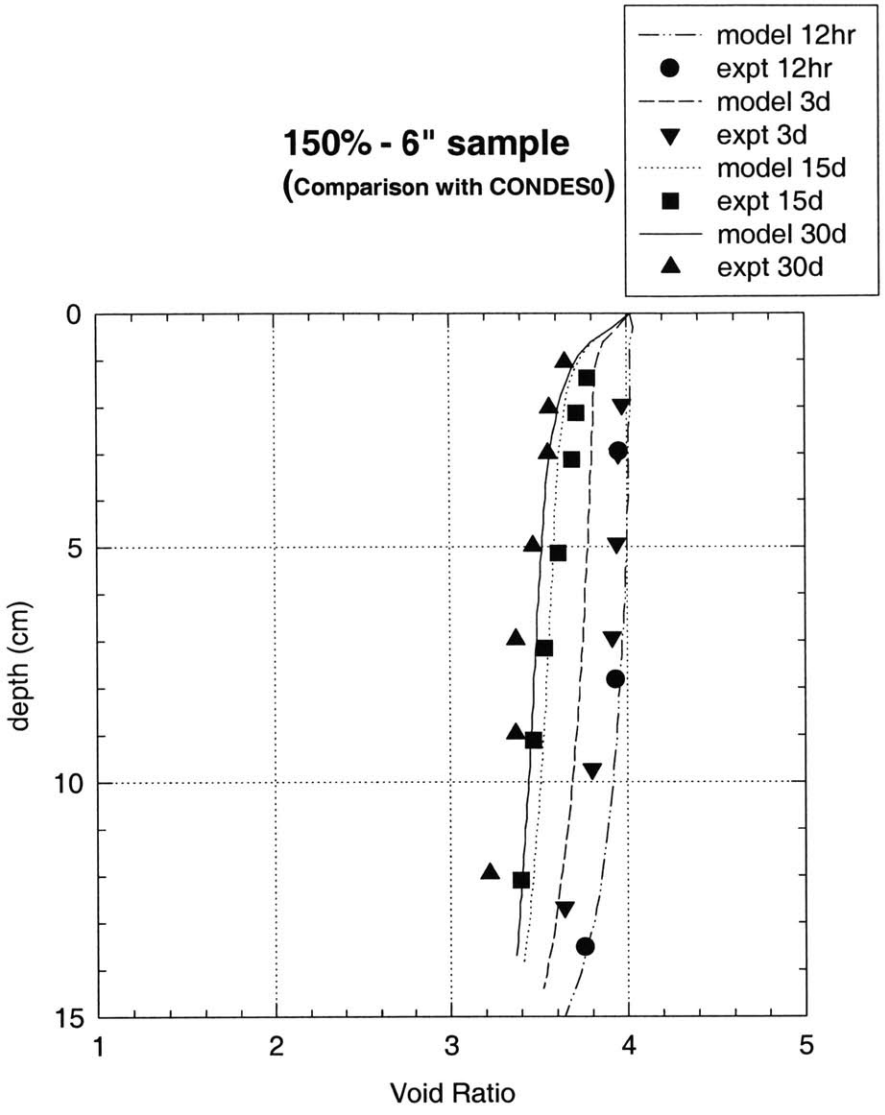

Figure 4-38: Comparison of void ratio - depth profiles for RCS 150% IWC 6-inch specimen

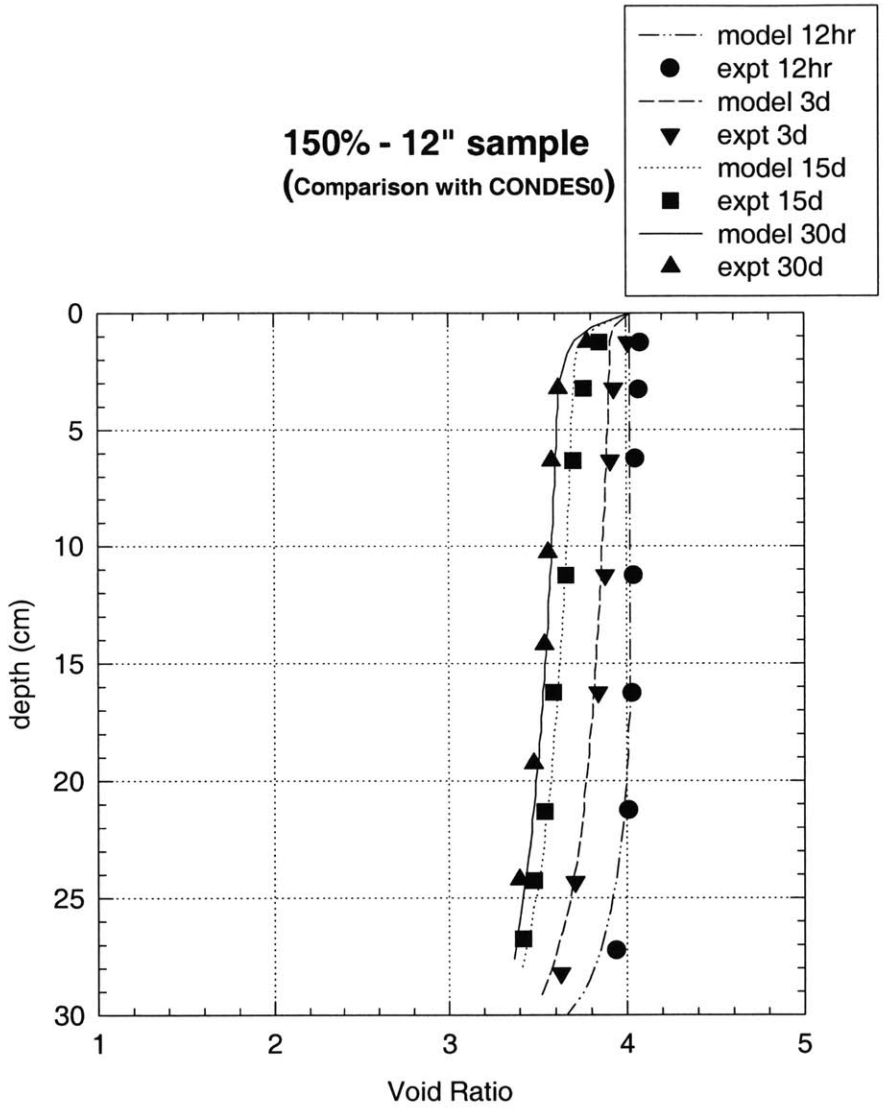

Figure 4-39: Comparison of void ratio - depth profiles for RCS 150% IWC 12-inch specimen

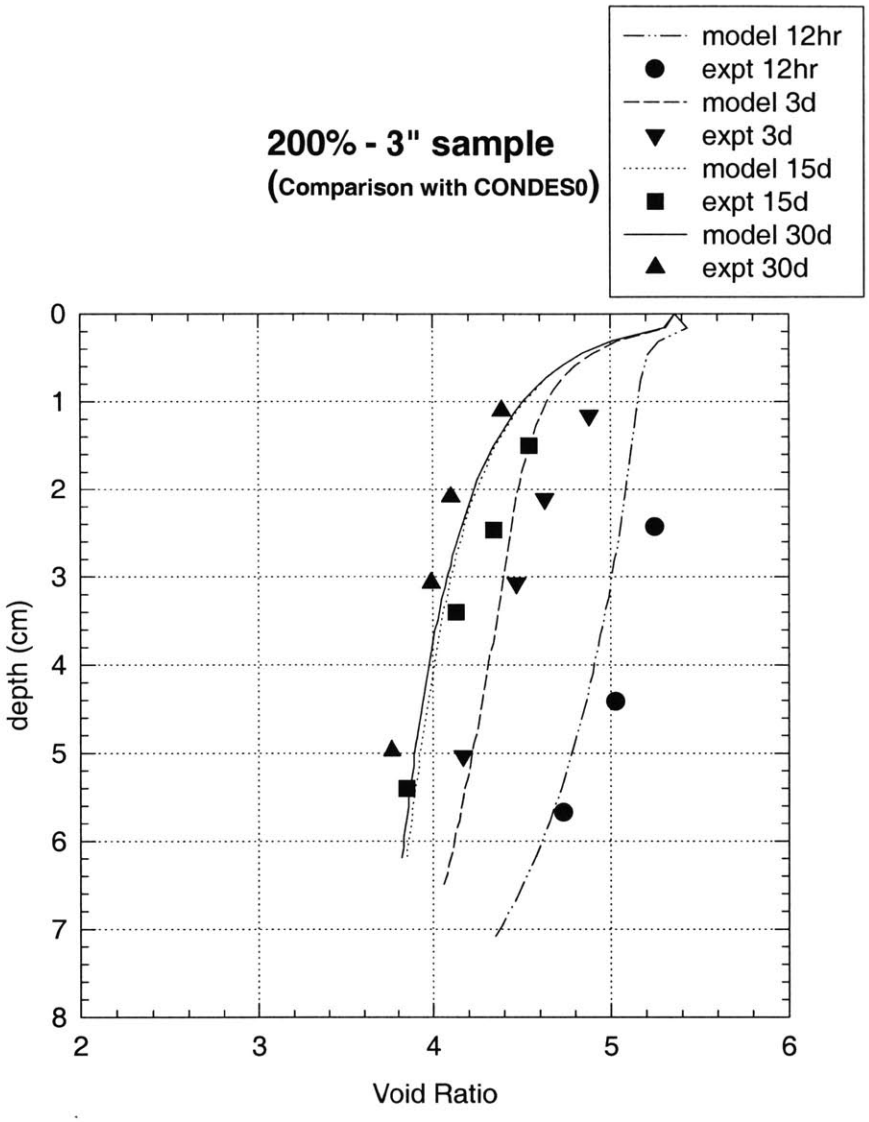

Figure 4-40: Comparison of void ratio - depth profiles for RCS 200% IWC 3-inch specimen

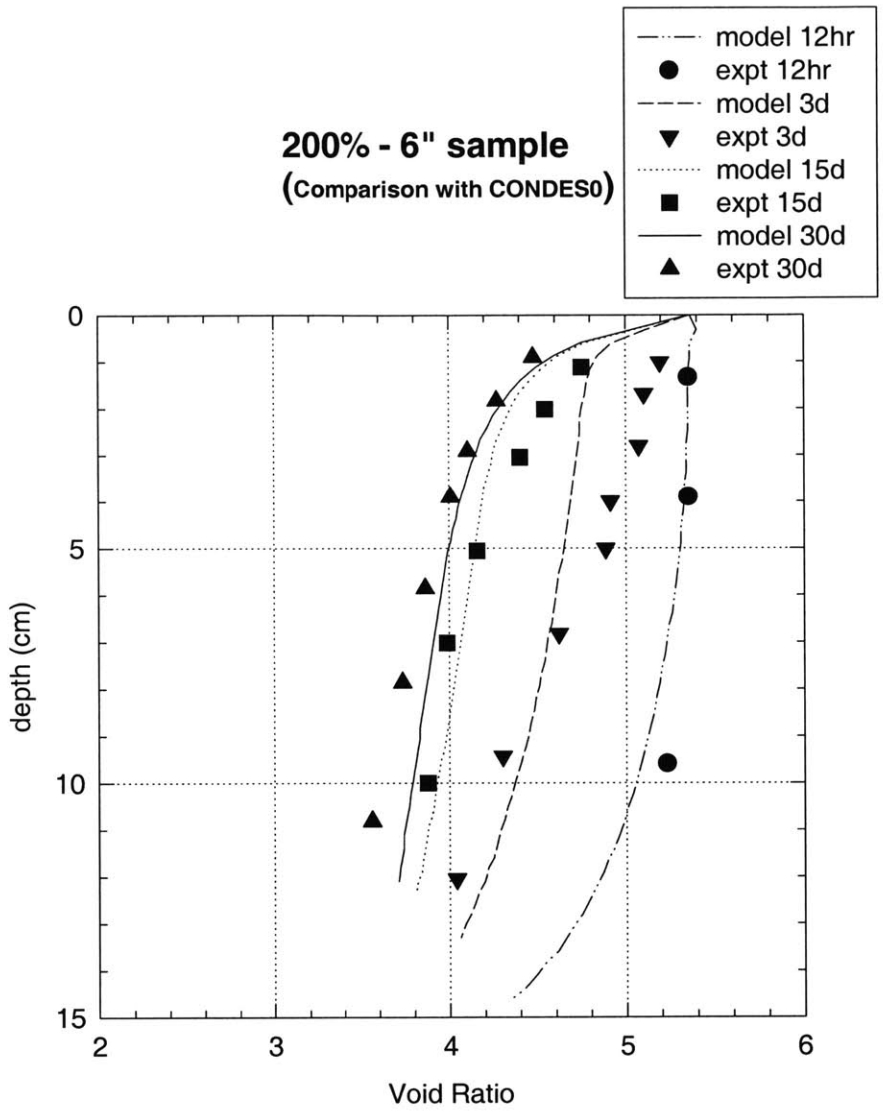

Figure 4-41: Comparison of void ratio - depth profiles for RCS 200% IWC 6-inch specimen

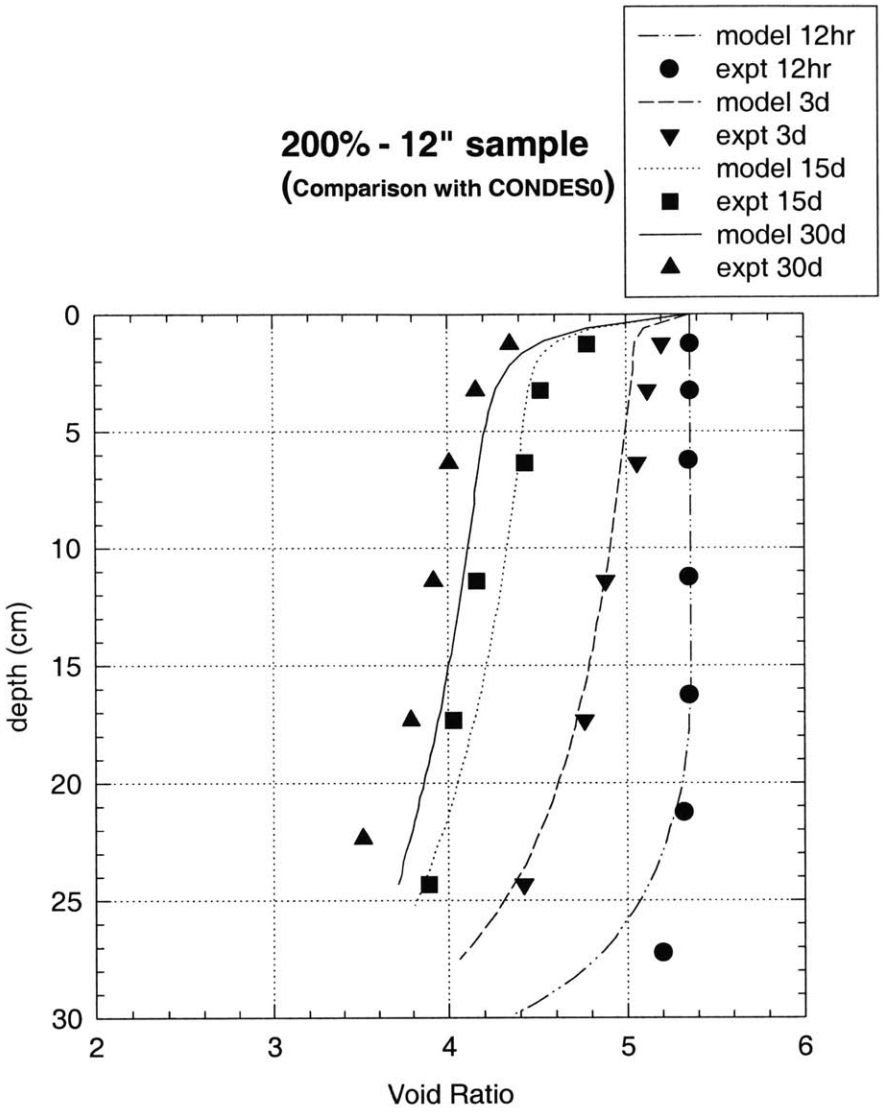

Figure 4-42: Comparison of void ratio - depth profiles for RCS 200% IWC 12-inch specimen

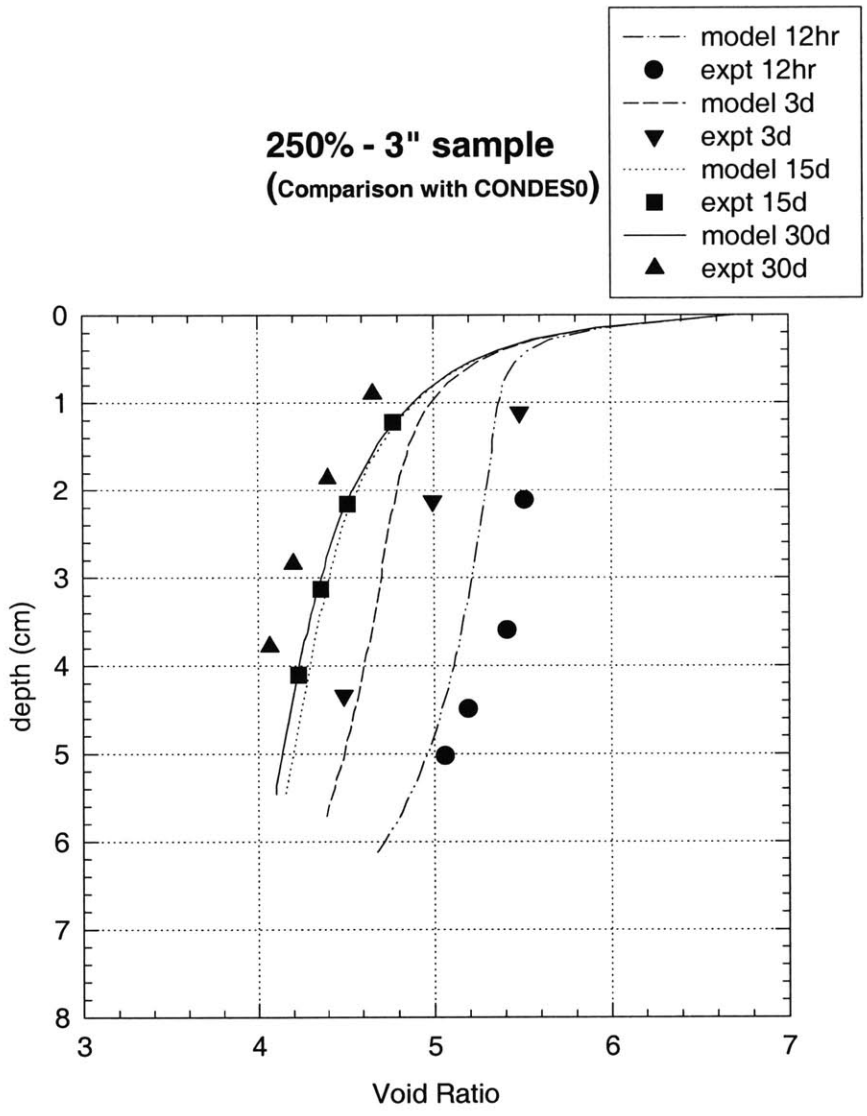

Figure 4-43: Comparison of void ratio - depth profiles for RCS 250% IWC 3-inch specimen

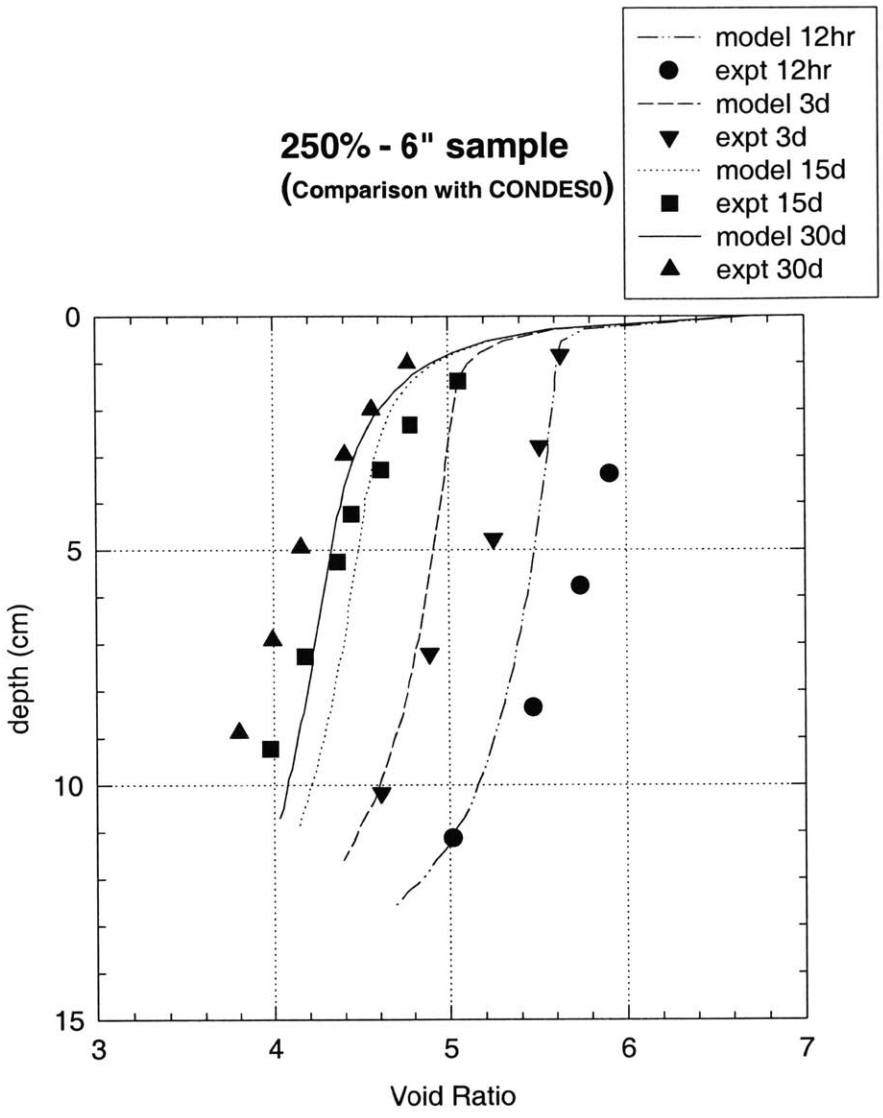

Figure 4-44: Comparison of void ratio - depth profiles for RCS 250% IWC 6-inch specimen

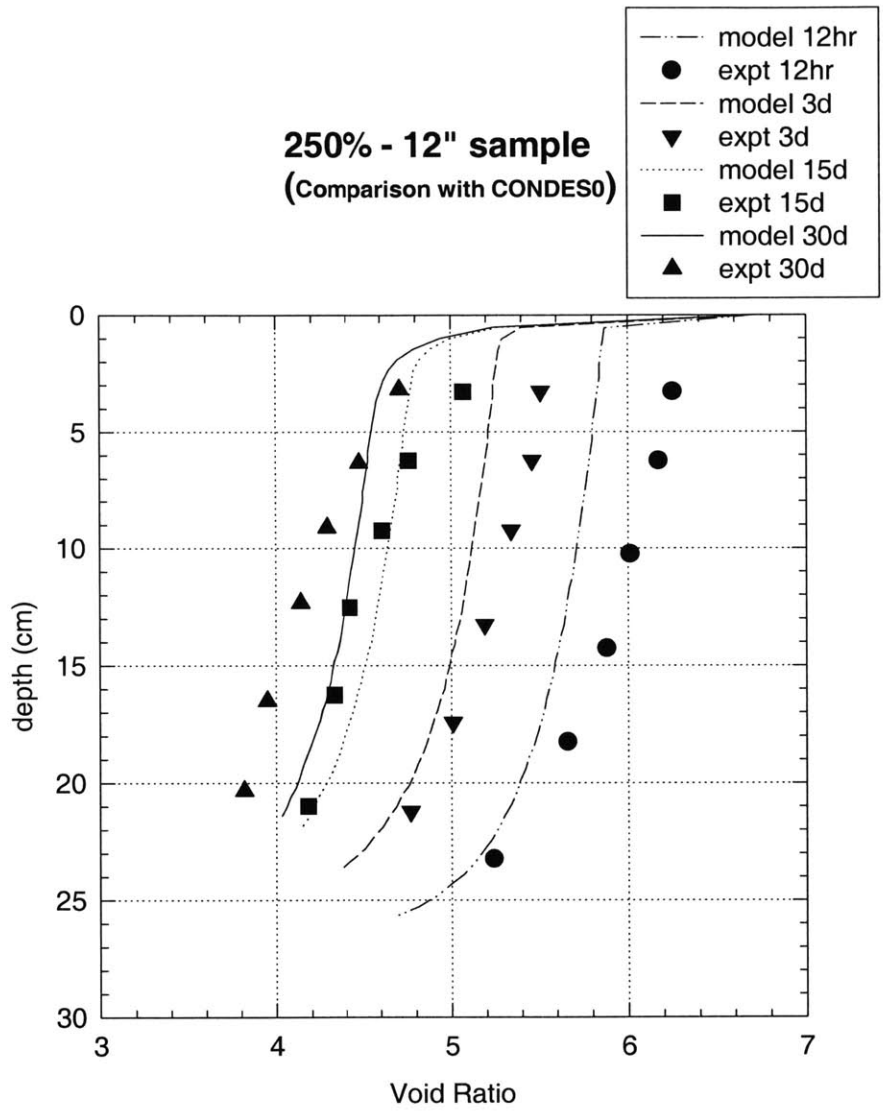

Figure 4-45: Comparison of void ratio - depth profiles for RCS 250% IWC 12-inch specimen

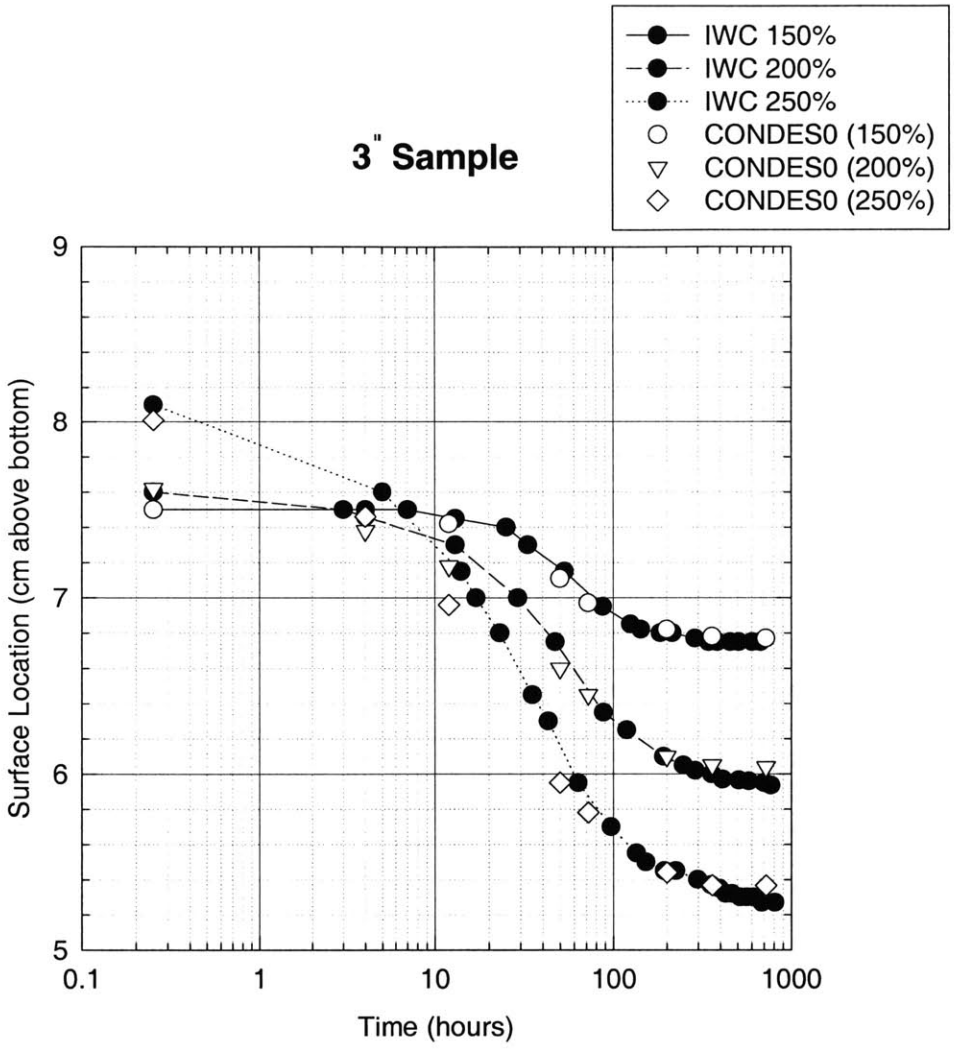

Figure 4-46: Comparison of RCS settlement in RCS curves: self-weight consolidation of 3-inch specimens with different initial water contents

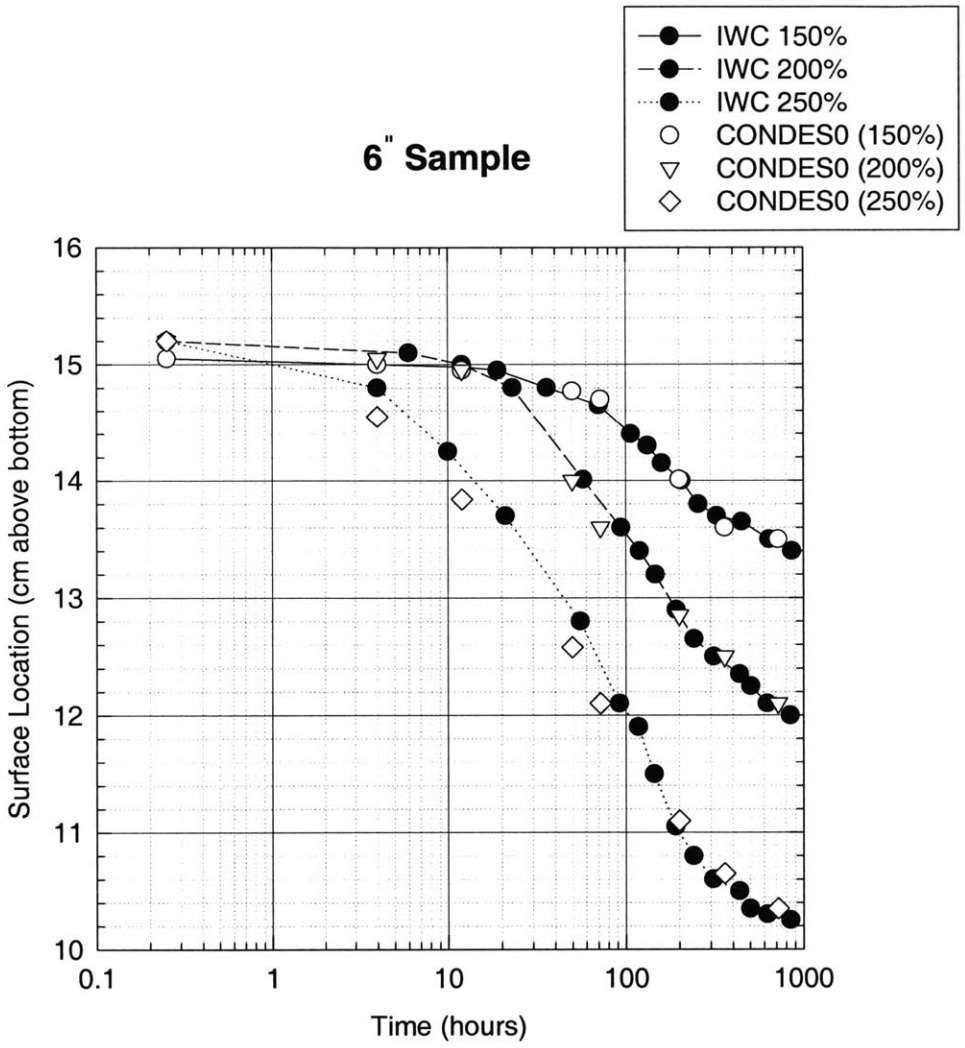

Figure 4-47: Comparison of RCS settlement in RCS curves: self-weight consolidation of 6-inch specimens with different initial water contents

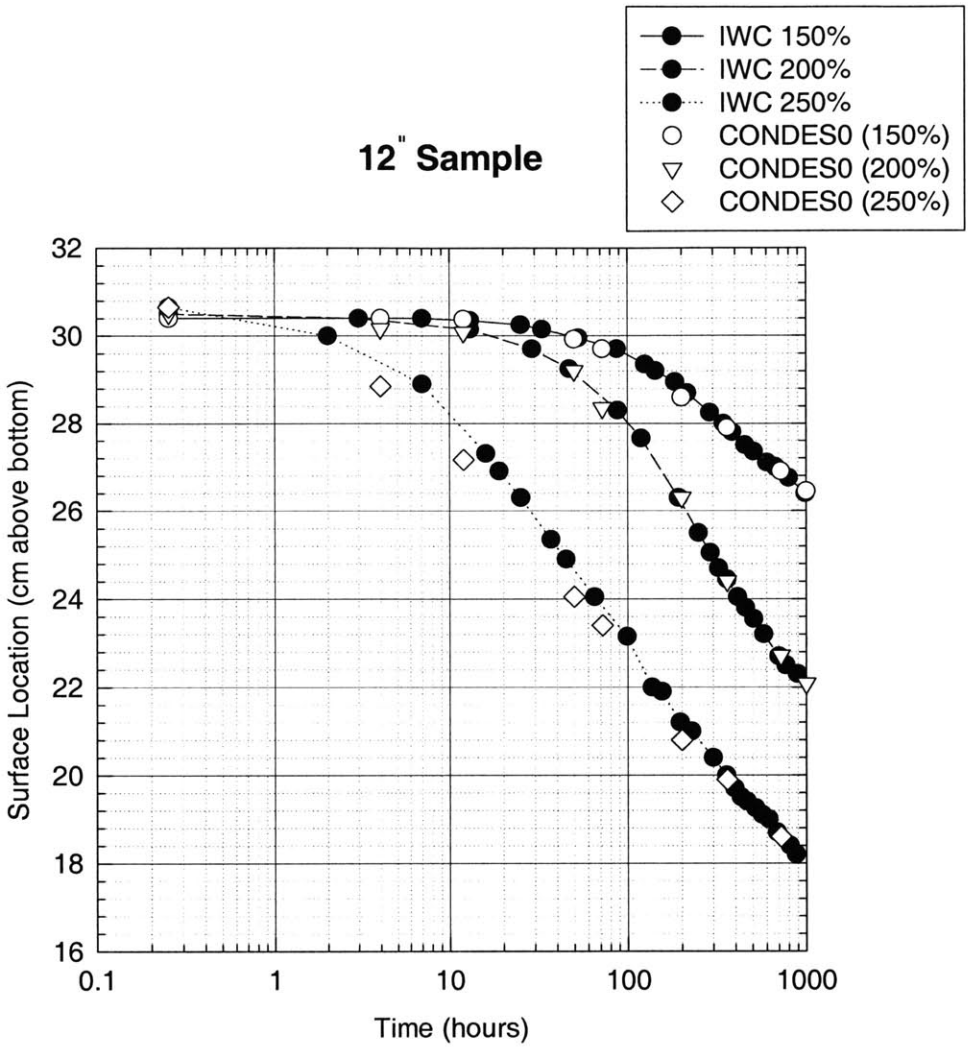

Figure 4-48: Comparison of RCS settlement in RCS curves: self-weight consolidation of 12-inch specimens with different initial water contents

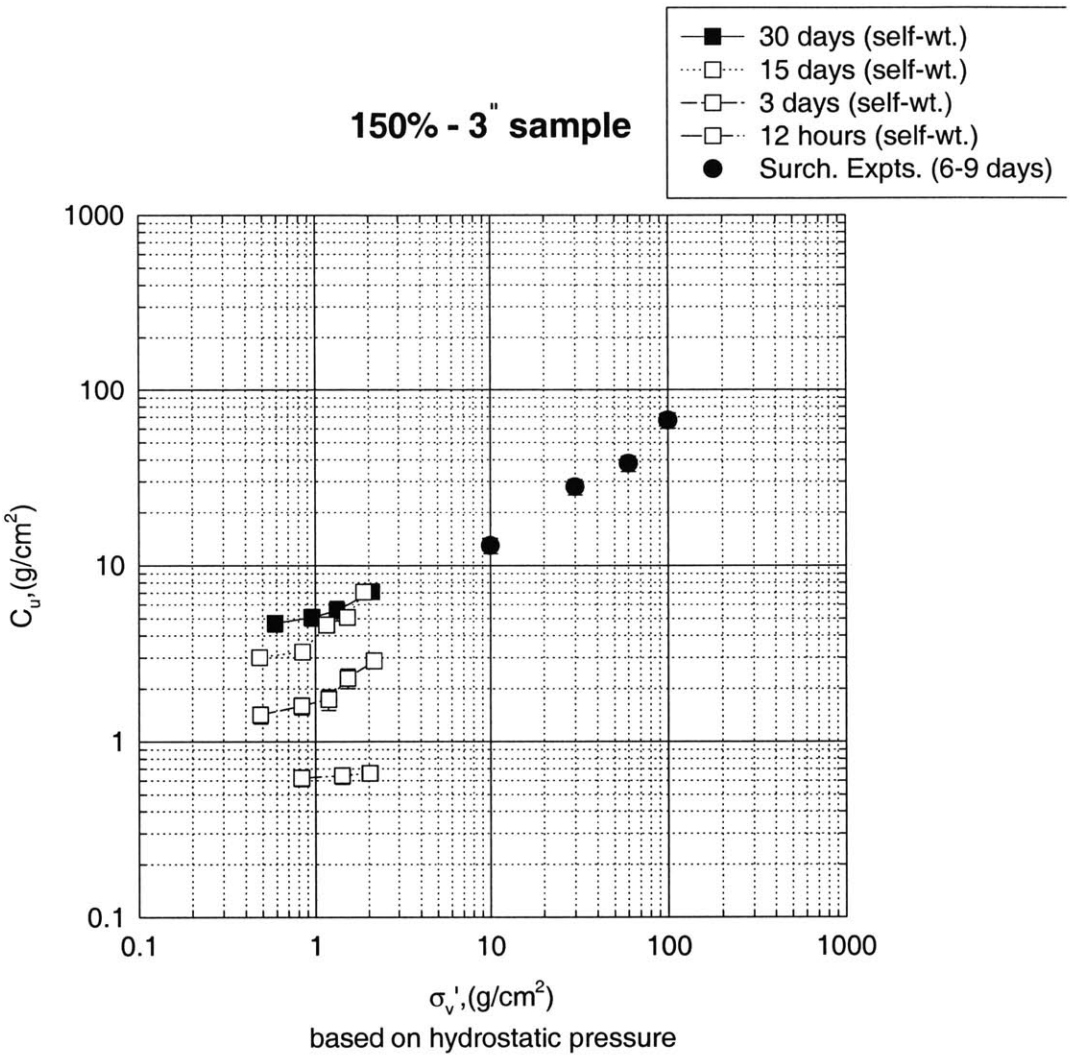

Figure 4-49: Undrained shear strength v/s. effective stress for RCS 150% IWC 3-inch specimen

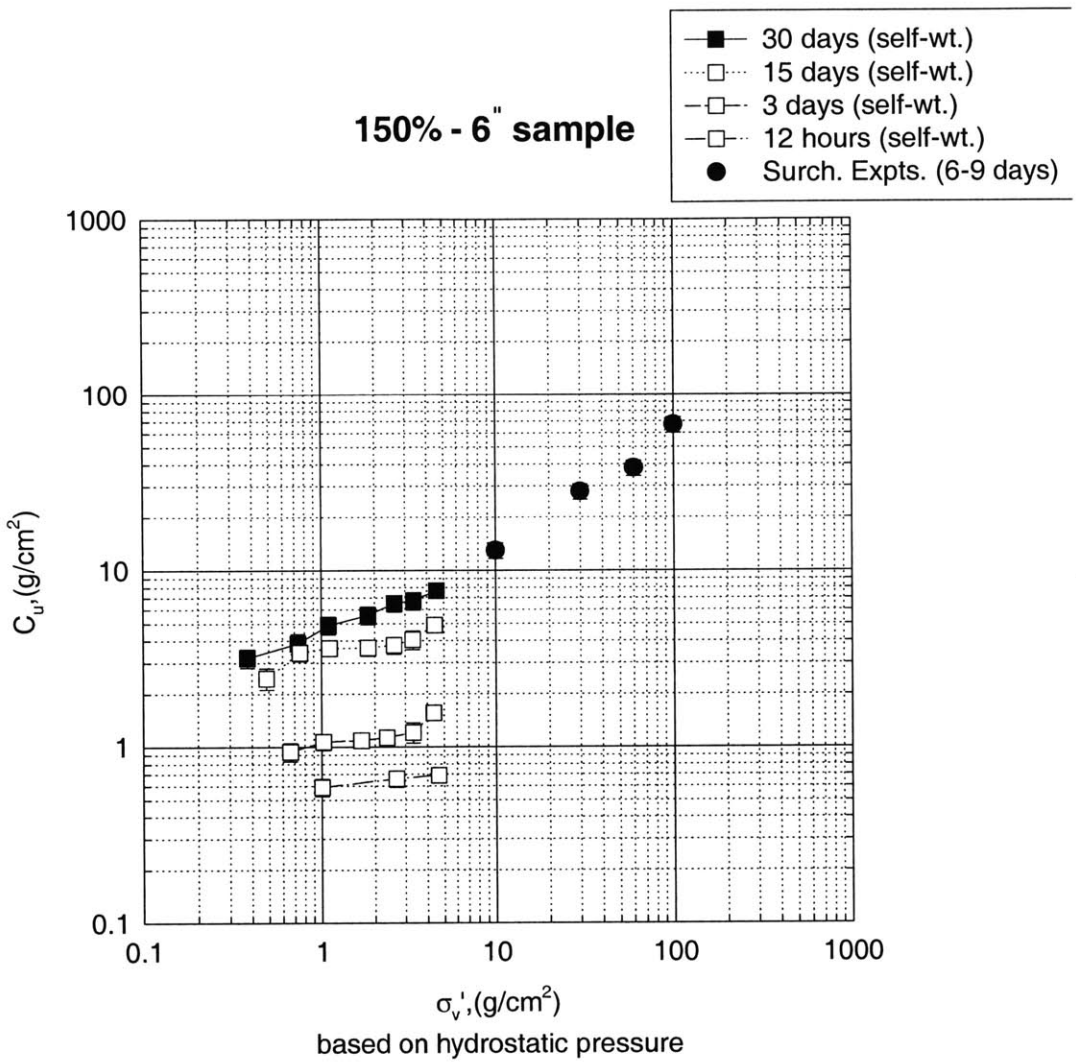

Figure 4-50: Undrained shear strength v/s. effective stress for RCS 150% IWC 6-inch specimen

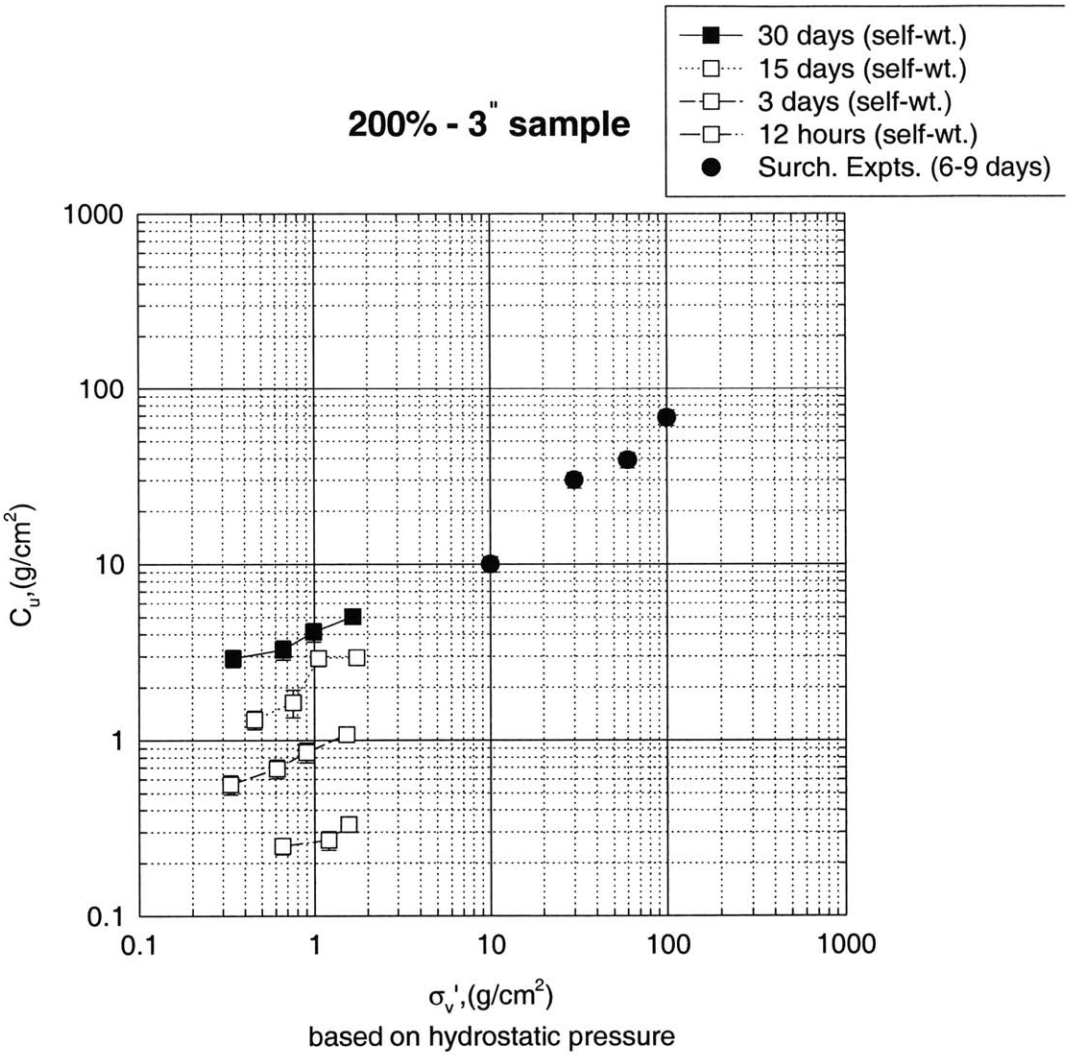

Figure 4-51: Undrained shear strength v/s. effective stress for RCS 200% IWC 3-inch specimen

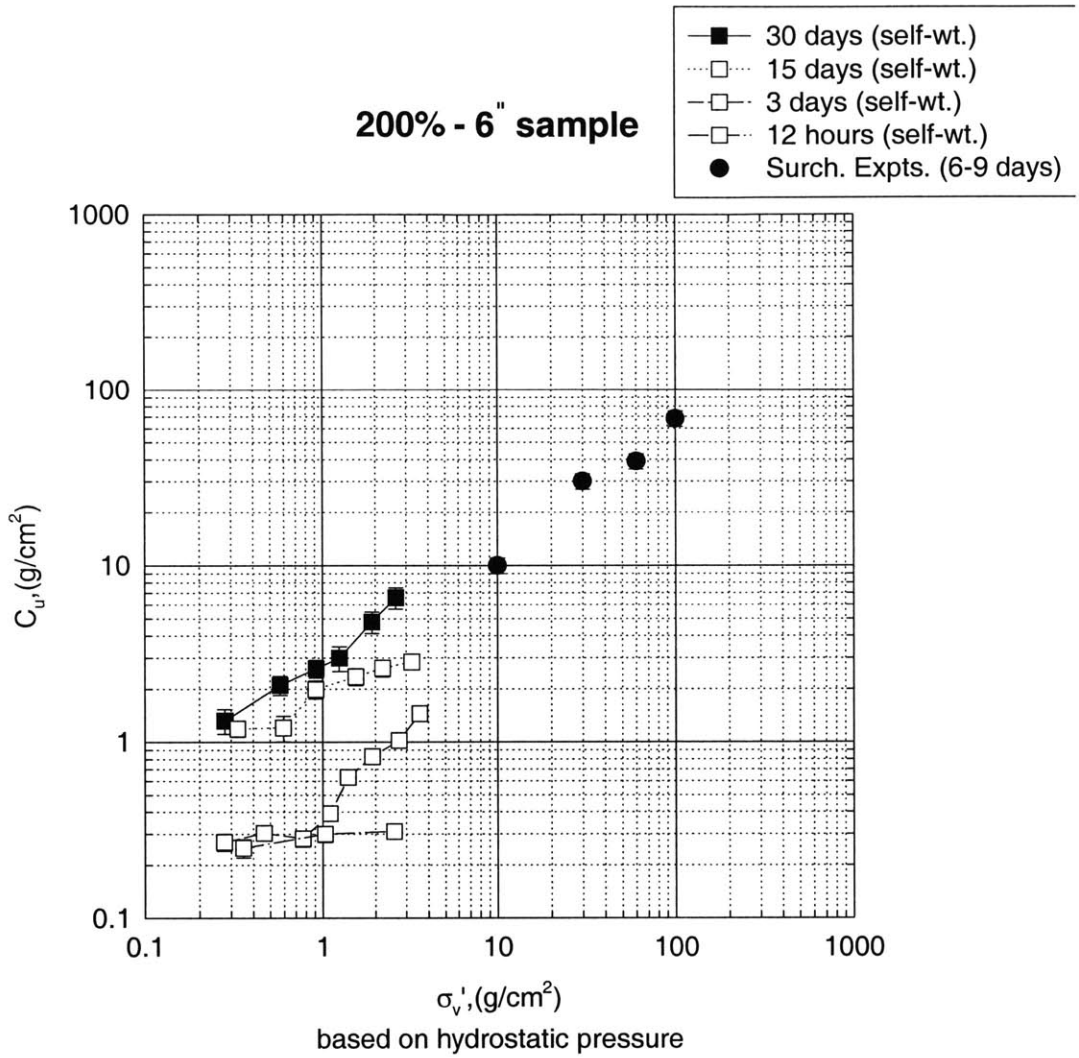

Figure 4-52: Undrained shear strength v/s. effective stress for RCS 200% IWC 6-inch specimen

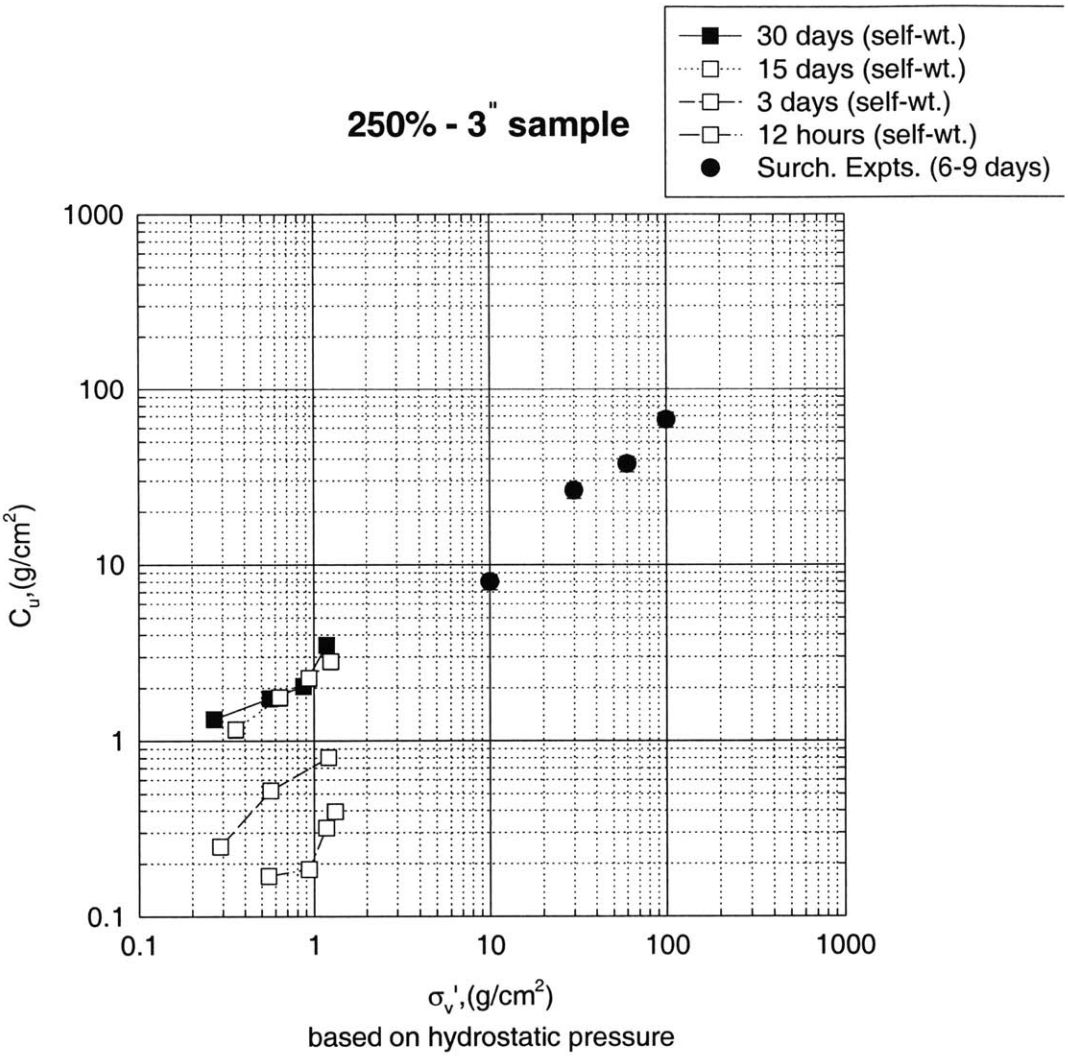

Figure 4-53: Undrained shear strength v/s. effective stress for RCS 250% IWC 3-inch specimen

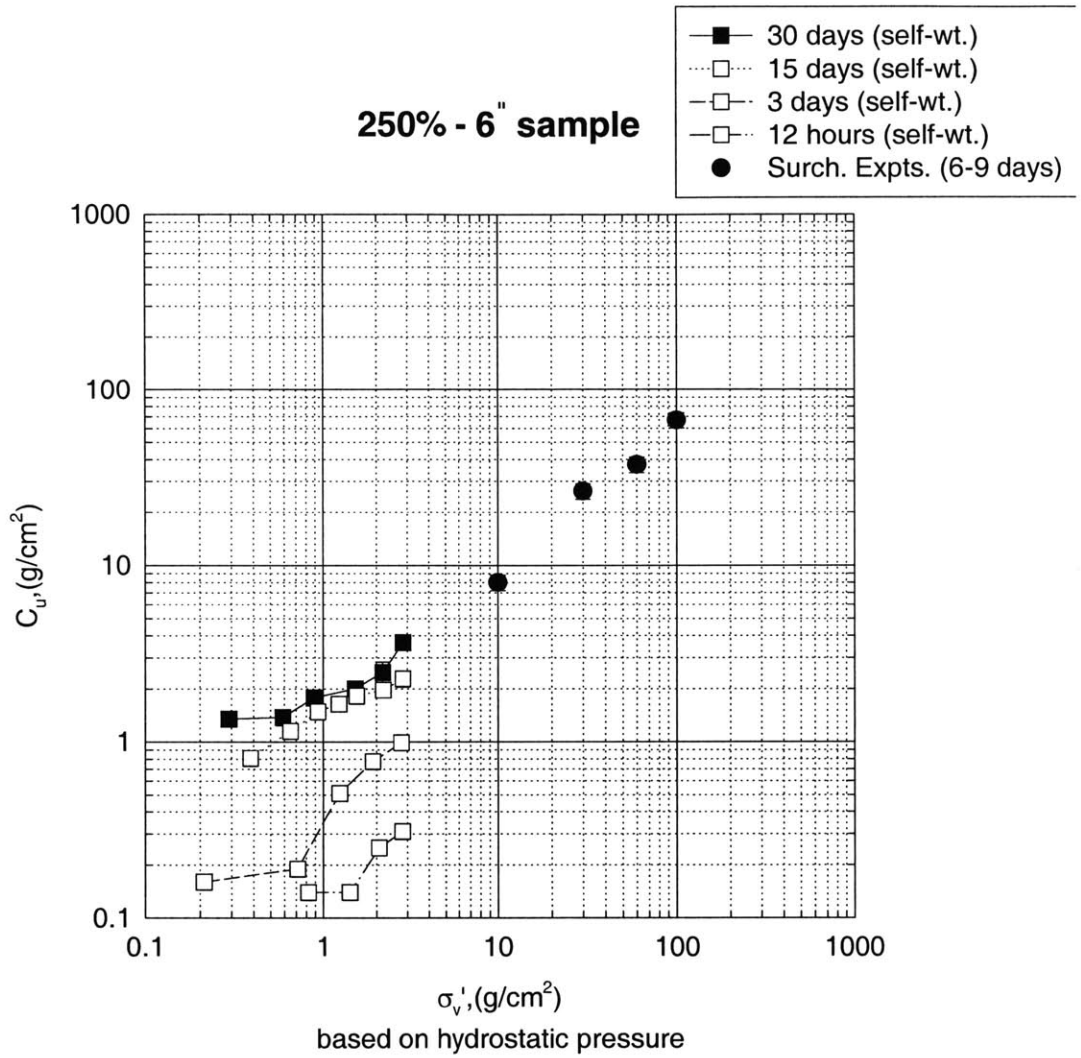

Figure 4-54: Undrained shear strength v/s. effective stress for RCS 250% IWC 6-inch specimen

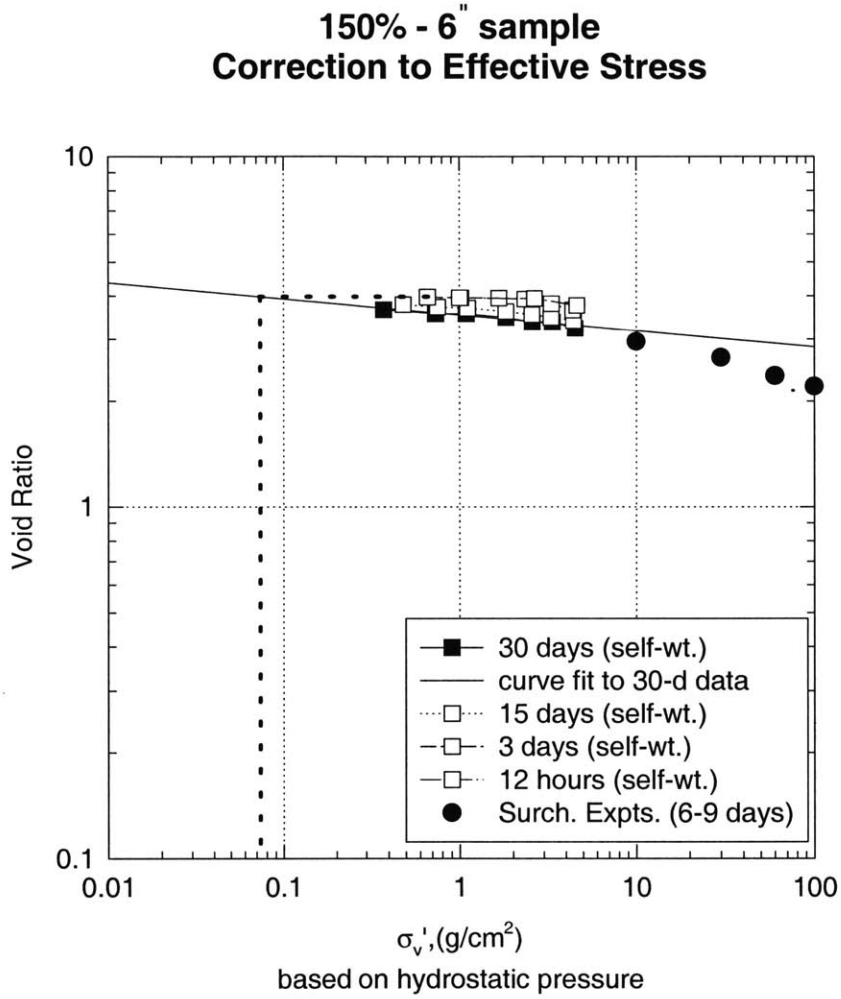

Figure 4-55: Correction of effective stress by using the void ratio - effective stress relationship for the consolidated specimen

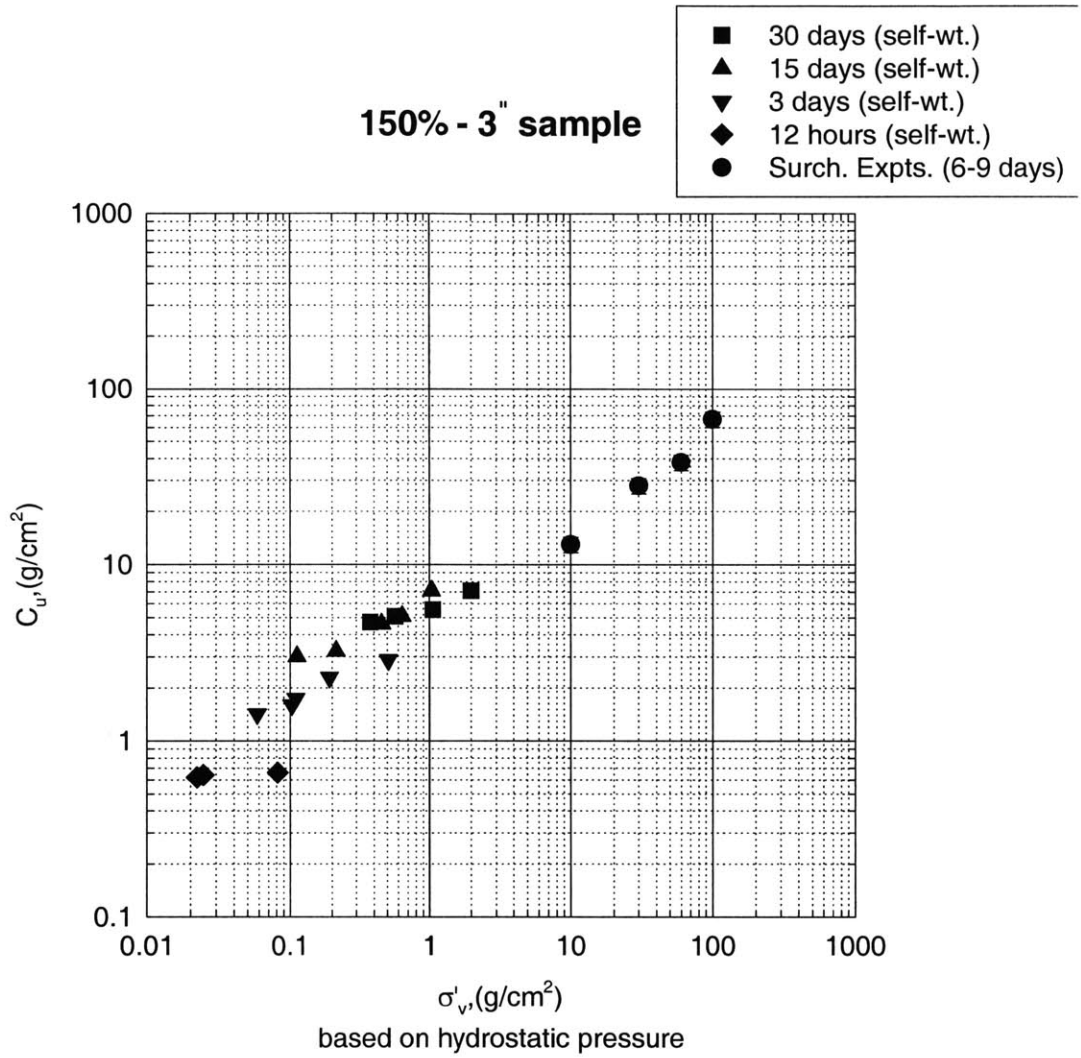

Figure 4-56: Undrained shear strength v/s. corrected effective stress for RCS 150% IWC 3-inch specimen

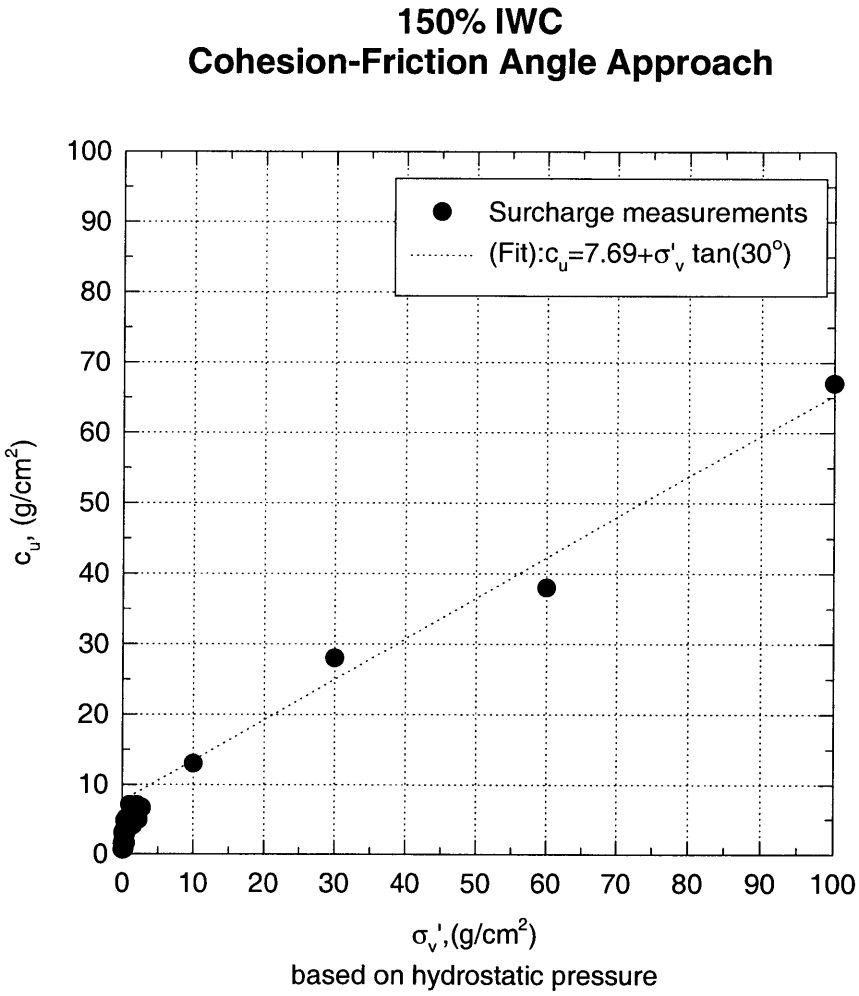

Figure 4-57: Undrained shear strength v/s. corrected effective stress for RCS 150% IWC surcharge data: Linear fit

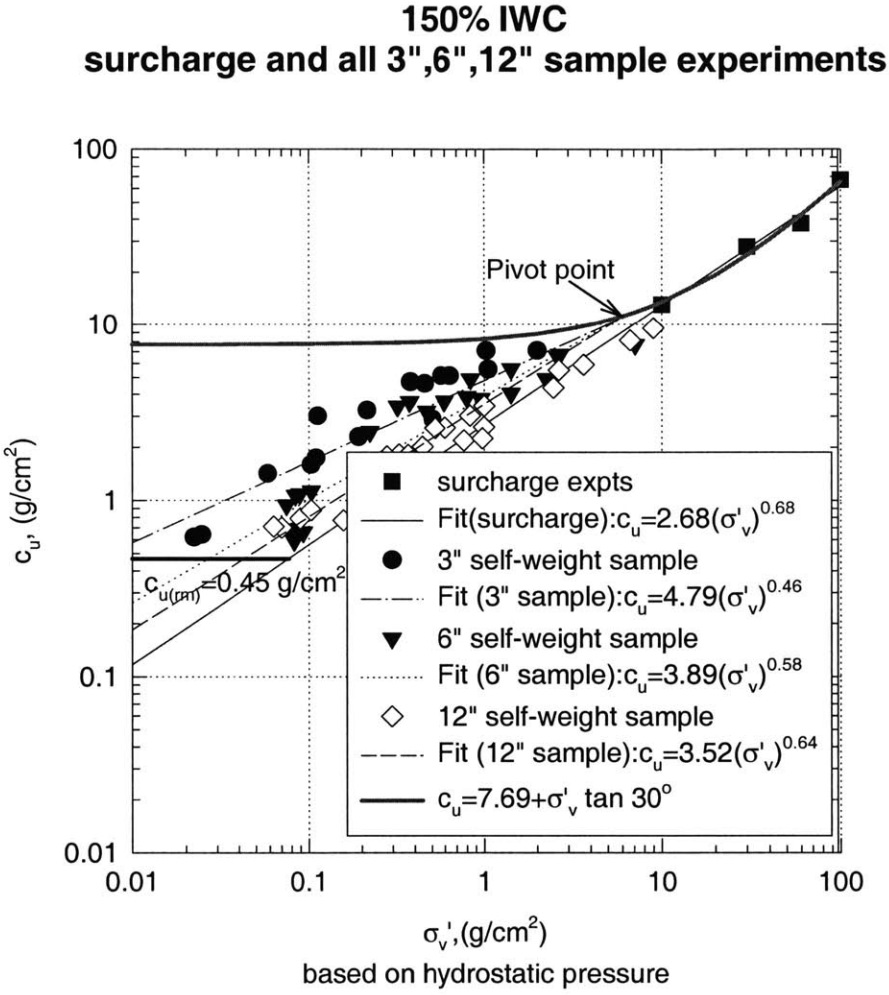

Figure 4-58: Undrained shear strength v/s. corrected effective stress for RCS 150% IWC: self-weight consolidation and surcharge data: Log-log linear fit

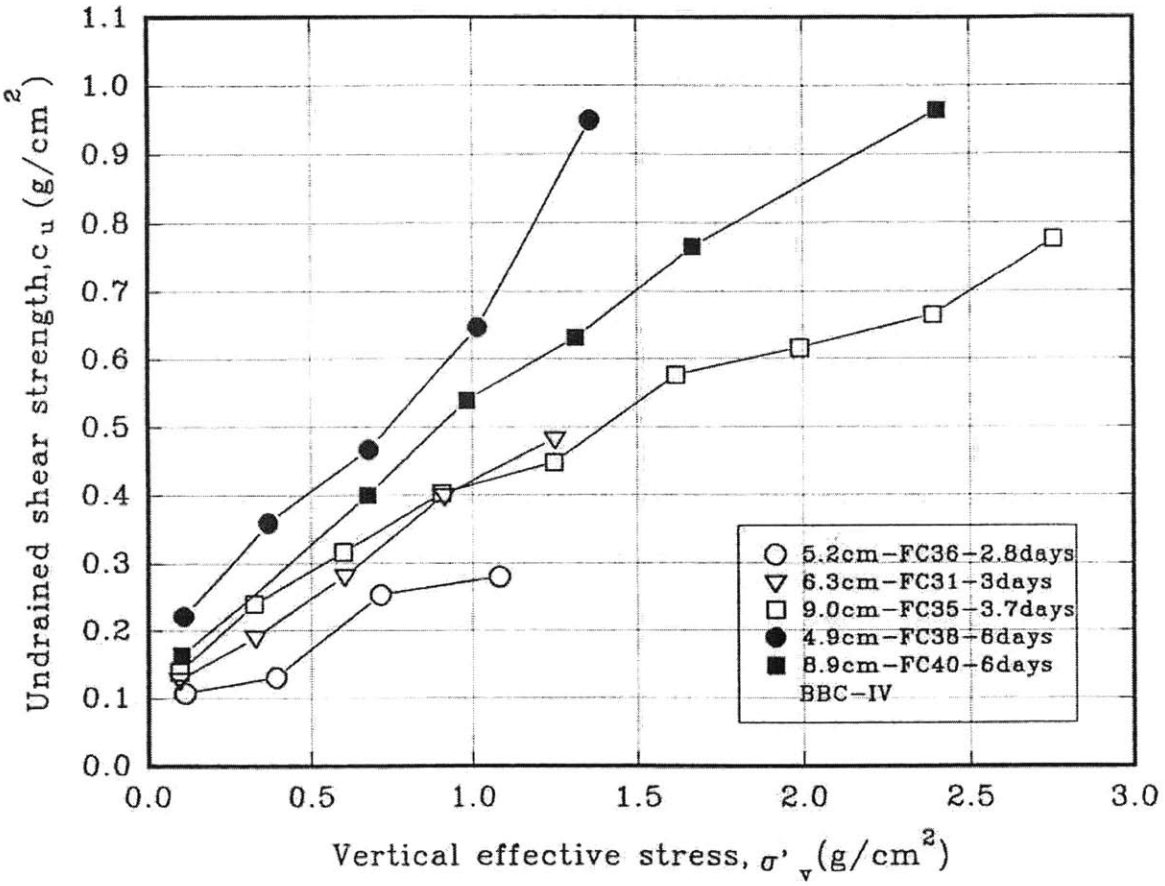

Figure 4-59: Variation of undrained shear strength with effective stress in Boston Blue Clay beds deposited from 550% IWC slurry (Zreik, 1994)

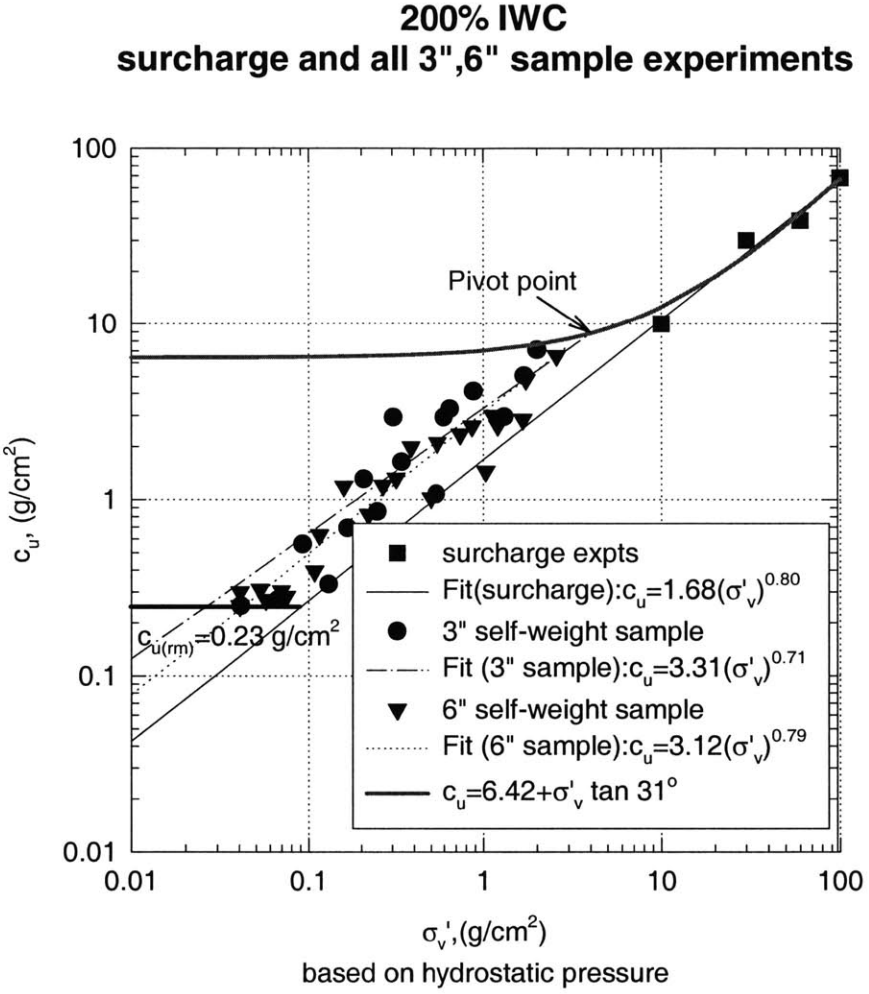

Figure 4-60: Undrained shear strength v/s. corrected effective stress for RCS 200% IWC: self-weight consolidation and surcharge data: Log-log linear fit

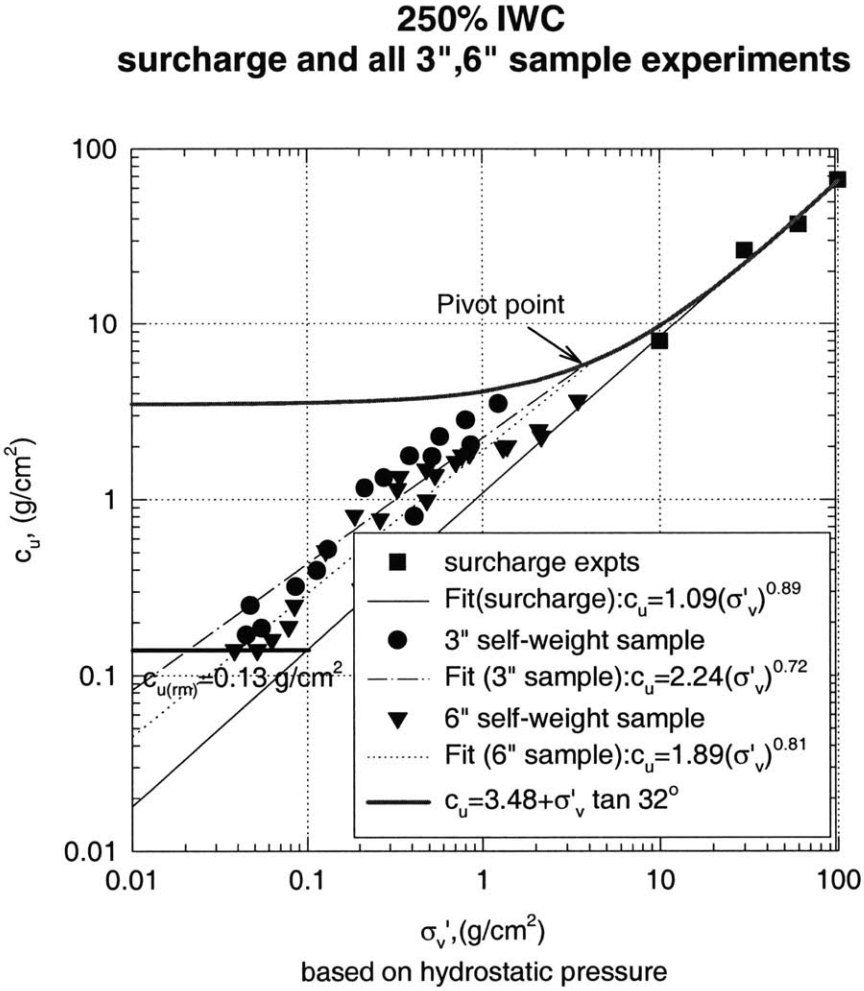

Figure 4-61: Undrained shear strength v/s. corrected effective stress for RCS 250% IWC: self-weight consolidation and surcharge data: Log-log linear fit

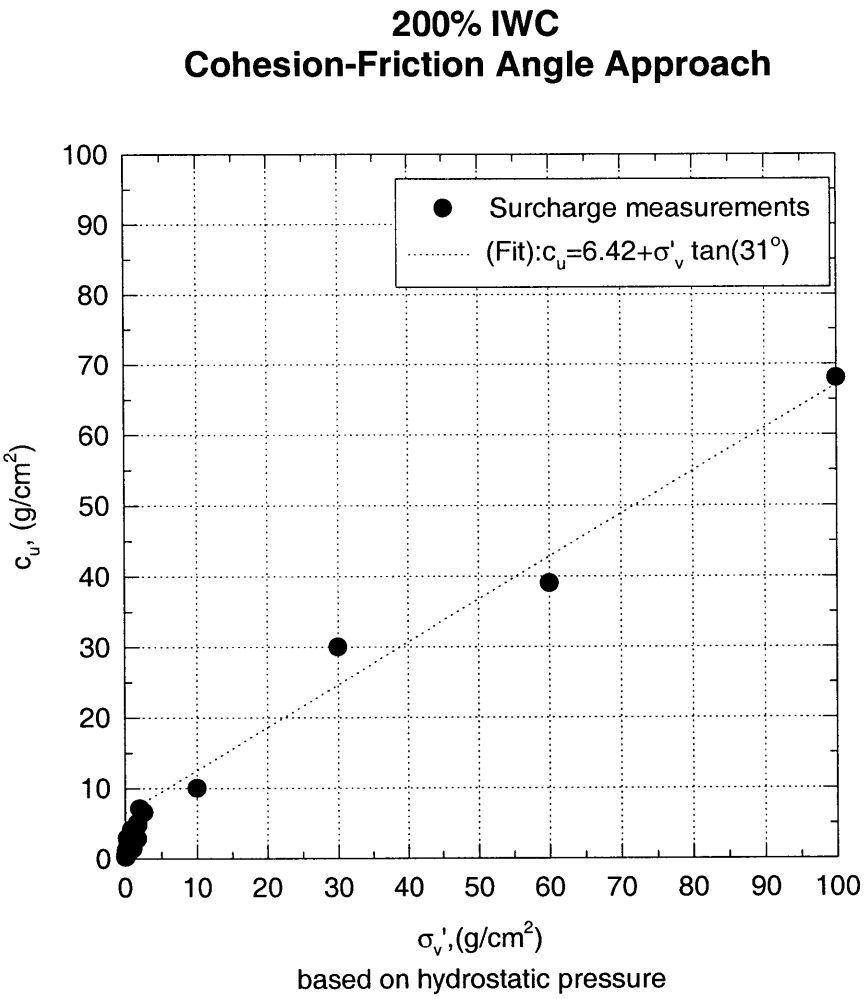

Figure 4-62: Undrained shear strength v/s. corrected effective stress for RCS 200% IWC surcharge data: Linear fit

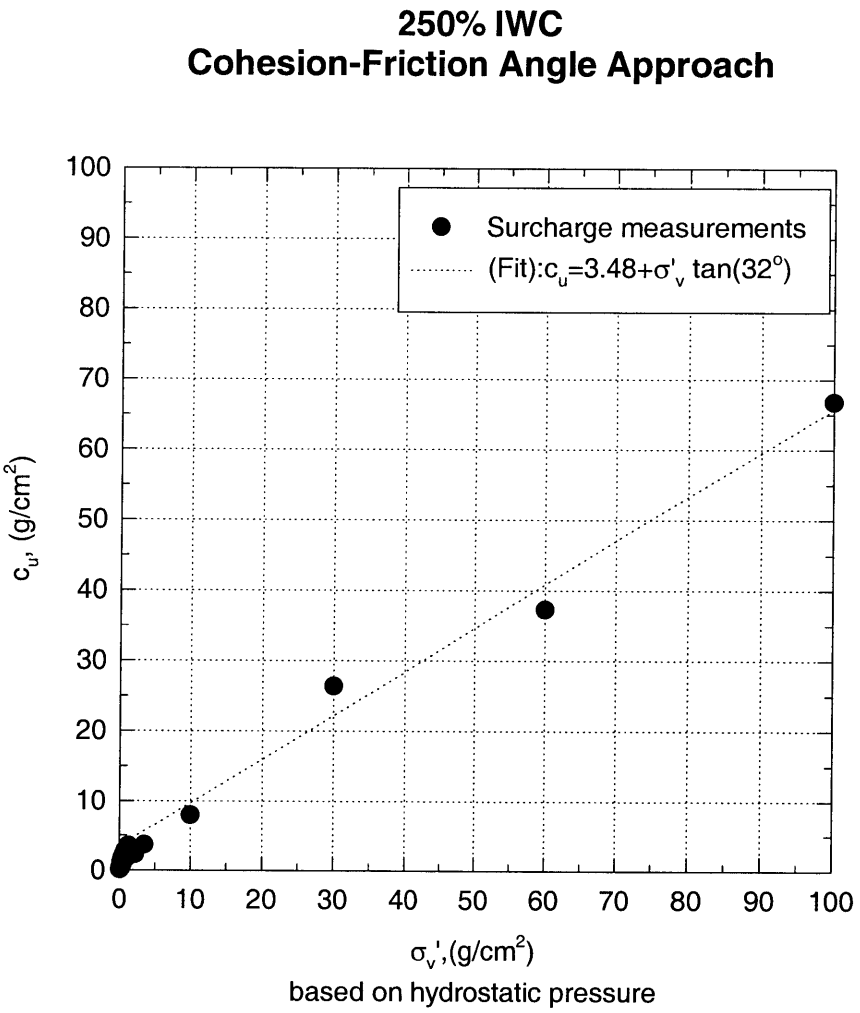

Figure 4-63: Undrained shear strength v/s. corrected effective stress for RCS 250% IWC surcharge data: Linear fit

Chapter 5

Conclusions and Recommendations

A simplified example application of the research results is presented in the first section. The conclusions of the research program are summarized in the following sections. A methodology is recommended for determination of the shear strength behavior of sediments that are different from the Reserved Channel Sediment (RCS). Finally, suggestions are presented for future research efforts in this field.

5.1 Example Application of Results

This section provides an illustration of how the research results presented in this work can be used to improve the design of capping projects. The capping of a pilot CAD cell in the Conley Terminal of Boston Harbor (Murray, 1999) is taken as an example case.

The CAD cell is 500 feet long and 200 feet wide. The cell was filled with up to 40 feet of sediments dredged from Boston's inner harbor. It is assumed that the fill material has the same properties at the beginning of consolidation as RCS at 150% water content.

5.1.1 Consolidation and Strength analysis

The large-strain consolidation model CONDES0 is used to perform the consolidation analysis of the sediment deposit. The following are the important input parameters required by CONDES0:

Constitutive Relationships:

The void ratio-effective stress and hydraulic conductivity-void ratio relationships are required as input for the model. These relationships should represent the entire range of void ratios and effective stresses expected during consolidation. For RCS specimens, the measurements from self-weight consolidation and surcharge experiments were combined with the measurements from CRS test in order to obtain the void ratio-effective stress relationship to be used for modeling.

In order to obtain the void ratio-effective stress relationship for RCS at 150% IWC, representative points were selected from the continuous CRS data (shown in Figure 4.29) and combined with the measurements from self-weight consolidation and surcharge experiments. The data and regression line are shown in Figure 5.1.

Similarly, the data on hydraulic conductivity at high effective stresses are available from the CRS tests, as mentioned in Section 3.6. A limited number of points from the high stress range are regressed with the hydraulic conductivity estimates from the self-weight consolidation experiments (presented in Table 4.4), in order to derive the relationship shown in Figure 5.2.

The following constitutive relationships, obtained in the manner described above, were provided as input for CONDES0:

$$e = 4.95(\sigma_v^{'} + 0.005)^{-0.17} \tag{5.1}$$

$$k = 1.18x10^{-8}(e)^{3.94} \tag{5.2}$$

The other inputs were specified as follows:

Specific gravity of sediment:	2.68
Initial height of deposit:	1200 cm (approx. 40 feet)
Top boundary condition:	Zero load
Bottom boundary condition:	Impervious Boundary
Initial void ratio distribution:	Uniform with value of 4.02 (for 150% IWC)

Shear strength was calculated from the predicted effective stress values by using the relationships for 150% IWC specimens given in Table 4.7. For effective stresses below 5 g/cm^2, the strength was predicted by using the relationship derived from the 3-inch RCS specimen.

Results

The model was run to provide the void ratio profiles at 5 days, 1 month, 6 months, 12 months, and 18 months after the filling of the CAD cell. The settlement of the deposit is shown in Figure 5.3. The deposit height decreases by 3.2 m in 18 months. The void ratio profiles predicted by the model are translated first to effective stress and then to shear strength profiles, using the relationships for RCS at 150% IWC (Tables 4.5 and 4.7). The resulting variation of shear strength with depth at different times is shown in Figure 5.4. It should be noted that the depth is measured from the surface of the deposit, which is moving downwards with time. Furthermore, the shear strength in the low effective stress range has been computed from the effective stress by using the relationship obtained from the 3-inch specimen results (see Table 4.7). The strength at all depths in the deposit, therefore, is higher than the minimum value corresponding to the remolded sediment.

The shear strength gain with time in the top layers of the deposit is masked in the figure due to scaling. Figure 5.5 shows the change in strength with time, for layers that are 1m, 3m, 6m, and 8m below the surface. The strength gain ratio over 18 months is 5 for the 1m-depth layer and 17,000 for the 8 m-depth layer.

5.1.2 Bearing Capacity Analysis

Bearing capacity calculations were conducted for the Conley Terminal CAD cell at 5 days and 18 months after the fill. It was assumed that an infinitely long load is uniformly applied over a width of 10 m. A commercial slope-stability model called SLOPE-W was used for this purpose, and Bishop's circular slip surface (Lambe and Whitman, 1969) procedure was used to calculate the critical loads for two different factors of safety. A non-rigid interface was assumed between the load and the fill material.

Figure 5.6 shows the geometry of the problem for the deposit age of 5 days. Since the shear strength is almost uniform except near the bottom one meter, the fill was modeled with two layers: the top layer with undrained shear strength of 1.2 g/cm^2 and the bottom layer that is 1 m thick and has an average shear strength of 7.5 g/cm^2. The figure shows the slip circle for factor of safety approximately 0.996, corresponding to a load of 58 kg/m^2. The load for factor of safety 1.5, which conforms to industry practice, is 37 kg/m^2. If the cap material consists entirely of sand, these loads correspond to approximate cap thicknesses of 6 and 4 cm, respectively.

The analysis for deposit age of 18 months is shown in Figure 5.7. Here, the sediment deposit is divided into eight layers of increasing shear strength with depth. The figure shows the slip circle for factor of safety 1, which corresponds to a cap thickness of 51 cm. The cap thickness for a factor of safety 1.5 is 34 cm.

It should be noted that these results have been presented in this section only to illustrate the applications of the research results. The actual bearing capacity calculations for placing a sand cap on very weak sediment requires a more detailed analysis that is beyond the scope of this work.

5.2 Conclusions: Shear strength behavior

Based on the results of the research conducted on RCS, the following conclusions can be drawn about the low effective stress behavior of undrained shear strength:

1. There exist two distinct regimes of shear strength variation with effective stress. The classical cohesion-friction angle formulation for shear strength does not accurately predict shear strength at low effective stresses. Below a certain value of effective stress, shear strength is better modeled as a power function of effective stress. The transition value of effective stress is around 10 g/cm^2 for RCS. Hence, two different equations are needed for predicting undrained shear strength.

2. The contribution of thixotropy to undrained shear strength is negligible during primary consolidation for RCS. This fact is borne out by the shear strength-effective stress correlations that do not have an explicit time dependence. During primary consolidation, the undrained shear strength can be modeled as a function only of effective stress, initial water content, and deposit height.

3. The height of the deposit and its initial water content determine the dependence of shear strength on effective stress. For RCS, the effects diminish above the effective stress value of 10 g/cm^2.

4. Exponential correlations have been provided for shear strength dependence on effective stress, in the low effective stress range. A simple example has been provided to illustrate the use of numerical consolidation models, to predict the shear strength as a function of depth and time in a deposit of any given height and initial water content.

5.3 Conclusions: RCS

1. The large strain consolidation behavior of RCS can be parameterized by performing surface settlement and consolidation experiments.

   The coefficients of primary consolidation, and secondary compression, were obtained from the surface settlement data. Variation of hydraulic conductivity with void ratio was estimated by using Terzaghi's small-strain theory in conjunction with the surface settlement data, for sediment specimens with different

values of initial height and initial water content. The void ratio-effective stress dependence was ascertained from the depth profiles of water content.

In the effective stress range of 0.1-10 g/cm^2, the coefficient of consolidation is in the range of 0.5 x 10^{-4} to 2.4 x 10^{-4} cm^2/s. The coefficient of secondary compression ranges from 0.02 to 0.06. The hydraulic conductivity varies from 10^{-6} to 30 x 10^{-6} cm/s for a void ratio range of 3.64 to 5.46.

2. Self-weight consolidation of RCS can be modeled by the use of the relationships derived from consolidation and surface settlement experiments.

   The data obtained from surface settlement and self-weight consolidation experiments were used to successfully model the large-strain consolidation behavior of laboratory RCS specimens, using the finite-element model CONDES0. Model predictions of void ratio profiles and surface settlement with time agreed well with the measurements.

3. The virgin compression curve has been extended to low effective stresses.

   Three different techniques have been utilized to obtain the void ratio-effective stress measurements for the RCS compression curve. Void ratio profiles obtained from self-weight consolidation experiments cover the low effective stress range (0.1-10 g/cm^2), surcharge experiments are used in the range 10-100 g/cm^2, and CRS testing extends the curve from 100 g/cm^2 to approximately 2000 g/cm^2. The measurements show a remarkable degree of continuity, resulting in a smooth compression curve over four log-decades of effective stress.

4. Void ratio-effective stress relationship is non-unique at low effective stresses.

   RCS deposits with different values of initial height and initial water content exhibit different void ratio-effective stress relationships at effective stresses below 10 g/cm^2. The dependence diminishes with increasing effective stress. At and above the effective stress value of 100 g/cm^2, the void ratio is uniquely determined by effective stress.

5. RCS has a high undrained strength ratio.

   The undrained shear strength ranges from 0.14 g/cm^2 at an effective stress of 0.04 g/cm^2 to 67 g/cm^2 at an effective stress of 100 g/cm^2. The undrained strength ratio, therefore, ranges from 4 to 0.7, which classifies RCS as a very strong sediment.

5.4 Recommended methodology for determination of shear strength

Containment and capping in CAD cells is being increasingly adopted as the disposal solution for a wide variety of contaminated sediments. Based on the findings of this research program, a general procedure for determination of shear strength characteristics of very weak materials is presented in this section. This procedure assumes the availability of a device to measure small values of undrained shear strength.

1. After the general classification and characterization, the low effective stress properties of the material should be ascertained from surface settlement experiments. For the chosen value of initial water content, at least three specimen heights should be prepared in order to cover a range of average void ratios.

2. The remolded strength of sediment should be measured at the desired water content, to establish the lower limit of strength.

3. Specimens of a convenient height should be prepared for self-weight consolidation experiments. The initial height should be enough to allow the determination of void ratio and shear strength profiles at the end of consolidation. The initial water content should be the same as anticipated in the field conditions.

4. Void ratio and shear strength profiles should be obtained from the specimens at different times during the consolidation process and also after the end of consolidation. The void ratio profile from the consolidated specimen is required

for back-calculating the effective stresses for measurements performed during the consolidation process.

5. The consolidation behavior in the high effective stress range should be ascertained by performing the standard CRS test.

6. The effective stress range between the self-weight-consolidated specimen and CRS test data should be covered by performing surcharge tests on the sample. A simple load frame may be used for this purpose. After the end of primary consolidation at the desired value of surcharge, the specimens should be tested for strength and water content.

7. The strength-effective stress relationship for the sediment at the selected value of initial water content can be determined in the following manner, from the data thus collected:

   The strength-effective stress data from the surcharge experiments should be fit to the classical cohesion-friction angle formulation as well as for a log-log linear fit. The lower limit of the applicability of the classical relationship is ascertained by examining the trend in the self-weight data, as the value of the effective stress where the strength measurements from self-weight consolidation specimens begin to approach the values predicted by the classical relationship. A log-log linear fit should be obtained for the data from self-weight consolidation specimen while constraining the fit to pass through this transition point.

   For a given water content at any given effective stress, the lowest possible strength is either the remolded strength of the sediment or the value predicted by the log-log linear fit to the strength-effective stress data from the surcharge experiments, whichever is lower.

   For effective stress values below the transition point, the upper bound shear strength is given by the exponential relationship corresponding to the constrained log-log linear fit for the self-weight consolidation data. Above this value, strength should be predicted with the aid of the classical model.

5.5 Recommendations for Future Work

This research work has provided an understanding of many aspects of the low strength behavior of dredged materials. Based on the findings of this effort, it is suggested that the following directions be pursued for future research in this field:

1. The results show that the time effect on shear strength operates only through the change in effective stress during the consolidation process. Tests should be conducted in order to examine the time dependence of strength after the end of primary consolidation.

2. We have used the consolidated void ratio-effective stress profile in order to obtain effective stress values for measurements obtained during consolidation. Self-weight consolidation experiments could be conducted in containers that are instrumented for pore pressure measurements during consolidation.

3. There exists no equivalent data on low effective stress behavior of sediments. The entire testing program should be run for other sediments in order to examine the specificity of the shear strength behavior exhibited by RCS.

4. Only rudimentary theories and methodologies are available for analyzing the impact and foundation loads caused by cap placement on weak sediments. Both experimental and theoretical efforts are needed to advance the field in this direction.

5. A detailed field study of strength development in consolidating sediments is highly recommended. It should provide for measurements of pore pressures and their dissipation with time, as well as for measurement of shear strength as a function of depth and time. In this context, it would be very useful to develop a cone penetrometer that is able to measure very low values of shear strength in field conditions.

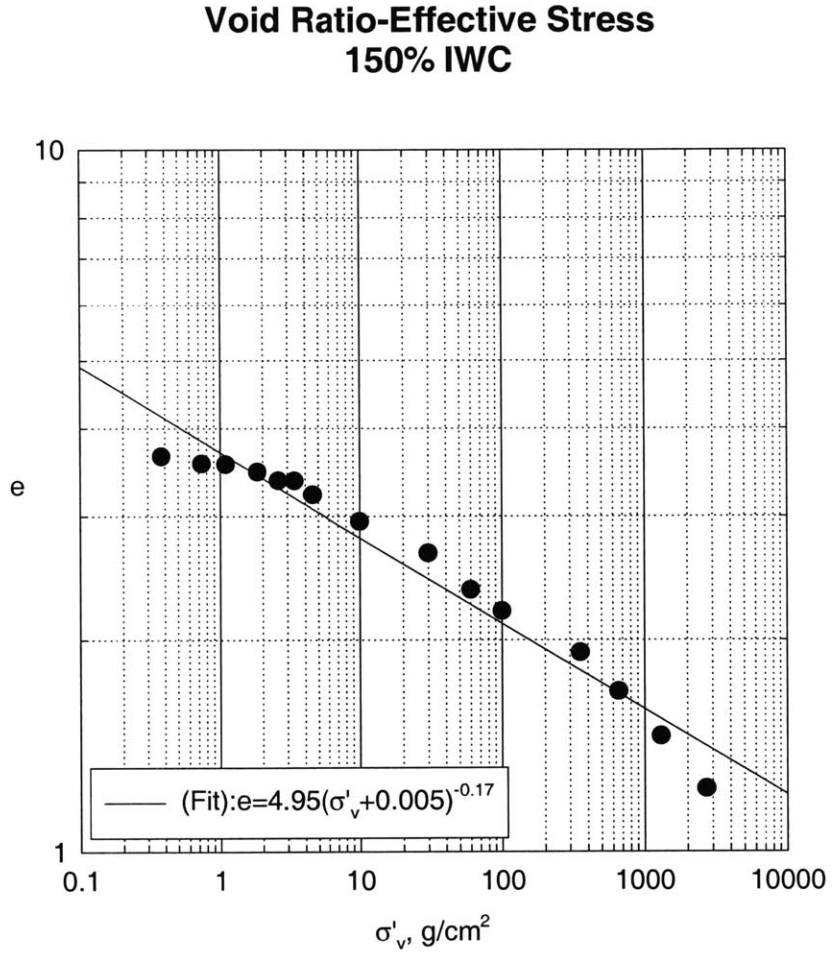

Figure 5-1: Estimation of void ratio - effective stress relationship RCS 150% IWC

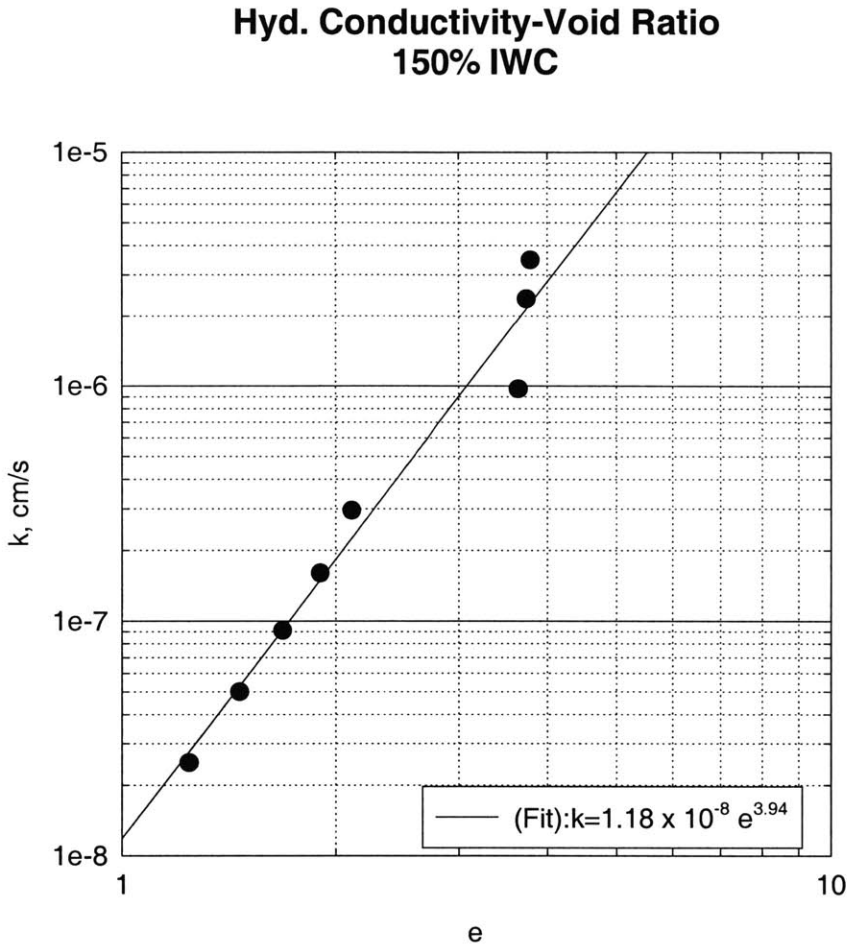

Figure 5-2: Estimation of hydraulic conductivity - void ratio relationship RCS 150% IWC

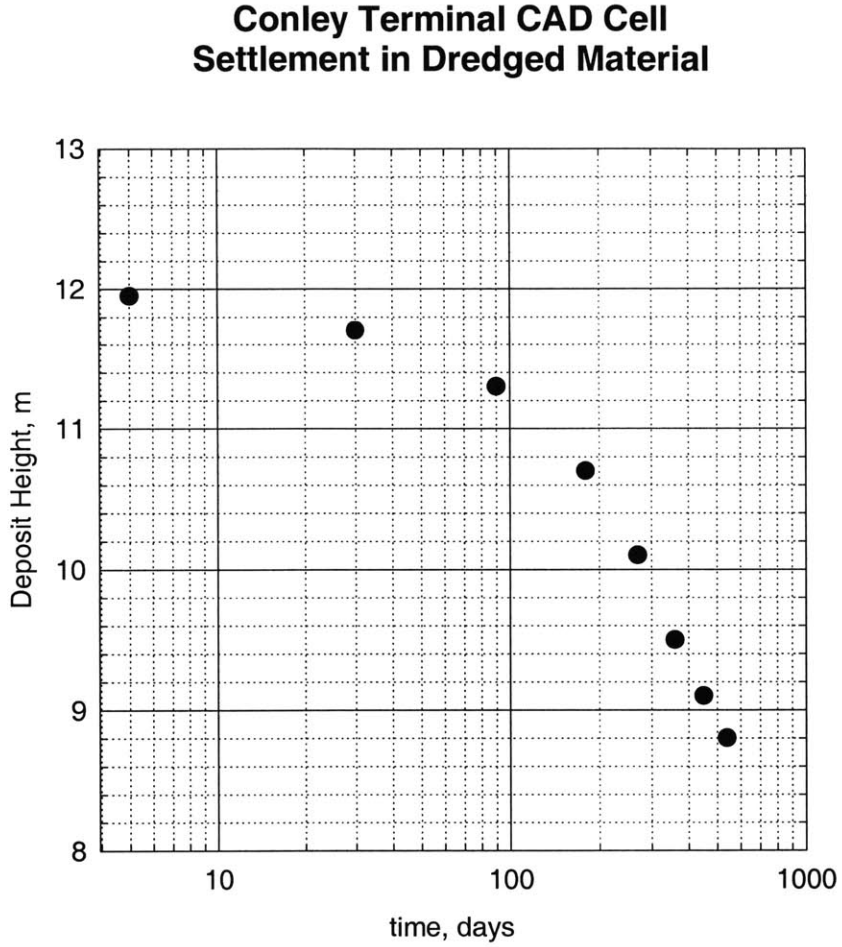

Figure 5-3: Conley Terminal CAD Cell: Settlement in RCS deposit due to consolidation

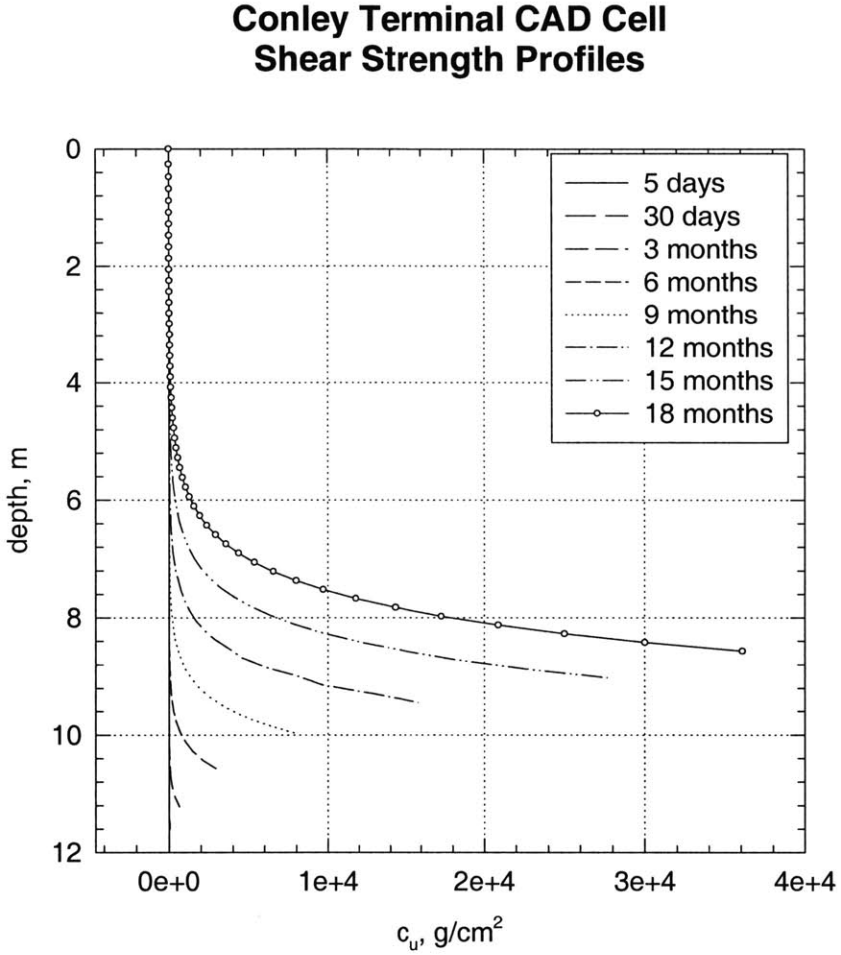

Figure 5-4: Conley Terminal CAD Cell: Shear strength profiles in RCS deposit at different consolidation times

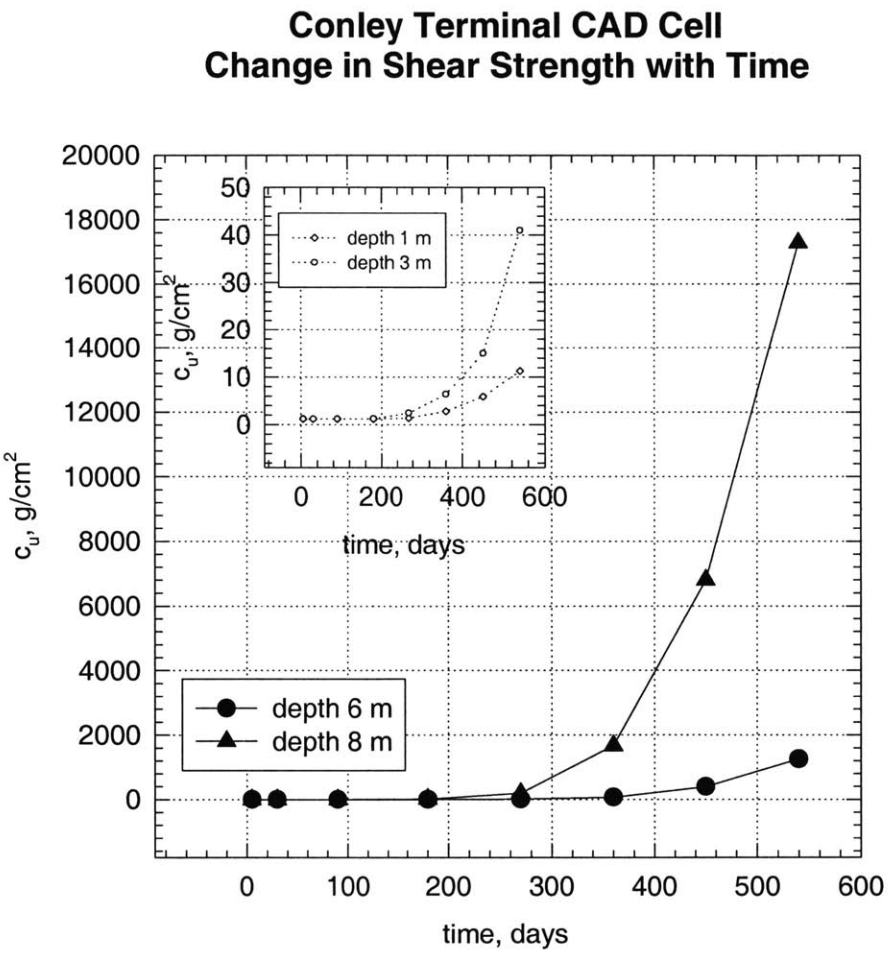

Figure 5-5: Conley Terminal CAD Cell: Change in shear strength with time at different depths in the RCS deposit

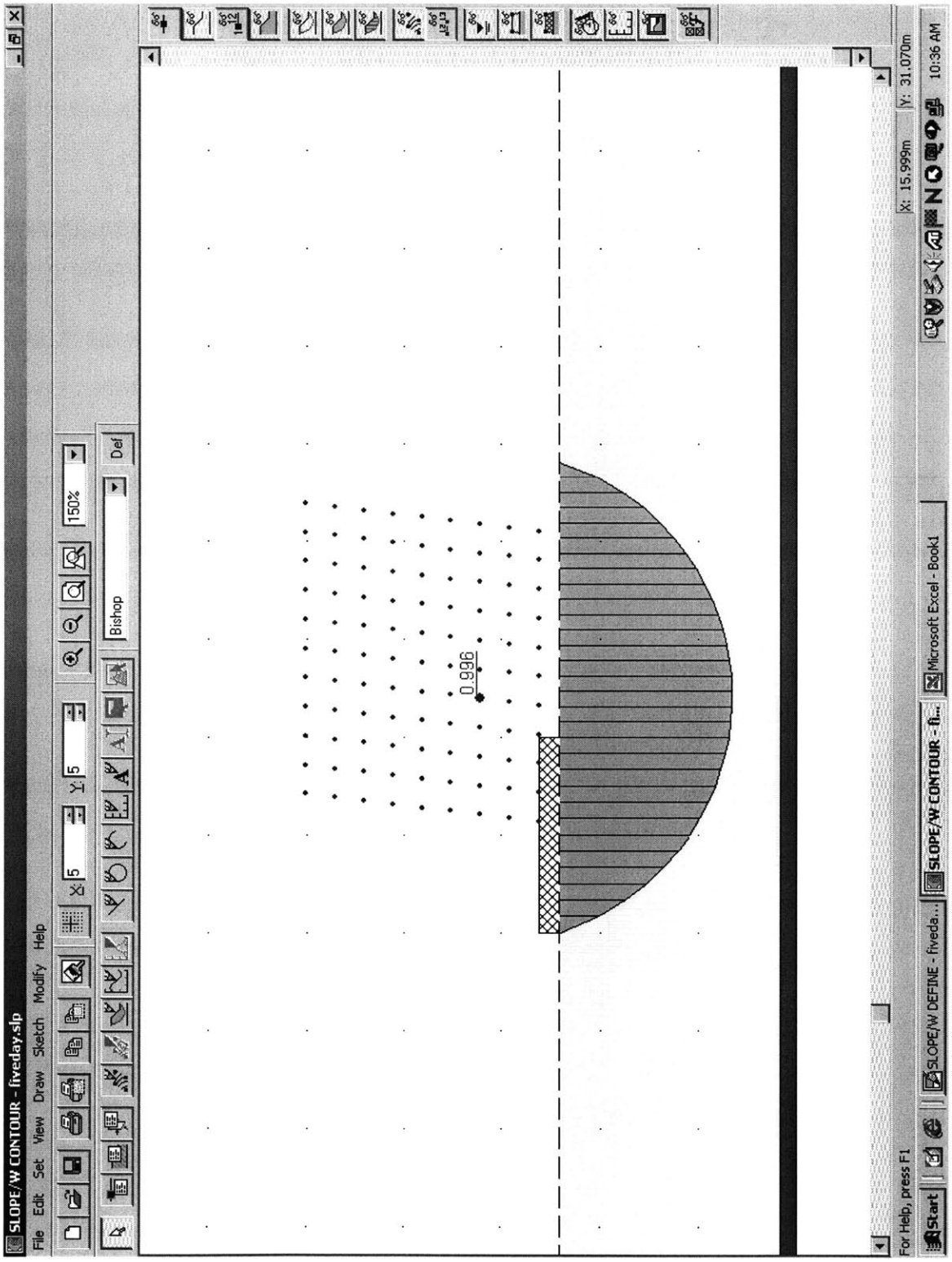

Figure 5-6: Conley Terminal CAD Cell: Bishop's critical circle analysis for cap placement at 5 days

Figure 5-7: Conley Terminal CAD Cell: Bishop's critical circle analysis for cap placement at 18 months

Bibliography

[1] Alexis, A., Basoullet, P., Le Hir, P., and Teisson, C. (1992), "Consolidation of Soft Marine Soils: Unifying Theories, Numerical Modelling and In Situ Experiments," Proceedings of Coastal engineering 1992, Venice, Italy, 2949-2961.

[2] Abu-Hejleh, A.N, Znidarcic, D., and Barnes, B.L. (1996), "Consolidation Characteristics of Phosphatic Clays," Journal of Geotechnical Engineering, Vol. 122, No. 4, 295-301.

[3] Abu-Hejleh, A.N, and Znidarcic, D. (1995), "Dessication Thory for Soft Cohesive Soils," Journal of Geotechnical Engineering, Vol. 121, No. 6, pp. 106-115.

[4] Al-Durrah, M. and Bradford, J.M. (1981), "New Methods of Studying Soil Detachment due to Waterdrop Impact," Soil Science Society of America Journal, Vol. 45, 949-953.

[5] Becher, H.H., Bruer, J., and Klinger, B. (1997), "An Index Value for Characterizing Hardsetting Soils by Fall-cone Penetration," Soil Technology, Vol. 10, No. 1, 47-56.

[6] Been, K. (1980), "Stress-Strain of a Cohesive Soil deposited under Water," Ph.D. Thesis, Balliol College, Oxford, UK.

[7] Been, K., and Sills, G.C. (1981), "Self-Weight Consolidation of Soft Soils: An Experimental and Theoretical Study," Geotechnique, Vol. 31, No. 4, 519-535.

[8] Benoit, J., Eighmy, T.T., and Crannell, B.S. (1999), "Landfilling Ash/Sludge

Mixtures," Journal of Geotechnical and Geoenvironmental Engineering, Oct. 1999, 877-888.

[9] Bentley, S.P. (1979), "Viscometric Assessment of Remoulded Sensitive Clays," Canadian Geotechnical Journal, Vol. 16, 414-419.

[10] Blomqvist, S. (1990), "Sampling Performance of Ekman Grabs - In situ Observations and Design Improvements," Hydrobiologia, vol. 206, no. 3, pp. 245-254.

[11] Brannon, J.M., R.E. Hoeppel and D. Gunnison (1984), "Efficiency of Capping Contaminated Dredged Material," In *Proceedings of the Conference on Dredging '84*. vol. 2: Dredging and Dredged Material Disposal, R.L. Montgomery and J. W. Leach (Eds.). American Society of Civil Engineers, New York, pp. 664-673.

[12] Broms, B.B. (1987), "Stabilization of very soft clay using geofabric," Geotextiles and Geomembranes, 5(1), 17-28.a

[13] Buscall, R. (1990), "The Sedimentation of Concentrated Colloidal Suspensions," Colloids Surf. Vol. 43, 33-53.

[14] Cargill, K.W. (1984), "Prediction of Consolidation of a Very Soft Soil," Journal of Geotechnical Engineering-ASCE, Vol. 110, No. 6, 775-795.

[15] Carrier, W.D., Bromwell, L.G., and Somogyi, F. (1983), "Design Capacity of Slurried Mineral Waste Ponds," Journal of Geotechnical Engineering, Vol. 109, No. 5, 699-716.

[16] Chen, W.F. (1975), Limit Analysis and Soil Plasticity, Elsevier Science, Amsterdam.

[17] Christian, H.A., Piper, D.J.W., and Armstrong, R. (1991), "Strength and Consolidation Properties of Surface Sediments, Flemish Pass- Effect of Biological Processes," Deep-Sea Research Part A: Oceanographic Research Papers, Vol. 38, No. 6, 663-676.

[18] Clayton, C.R. and Jukes, A.W. (1978), "A One Point Cone Penetrometer Liquid Limit Test?," Geotechnique, Vol. 28, No. 4, 469-472.

[19] Colliat, J.L., Boisard P., Sparrevik, P., and Gramet, J.C. (1998), "Design and Installation of Suction Anchor Piles at Soft Clay Site," Journal of Waterway, Port, Coastal, and Ocea Engineering- ASCE, Vol. 124, No. 4, 179-188.

[20] Consoli, N.C., and Sills, G.C. (2000), "Soil Formation from Tailings: Comparison of Predictions and Field Measurements," Geotechnique, Vol. 50, No. 1, 25-33.

[21] Corapciouglu, M.Y. (1984), "Land Subsidence (A): A State-of-the-art Review," Fundamentals of Transport Phenomena in Porous Media, J. Beaer and M.Y. Corapcioglu (eds.), Martinus Nijhoff, The Hague, The Netherlands, 369-444.

[22] Davis, E.H., and Raymond, G.P. (1965), "A Non-linear Theory of Consolidation," Geotechnique, Vol. 15, No. 2, 161-173.

[23] Dzuy N.Q. and Boger, D.V. (1985), "Direct Yield Stress Measurement with the Vane Method," Journal of Rheology, Vol. 21, No. 3, 335-347.

[24] Elder, D. McG. and G.C. Sills (1985), "Thickening and Consolidation of Sediment due to Self Weight," In: *Flocculation, Sedimentation, and Consolidation*, B.M. Moudgil and P. Somasundaran (Eds.), pp. 349-362.

[25] ENSR (1997), "Summary Report of Independent Observations, Phase I- Boston Harbor Navigation Improvement Project," ENSR doc. No. 4479-001-150, prepared for Massachusetts Coastal Zone Management, ENSR, Acton, MA.

[26] Fahey, M., and Toh, S. (1992), "A Methodology for Predicting the Consolidation Behaviour of Mine Tailings," Proc. of Western Australian Conference on Mining Geomechanics, Kalgoorie, Australia.

[27] Fakher, A., Jones, C.J.F.P., and Clarke, B.G. (1999), "Yield stress of super soft clays," Journal of Geotechnical and Geoenvironmental Engineering, June 1999, 499-509.

[28] Fakher, A. and Jones, C.J.F.P. (1996), "Land Reclamation using Super Soft Clay," Proceedings of 2nd International Conference On Soft Soil Engineering, Vol. 2, 775-780.

[29] Farrell, E., Schuppener, B., and Wassing, B. (1997), "ETC 5 Fall-Cone Study," Ground Engineering, vol. 30, no. 1, pp. 33-36.

[30] Feldkamp, J.R. (1989), "Numerical Analysis of One-Dimensional Nonlinear Large Strain Consolidation by Finite Element Method," Transport in Porous Media, Vol. 4, 239-257.

[31] Feng, T.W. (2000), "Fall-Cone Penetration and Water Content Relationship of Clays," Geotechnique, vol. 50, no. 2, pp. 181-187.

[32] Fox, P.J. and Berles, J.D. (1997), "CS2: A Piecewise-Linear Model for Large Strain Consolidation," International Journal of Numerical and Analytical Methods in Geomechanics, Vol. 21, 453-475.

[33] Fox, P.J. (1999), "Solution Charts for Finite Strain Consolidation of Normally Consolidated Clays," Journal of Geotechnical and Geoenvironmental Engineering, Vol. 125, No. 10, 847-867.

[34] Fredette, T.J. (1994), "A Summary of Recent Capping Investigations with Dredged Sediments in New England," In *Management of Bottom Sediments Containing Toxic Substances: Proceedings of the 15th U.S./Japan Experts Meeting*, T.R. Patin (ed.), U.S. Army Corps of Engineers, Water Resources Support Center.

[35] Freeland, G.L., R.A. Young, G. Drapeau, T.L. Clarke, and B.L. Benggio (eds.) (1983), "Sediment Cap Stability Study: New York Dredged Material Dumpsite," Report to U.S. Army Corps of Engineers, New York District.

[36] Gibson, R.E., England, G.L. and Hussey, M.J.L. (1967), "The Theory of One-Dimensional Consolidation of Saturated Clays (I)," Geotechnique, Vol. 17, 261-273.

[37] Gonzalez, J.H. (2000), "Experimental and Theoretical Investigation of Constant Rate of Strain Consolidation," M.S. Thesis, Massachusetts Institute of Technology, Cambridge, Massachusetts, U.S.A.

[38] Hansbo, S. (1957), "A New Approach to the Determination of the Shear Strength of Clay by the Fall Cone Test," Royal Swedish Geotechnical Institute, No. 14, Stockhom.

[39] Harison, J.A. (1988), "Using the BS Cone Penetrometer for the Determination of the Plastic Limit of Soils," Geotechnique, Vol. 38, No. 3, 433-438.

[40] Houlsby (1982), "Theoretical Analysis of the Fall Cone Test," Geotechnique, Vol. 32, No. 2, 111-118.

[41] Hu, Y., Randolph, M.F., and Watson, P.G. (1999), "Bearing Response of Skirted Foundation on Nonhomogenous Soil," Journal of Geotechnical and Geoenvironmental Engineering, Nov. 1999, 924-935.

[42] Huerta, A., Kriegsmann, G.A., and Krizek, R.J. (1988), "Permeability and Compressibility of Slurries from Seepage-Induced Consolidation," Journal of Geotechnical Engineering, Vol. 114, No. 5, 614-627.

[43] Huerta, A., and Rodriguez, A. (1992), "Numerical Analysis of Nonlinear Large Strain Consolidation and Filling," Computers and Structures, Vol. 44, No. 1-2, 357-365.

[44] Imai, G. (1979), "Development of a New Consolidation Test Procedure Using Seepage Force," Soils and Foundations, Vol. 19, No. 3, 45-60.

[45] Imai, G. (1981), "Experimental Studies on Sedimentation Mechanism and Sediment Formation of Clay Materials," Soils and Foundations, Vol. 21, No. 1, 7-20.

[46] Inoue, T., Tan, T.-S., and Lee, S.-L. (1990), "An Investigation of Shear Strength of Slurry Clay," Soils and Foundations, Vol. 30, No. 4, 1-10.

[47] Karlsson, R. (1961), "Suggested Improvements in the Liquid Limit Test, with Reference to Flow Properties of Remoulded Clays," Proc. of the 5th Int. Conf. on Soil Mechanics and Foundation Engr., Paris, France, July 1961. 171-184.

[48] Koester, J.P. (1992), "The Influence of Test Procedure on Correlation of Atterberg Limits with Liquefaction in Fine-Grained Soils," Geotechnical Testing Journal, Vol. 15, No. 4, 352-361.

[49] Kravitz, J.H. (1970), "Repeatability of Three Instruments used to Determine the Undrained Shear Strength of Extremely Weak, Saturated, Cohesive Sediments," Journal of Sediementary Petrology, Vol. 40, No. 3, 1026-1037.

[50] Krizek, R.J, and Somogyi, ,F. (1984), "Perspectives on Modeling Consolidation of Saturated Clays (II): Finite Non-Linear Consolidation of Thick Homogeneous Layers," Canadian Geotechnical Journal, Vol. 18, 280-293.

[51] Krizek, R.J., and Salem, A.M. (1977), "Time-dependent Development of Strength in Dredgings," Journal of Geotechnical Engineering, Vol. 103, No.3, 169-184.

[52] Kumar, G.V. and Wood, D.M. (1999), "Fall-Cone and Compression Tests on Clay-Gravel Mixtures," Geotechnique, vol. 49, no. 6, pp. 727-739.

[53] Kurumada, Y., Shinsha, H., Watari, Y. (1992), "Earth spreading on very soft ground by geotextile reinforcement." Proc. of Earth Reinforcement Practice, Vol. 1, 625-630.

[54] Ladd, C.C., and Foott, R. (1974), "New Design Procedure for Stability of Soft Clays," Journal of Geotechnical Engineering, Vol. 100, No. 7, 763-786.

[55] Lambe, T.W. and Whitman, R.V. (1969), Soil Mechanics, John Wiley and Sons, New York.

[56] Lee, K., and Sills, G.C. (1981), "The Consolidation of a Soil Stratum Including Self-Weight Effects and Large Strains," International Journal of Numerical and Analytical Methods in Geomechanics, Vol. 5, 405-428.

[57] Lee, S.R., Kim, Y.S., and Kim, Y.S. (2000), "Analysis of Sedimentation/Consolidation by Finite Element Method," Computers and Geotechnics, Vol. 27, 141-160.

[58] Ling, H.I., Leschinsky, D., Gilbert, P.A., and Palermo, M.R. (1996), "In-situ capping of contaminated submarine sediments: Geotechnical considerations," Proc. of the 2nd Int. Confr. on Environmental Geotechnics, Balkema, Rotterdam, The Netherlands, 575-580.

[59] Liu, J.C., and Znidarcic, D. (1991), "Modeling One-Dimensional Compression Characteristics of Soils," Journal of Geotechnical Engineering, Vol. 117, No. 1, 162-169.

[60] Locat, J., and Demers D. (1988), "Viscosity, Yield Stress, Remolded Strength, and Liquidity Index Relationships for Sensitive Clays," Can. Geotech. J., Ottawa, 25(4), 799-806.

[61] Lowe, J., III, Zaccheo, P.F., and Feldman, H.S. (1964), "Consolidation Testing with Back Pressure," Journal of the Soil Mechanics and Foundations Division, ASCE, vol. 90, no. SM5, pp. 69-86.

[62] Lu, N.Z., Suhayda, J.N., Prior, D.B., Bornhold, B.D., Keller, G.H., Wiseman, W.J., Wright, L.D., and Yang, Z.S. (1991), "Sediment Thixotropy and Submarine Mass Movement, Huanghe Delta," Geo-marine Letters, Vol. 11, No. 1, 9-15.

[63] Massport and USACE (1995), "Boston Harbor, Massachusetts: Navigation Improvement Project and Berth Dredging Project L," Massachusetts Port Authority, Boston, MA.

[64] Mesri, G., Stark, T.D., Ajlouni, M.A. et al (1997), "Secondary Compression of Peat with or without Surcharging," Journal of Geotechnical and Geoenvironmental Engineering, vol. 123, no. 5, pp. 411-421.

[65] Mesri, G., and Choi, Y.K. (1985), "Settlement Analysis of Embankments on Soft Clays," Journal of Geotechnical Engineering, Vol. 111, No. 4, 441-464.

[66] Mitchell, J.K. (1960), "Fundamental Aspects of Thixotropy in Soils," Journal of the Soil Mechanics and Foundations Division, ASCE, vol. 86, no. SM3, pp. 19-52.

[67] Murff, J.D. Wagner, D.A., and Randolph, M.F. (1989), "Pipe Penetration in Cohesive Soil," Geotechnique, London, 39(1), 213-229.

[68] Murray, P.G. (1999), "Monitoring Results from the first Boston Harbor Navigation Improvement Project Confined Aquatic Disposal Cell," U.S. Army Corps of Engineers, New England District; Contribution (Disposal Area Monitoring System (DAMOS) Program) no. 124, Concord, MA.

[69] Nadaoka, K., H. Yagi, and H. Kamata (1991), "A Simple Quasi-3-D Model of Suspended Sediment Transport in a Nonequilibrium State" Coastal Engineering, vol. 15, no. 5-6, pp. 459-474.

[70] Nagaraj, T.S. and Jayadeva, M.S. (1981), "Re-examination of One Point Methods of Liquid Limit Determination," Geotechnique, Vol. 31, No. 3, 413-425.

[71] Nagaraj, T.S., Murthy, B.R.S., and Bindumadhava (1987), "Liquid Limit Determination - Further Simplified," Geotechnical Testing Journal, Vol. 10, No. 3, 142-145.

[72] National Research Council (1997), Contaminated Sediments in Ports and Waterways: Cleanup Strategies and Technologies. Committee on Contaminated Marine Sediments. National Academy Press, Washington, D.C.

[73] Nguyen, Q.D., and Boger, D.V. (1983), "Yield Stress Measurement for Concentrated Suspensions," Journal of Rheology, 27(4), 321-329.

[74] Ockenden, M.C., and Delo, E.A., (1991), "Laboratory Testing of Muds," Geo-Marine Letters, Vol. 11, No. 3-4, 138-142.

[75] Palermo, M.A. (1991), "Design Requirements for Capping," United States Waterways Experiment Station, Vicksburg, Mississippi. Dredging Research Technical Notes DRP-5-03.

[76] Pane, V., Croce, P. Znidarcic, D., Ko, ,H.Y., Olsen, H.W., and Schiffman, R.L. (1982), "Effects of Consolidation on Permeability Measurements for Soft Clays," Geotechnique, Vol. 33, 67-72.

[77] Pane, V., and Schiffman, R.L. (1985), "A Note on Sedimentation and Consolidation," Geotechnique, Vol. 35, No. 1, 69-77.

[78] Papanicolaou, A.N. and Diplas, P. (1999), "Numerical Solution of a Non-linear Model for Self-weight Solids Settlement," Applied Mathematical Modeling, Vol. 23, 3445-362.

[79] Partheniades, E. (1986), "A Fundamental Framework for Cohesive Sediment Dynamics," Estuarine Cohesive Sediment Dynamics, Lecture Notes on Coastal and Estuarine Studies, A.J. Mehta (ed.), Springer-Verlag, 219-250.

[80] Pastor, J. Turgeman, S., and Avallet, C. (1989), "Predicting the Phenomenon of Burying through Gravity in Purely Cohesive Sedimentary Sea Beds," Geotechnique, London, 39(4), 625-639.

[81] Rao, S.N., Ravi, R., and Prasad, B.S. (1997), "Pullout Behavior of Suction Anchors in Soft Marine Clays," Marine Georesources and Geotechnology, Vol. 15, No. 2, 95-114.

[82] Rabia, H. (1989). Rig Hydraulics. Entrac Software, Newcastle Upon Tyne, U.K., 249.

[83] Rassam, D.W. and Williams, D.J. (1999), "Bearing Capacity of Desiccated Tailings" Journal of Geotechnical and Geoenvironmental Engineering, July 1999, 600-609.

[84] SAIC (Science Applications International Corporation) (1997), "Postcap Monitoring of Boston Harbor Navigation Improvement Project (BHNIP) Phase I: Assessment of Inner Confluence CAD Cell," SAIC Report No. 413, prepared for the New England Division of the U.S. Army Corps of Engineers, Waltham, MA.

[85] Schiffman, R.L., Vick, S.G., and Gibson, R.E. (1988), "Behaviour and Properties of Hydraulic Fills," Geotechnical Engineering Special Publication No. 21, D.J.A. van Zyl and S.G. Vick (eds.), ASCE, 166-202.

[86] Seah, T.H. (1990), "Anisotropy of Resedimented Boston Blue Clay," Sc.D. Thesis, Massachusetts Institute of Technology, Cambridge, Massachusetts, USA.

[87] Seneviratne, N.H., Fahey, M., Newson, T.A., and Fujiyasu, Y. (1996), "Numerical Modeling of Consolidation and Evaporation of Slurried Mine Tailings," International Journal for Numerical and Analytical Methods in Geomechanics, Vol. 20, No. 9, 647-671.

[88] Sharma, P.P., Gupta, S.C., and Rawls, W.J. (1991), "Soil Detachment by Single Raindrops of Varying Kinetic Energy," Soil Science Society of America Journal, Vol. 55, No. 2, 301-307.

[89] Sheahan, T.C., Ladd, C.C., and Germaine, J.T. (1996), "Rate-Dependent Undrained Shear Behavior of Saturated Clay," Journal of Geotechnical Engineering, Vol. 122, No.2, 99-108.

[90] Shodja, H.M., and Feldkamp, J.R. (1993), "Numerical Analysis of Sedimentation and Consolidation by the Moving Finite Element Method," International Journal for Numerical and Analytical Methods in Geomechanics, Vol. 17, No. 11, 753-769.

[91] Silva, A.J., Brandes, H.G., Uchytil, C.J., Fredette, T.J., and Carey, D. (1994), "Geotechnical Analysis of Capped Dredged Material Mounds," Dredging'94, E. Clark McNair, Jr. (ed.), Proc. of the Second International Conference on Dredging and Dredged Material Placement, Lake Buena Vista, FL, Nov. 1994.

[92] Stewart, D., and Randolph, M.F. (1991), "A New Site Investigation Tool for the Centrifuge," Proceedings of Centrifuge'91, Balkema, Rotterdam, The Netherlands.

[93] Stone, K.J.L., Randolph, M.F., Toh, S., and Sales, A.A. (1994), "Evaluation of

Consolidation Behavior of Mine Tailings," Journal of Geotechnical Engineering, Vol. 120, No. 3, 473-490.

[94] Suthaker, N.N., and Scott, J.D. (1997), "Thixotropic Strength Measurement of Oil Sand Fine Tailings," Canadian Geotechnical Journal, 974-984.

[95] Tan, S.A., Tan, T.S., Ting, L.C., Yong, K.Y., Karunaratne, G.P., and Lee, S.L., (1988), "Determination of Consolidation Properties for Very Soft Clay," Geotechnical Testing Journal, Vol. 11, No. 14, 233-240.

[96] Tan, T.S., Yong, K.Y., Leong, E.C.,, and Lee, S.L. (1990), "Sedimentation of Clayey Slurry," Journal of Geotechnical Engineering, Vol. 116, No. 6, 885-898.

[97] Terzaghi, K. (1943), Theoretical Soil Mechanics. Wiley, New York.

[98] Terzaghi, K. and Peck, R.B. (1967), Soil Mechanics in Engineering Practice. John Wiley and Sons, New York.

[99] Tiller, F.M. and Khatib, Z. (1984), "The Theory of Sediment Volumes of Compressible, Particulate Structures," Journal of Colloid and Interface Science, Vol. 100, No. 1, 55-67.

[100] Toorman, E.A. (1992), "Modeling of Fluid Mud Flow and Consolidation," PhD Thesis, Katholieke Universiteit, Leuven, Belgium.

[101] Toorman, E.A. (1996), "Sedimentation and Self-Weight Consolidation: General Unifying Theory," Geotechnique, Vol. 46, No. 1, 103-113.

[102] Toorman, E.A. (1999), "Sedimentation and Self-Weight Consolidation: Constitutive Equations and Numerical Modeling," Geotechnique, Vol. 49, No. 6, 709-726.

[103] Toorman, E.A. and Huysentruyt, H. (1997), "Towards a New Constitutive Equation for Effective Stresses in Consolidating Mud," In *Cohesive Sediments*, N. Burt, R. Parker, and J. Watts (eds.), pp. 121-132. Chichester-Wiley.

[104] Torrance, J.K. (1987), "Shear Resistance of Remoulded Soils by Viscometric and Fall-cone Methods: A comparison for Canadian Sensitive Marine Clays," Can. Geotech. J., 24(2), 318-322.

[105] Townsend, F.C., and McVay, M.C. (1990), "SOA: Large Strain Consolidation Predictions," Journal of Geotechnical Engineering, Vol. 116, No. 2, 222-243.

[106] Tsuruya, H., Nakano, S., and Tanaka, J. (1986), "Investigation in Rheological Properties of Soft Muds with a Rotary Viscometer," Res. Report No. 566, Port and Harbor Research Institute, Ministry of Transport, Japan.

[107] Tuncay K., Kambham K.K.R., and Corapcioglu, M.Y. (1998), "Self-Weight Subsidence of Saturated Soft Porous Media," Journal of Engineering Mechanics-ASCE, Vol. 124, No. 6, 630-638.

[108] Umehara, Y., and Zen, K. (1980), "Constant Rate of Strain Consolidation for Very Soft Clayey Soils," Soils and Foundations, Vol. 20, No. 2, 33-65.

[109] Umehara, Y., and Zen, K. (1982), "Consolidation Characteristics of Dredged Marine Bottom Sediments with High Water Content," Soils and Foundations, Vol. 22, No. 2, 40-54.

[110] U.S. Navy (1971), "Soil Mechanics, Foundations, and Earth Structures," NAVFAC Design Manual DM-7, Washington, D.C.

[111] Wasti, Y. (1987), "Liquid and Plastic Limits as Determined from the Fall Cone and the Casagrande Methods," Geotechnical Testing Journal, Vol. 10, No. 1, 26-30.

[112] Williams, D.J. (1992), "Covering crusted tailings," Environmental issues and waste management in energy and minerals production, Balkema, Rotterdam, The Netherlands, 419-425.

[113] Williams, D.J., Wilson, G.W., and Currey, N.A. (1997), "A cover for a potentially acid forming waste rock dump in a dry climate," Proc. of 4th Int. Conf. on Tailings and Mine Waste, Balkema, Rotterdam, The Netherlands, 231-235.

[114] Wissa, A.E.Z., Christian, J.T., Davis, E.H., and Heiberg, S. (1971), "Consolidation Testing at Constant Rate of Strain," Journal of Soil Mechanics and Foundations, ASCE, vol. 97, no.10, pp. 1393-1413.

[115] Wood, D.M. (1985), "Some Fall Cone Tests," Geotechnique, Vol. 35, No. 1, 64-68.

[116] Wood, D.M. (1982), "Cone Penetrometer and Liquid Limit," Geotechnique, Vol. 32, No. 2, 152-157.

[117] Wroth, C.P. and Wood, D.M. (1978), "The Correlation of Index Properties with Some Basic Engineering Properties of Soils," Canadian Geotechnical Journal, Vol. 15, No. 2, 137-145.

[118] Yano, K., Watari, Y., and Yamanouchi, T. (1985), "Earthworks on soft clay grounsd using rope-netted fabrics," Proc. of Recent Developments in Ground Improvement Techniques, pp. 225-237.

[119] Yong, R.L., Siu, S.K.H., and Sheeran, D.E. (1983), "On the Stability and Settling of Suspended Solids in Settling Ponds (I): Piece-wise Linear Consolidation Analysis of Sediment Layer," Canadian Geotechnical Journal, Vol. 20, 817-826.

[120] Zakaria, N.A. (1994), "Construction of Supersoft Soils using Geogrids," PhD thesis, University of Newcastle Upon Tyne, U.K.

[121] Znidarcic, D. (1982), "Laboratory Determination of Consolidation Properties of Cohesive Soils," PhD Thesis, University of Colorado, Boulder.

[122] Zreik, D.A. (1991), "Determination of the Undrained Shear Strength of Very Soft Cohesive Soils by a New Fall Cone Apparatus," M.S. Thesis, Massachusetts Institute of Technology, Cambridge, Massachusetts, U.S.A.

[123] Zreik, D.A. (1994), "Behavior of Cohesive Soils and Their Drained, Undrained, and Erosional Strengths at Ultra-Low Stresses," Ph.D. Thesis, Massachusetts Institute of Technology, Cambridge, Massachusetts, U.S.A.

[124] Zreik, D.A., Krishnappan, B.G., Germaine, J.T., Madsen, O.S., and Ladd C.C. (1998), "Erosional and Mechanical Strengths of Deposited Cohesive Sediments," Journal of Hydraulic Engineering, Vol. 124, No. 11, 1076-1085.

[125] Zreik, D.A., Ladd, C.C., and Germaine, J.T. (2000), Discussion on "Yield Stress of Super Soft Clays." Journal of Geotechnical and Geoenvironmental Engineering, Aug. 2000, 1-3.

Chapter 6

PART II: Background

Suspended sediment influences the aquatic environment in a variety of ways. In addition to the capping concerns described in Chapter 1, the evolution of bottom topography, water clarity, transport of contaminants attached to fine particles, and development of stratigraphy are just a few examples of the areas where the study of suspended sediment has scientific and practical importance. A significant amount of research in this field has been devoted to understanding the processes controlling the sediment suspension and transport, so that models can be developed that are capable of predicting these processes.

A variety of methods have been employed to predict the suspended sediment behavior. They can be broadly categorized as steady-state analytical methods, time- and rate-dependent analytical methods, and numerical modeling.

The steady-state approach assumes equilibrium conditions that are representative of the long-term average conditions on the site. The suspended sediment concentration profiles and transport rates are calculated corresponding to a unique set of equilibrium conditions. Eyre *et al.* (1998), for example, used this approach to quantify the suspended sediment inputs and outputs to the Brisbane River estuary over an annual time scale. Rondeau *et al.* (2000) used a steady-state approach for estimating the influx of suspended sediment into the St. Lawrence River from its tributaries. Similarly, Jiang and Mehta (2000) assumed equilibrium conditions while performing a study of the annual sedimentation rates at a site in East China Sea. Since the results

of this approach can only be used as rough estimates, its use is limited to applications like sediment budgeting and long-term geo-morphological studies.

Of the three different types of approaches mentioned above, the numerical modeling techniques are known to provide the most accurate and detailed information. This is because the numerical techniques attempt to directly solve the hydrodynamic and mass transport equations. Fully 3-dimensional models have been developed for hydrodynamic and sediment suspension modeling (Celik and Rodi, 1988; Cancino and Neves, 1999; Wu *et al.*, 2000). However, the models are complex and incur high computational expenses. Their applicability, therefore, has been limited to only short-term simulations or demonstration purposes.

Attempts have been made to make numerical modeling more accessible by reducing their complexity. Several research efforts have focussed on the development of quasi-3-D suspended sediment models, where a 2-D depth-integrated sediment transport model is forced by the output of a fully 3-D hydrodynamic model. Recent notable efforts in this direction include Rakha (1998) and Lou *et al.* (2000). Rakha obtained a good agreement of model results for selected test cases in the surf zone, whereas Lou *et al.* were able to reproduce general patterns of turbidity in southern Lake Michigan. The authors noted that notwithstanding the efficiency of the quasi-3-D and 2-D models, important 3-D effects in sediment suspension and transport are missed due to the necessary depth-integration in these models.

In the absence of a simple theoretical solution or simple but accurate models for the time-dependent suspended sediment concentration, the commonly used sediment transport models continue to be based on the time- and rate-dependent analytical methods. The approach adopted in these models is still based on the equilibrium assumption, except that the results are obtained by marching the model through a time series of hydrodynamic events. Hence, features like tides and storms can be added to the model. The hydrodynamic time series needed to drive the model can either be obtained directly from the available historic data, or may be derived from the data by using standard simulation techniques. Examples of the former include research efforts of Trawle and Johnson (1986), Scheffner (1996), Nicholas and Walling

(1998), and Fang and Wang (2000). Recent Studies of suspended sediment transport based on simulated hydrodynamic conditions include the works of Liden (1999) and Prandle *et al.* (2000).

A common drawback of all the models mentioned above is that they do not account for the non-equilibrium effect in suspended sediment transport. Based on the scheme commonly adopted in coastal oceanographic models (Kachel and Smith, 1989; Lyne *et al.*, 1990; Harris and Wiberg, 1997; Zhang *et al.*, 1999; Styles and Glenn, 2000), the problem of suspended sediment transport is treated in a quasi-steady state manner. It is assumed that the residence time of the moving water column is greater than the response time of the suspended sediment in it. The suspended sediment in the column is consequently always in equilibrium with the bottom sediment concentration. For a control volume of interest, the sediment influx and outflux are determined from the equilibrium suspended sediment concentration profiles at the boundaries of the control volume, thereby giving the net deposition or removal rate of the sediment. Although this procedure allows a quick estimation of the magnitude of suspended sediment transport, it completely neglects the important effects associated with the non-equilibrium nature of the process.

Efforts have been made to account for the time dependence of suspended sediment concentration in a simple and accurate manner. Irie and Kuriyama (1988) have attempted to model the suspended sediment transport by dividing the vertical domain into several layers. While this layered model captures the unsteady nature of the process, it yields appreciable errors in the estimation of vertical flux. This is because a crude division of the vertical domain is not enough to represent the vertical gradients of sediment concentration. Nadaoka *et al.* (1991) proposed a simple quasi-numerical solution for non-equilibrium sediment concentrations, based on the assumption that the non-equilibrium concentration profile is similar in shape (exponential) to the equilibrium concentration profile. This assumption is approximate at best, and only at large enough times, leading to a limited applicability of their solution.

The objective of this work is to devise a simple analytical solution for suspended sediment transport that accounts for the response time of the water column. The

goal is to avoid the computational burden associated with complete numerical simulation, so that the resultant solution can be easily integrated into the commonly used sediment transport models. The following chapter describes the development of a simple analytical solution and a sediment transport model. The subsequent chapters are devoted to the applications of the model and discussion of the sediment transport results obtained by it.

Chapter 7

Description of Model

This chapter describes a type of physical systems where non-equilibrium effects in suspended sediment concentration can cause a sustained net mass transport. Theory is developed for obtaining the non-equilibrium profile of suspended sediment concentration in the water column. A perturbation solution is presented for the case where near-bottom reference sediment concentration varies linearly in space. Based on this solution, a simple Lagrangian model is formulated for estimating the net sediment transport rate due to the non-equilibrium effect. The following sections provide detailed description of the various aspects of this model.

7.1 The Physical system

The amount of sediment suspended in a water column is a function of the bottom sediment concentration as well as the turbulence level in the water column. This research effort identifies a physical system where a net suspended sediment transport is sustained exclusively due to the finite response time of the water column. This system is characterized by the presence of an oscillating current in a region of spatially varying near-bottom reference sediment concentration.

For a water column with finite response time, the concentration profile of suspended sediment at any given time is dependent on the column's history of bottom sediment concentration and turbulence intensity. The physical system described here

exhibits an asymmetry in the near-bottom sediment concentration around any given spatial location. Hence, for a particular water column that passes through a spatial location in course of its oscillatory motion, the concentration profiles of suspended sediment are not the same at the two times of passage through this location. This difference in suspended sediment concentration is the basis of a net suspended sediment transport across this spatial location.

7.2 Governing Equation and Assumptions

For a water column of finite depth, assumed to be moving at a uniform velocity and neglecting longitudinal diffusion and dispersion, the equation governing the sediment suspension is

$$\frac{\partial c}{\partial \tilde{t}} = \frac{\partial}{\partial \tilde{z}}(\nu \frac{\partial c}{\partial \tilde{z}}) + w_f \frac{\partial c}{\partial \tilde{z}} \tag{7.1}$$

where w_f is the fall velocity of the sediment. Adopting a time-varying eddy viscosity that is constant in $\tilde{z}$,

$$\frac{\partial c}{\partial \tilde{t}} = \nu \frac{\partial^2 c}{\partial \tilde{z}^2} + w_f \frac{\partial c}{\partial \tilde{z}} \tag{7.2}$$

The boundary conditions are the prescribed bottom sediment concentration:

$$c(0, \tilde{t}) = c_b \tag{7.3}$$

and no flux at water surface:

$$\nu \frac{\partial c(h, \tilde{t})}{\partial \tilde{z}} + w_f c(h, \tilde{t}) = 0 \tag{7.4}$$

where h is the water depth.

This system of equations is solved by using a perturbation technique, whereby the concentration is assumed to be in the form of a series, the space-dependent components of the series decreasing in geometric sequence.

Eq.(7.2) is non-dimensionalized as

$$\frac{\partial c}{\partial t} = \frac{\partial c}{\partial z} + \frac{\nu}{h w_f} \frac{\partial^2 c}{\partial z^2} \tag{7.5}$$

where

$$z = \frac{\tilde{z}}{h}$$

$$t = \tilde{t} \frac{w_f}{h}$$

The constant eddy diffusivity is taken equal to the depth-averaged value of the classical parabolic eddy viscosity for fully developed turbulent flow, i.e.

$$\nu = \frac{\kappa u_* h}{6 \; r} \tag{7.6}$$

The parameter r is equal to the ratio of the depth of the water column to the boundary layer thickness, and is set equal to 1 when the eddy diffusivity is averaged over the the entire depth of the water column. κ is the von Karman constant and has the value 0.4.

The shear velocity is assumed to vary according to

$$u_* = \sqrt{\frac{\tau_b}{\rho}} \tag{7.7}$$

where τ_b is the magnitude of bottom shear stress and ρ is the density of water. For an oscillating current, the shear velocity u_* is expected to vary sinusoidally, and is therefore written as:

$$u_* = u_{*m} |cos(\omega t)| \tag{7.8}$$

where

$$\omega = \tilde{\omega} \frac{h}{w_f} \tag{7.9}$$

$$u_{*m} = \sqrt{C_f} u_m \tag{7.10}$$

in which C_f is a bottom friction factor and u_m is the velocity amplitude of tidal motion. Eq.(7.8) unrealistically lets shear velocity drop to zero, an anomaly that is fixed by expanding the cosine function in a Fourier series and retaining only the first two terms, i.e.

$$|cos(\omega t)| = \frac{2}{\pi} + \frac{4}{3\pi} cos(2\omega t) + ... \tag{7.11}$$

Hence

$$u_* = u_{*m}(\frac{2}{\pi} + \frac{4}{3\pi} cos(2\omega t) + ...) \tag{7.12}$$

The shear velocity variation obtained by limiting this expansion to the first two terms is depicted in Figure 7.1. Thus the shear velocity has a certain cutoff, at approximately 20% of the peak value, which reflects the minimum turbulence level in the water column. It is only in the vicinity of $cos(\omega t) = 0$ that the shear velocity deviates significantly from the value obtained from Eq.(7.8).

From Eqs. (7.6) and (7.12), we get

$$\nu = \frac{\kappa h}{3r\pi} u_{*m}(1 + \frac{1}{3}e^{i2\omega t} + \frac{1}{3}e^{-i2\omega t} + ...) \tag{7.13}$$

where $i = \sqrt{-1}$ is the imaginary unit.

Substituting in Eq.(7.5) leads to

$$\alpha \frac{\partial c}{\partial t} = \alpha \frac{\partial c}{\partial z} + \frac{\partial^2 c}{\partial z^2} + \frac{1}{3}(e^{i2\omega t} + e^{-i2\omega t}) \frac{\partial^2 c}{\partial z^2} \tag{7.14}$$

where

$$\alpha = \frac{3r\pi w_f}{\kappa u_{*m}} \tag{7.15}$$

7.3 Mathematical Model

For a water parcel oscillating about its mean position with the excursion amplitude A_b, the motion is described by

$$x = \bar{x} + A_b sin(\tilde{\omega}\tilde{t}) \tag{7.16}$$

where $\bar{x}$ is the mean position of the column and $\tilde{\omega}$ is the angular frequency corresponding to the period.

A_b and $\tilde{\omega}$ are related by

$$A_b = \frac{u_m}{\tilde{\omega}} \tag{7.17}$$

where u_m is the velocity amplitude of motion. As a result of this motion, the water column experiences continuously changing sediment concentration at the bottom. Further since the shear velocity is dependent on the absolute velocity, the sediment carrying capacity of the water column also changes continually.

If, for simplicity, the bottom sediment concentration is assumed to increase linearly in x, then

$$c_b(x) = C_{b0} + \frac{dc_b}{dx}x \tag{7.18}$$

where C_{b0} is the sediment concentration at x=0. Eqs. (7.16) and (7.18) give

$$\begin{aligned} c_b(x) &= C_{b0} + \frac{dc_b}{dx}(\bar{x} + A_b sin(\tilde{\omega}\tilde{t})) \\ &= C_{b0} + \bar{c}_g + \tilde{c}_g sin(\tilde{\omega}\tilde{t}) \end{aligned} \tag{7.19}$$

where

$$\bar{c}_g = \frac{dc_b}{dx}\bar{x} \tag{7.20}$$

$$\tilde{c}_g = \frac{dc_b}{dx}A_b \tag{7.21}$$

Since the motion of the water parcel is known from Eq.(7.16), any given variation of bottom sediment concentration in space can be translated to a time-varying bottom boundary condition for suspended sediment in the column.

With the bottom sediment concentration given as a function of time, Eq.(7.19), the boundary conditions, Eqs. (7.3) and (7.4), can be written as

$$c(0,t) = C_{b0} + \bar{c}_g + \tilde{c}_g sin(\omega t) \tag{7.22}$$

$$\alpha c(1,t) + |\frac{\pi}{2}cos(\omega t)|\frac{\partial c(1,t)}{\partial z} = 0 \tag{7.23}$$

Substitution for the sine and cosine terms gives

$$c(0,t) = C_{b0} + \bar{c}_g + \frac{\tilde{c}_g}{2i}(e^{i\omega t} - e^{-i\omega t}) \tag{7.24}$$

$$\alpha c(1,t) + (1 + \frac{1}{3}e^{i2\omega t} + \frac{1}{3}e^{-i2\omega t} + ...)\frac{\partial c(1,t)}{\partial z} = 0 \tag{7.25}$$

where Eq.(7.11) has been used to substitute for the cosine term in Eq.(7.23).

The system of equations described by Eqs. (7.14), (7.24) and (7.25) is solved by assuming a solution of the harmonic form

$$c(z,t) = \sum_{n=-\infty}^{\infty} c_n(z)e^{in\omega t} \tag{7.26}$$

Substitution in Eq.(7.20) gives an equation for each value of n, from -∞ to ∞,

$$\begin{aligned} -in\omega\alpha c_n + \alpha\frac{\partial c_n}{\partial z} + \frac{\partial^2 c_n}{\partial z^2} + \frac{1}{3}(\frac{\partial^2 c_{n-2}}{\partial z^2} + \frac{\partial^2 c_{n+2}}{\partial z^2}) &= 0; \\ n &= 0, \pm 1, \pm 2, ... \end{aligned} \tag{7.27}$$

Boundary conditions on c_n for different values of n are obtained by substituting Eq.(7.26) in Eqs. (7.24) and (7.25) and then equating coefficients of the exponential terms. Eq.(7.24) leads to

$$c_0(0) = C_{b0} + \bar{c}_g \tag{7.28}$$

$$c_1(0) = \frac{\tilde{c}_g}{2i} \tag{7.29}$$

$$c_{-1}(0) = -\frac{\tilde{c}_g}{2i} \tag{7.30}$$

$$c_n(0) = 0; n \neq 0, \pm 1 \tag{7.31}$$

The condition for no flux at the surface, Eq.(7.25), reduces to

$$\begin{aligned} \alpha c_n(1) + \frac{\partial c_n(1)}{\partial z} + \frac{1}{3}(\frac{\partial c_{n-2}(1)}{\partial z} + \frac{\partial c_{n+2}(1)}{\partial z}) &= 0; \\ n &= 0, \pm 1, \pm 2, ... \end{aligned} \tag{7.32}$$

The solution to the governing equation, (7.27), can be obtained for a chosen number of values of n, with appropriate boundary conditions given by Eqs. (7.28)-(7.32). It can be observed that the governing equation, as well as the boundary conditions for any order n, are the complex conjugate of those for -n. Hence the solution for c_{-n} is the complex conjugate of that for c_n, and only one of them needs to be calculated.

We assume that each of the $c_n(z)$ terms in the series solution, Eq.(7.26), is a perturbation series given by

$$c_n = {c_n}^{(0)} + {c_n}^{(1)} + {c_n}^{(2)} + {c_n}^{(3)} + ... \tag{7.33}$$

where

$$\frac{{c_n}^{(1)}}{{c_n}^{(0)}} = \frac{{c_n}^{(2)}}{{c_n}^{(1)}} = O(\epsilon) \tag{7.34}$$

Further in accordance with Eq.(7.27), we expect that

$$\epsilon = O(\frac{1}{3}) \tag{7.35}$$

The governing equation, Eq.(7.27), now needs to be solved for each order in ϵ. The general equation for ${c_n}^{(m)}$ (i.e. the ϵ^m-term of the n-th harmonic) is

$$-in\omega\alpha{c_n}^{(m)} + \alpha\frac{\partial {c_n}^{(m)}}{\partial z} + \frac{\partial^2 {c_n}^{(m)}}{\partial z^2} + \epsilon(\frac{\partial^2 {c_{n-2}}^{(m-1)}}{\partial z^2} + \frac{\partial^2 {c_{n+2}}^{(m-1)}}{\partial z^2}) = 0;$$

$$\begin{aligned} n &= 0, \pm 1, \pm 2, ... \\ m &= 0, 1, 2, ... \end{aligned} \tag{7.36}$$

Further, ${c_n}^{(-1)} = 0$ for all n.

We solve for the first three terms (i.e., up to ϵ^2-terms) in each series of c_n, for n ranging from 0 to 4. The solutions for c_{-n} are the complex conjugates of the corresponding c_n solutions, as explained earlier. It is found that the ϵ^3- and higher order terms as well as the higher harmonics provide negligible refinement to the

solution. This fact is supported by the results of the series-based numerical solution that is described in Appendix A, and is discussed in section 7.6.

Note from Eq.(7.36) that an even harmonic is linked only to the other even harmonics, and similarly an odd harmonic is forced only by the other odd ones. This, coupled with the fact that the bottom boundary condition on c_n is zero for n > 1, Eqs. (7.28)-(7.31), shows that the system of equations for even harmonics is basically forced by c_0, and that similarly the first harmonic provides the forcing for all the other odd harmonics.

Since the governing equation is linear, we can consider each concentration term c_n to be a superposition of three solutions, as follows

$$c_n(z) = C_n(z) + \bar{c}_n(z) + \tilde{c}_n(z) \tag{7.37}$$

This is analogous to the manner in which the bottom boundary condition, Eq.(7.22), has been specified. C_n is the solution that satisfies the C_{b0} component of the bottom boundary condition. The $\bar{c}_n$ and $\tilde{c}_n$ solutions correspond, respectively, to the $\bar{c}_g$ and $\tilde{c}_g sin(\omega t)$ components of the boundary condition.

Since C_{b0} is constant, the C_n component of the solution is valid for a water column irrespective of its mean position. In contrast to this, Eq.(7.20) shows that the $\bar{c}_n$ component of the solution will depend on the mean position of the water column as well as the concentration gradient. Finally the $\tilde{c}_n$ terms provide the oscillatory component of the total solution.

The bottom boundary conditions, Eqs. (7.28)-(7.31), can be decomposed in terms of each component of c_n, i.e. in terms of C_n, $\bar{c}_n$ and $\tilde{c}_n$. For ϵ^1 and higher order terms in each harmonic, the bottom boundary condition is zero for all three components.

$$\left.\begin{array}{l} {C_n}^{(m)}(0) \\ \bar{c}_n^{(m)}(0) \\ \tilde{c}_n^{(m)}(0) \end{array}\right\} = 0; m \neq 0; all\ n \tag{7.38}$$

We further have

$$\left.\begin{array}{l} {C_n}^{(0)}(0) \\ \bar{c}_n^{(0)}(0) \end{array}\right\} = 0; n \neq 0 \tag{7.39}$$

and

$$\tilde{c}_n^{(0)}(0) = 0; n \neq 1 \tag{7.40}$$

The non-zero bottom boundary conditions exist only for the ϵ^0 terms of c_0 and c_1, and are as follows:

$${C_0}^{(0)}(0) = C_{b0} \tag{7.41}$$

$$\bar{c}_0^{(0)}(0) = \bar{c}_g \tag{7.42}$$

$$\tilde{c}_1^{(0)}(0) = \frac{\tilde{c}_g}{2i} \tag{7.43}$$

The surface boundary condition, Eq.(7.32), now applies to each component of c_n and can generally be written for ${c_n}^{(m)}$ as:

$$\alpha {c_n}^{(m)}(1) + \frac{\partial {c_n}^{(m)}(1)}{\partial z} + \epsilon\left(\frac{\partial {c_{n-2}}^{(m-1)}(1)}{\partial z} + \frac{\partial {c_{n+2}}^{(m-1)}(1)}{\partial z}\right) = 0 \tag{7.44}$$

7.4 Solution Strategy for Single Water Column

The solution for ${C_n}^{(m)}$ is presented here to demonstrate the technique. We start with ${C_0}^{(0)}$. The governing equation, (7.36), has no forcing terms for m = 0.

$$\alpha \frac{\partial {C_0}^{(0)}}{\partial z} + \frac{\partial^2 {C_0}^{(0)}}{\partial z^2} = 0 \tag{7.45}$$

Equation (7.41) provides the bottom boundary condition for ${C_0}^{(0)}$, and the surface boundary condition is given by Eq.(7.44) as:

$$\alpha {C_0}^{(0)}(1) + \frac{\partial {C_0}^{(0)}(1)}{\partial z} = 0 \tag{7.46}$$

The solution is:

$$C_0{}^{(0)} = C_{b0}e^{-\alpha z} \tag{7.47}$$

The equation to be solved for $C_0{}^{(1)}$ is:

$$\alpha\frac{\partial C_0{}^{(1)}}{\partial z} + \frac{\partial^2 C_0{}^{(1)}}{\partial z^2} + \epsilon(\frac{\partial^2 C_{-2}{}^{(0)}}{\partial z^2} + \frac{\partial^2 C_2{}^{(0)}}{\partial z^2}) = 0 \tag{7.48}$$

It can be seen that all $C_n{}^{(0)}$ terms will be zero for n$\neq$ 0, because of the zero bottom boundary condition, Eq.(7.39). Hence the forcing terms in the above equation are zero. Further, $C_0{}^{(1)}(0)$=0, from Eq.(7.38). This leads to

$$C_0{}^{(1)} = 0 \tag{7.49}$$

The equation for $C_0{}^{(2)}$ is:

$$\alpha\frac{\partial C_0{}^{(2)}}{\partial z} + \frac{\partial^2 C_0{}^{(2)}}{\partial z^2} + \epsilon(\frac{\partial^2 C_{-2}{}^{(1)}}{\partial z^2} + \frac{\partial^2 C_2{}^{(1)}}{\partial z^2}) = 0 \tag{7.50}$$

The forcing terms in this case are non-zero, and therefore need to be known before we can solve for $C_0{}^{(2)}$. Consider the equation for $C_2{}^{(1)}$ obtained from Eq.(7.36):

$$-i2\omega\alpha C_2{}^{(1)} + \alpha\frac{\partial C_2{}^{(1)}}{\partial z} + \frac{\partial^2 C_2{}^{(1)}}{\partial z^2} + \epsilon(\frac{\partial^2 C_0{}^{(0)}}{\partial z^2} + \frac{\partial^2 C_4{}^{(0)}}{\partial z^2}) = 0 \tag{7.51}$$

$C_4{}^{(0)}$ is zero and $C_0{}^{(0)}$ is known from Eq.(7.47). Hence Eq.(7.51) can be solved to get $C_2{}^{(1)}$. It is further known that $C_{-2}{}^{(1)}$ is complex conjugate of $C_2{}^{(1)}$. This makes it possible to solve Eq.(7.50) for $C_0{}^{(2)}$. This back-and-forth solving for terms in alternate harmonics can thus be continued.

The procedure is exactly similar for the $\bar{c}_n^{(m)}$ terms in the even harmonics. The $\bar{c}_0^{(0)}$ solution drives the other harmonics, and the solution is:

$$\bar{c}_0^{(0)} = \bar{c}_g e^{-\alpha z} \tag{7.52}$$

For the odd harmonics, the oscillatory component ($\tilde{c}_1^{(0)}$) is the only term having a non-zero bottom boundary condition. This first harmonic term provides forcing for all the other odd harmonics. The governing equation for ($\tilde{c}_1^{(0)}$) is:

$$-i\omega\alpha\tilde{c}_1^{(0)} + \alpha\frac{\partial\tilde{c}_1^{(0)}}{\partial z} + \frac{\partial^2\tilde{c}_1^{(0)}}{\partial z^2} = 0 \tag{7.53}$$

The bottom boundary condition is Eq.(7.43), and the surface boundary condition, Eq.(7.44), is:

$$\alpha\tilde{c}_1^{(0)}(1) + \frac{\partial\tilde{c}_1^{(0)}(1)}{\partial z} = 0 \tag{7.54}$$

The solution is:

$$\tilde{c}_1^{(0)} = \frac{\tilde{c}_g}{2i}(Ae^{r_{1+}z} + Be^{r_{1-}z}) \tag{7.55}$$

where

$$\begin{aligned}
r_{1+} &= -\frac{\alpha}{2} + \sqrt{\frac{\alpha^2}{4} + i\omega\alpha} \\
r_{1-} &= -\frac{\alpha}{2} - \sqrt{\frac{\alpha^2}{4} + i\omega\alpha} \\
B &= \frac{(\alpha + r_{1+})e^{r_{1+}}}{(\alpha + r_{1+})e^{r_{1+}} - (\alpha + r_{1-})e^{r_{1-}}} \\
A &= -\frac{(\alpha + r_{1-})e^{r_{1-}}}{(\alpha + r_{1+})e^{r_{1+}} - (\alpha + r_{1-})e^{r_{1-}}}
\end{aligned}$$

Back-and-forth solving between the first and the third harmonics leads to the solution of the desired number of terms.

Once all the three components of $c_n(z)$ are calculated for each harmonic of a particular water column, the concentration profiles can be computed at any specified time for this column, by using Eq.(7.26). As described in the following section, this makes it possible to calculate the total sediment transport rate at any given spatial location in the physical system.

7.5 Sediment Flux Across a Given Spatial Location

A schematic of concentration gradient and distribution of water columns is shown in Figure 7.2. We are interested in finding the net sediment transport rate at a given crossection, located at x=0 and characterized by a given bottom sediment concentration C_{b0}. The concentration gradient is $\frac{dc_b}{dx} = \frac{C_h - C_l}{4A_b}$, where C_h and C_l, respectively, denote the high and the low ends of the bottom sediment concentration gradient and A_b denotes the excursion amplitude of the oscillating water columns.

It is clear that in order to determine the transport rate through x=0, we need to consider only those water parcels whose mean position is within the distance A_b of x=0, i.e.

$$|\bar{x}| < A_b \tag{7.56}$$

The motion of all other water columns does not affect the sediment transport at x=0 because these columns never pass through this point.

For a water column with mean position $\bar{x} < A_b$, the motion is described by Eq.(7.16). Hence the two times t_u and t_d can be calculated when this water column will pass through x=0, once going in positive x-direction (up-gradient) and once in the negative direction (down-gradient). The velocity of the water column has the same magnitude but opposite directions at the times of these two passings. However, the 0 sediment concentration profiles at these two times may be different, due to the finite response time of the water column. The sediment transport vector is given as the product of the column velocity and the suspended sediment concentration. With the solution for suspended sediment concentration as a function of time, Eq.(7.26), we can find the total amount of sediment suspended in the water column at these two different instants. The difference in the amounts, multiplied by the velocity of the water column represents the net sediment flux across x=0, caused due to the motion of the particular water column under consideration. When all such water columns have been considered, the sum of their individual contributions constitutes the net

sediment flux across x=0, evaluated over one oscillation period.

For the purpose of our Lagrangian analysis, we divide the region $|\bar{x}| < A_b$ (Figure 7.2) into 20 water parcels. Instead of specifying the water columns such that their mean positions are uniformly spaced in the region $|\bar{x}| < A_b$, we specify them such that they pass through x=0 at regular intervals. Hence the interval between passing of two water columns at x=0 is $\frac{T}{40}$, where T is the tidal period.

This discretization of water parcels which contribute to the sediment transport at x=0 is crucial, since water parcels located at different mean positions will contribute differently to the transport through crossection x=0. It was found that 20 water parcels suffice, and further increasing the number of water parcels did not provide any incremental gains in accuracy.

The order of these 20 columns has been indicated in Figure 7.2 by their mean positions, which coincide with their position at time t=0. Since the time interval between passing of any two consecutive columns through x=0 is constant, the time of the up-gradient passage (t_u) and the down-gradient passage (t_d) for each column through x =0 can be calculated as follows:

For columns with $\bar{x} < 0$:

These columns (numbered 0 to 10 in Figure 7.2) start moving in the up-gradient direction at t=0. For a column numbered k,

$$t_u = (10 - k)\frac{T}{40}; 0 \leq k \leq 10 \tag{7.57}$$

As illustrated in Figure 7.3, the times of up-gradient and down-gradient passage for these columns are symmetric around the time when they reach their extreme up-gradient position. The time for extreme up-gradient position is $\frac{T}{4}$. Hence the time of down-gradient passage is:

$$\begin{aligned} t_d &= \frac{T}{4} + (\frac{T}{4} - t_u) \\ &= (10 + k)\frac{T}{40}; 0 \leq k \leq 10 \end{aligned} \tag{7.58}$$

For columns with $\bar{x} > 0$:

These columns (numbered 11 to 20 in Figure 7.2) start moving in the up-gradient direction at t=0, reach their extreme position at t=$\frac{T}{4}$, and then pass through x=0 in the down-gradient direction (Figure 7.3). For a column numbered k,

$$\begin{aligned} t_d &= \frac{T}{2} + (k-10)\frac{T}{40} \\ &= (10+k)\frac{T}{40}; 10 \leq k \leq 20 \end{aligned} \tag{7.59}$$

For these columns the times of up-gradient and down-gradient passage are symmetric around the time they reach their extreme down-gradient position, i.e. around $\frac{3T}{4}$. Hence the time of up-gradient passage is:

$$\begin{aligned} t_u &= \frac{3T}{4} + (\frac{3T}{4} - t_d) \\ &= (50-k)\frac{T}{40}; 10 \leq k \leq 20 \end{aligned} \tag{7.60}$$

The mean position $\bar{x}$ for the columns is given by

$$\bar{x} = -A_b sin(\frac{2\pi}{T} t_u) \tag{7.61}$$

The bottom sediment concentration at the mean position of the column is given by

$$c_b(\bar{x}) = C_{b0} + \bar{x}\frac{dc_b}{dx} \tag{7.62}$$

With the characterizing parameters for a water column given by Eqs. (7.55)-(7.60), it is possible to calculate the difference in the suspended sediment amounts for each column, at the times t_u and t_d. This difference, multiplied by the velocity of that column at the time of passage through x=0, denotes a sediment transport rate. This transport rate can be seen to be effective at x=0, for a duration equal to the time-interval between passage of consecutive columns, i.e. $\frac{T}{40}$ in the present case. The value of this transport rate is calculated for each of the 20 columns to get the net amount of sediment transported during one oscillation period.

7.6 Results

The mutually exclusive coupling of even and odd harmonics is an important feature of the physical system presented here. The zeroth harmonic provides the forcing for all even harmonics. The solutions for all even harmonics therefore will have two non-zero components, the C_n solution corresponding to Eq.(7.47) and the $\bar{c}_n$ solution corresponding to Eq.(7.52).

For a given water column, the zeroth harmonic is time-invariant by definition. It contributes to the instantaneous value of the suspended sediment load of the water column, but its value is the same at times of up-gradient and down-gradient passages. Although this harmonic contributes nothing to the net transport and is therefore of no direct interest, it determines the forcing for even harmonics.

Figure 7.4 shows the Lagrangian variation of the suspended sediment load with time, corresponding to the C_n component of the second harmonic, for columns 6 and 14. This quantity is obtained by integrating over depth all the terms in the C_2(z) solution. Note that the variation is the same for both columns. This is expected because the C_n component of the solution corresponds to the C_{b0} bottom boundary condition, which is constant for all the columns. This also means that the C_4(z) solution will be the same for all columns, since C_n solutions for all even harmonics are eventually forced by the C_0 solution.

Due to the symmetric location of the water columns about x=0, the oscillatory motion of a given water column is exactly replicated in the opposite sense by another column situated symmetrically across x=0 (see Figure 7.3). Columns 6 and 14 constitute one such pair. Their velocities at the times of passage through x=0 are therefore the same. Furthermore, the C_2 solution is identical for all the columns. The result is that the sediment load for column 6 at the time of up-gradient passage is the same as that for column 14 at the time of down-gradient passage, and vice versa. This is illustrated in Figure 7.4, where N_u and N_d respectively refer to the times of up-gradient and down-gradient passage, for column N. It can now be seen that the C_2 contribution of column 6 to the total transport at x=0 will be identically cancelled by

the C_2 contribution of column 14. The same is true for the C_4 solution. This identical cancellation of C_n contributions to the net transport happens for all the columns, and consequently the C_n solution has zero contribution to the net transport across x=0. The net transport therefore does not depend on the value of C_{b0}.

The $\bar{c}_n$ solution, although similar to the C_n solution, depends on the mean position and is different for each column. The transport due to this term therefore does not get cancelled out completely. This solution constitutes the only contribution of the even harmonics to the net transport. Note from Eq.(7.5) that this contribution is proportional to the concentration gradient.

The forcing for all odd harmonics arises from the first harmonic. Since the first harmonic solution is proportional to the concentration gradient, Eq.(7.6), this feature will be reflected in all the odd harmonics. Their contribution to the net transport will consequently be proportional to the concentration gradient.

The above discussion leads to the result that the net transport across the spatial location x = 0 is proportional to the spatial gradient of the bottom sediment concentration and does not depend on the value of C_{b0}. The results presented in this section are based on the following choice of parameters, unless otherwise stated: u_m = 1 m/s; $\omega = 2\pi/(12.2$ hrs) corresponding to tidal motion; h= 10m; w_f = 0.01 m/s, corresponding to quartz sand of approx. 0.1 mm diameter; C_f = 0.0025 and $\frac{dc_b}{dx}$ = 7.3 x 10^{-5} kg/m^4. The value of bottom sediment concentration at x = 0 is nominally chosen to be C_{b0}= 1 kg/m^3. It should be noted that although the magnitude of C_{b0} does not affect the net transport across the location x = 0 over one oscillation period, it influences the total amount of suspended sediment in the water column at any given time.

Equation (7.5) suggests that a single $\bar{c}_n$ solution will be valid for all the columns if it is normalized by the mean position of the water column. Figure 7.5 shows the variation of the suspended sediment load with time, corresponding to the $\bar{c}_2$ solution, for column 20. Note that for this column, $\frac{\bar{x}}{A_b}$=1. The $\bar{c}_2$ solution for any other column can be obtained from this curve by multiplying with the appropriate value of $\frac{\bar{x}}{A_b}$. For purpose of illustration, Figure 7.6 shows the $\bar{c}_2$ solutions for columns 6 and

14, obtained in this manner. The times of up-gradient and down-gradient passage are known for each column, and are indicated in the figure.

At both up-gradient and down-gradient passages, column 6 has negative sediment load corresponding to $\bar{c}_2(z)$. Column 14 has positive sediment load at both instants. Due to symmetry, the sediment load of column 6 at up-gradient passage is equal in magnitude to that of column 14 at down-gradient passage, although opposite in sign. Similarly, the sediment load of column 6 at down-gradient passage is equal and opposite in sign to that of column 14 at up-gradient passage. The difference in sediment loads at the times of up-gradient and down-gradient passage is therefore the same for both the columns. Further since columns 6 and 14 have the same velocity when they pass through x=0, they contribute equally to the net up-gradient sediment transport through x=0. By knowing the times of passage of each such column pair through x=0, the transport rate due to the $\bar{c}_2$ terms can be calculated for all the columns. The procedure is exactly the same for transport due to the $\bar{c}_4$ solution.

The C_n and $\bar{c}_n$ components of concentration are zero for the odd harmonics. From Eqs. (7.6) and (7.55), it can be inferred that the first harmonic solution $\tilde{c}_1$ is the same for all the columns. Figure 7.7 shows this solution. The times of up-gradient and down-gradient passages are depicted in the figure for columns 6 and 14, as an example. Notice that although the sediment loads at the times of up-gradient and down-gradient passage for a given column appear to be same, they actually are not so. There is a small but discernible phase shift that causes these loads to be different, hence causing a net transport.

The sediment load corresponding to $\tilde{c}_1$ (z) is positive for column 6, at both up-gradient and down-gradient passages. The opposite is true for column 14. Again due to symmetry, the sediment loads for column 6 at times of up-gradient and down-gradient passage are equal and opposite in sign to the sediment loads for column 14 at the times of down-gradient and up-gradient passage, respectively. The contributions of these columns to the net transport rate are therefore the same. This similarity in contribution is featured by all the symmetric column pairs, and hence the transport calculation is done for 10 column pairs, instead of 20 columns, to get the net up-

gradient transport over one oscillation period. The procedure is repeated to find the transport arising from the third harmonic (the $\tilde{c}_3$ terms).

Having examined the behavior of each component of the solution, we now look at the actual sediment concentration profiles. Figure 7.8 shows the suspended sediment concentration profiles at the times of up-gradient and down-gradient passage through x=0, for columns 6 and 14. The difference in the amount of sediment suspended in the column at the two instances is clearly noticeable, and represents a net sediment transport. The difference in the amount of suspended sediment is about 8% of the total suspended sediment for column 6 and about 11% for column 14. For column 6, the profile at the time of up-gradient passage is fuller than the one at the time of down-gradient passage, and hence will cause a net up-gradient sediment transport. The opposite is true for column 14.

It should be noted that the two concentration profiles are different basically due to the finite response time of water column. The equilibrium sediment concentration profile, which would have resulted from the assumption of an instantaneous response, lies in between the two curves shown, and is the same for up-gradient and down-gradient passages.

As explained earlier, the constantly changing sediment concentration at the bottom acts as a forcing imposed on the water column, which in turn responds with a finite lag. In addition to this, the suspension capacity of the water column is not constant, since it is a function of the shear velocity, which varies according to Eq.(7.18). The complicated interaction of the time-varying boundary condition and the shear velocity results in the situation where the total amount of suspended sediment is a function of the history of the water column. Hence we expect that different water columns will contribute differently to the net sediment transport at x=0.

Referring to Figure 7.2, beginning at t=0, an observer at x=0 sees columns 10-1 passing in the up-gradient direction, followed by columns 1-20 coming in the down-gradient direction, and then columns 20-11 going in the up-gradient direction. Computing the instantaneous transport rate as the product of suspended sediment amount and the velocity of the water column, we can obtain the variation of this transport

rate at the location x = 0 as a function of time. Figure 7.9 depicts this variation.

The net up-gradient transport rate can be calculated as the difference in transport rates at the two times a column passes through x = 0. Figure 7.10 shows this net transport rate for different columns, plotted for each column, at that time in the oscillation period when it traverses the point x = 0 in the down-gradient direction. Integration of this curve over the oscillation period gives a negative net up-gradient transport, and we note that not all columns contribute equally to this net sediment transport across the location x = 0.

Although the oscillatory motion is the same for all columns, the contribution of each column to the net up-gradient transport is different, and is positive for some (columns 1-8 cause net up-gradient transport, in the case shown), and negative for the others (columns 9-19 cause net down-gradient transport). Further, the variation of the amount of sediment transport is not simply related to the variation of the bottom sediment concentration. Nevertheless, the results can be physically explained if the time-varying shear velocity and the finite response time of the water column are taken into account.

Consider the two water columns, numbered 6 and 14, for which results have been presented in Figures 7.4,7.6,7.7, and 7.8. Both columns experience increasing sediment concentrations at the bottom as they pass through x = 0 in the up-gradient direction, and decreasing concentrations in the opposite direction.

The time of up-gradient passing of column 6 at x=0 is t_s=0.1T, Eq.(7.57). It can be seen from Figure 7.1 that in the interval preceding this instant, column 6 has high shear velocity and therefore is near its peak capacity to suspend sediment. The situation is different at the time of down-gradient crossing t_s=0.4T, Eq.(7.58). Although the bottom sediment concentrations experienced by this column in the interval preceding t_s=0.4T are higher, the shear velocity during this interval is much lower, and therefore this column is not able to suspend a proportionately higher amount of sediment. The net effect is a total up-gradient transport, despite the lower bottom sediment concentrations on the down-gradient side of the estuary inlet.

In contrast to this, when column 14 crosses the inlet in the up-gradient direction at

t_s=0.9T, Eq.(7.60), it has experienced both low bottom sediment concentrations and low shear velocities in the preceding period. Conversely, the time of down-gradient passage, t_l=0.6T, Eq.(7.59), is preceded by both high bottom sediment concentrations and high shear velocities. The high sediment concentrations on the up-gradient side are therefore duly reflected in the suspended sediment profile, which is richer than the profile at the instant of up-gradient crossing, causing a net down-gradient sediment transport.

Whether a given column creates down-gradient or up-gradient transport and the magnitude of its contribution to the total sediment transport are governed by the sediment fall velocity and the bottom concentration gradient, for a given water depth and oscillation velocity amplitude.

As mentioned in Section 7.1, only the first 4 harmonics (n=1 to n=4, in Eq.(7.26)) were used to derive the concentration profiles for each column. Further, the perturbation series for each harmonic was calculated only up to ϵ^2 terms, with the assumption that higher order terms have negligible contribution. Figure 7.11 shows that the variation of net up-gradient transport rate across x = 0 with time is basically defined by the first and the second harmonics. Although the addition of higher harmonic terms influences this variation, the quantity of interest is the net transport integrated over the oscillation period. We found this integrated transport to be comprised almost entirely of the first and the second harmonic terms, with less than 0.1% of the contribution coming from the third or the fourth harmonic.

The negligible effect of higher harmonics is demonstrated also in the total suspended sediment load of a water column. Figure 7.12 depicts the Lagrangian variation of the depth integrated sediment concentration ($\int cdz$) with time for columns 6 and 14. The addition of fourth harmonic does not have any significant effect on either the total amount of suspended sediment or its variation with time. This fact is further corroborated by the results of the series solution which is discussed in Appendix A. Fourier spectrum of the depth integrated sediment concentration ($\int cdz$) obtained from the series solution showed the amplitude of the fifth harmonic to be less than 1% of that of the zeroth harmonic.

The magnitude of sediment transport corresponding to different sediment fall velocities and different water depths is shown in Table 7.1. All other parameters are the same as stated earlier. The number W in the table corresponds to the amount (in tons) of the sediment transported in per unit width of flow, per oscillation period. We see that the mechanism discussed here can transport large amounts of sediment.

The response of the water column to a change in the bottom boundary condition depends on the effective depth of the column that is influenced by the changes in the sediment concentration. As the fall velocity decreases, the lighter sediment is able to reach higher into the water column. The effective depth therefore increases with decreasing fall velocity, to the limit where the whole water column participates in the process. For w_f=0.01 m/s, the effective depth is relatively small (See Figure 7.8). The response of the column is therefore fast. For lower values of w_f, the response of the water column is slower, leading to higher phase lag and consequently higher transport rate. The transport rate is therefore seen to be increasing with decreasing fall velocity. The same effect causes the transport rate to increase with increasing depth, because the effective depth participating in the sediment suspension process increases with increasing depth. The effect of different parameters on the net suspended sediment transport rate is examined in detail in Chapter 9.

Table 7.1: Sediment Transported (per unit width) at x=0, tons per meter per period

w_f,m/s	Sediment Influx W, tons/meter/period		
	5m depth	10m depth	20m depth
0.01	0.23	0.92	3.59
0.005	0.97	3.78	13.60
0.0025	2.22	8.25	27.10
0.00125	3.19	11.66	37.28
0.0001	4.02	15.10	49.61

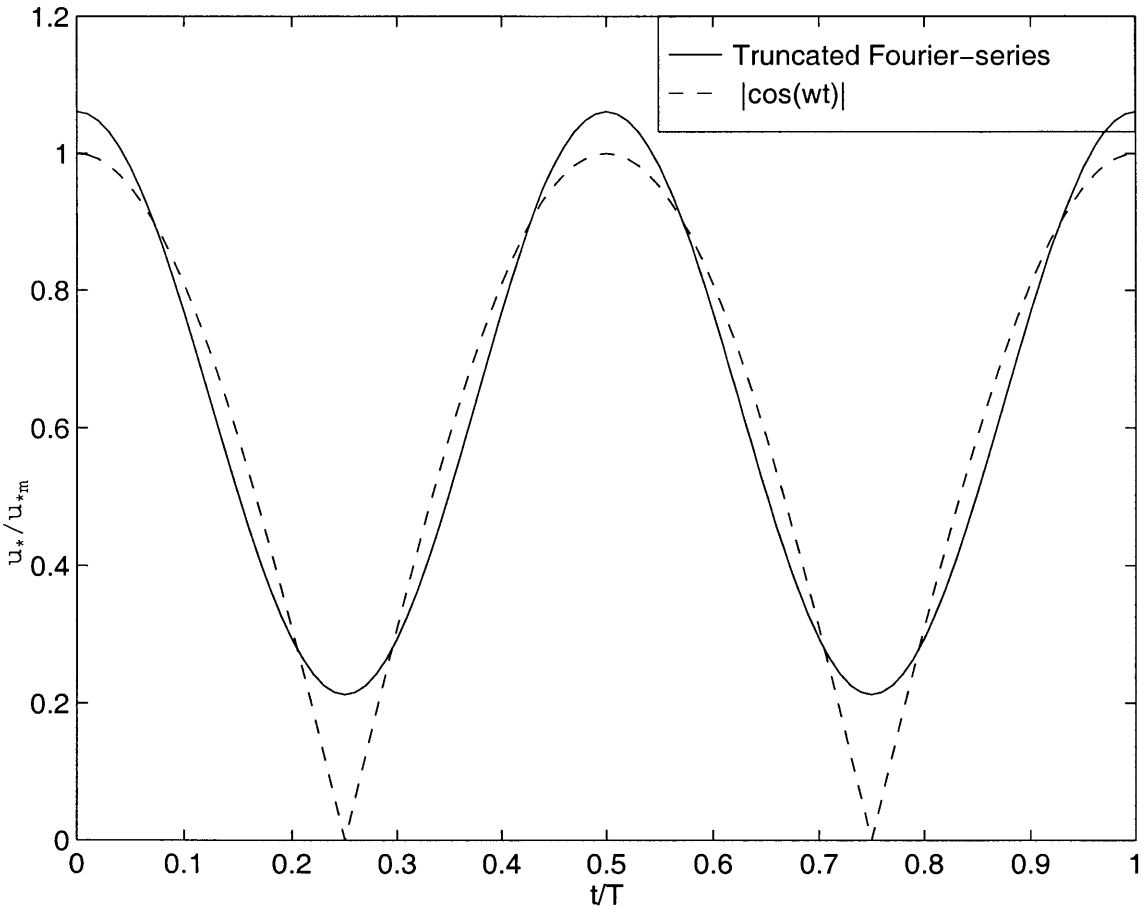

Figure 7-1: Variation of Shear velocity during the oscillation period

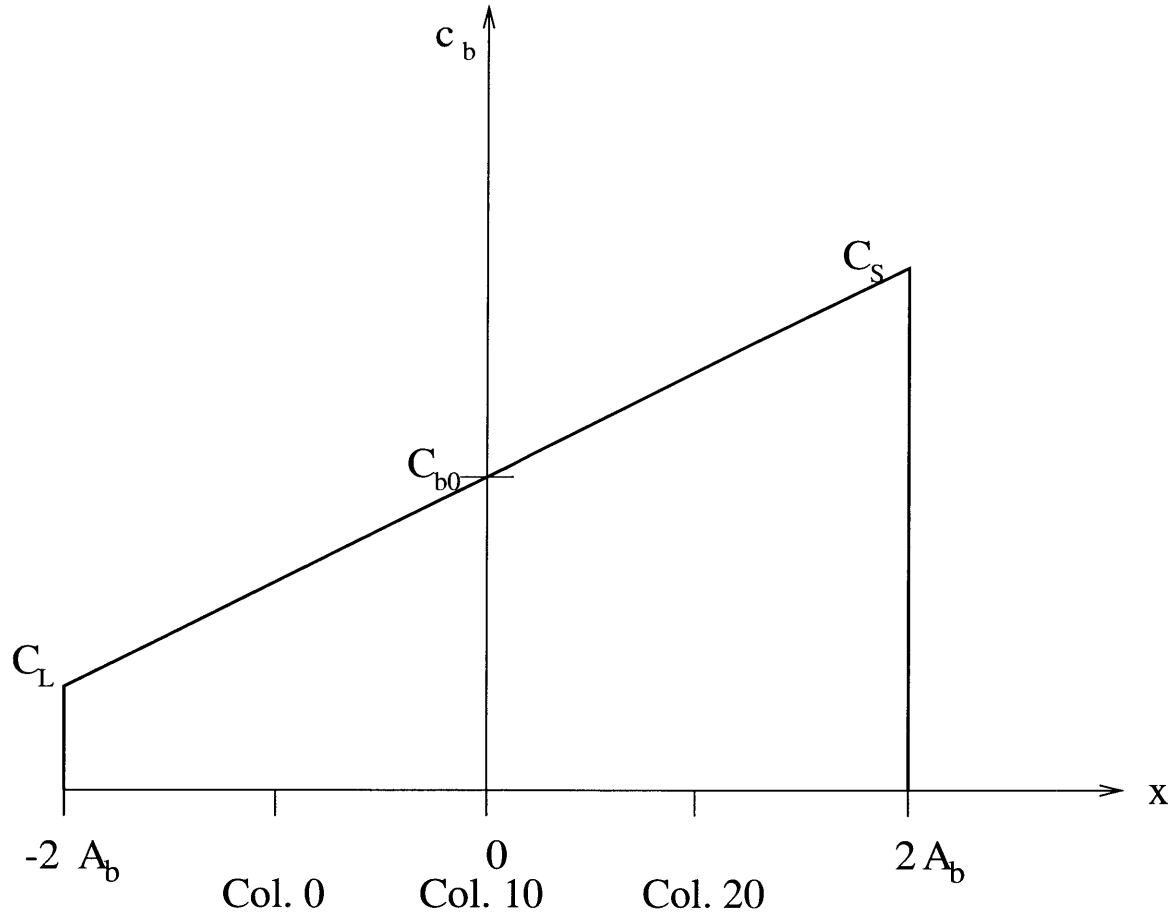

Figure 7-2: Bottom Sediment Concentration Distribution

Columns with $\bar{x} < 0$:

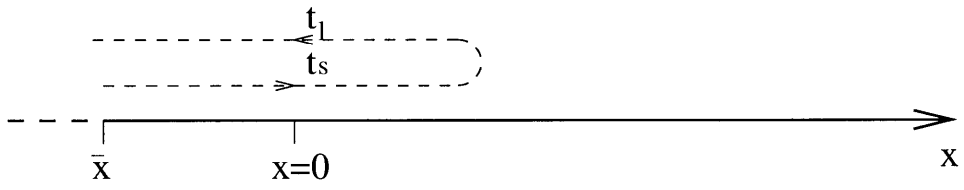

Columns with $\bar{x} > 0$:

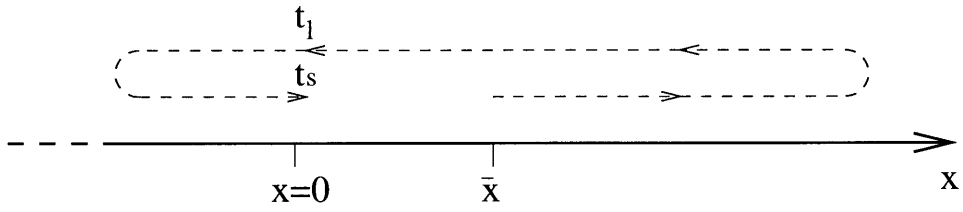

Figure 7-3: Passage times for different columns at x=0

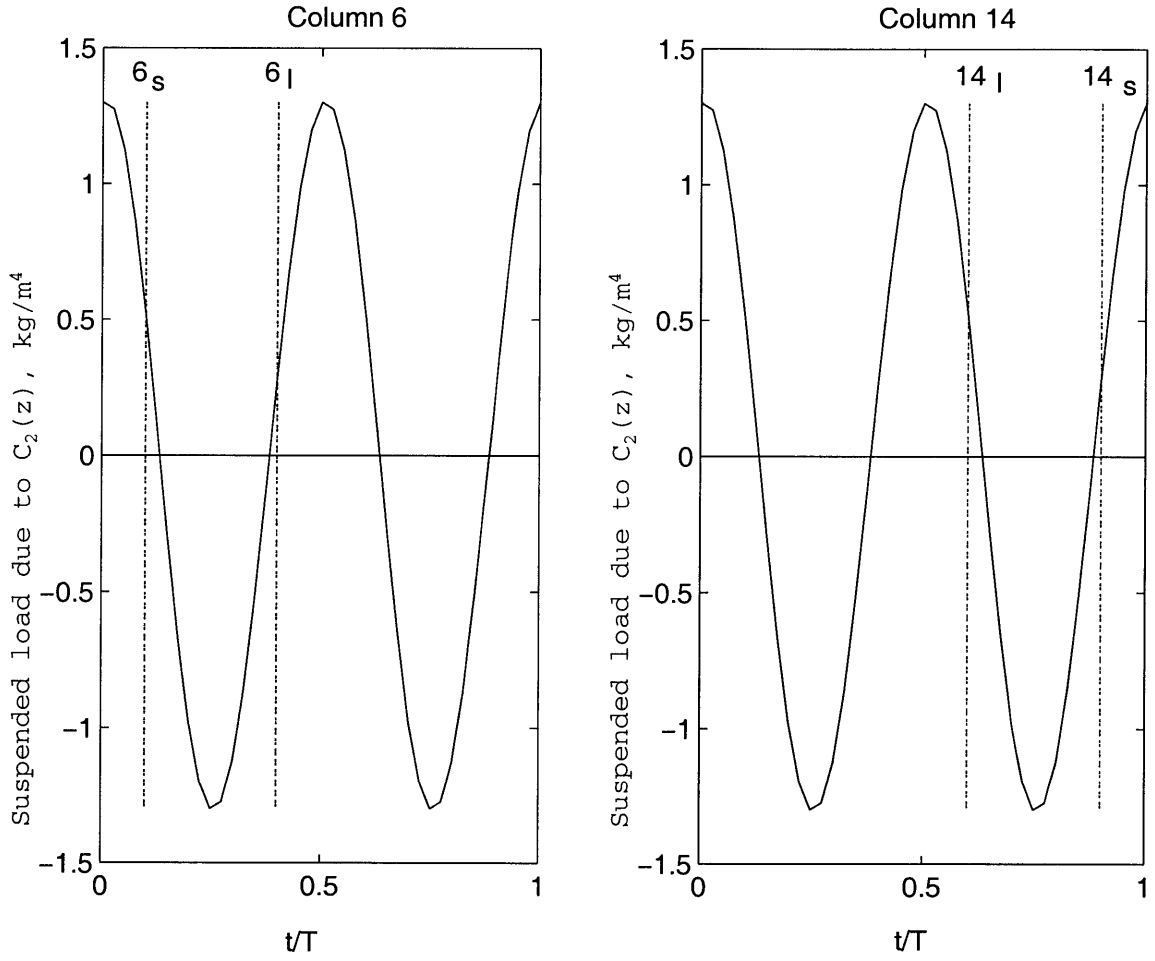

Figure 7-4: Variation of Suspended Sediment Load due to C_2(z), for columns 6 and 14

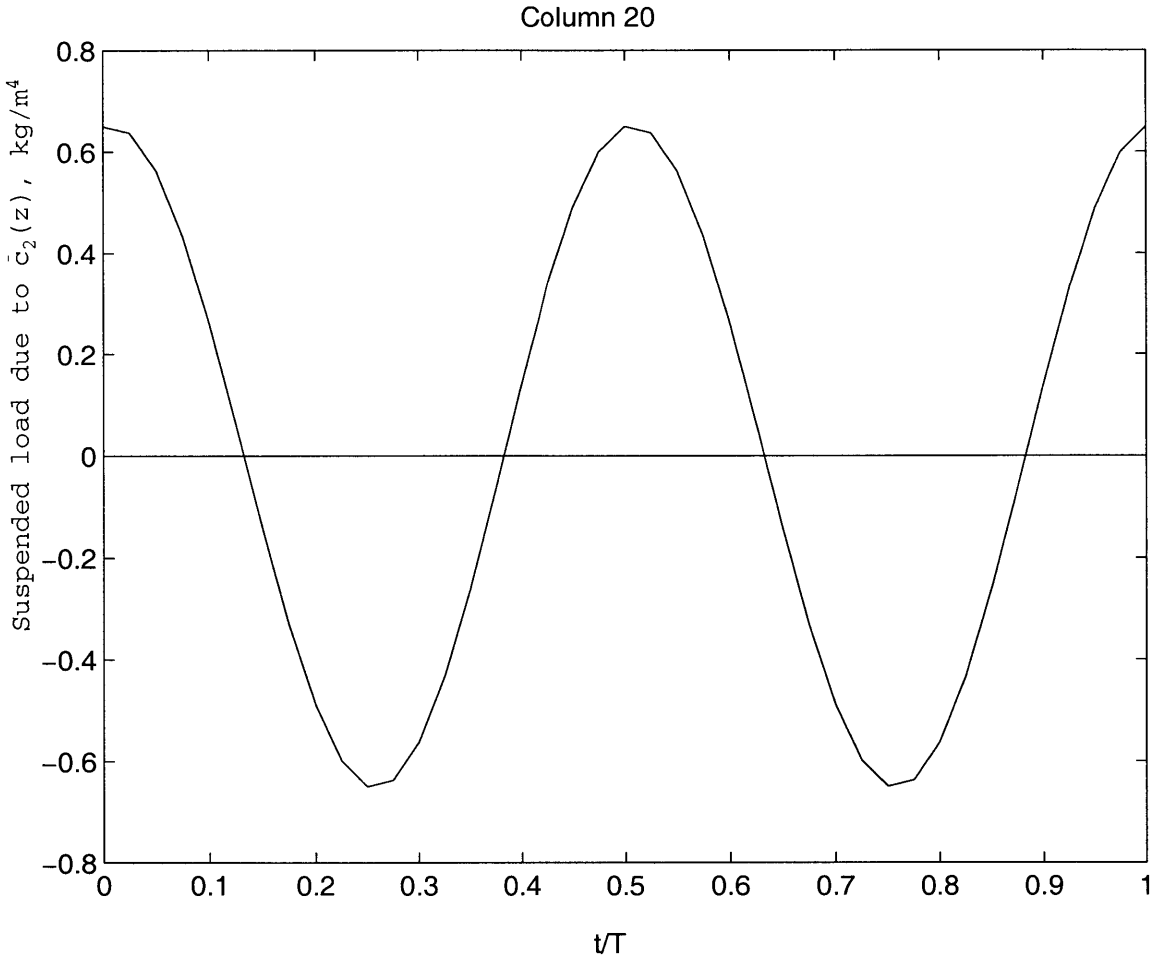

Figure 7-5: Variation of Suspended Sediment Load due to $\bar{c}_2(z)$, for column 20

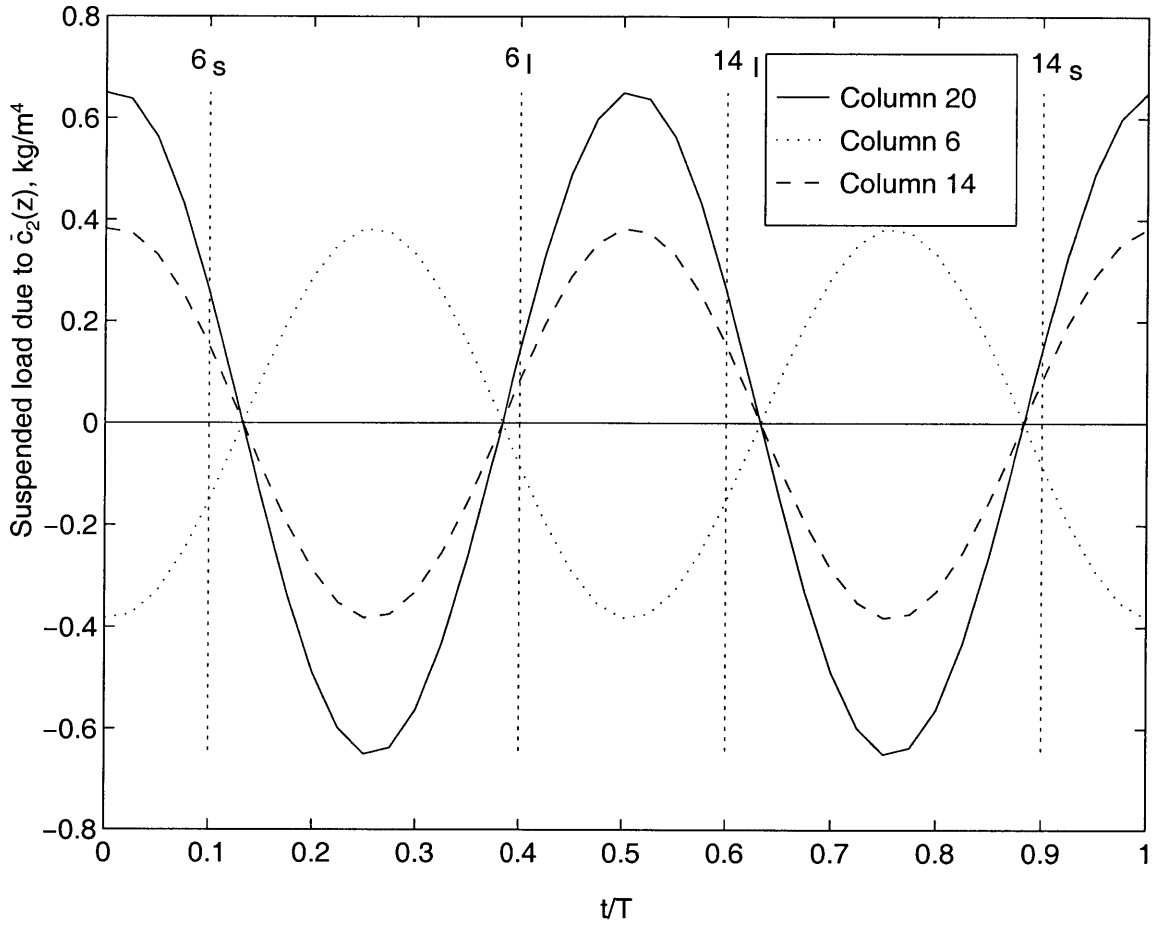

Figure 7-6: Variation of Suspended Sediment Load due to $\bar{c}_2(z)$, for columns 6 and 14, as derived from column 20

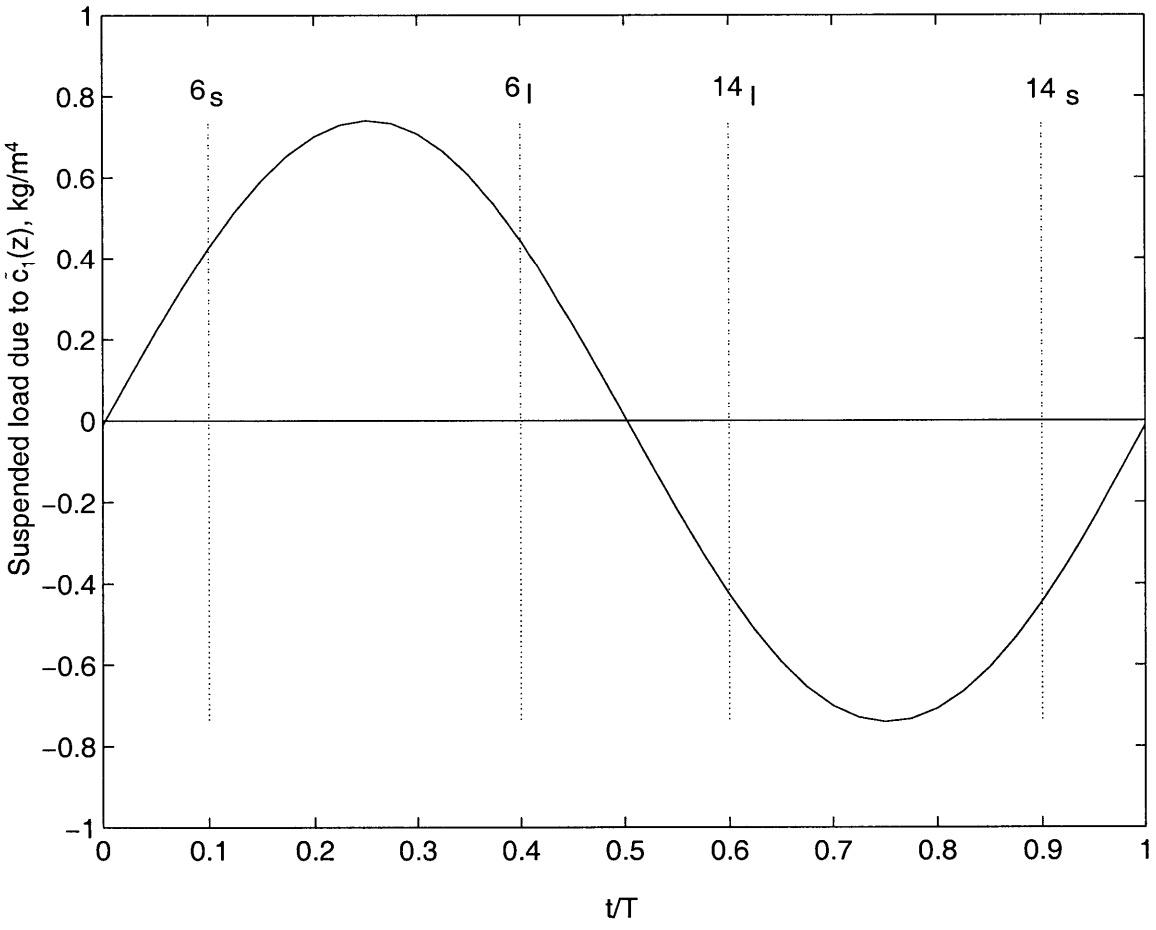

Figure 7-7: Variation of Suspended Sediment Load due to $\tilde{c}_1(z)$

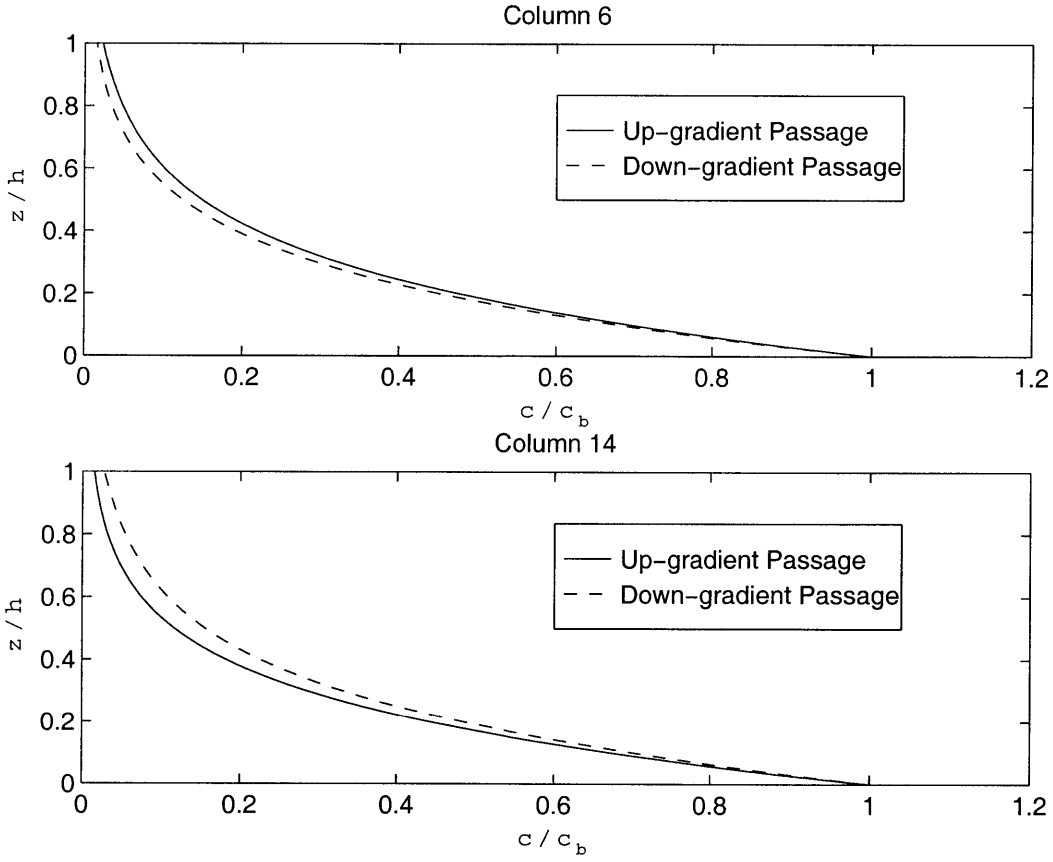

Figure 7-8: Suspended Sediment profiles for columns 6 and 14

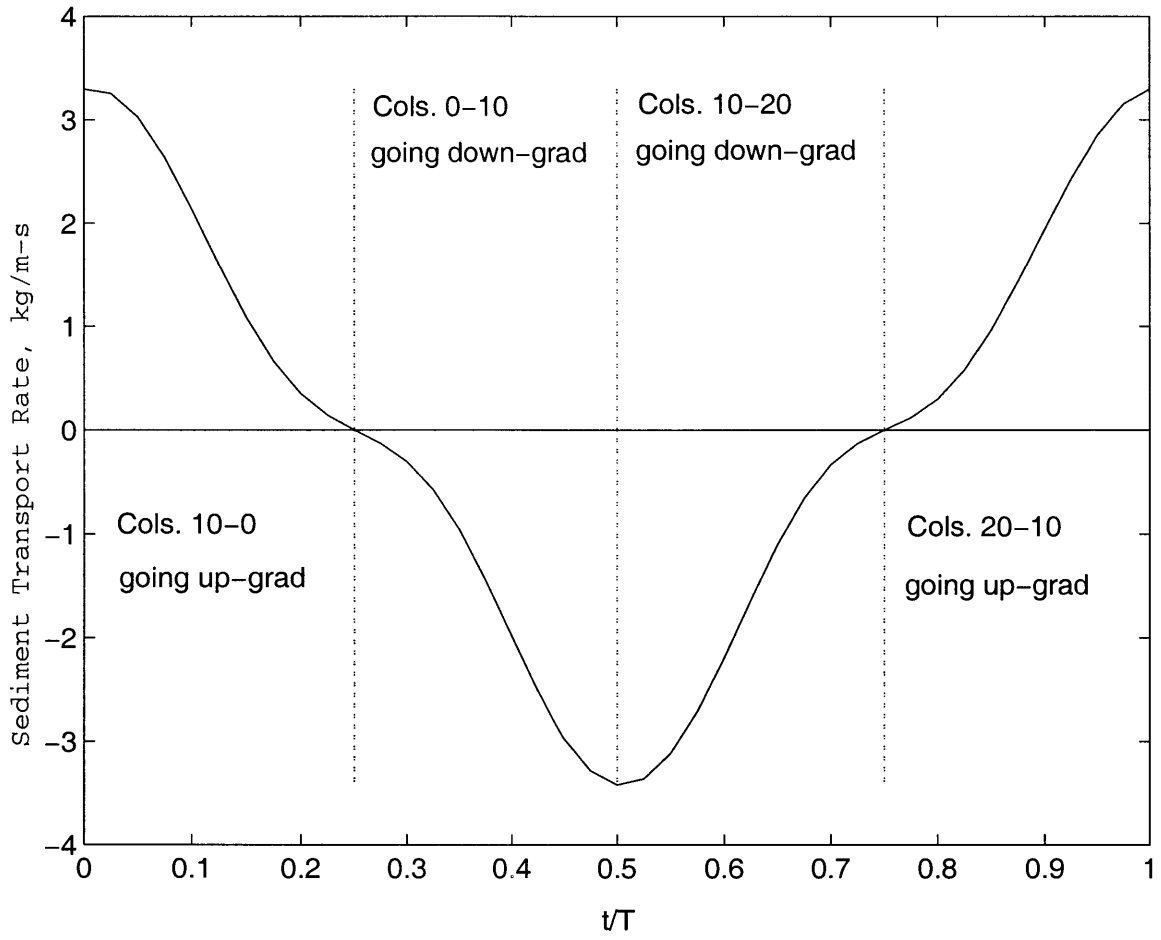

Figure 7-9: Instantaneous Sediment Transport Rate as a function of time, at x=0

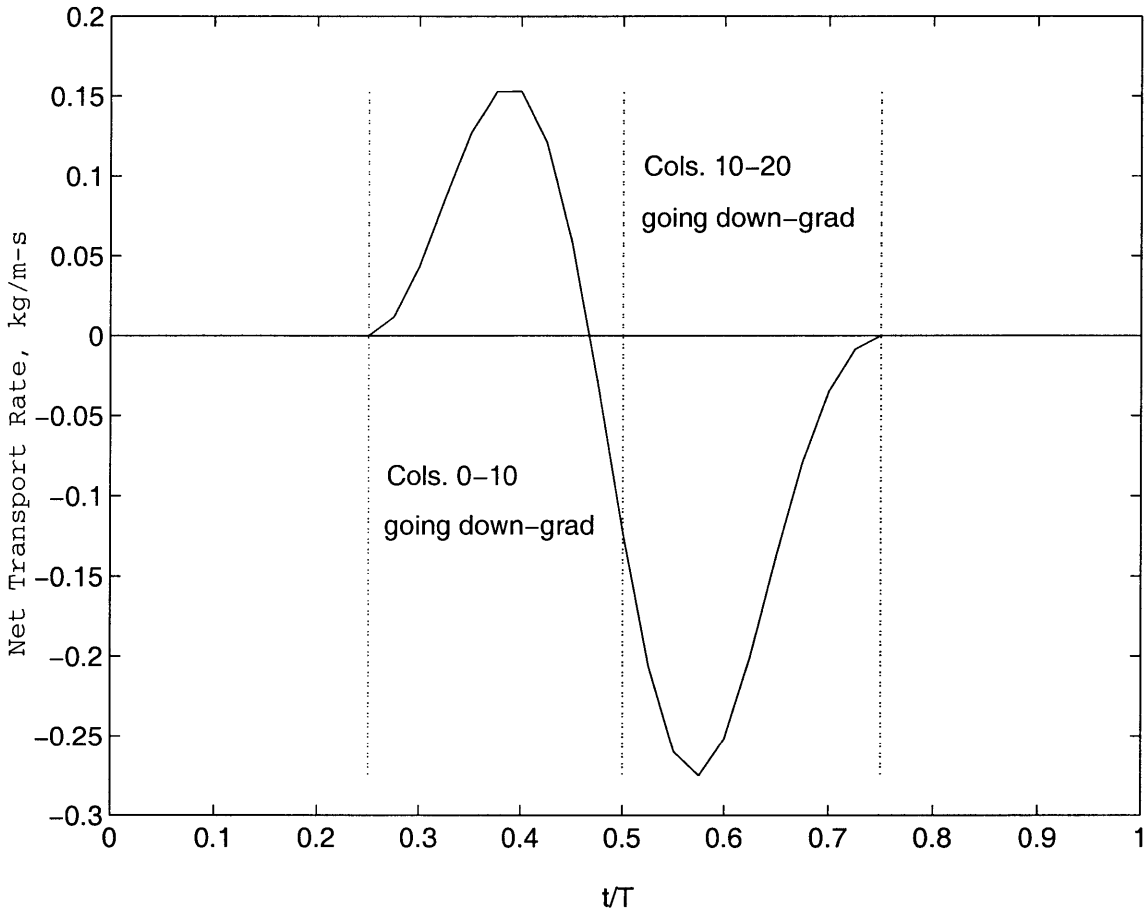

Figure 7-10: Net Up-gradient Sediment Transport Rate as a function of time, at x=0

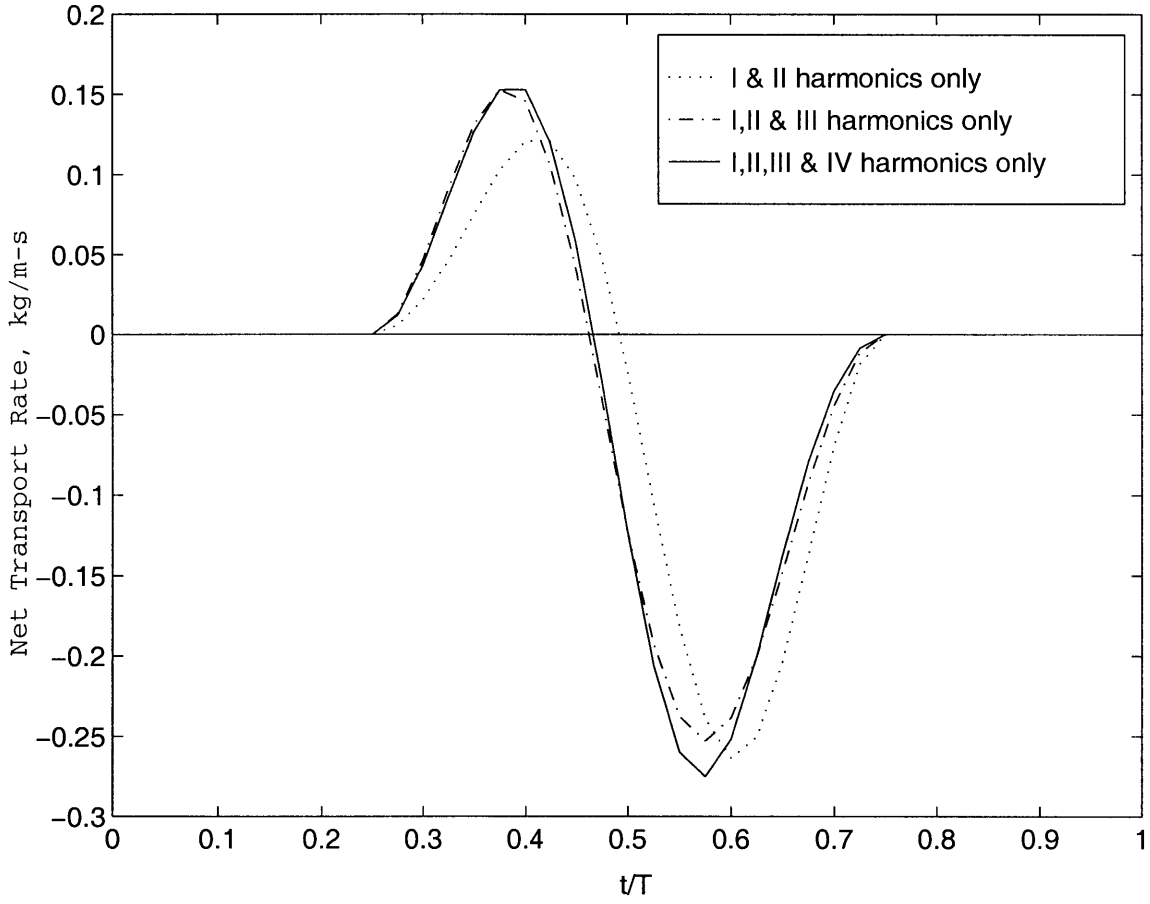

Figure 7-11: Effect of addition of higher harmonics on variation of the Net Up-gradient Sediment Transport Rate, at x=0

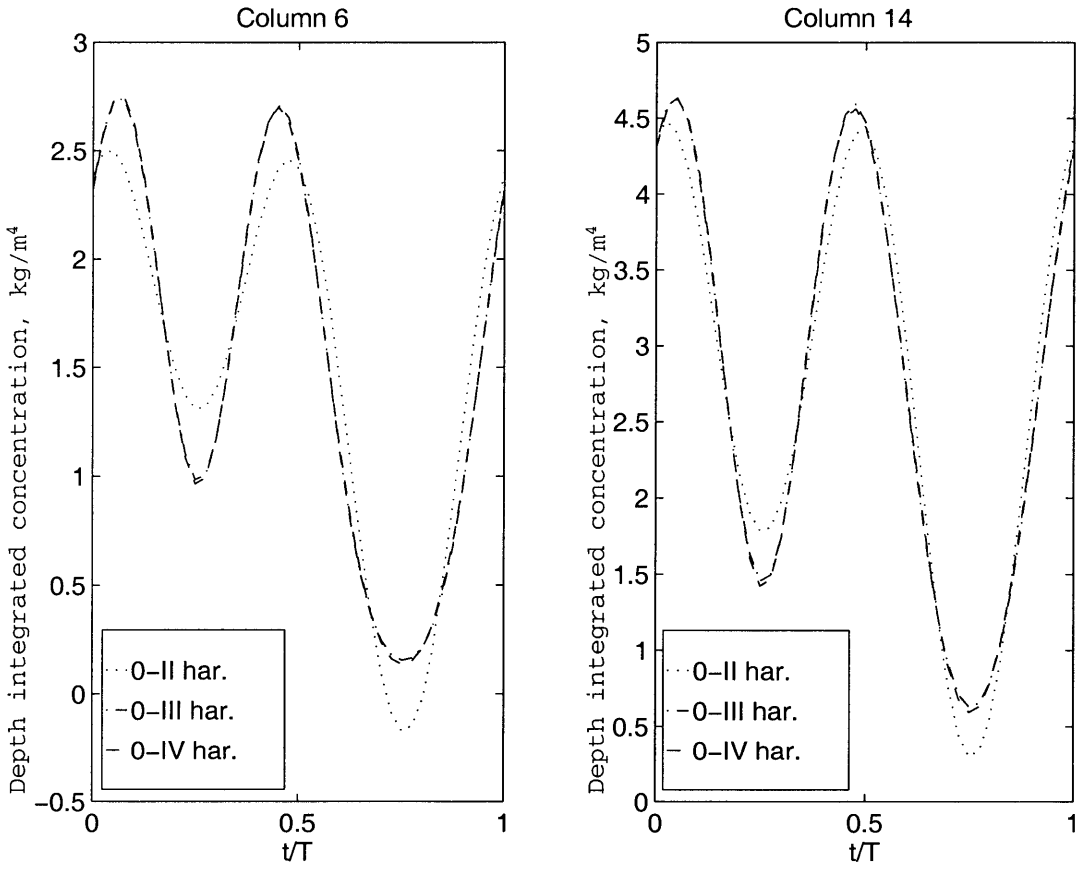

Figure 7-12: Variation of depth-integrated concentration ($\int$cdz)over a period, for columns 6 and 14

Chapter 8

Model Results and Analysis

This chapter provides examples which illustrate the importance of non-equilibrium effects in suspended sediment concentration. In one example, the shoaling of waves on the continental shelf near the coast creates a gradient of bottom sediment concentration. In the other example, a difference in the wave climate between a harbor and the open ocean causes the spatial variation in bottom sediment concentration. Sections 8.1 and 8.2 provide the site descriptions, selection of input parameters for the model, and the methodology for applying the model. Model results are presented and compared with the values available in the literature. In sections 8.3 and 8.4, we examine the sensitivity of the results to the various assumptions made for the model input parameters as well as in the structure of the model itself. The effect of the choice of different values of input parameters is examined. An empirical formulation is presented in Section 8.5 for a Fickian-type diffusion coefficient.

8.1 Northern California Continental Shelf

The Russian River continental shelf, off northern California, has been the focus of extensive observational studies over the last two decades. It occupies the region north of San Francisco, extending from Point Reyes ($38^o00'$) to Point Arena ($39^o00'$). The site is characterized by a simple bottom topography and strong wind fields that directly affect the circulation over the shelf. The continental shelf in this region is markedly

wave-dominated, with stormy winters and relatively calm summer periods. The major field programs undertaken on the Russian River continental shelf include Northern California Coastal Circulation Study (NCCCS), (1988-1989), Coastal Ocean Dynamics Experiment (CODE), (1981-1982), and Sediment TRansport Events on Shelves and Slopes (STRESS), (1988-1991). Many smaller scale measurement programs (e.g. Drake and Cacchione, 1985) have also been conducted at this site.

In this section, the calculations of suspended sediment transport are performed under different conditions for a particular mid-shelf location. This location, called C3, is situated in 90 m water depth in a gently sloping and featureless region of the shelf (Figure 8.1). The bottom slope is 1 in 100. The sediment grain size composition for upper 1 cm of bed at C3 is shown in Table 8.1, after Wheatcroft and Butman (1997). The table also includes critical shear stress and settling velocity corresponding to each sediment fraction. Wheatcroft and Butman (1997) accounted for the stabilizing cohesive forces in fine sediment fractions by specifying a minimum critical shear stress of $\tau_{cr} = 1.0\ dy/cm^2$. These sediment parameters are used for the subsequent calculations in this section, so that meaningful comparisons can be made.

The wave climate at the Russian River continental shelf is determined from the observations of National Data Buoy Center (NDBC) Buoy 46013, which takes hourly measurements of significant wave height, dominant and average wave period, and spectral wave energy. The buoy is located 52 km south-southeast of C3 in a water depth of 130 m (Figure 8.1). The current data at C3 are available from the records of observational programs mentioned earlier.

Biogenic mounds of various sizes have been observed in the bottom photographs of C3 site. According to Wheatcroft (1994), the bottom roughness k_n at the site ranges from 0.5 cm to 3 cm, depending on the flow conditions. The low values of k_n correspond to high flows and vice versa.

The model is applied to predict the sediment transport rate at C3, due to the non-equilibrium effect in suspended sediment concentration. Three different hydrodynamic scenarios are examined: moderate wave climate with diurnal wind-forced current oscillation, moderate wave climate with semi-diurnal tidal current oscillation,

and extreme wave climate with semi-diurnal tidal current oscillation. The first two scenarios correspond to summer and spring weather at the northern California shelf, whereas the last scenario corresponds to a winter storm. The data for these scenarios were obtained from observations of experimental programs described below.

8.1.1 Moderate Wave Climate Scenarios

During the spring and summer months of 1981 and 1982, densely-instrumented observational studies were conducted at the Russian River continental shelf. This program, called the Coastal Ocean Dynamics Experiment (CODE), was designed to study the wind-forced motion of water over the continental shelf (Beardsley and Lentz, 1987). Extensive current measurements were performed during these experiments, with the objective of resolving the three-dimensional spatial structure of the flow. The data collected during CODE are used in this section for calculating the suspended sediment transport due to the non-equilibrium effect.

The wave conditions for the CODE experiment are obtained from NDBC Buoy 46013 ($http://www.ndbc.noaa.gov/station\_history.phtml?station = 46013$). For the month of April, the average significant wave height H_s is 2.2 m, and the average wave period T is 12 s. We use linear wave theory to predict the significant wave height H_s and near-bottom orbital velocity u_{bm} at C3 and in its surrounding area.

For a wavefront normally incident to the shore, the near-bottom orbital velocity increases with decreasing water depth in the cross-shore direction due to the effect of wave shoaling. For a wave with deep-water wave height H_{s0} and period T the wave height H_s in water depth, h is given by

$$\frac{H_s}{H_{s0}} = \sqrt{\frac{1}{(1+G)tanh(kh)}} \tag{8.1}$$

where

$$G = \frac{2kh}{sinh(2kh)} \tag{8.2}$$

and k is the solution to the dispersion equation

$$\omega^2 = kgtanh(kh) \tag{8.3}$$

where g is acceleration due to gravity and ω is the angular frequency corresponding to the wave period.

The near-bottom wave orbital velocity, u_{bm}, at each water depth is calculated as:

$$u_{bm} = \frac{H_s}{2} \frac{\omega}{sinh(kh)} \tag{8.4}$$

For a wave with significant wave height of 2.2 m and period of 12 sec in water depth of 130 m, the near-bottom wave orbital velocity, u_{bm} at different water depths is shown in Table 8.2.

SCENARIO I: Moderate Wave Climate with Diurnal Current Oscillation

In this example, the suspended sediment transport is calculated for moderate (summer) wave conditions with diurnal wind-forced current oscillation. The CODE data of hourly averaged currents were high-passed to remove the tidal components, and then processed using Empirical Orthogonal Function (EOF) analysis (Rosenfeld, 1986). Figure 8.2 shows the surface wind stresses and the diurnal current ellipses along the centerline moorings array (C-line) in the CODE experiment. The averaged diurnal band currents, which are mainly forced by the diurnal wind and land-heating cycles, are strongly surface-intensified with amplitudes up to 15 cm/s. The size of diurnal band currents decreases with depth. In water depths of more than 30-40 m, the semi-major axis of the current ellipse is relatively constant at 3 cm/s and does not change in the cross-shelf direction.

In order to perform the wave-current interaction calculations in the bottom boundary layer, the measurements from C3 mooring at 10 meters above bottom (mab) were used. The lowest ellipse at C3 in Figure 8.2 corresponds to these measurements. The maximum current velocity vector is 3 cm/s and is oriented at 30^o off-shelf polewards

from the shelf-parallel direction. This magnitude is chosen as the value of current velocity u_c, ignoring the rotation of the current vector at this stage. Furthermore, this current is assumed to be oriented in the cross-shelf direction. Since the hydrodynamic regime at this location is expected to be wave-dominated, variation in magnitude and orientation of current will have negligible effect on the bottom shear stress. Calculations are presented in the next chapter to justify this assumption. Corresponding to diurnal band currents, the period of current oscillation is $T_c = 24$ hours. This choice of current amplitude and period gives an excursion amplitude of 412 m. Since the bottom slope is 1 in 100, the region of interest (Eq. [7.56]) around C3 lies in the depth range of approximately 85-95 m.

The bottom roughness scale, k_n, is chosen as 3 cm, according to the observations of Wheatcroft (1994). The hydrodynamic regime, inferred from the combined wave-current boundary layer calculations (Madsen, 1994) at different depths around C3 is presented in Table 8.2. It should be noted that the wave-current boundary layer calculations were performed by assuming a constant current velocity of 3 cm/s and a current oscillation direction aligned with the direction of the waves.

The value of current shear velocity u_{*c} is 0.17 cm/s. If the current is considered as a wave of very long (24 hours) period, then an estimate of the boundary layer thickness for the oscillating current can be obtained as:

$$\delta_{cbl} = \kappa \frac{u_{*c}}{\omega_c} \tag{8.5}$$

where ω_c is the angular frequency corresponding to the oscillating current. This gives the estimate of current boundary layer thickness as 9.35 m. For purpose of calculating the depth-averaged value of eddy diffusivity, this length scale based on the boundary layer is used, instead of the depth of water column. The ratio r (Eq.[7.6]), therefore, is set to 9.7. The values of current and current shear velocities correspond to a C_f value of 0.0032 (Eq. [7.10]).

The near-bottom reference sediment concentration is calculated for each fraction

as:

$$c_{R,n} = \gamma_0 c_{b,n}(\frac{2}{\pi}\frac{\tau_{wm}}{\tau_{cr,n}} - 1) \tag{8.6}$$

where $\tau_{cr,n}$ is the critical value of shear stress for the nth sediment fraction, $c_{b,n}$ is the bed concentration for the sediment fraction, and γ_0 is the resuspension coefficient (Madsen, 1993). τ_{wm} is the wave-associated bottom shear stress, and is related to the wave shear velocity u_{*wm} as:

$$\tau_{wm} = \rho {u_{*wm}}^2 \tag{8.7}$$

A porosity of 0.73 was measured for the bottom sediments at C3 (Jackson and Briggs, 1992). This gives the bed concentration of 0.27, which was multiplied by the mass fraction of each sediment size (Table 8.1) to find $c_{b,n}$. A value of 0.002 was used for γ_0 at the C3 site (Glen and Grant, 1987; Wiberg *et al.*, 1994).

The values of bottom reference concentrations of each sediment fraction at different depths are shown in Table 8.3. The sediment fraction of 350μ diameter could not be mobilized at all, and the 180μ fraction could not be mobilized in water depths more than 90 m.

The bottom concentrations at 95 m and 85 m depths are used to find the spatial gradient of bottom sediment concentration. The depth difference of 10 m between these two stations translates to a horizontal span of 1000 m. The concentration gradient is expressed in the units of $kg/m^3/m$, obtained by multiplying the volumetric concentration gradient with the density of the sediment material (2650 kg/m^3) (Harris and Wiberg, 1997).

The net suspended sediment transport rates calculated with the choice of parameters described above are presented in Table 8.4. The rates refer to the total transport of sediment in the offshore direction, and are presented in the units of $g/cm/s$. 1 $g/cm/s$ is equivalent to a sediment transport of 31 $tons/m/year$.

Prior to a discussion of these estimates, the sediment transport rates are estimated for other scenarios at the C3 site.

SCENARIO II: Moderate Wave Climate with Semi-diurnal Current Oscillation

In this example, the suspended sediment transport is calculated for moderate (summer) wave conditions with semi-diurnal tidal current oscillation.The semi-diurnal tidal currents at C3 were estimated by superposition of low-pass filtered currents and a sinusoidal semi-diurnal frequency current, and matching the resultant simulated amplitudes with the observed mean tidal amplitudes (Harris and Wiberg, 1997). In this manner, the cross-shore amplitude of tidal oscillations at a distance of 10 mab at C3 was determined to be 8 cm/s. This is chosen as the magnitude of the oscillatory current u_c. The wave climate and the bottom roughness are the same as in the previous section. The values of various hydrodynamic variables from the combined wave-current boundary layer calculations are shown in Table 8.5. The values of current shear velocity u_{*c} gives an estimate of 12.1 m for δ_{cbl} and a value of 7.4 for r. The value of the friction factor, C_f, is 0.0030. The bottom reference concentrations are given in Table 8.6, with the 350μ fraction remaining completely immobile at all depths. The net suspended sediment transport rates (due to the non-equilibrium effect) are presented for each fraction in Table 8.7, along with the fall velocity and the bottom sediment concentration gradient.

8.1.2 Extreme Wave Climate Scenario

The STRESS measurement program was conducted on the Russian River continental shelf during the winter months of 1988-89 and 1990-91. The objective of the program was to obtain comprehensive high-quality data on the processes controlling sediment transport in a storm-dominated environment (Trowbridge and Nowell, 1994). A severe winter storm hit the region during the STRESS experiment, in the mid-January of 1991. In this section, we estimate the non-equilibrium suspended sediment transport rate due to these storm conditions at the mid-shelf site.

SCENARIO III: Extreme Wave Climate with Semi-diurnal Current Oscillation

A value of 8 cm/s at 10 mab was used for the magnitude of semi-diurnal tidal current u_c, which is the same as the one used for Scenario II (moderate wave climate with semi-diurnal tidal current). The wave climate data were obtained from the NDBC Buoy 46013 records. During the storm event of January 12-17, 1991, the station recorded maximum significant wave height, H_s, of 4 m and a period of 20 s. Table 8.8 shows the wave heights H_s and near-bottom orbital velocities u_{bm} around C3, corresponding to these storm wave characteristics. The combined wave-current bottom boundary layer parameters are calculated with this wave climate and the semi-diurnal tidal currents. The hydrodynamic variables are presented in Table 8.8. These values have been calculated with a bottom roughness k_n of 0.5 cm, in view of the high bottom stresses and orbital velocities (Wheatcroft, 1994).

For this hydrodynamic regime, the current shear velocity u_{*c} is found to be 0.53 cm/s. This gives the estimate of current boundary layer as $\delta_{cbl} = 14.6$ m. The factor r is 6.2 and the friction factor C_f is 0.0044. Table 8.9 shows the bottom reference concentration for each sediment fraction, and Table 8.10 presents the concentration gradient along with the sediment transport rates.

8.1.3 Comparison of Net Sediment Transport Rates

Table 8.11 compares the estimates of suspended sediment transport rate obtained from the present model with values found in the literature for the Russian River mid-shelf C3 site. The cited data are obtained from Drake and Cacchione (1985) and Harris and Wiberg (1997). Drake and Cacchione calculated the suspended sediment transport rate as a product of observed suspended sediment concentration and the measured current, at a distance of 1.5 m above the bottom. The mean suspended sediment transport rate at this location, vector-averaged over a period of 47 days, was found to be 0.24 $g/cm^2/s$. The transport vector was aligned in the along-shelf direction, with almost zero cross-shelf component. No information was provided

about the value of the suspended sediment transport rate at other locations above the bottom, or about the variation of the transport rate with depth. If it is assumed that the value provided is representative of the sediment transport in the bottom 1.5 m of water, the mean suspended sediment transport rate in this bottom layer is 3.6 $g/cm/s$. This number is quite large in comparison with the sediment transport rates caused due to the non-equilibrium effect.

The comparison with results of Harris and Wiberg (1997) is more meaningful, since they provide the depth-integrated sediment transport rate at C3. Their estimates were obtained from long-term simulation of hydrodynamic conditions (including tides) at the site, along with an equilibrium-based resuspension model to obtain the equlibrium suspended sediment concentrations. Again, the resultant transport is in the along-shelf direction. Since the low-pass filtered currents at C3 are always almost oriented in the along-shelf direction, the net suspended sediment transport vector will always be oriented along-shelf.

In contrast, the suspended sediment transport rates estimated in the previous sections are in the cross-shelf direction. With the exception of the estimates for moderate wave climate-diurnal current scenario[1], the suspended sediment transport rates predicted by the non-equilibrium model are of the same order of magnitude as the values found in literature. This implies that the non-equilibrium effect creates an active sediment transport mechanism that is of an equal importance as the mechanisms usually considered in the physical situations described here.

[1]The sediment transport rates for Scenario I (moderate wave climate with diurnal wind-forced currents) are upper-bound estimates. Although the change in the current velocity magnitude in these conditions does not have much effect on the maximum near-bottom wave shear velocity and hence, on the near bed sediment concentrations, the assumption of a high value for the current velocity magnitude overestimates the transport of suspended sediment. The assumption of an oscillatory current oriented in the cross-shelf direction increases the extent of the overestimation of transport, since the current vector is actually rotating with time.

8.2 Boston Harbor's Main Approach Channels

Two shipping channels, President Roads and Nantasket Roads, provide access to Boston's inner harbor, which is otherwise sheltered from the open ocean (Figure 8.3). The wave climate inside the harbor is extremely calm, leading to a highly depositional environment (Cohen, 1997). Outside the harbor, the wave-generated bottom shear stresses mobilize the bed sediment fractions and make them available for resuspension. Hence, there exists a spatial gradient in bottom sediment reference concentration. The motion of tidal currents in the shipping channels provides the oscillatory flow that can lead to a sustained suspended sediment transport into the harbor.

It should be noted that unlike previous examples, the depth of the shipping channels is constant. The spatial gradient in bottom sediment concentration, therefore, is completely due to the difference in wave climates and not due to wave shoaling.

The wave climate outside the harbor is obtained from the data on Atlantic coast hindcast significant wave information (U.S. Army Corps of Engineers, 1983). Station 24 of the Atlantic Coast Wave Information Study (ACWIS), located at East Point, Nahant, provides the average significant wave height for different approach angles. For all approach angles combined, the average significant wave height is $H_s = 0.4$ m, while the most frequent wave period lies between 7 and 8 seconds. A wave period of $T = 8$ seconds is assumed for this calculation. The wave height is assumed to be zero inside the harbor.

Depending on the location and time, the magnitude of tidal currents in the channels 3 m below the surface exhibits a variability in the range of 0.1-1.1 m/s (NOAA, 1977). A value of 0.3 m/s is arbitrarily selected for the purpose of estimating suspended sediment transport rate due to the non-equilibrium effect.

Regular dredging operations maintain the depths of President Roads and Nantasket Roads channels at approximately 17 m and 12 m, respectively. From the inner reaches of the harbor to the point where the channels meet the open ocean at Lovell Island, both channels measure approximately 8000 m in length.

A median sediment diameter of 0.1 mm is assumed for the sediment in the channels, which is fairly typical of Boston harbor sediments (Ravens and Gschwend, 1999). The combined wave-current boundary layer is solved with a roughness length of k_n = 1 cm, which is adopted from Knebel *et al.* (1996). For the oscillating tidal water columns, the hydrodynamic parameters are obtained with a mean significant wave height of 0.2 m. The values of the friction factor, C_f, are 0.0017 and 0.0019, for President Roads and Nantasket Roads, respectively.

At the ocean end of the channel, the reference bottom sediment concentration is found from Eq. 8.6, corresponding to the average wave conditions at East Point, Nahant. The bottom concentration at the harbor end is assumed to be zero. The spatial gradient of the bottom concentration is obtained by dividing this difference by the channel length (8000 m). For a semi-diurnal tidal current magnitude of 0.3 m/s, the whole length of the channel is almost equal to four times the tidal excursion amplitude.

Table 8.12 gives the values of hydrodynamic parameters for the two channels, along with the bottom sediment concentration gradients and net sediment transport rates. For channel widths of 1600 m and 2500 m respectively, President Roads and Nantasket Roads cause, in this scenario, a net annual sediment influx into the harbor of 27,000 tons and 63,000 tons, respectively. Hence, the quantity of sediment that might be entering the harbor due to the non-equilibrium effects in suspended concentration is quite significant. In a harbor-wide budget of total solids carried out by Adams and Stolzenbach (1998), the authors accounted for the main solid import and export processes (effluent and sludge discharges, shoreline sources, etc.), as well as the steady-state sediment transport processes associated with the tides in the harbor. They concluded with an unaccounted influx of 140,000 *tons/year* into the Boston Harbor. The non-equilibrium sediment transport mechanism illustrated here can potentially explain a fraction of this discrepancy in the total solids budget of Boston harbor.

8.3 Effect of Hydrodynamic Parameters

The suspended sediment transport mechanism proposed here is operative in situations where an oscillating current exists in a region of spatially varying bottom sediment concentrations. In all of the four scenarios considered in the previous sections, the bottom sediment concentrations as well as the sediment suspension and transport mechanisms are governed by the prevailing hydrodynamic regime. In this section we examine the assumptions made in the hydrodynamic calculations for their effects on the model results.

8.3.1 Current Velocity Profile

We examine the effect of the uniform current velocity assumption for the scenario with extreme wave climate and semi-diurnal tidal currents (Section 8.1.2). The suspended sediment transport rates at the mid-shelf location C3 are calculated by multiplying the non-equilibrium concentration profile of a water column with the velocity profile of the column, at the two instants of the passing of this water column through C3. The net suspended sediment transport rate at C3 due to this column is equal to the difference of the suspended transport rates thus found for the column at the two passage times through C3.

The sediment transport rates indicated in Table 8.10 assumed a velocity profile that is uniform in depth. The assumption of a uniform velocity profile is the basis for quantifying the sediment transport rates associated with water columns that are distinctly identifiable at all times. This assumption is internally consistent with the Lagrangian approach adopted in the solution.

The uniform velocity profile, however, leads to an overestimation of sediment transport rates, as explained below. The sediment transport mechanism under investigation here is essentially based on a finite response time of the suspended sediment to the changing bottom boundary condition. The lowest layer of the water column is constrained to respond instantaneously to the changes in bottom sediment concentration (Eq.[7.3]), and shows no non-equilibrium effect. The response time of the

fluid layers increases with increasing distance from the bottom. Consider a small increment in time during which the the bottom sediment concentration experienced by a water column changes by a certain amount. The change in the suspended sediment concentration profile due to this change in the bottom boundary condition is significant only for the fluid layers in a certain region of the water column that are close to, but some distance above the bottom. Above this region, the response time of the fluid layers is so high that the concentration profile there shows no significant change. Therefore, the difference in concentration profiles of a water column at the two passage times is most pronounced in the intermediate region. Since the transport is caused due to the difference in the suspended sediment concentration profiles, the bulk of the non-equilibrium suspended sediment transport comes from the bottom layers of the water column. The actual current velocity in this region is given by the current boundary layer profile. As a result, the use of potential flow velocity for finding suspended sediment transport rates in this region will result in an overestimation of transport.

For different water columns passing through the mid-shelf location C3, Figure 8.4 shows the velocity profiles when boundary layer effects are recognized. Table 8.13 compares the transport rates estimated by using boundary layer velocity profiles with those obtained with the uniform velocity profiles. It should be noted that outside the boundary layer region, the uniform potential velocity is used for estimating the transport in both cases.

The magnitude of the difference in transport rates due to different current velocity profiles depends on the size of the sediment fraction. As explained in Section 7.6, the finer sediment fractions reach higher in the water column than the coarser ones, for the same turbulence intensity in the water column. If the non-equilibrium effect causing the difference in the suspended sediment concentration profiles is mainly limited to the regions very close to the bottom, then the assumption of a uniform current velocity is going to significantly over-estimate the net suspended sediment transport. This is the case for the coarse sediment fractions, where the non-equilibrium effect in suspended sediment concentration is confined to within the current boundary layer. This can be

seen from Figure 8.5, which shows the variation of net suspended sediment transport rate with depth for different sediment fractions. The sediment transport rates in this figure were calculated based on the current boundary layer velocity profile.

Although the difference in sediment transport rates for each sediment fraction varies from 8% (2.8μ fraction) to 71% (350μ fraction), the difference in net suspended sediment transport rate summed over all sediment sizes is close to 10%. This is because of the relative abundance of the middle fractions (11-88μ) in the sediment, which account for 96% of the total sediment mass. The variation of net suspended sediment transport rate with grain size is shown in Figure 8.6. The middle fractions (11-88μ) account for 94% of the total net suspended sediment transport rate estimated at C3.

In conclusion, the assumption of uniform velocity profile affects the sediment transport rate in the boundary layer region. For coarse grain fractions, the non-equilibrium effects are confined to a narrow layer near the bottom. The assumption, therefore, does not cause appreciable error when coarse fractions are negligible in the bed sediments. The error, however, may be significant if the boundary layer is large. This is illustrated with the example of the President Roads shipping channel in Boston harbor.

The current velocity profile for President Roads is depicted on normalized depth scale in Figure 8.7. The depth of the channel is 17 m and the flow is entirely characterized as a boundary layer. The variation of suspended sediment transport rate with depth in the channel is shown in Figure 8.8. The solid line shows the sediment transport rates calculated with the assumption of uniform velocity profile. The total sediment transport (summed over depth) is 20% more than the transport estimated on the basis of logarithmic velocity profile, whose variation over depth is shown by the dotted line in Figure 8.8. The change in sediment transport rates and tonnage of sediment imported in the harbor are shown in Table 8.14, for President Roads and Nantasket Roads channels.

8.3.2 Wave-Current Boundary Layer

For the moderate wave-diurnal current oscillation conditions at mid-shelf C3 site (Section 8.1.1, Scenario I), it was assumed that the magnitude of current oscillation velocity is constant at 3 cm/s and that the oscillation axis is always aligned with the direction of the wave propagation. As mentioned in Section 8.1.1, the actual current vector at C3 site corresponding to the diurnal wind-forced currents varies with time in magnitude and direction (Figure 8.2).

Effect of Current Velocity

The wave-current boundary layer parameters presented in Table 8.2 for each depth location around the C3 site are based on a current velocity of 3 cm/s. Since the values of the maximum shear velocity and the maximum wave shear velocity are almost the same, it is clearly a wave-dominated environment. Any decrease in the current velocity is therefore expected to have no effect on the near bottom maximum shear velocity. It will, however, affect the current shear velocity. This is illustrated in Table 8.15, where the hydrodynamic regime at 90 m depth (C3 site) is solved with current velocities of the 3 cm/s and zero cm/s. It can be seen that the bottom shear velocity does not register a significant change even when the current velocity is set to zero. However, the current shear velocity drops from its previous value of 0.17 cm/s to zero, as expected. We have argued earlier that a minimum level of turbulence is always maintained in the water column, modeled by a shear velocity variation with a cut-off value (Eq.[7.11]). Over one period of current oscillation, the average value of current shear velocity is found from Eq. [7.11] as

$$u_{*c,av} = \frac{2}{\pi} u_{*c,max} \tag{8.8}$$

The average current shear velocity thus computed for a current velocity amplitude of 3 cm/s is 0.11 cm/s, which gives a friction factor value of 0.0013. This is much smaller compared to the previous value of 0.0032 (Section 8.1.1, Scenario I). Using this reduced value of friction factor results in the non-equilibrium sediment transport

rate of 0.015 $g/cm/s$, combined for all sediment fractions. This is approximately half of the sediment transport rate estimated by using the peak value of current shear velocity in evaluating the eddy diffusivity. Hence, even though the choice of current velocity does not affect the bottom sediment concentration gradient, it significantly influences the eddy diffusivity and, consequently, the net non-equilibrium sediment transport rate.

Effect of Change in Wave-Current Angle

The calculations in Table 8.2 assumed that the current oscillated in the direction of wave propagation. In Table 8.16 the calculations are performed again, with values of wave-current angle, ϕ_{w-c}, equal to 30^o, 60^o, and 90^o. The results show negligible effect of the wave-current angle on the model input parameters, as expected in a wave-dominated environment.

8.4 Effect of Sediment Parameters

8.4.1 Bottom Sediment Concentration Gradient

The semi-analytical solution provided in Chapter 7 is based on the assumption of a linear gradient of reference bottom sediment concentration. In natural settings, the spatial variation of reference bottom sediment concentration can be expected to be gradual for most of the cases. Only highly localized natural phenomena or anthropogenic activity can cause an abrupt change in the bottom sediment concentration. An example of the latter is the edges of a CAD cell that has been capped with non-native sediments.

For the semi-diurnal tidal currents at the mid-shelf C3 site, the excursion amplitude of the water columns (based on the magnitude and period of current velocity oscillations) is 550 m. The net suspended sediment transport across the C3 site is influenced only by the water columns with mean position within one excursion amplitude of C3 (Eq. [7.56]). Therefore, the region of interest around the mid-shelf site C3

spans four excursion amplitudes around C3. For the storm wave scenario at C3 site (Section 8.1.2), the spatial variation of reference bottom sediment concentration for different size fractions (given in Table 8.10) for this region is depicted in Figure 8.9. It can be seen that the assumption of a linear concentration gradient is appropriate in this case. The local value of concentration gradient around C3 can be used to approximate the concentration gradient across a 2000-m-distance in the cross-shore direction.

As described in Chapter 7, the net suspended sediment transport rate is directly proportional to the reference bottom sediment concentration gradient. When the concentration distribution is not linear over the scale of the region being considered (that is, over four excursion amplitudes), an approximate value for the concentration gradient to be used as the input for the model can be obtained as follows. The bottom reference concentration may be evaluated for each sediment fraction over an appropriate length scale around the point of interest. The response time of the oscillating water column should be used as a guide for the choice of this length scale. In the context of suspended sediment concentration, the response time t_{res} of the water column can be approximated as

$$t_{res} = \frac{l_{char}}{u_{char}} \tag{8.9}$$

where l_{char} and u_{char} are the characteristic depth scale and the characteristic velocity, respectively. The characteristic depth equals that fraction of the total depth where the suspended sediment concentrations are non-negligible. Hence, for fine sediment fractions in a shallow area, the entire water depth may be taken as the characteristic depth. Given the values of the water column shear velocity and the sediment fall velocity, the characteristic depth may be estimated by examining the equilibrium suspended sediment concentration profile. For a sediment with fall velocity w_f in a water column with shear velocity u_*, the equilibrium concentration c at distance z above the bottom is given by:

$$c = c_b e^{-\frac{w_f}{\nu} z} \tag{8.10}$$

where ν is the eddy diffusivity and c_b is the bottom sediment reference concentration specified at a height of z_b above the bottom (Madsen and Wikramanayake, 1988). z_b is generally taken as two sediment diameters.

The process of sediment suspension in the water column involves two characteristic velocities: the sediment fall velocity and the turbulent shear velocity in the water column. Therefore, a conservative estimate of the response time should be obtained by using the smaller of the two. The length scale l_{res} for estimation of concentration gradient around the point of interest is then

$$l_{res} = t_{res} u_c \tag{8.11}$$

where u_c is the magnitude of current oscillation velocity.

It should be mentioned here that in contrast to the semi-analytical model, an arbitrary variation of bottom sediment concentration can be specified for the numerical model based on a Fourier-series solution. (Appendix A). Hence, for the cases where linear variation of bottom sediment concentration can not be assumed, use of the numerical model is recommended.

8.4.2 Resuspension Coefficient

The value of resuspension parameter γ_0 determines the reference bottom sediment concentration (Eq.[8.6]). In numerical modeling of storm deposition on northern California shelf, Zhang *et al.* (1999) found the resuspension coefficient γ_0 and the critical shear stress τ_{cr} to be the most important parameters in determining sediment transport patterns on the shelf. In the present model, the net suspended sediment transport rate due to the non-equilibrium effect is directly proportional to the value of γ_0. For all transport calculations at the northern California mid-shelf site C3, a value of γ_0 equal to 0.002 has been used, a value determined by Glen and Grant

(1987) by matching the observed suspended sediment concentrations at C3 with model predictions.

8.5 Fickian Diffusion Formulation

As discussed in Chapter 7, the net sediment transport rate due to the non-equilibrium effect is proportional to the gradient of the bottom sediment reference concentration, and is independent of the absolute magnitude of the concentrations. Hence, it was decided to propose a Fickian-type diffusion coeffcient for this transport mechanism, such that

$$W = -K\frac{\partial c_b}{\partial x} \tag{8.12}$$

where W is the net sediment transport rate in $g/cm/s$, $\frac{\partial c_b}{\partial x}$ is the bottom reference concentration gradient in $kg/m^3/m$, and K is the diffusion coefficient. The following formulation is adopted:

$$K = k^{'} {w_f}^a {u_c}^b h^c T^d \tag{8.13}$$

where w_f, u_c, h, and T are the sediment fall velocity, current velocity, water depth, and current oscillation period, respectively. A limited parametric study was conducted to evaluate the coefficients a, b, c, and d. The net sediment transport rate was evaluated by varying one of the parameters while keeping the others constant. Ten different values were used for varying each parameter. The range of values covered for each parameter is given in Table 8.17. All calculations were done with a uniform current velocity profile and a value of r (Equation 7.6) equal to 1, implying that the whole depth was considered for finding the depth-averaged value of eddy diffusivity. Furthermore, the friction factor, C_f was kept constant with a value of 0.0025 for all calculations. The results were subjected to multi-variate linear regression, and the following formulation was obtained for the diffusion coeffcient:

$$K = (0.2){w_f}^{-0.8} {u_c}^{3.6} h^{1.6} T^{0.3} \tag{8.14}$$

Both the current velocity, u_c, and the sediment fall velocity, w_f are in units of m/s, the depth, h is in meters, and the period, T is in seconds. The above equation gives the value of diffusion coefficient, K, corresponding to the net transport rate, W, expressed in $g/cm/s$, and the concentration gradient, $\frac{\partial c_b}{\partial x}$, expressed in $kg/m^3/m$.

In order to estimate the accuracy of this formulation, the net suspended sediment transport rates were calculated by using this approach for the Boston harbor navigation channels. With the choice of input parameters given in Table 8.12, the diffusion coefficient predicts net sediment transport rates of 0.019 $g/cm/s$ and 0.011 $g/cm/s$, for President Roads and Nantasket Roads, respectively. These estimates are of the same order of magnitude as the model predictions given in Table 8.12.

It should be noticed that the above exercise was conducted only to explore the analogy of the non-equilibrium-related net transport with the classical diffusion model. The diffusion coefficient was derived from the model calculations which assumed that the whole water depth contributes to the eddy diffusivity, that is, when the ratio r is set to unity. This assumption is not valid for deep water locations, and therefore the use of this parametric formulation is recommended only in shallow water situations. Furthermore, the results of this formulation are valid only for low fall velocities and a friction factor value of 0.0025. These restrictions should be borne in mind while using the diffusion coefficient given by Eq. 8.14 for estimating sediment transport.

Table 8.1: Sediment characteristics for the Russian River C3 Site (Wheatcroft and Butman, 1997)

Size Range ϕ	Median diameter (μm)	Mass fraction	Critical Shear Stress (dy/cm^2)	Fall velocity (cm/s)
9-8	2.8	0.0022	1.00	0.0003
8-7	5.5	0.031	1.00	0.0013
7-6	11	0.17	1.00	0.0064
6-5	22	0.35	1.00	0.029
5-4	44	0.32	1.00	0.12
4-3	88	0.12	1.3	0.42
3-2	180	0.0160	1.9	1.3
2-1	350	0.0010	2.4	3.6

Table 8.2: Hydrodynamic Parameters: Scenario I (Russian River C3 Site)

Depth h (m)	Wave bot. orb. vel. u_{btm} (m/s)	Max. wave shear vel. u_{*wm} (m/s)	Max. shear vel. u_{*m} (m/s)	Current shear vel. u_{*c} (m/s)
95	0.0779	0.016	0.016	0.0017
92.5	0.0835	0.0168	0.0169	0.0017
90	0.0889	0.0176	0.0176	0.0017
87.5	0.0947	0.0184	0.0185	0.0018
85	0.1015	0.0193	0.0194	0.0018

Table 8.3: Bottom Reference Concentrations, (cm^3/m^3): Scenario I (Russian River C3 Site)

Depth (m)	Diameter (μm)							
	2.8	5.5	11	22	44	88	180	350
95	0.8	11.2	61.6	126.8	115.8	18.5	*	*
92.5	1	14.1	77.3	159.2	145.4	27.1	*	*
90	1.2	17.1	93.8	193.1	176.5	36.0	0.5	*
87.5	1.4	20.2	111.1	228.7	209.0	45.4	1.4	*
85	1.7	23.9	131.4	270.5	247.2	56.5	2.4	*

Table 8.4: Net Suspended Sediment Transport Rate: Scenario I (Russian River C3 Site)

Diameter (μm)	Fall velocity (m/s)	Conc. gradient $(kg/m^3/m$	Net transport rate $(g/cm/s)$
2.8	3e-6	2e-6	2.1e-4
5.5	1.3e-5	3.4e-5	2.9e-3
11	6.4e-5	1.86e-4	0.0134
22	2.9e-4	3.83e-4	0.0126
44	1.2e-3	3.5e-4	5.8e-4
88	4.2e-3	1e-4	1.2e-6
Total			0.0297

Table 8.5: Hydrodynamic Parameters: Scenario II (Russian River C3 Site)

Depth h (m)	Wave bot. orb. vel. u_{bm} (m/s)	Max. wave shear vel. u_{*wm} (m/s)	Max. shear vel. u_{*m} (m/s)	Current shear vel. u_{*c} (m/s)
95	0.0779	0.0162	0.0167	0.0044
92.5	0.0835	0.017	0.0175	0.0044
90	0.0889	0.0178	0.0183	0.0044
87.5	0.0947	0.0186	0.0191	0.0045
85	0.1015	0.0195	0.02	0.0045

Table 8.6: Bottom Reference Concentrations,(cm^3/m^3): Scenario II (Russian River C3 Site)

Depth (m)	Diameter (μm)							
	2.8	5.5	11	22	44	88	180	350
95	0.8	11.9	65.4	134.8	123.1	20.6	*	*
92.5	1.0	14.8	81.4	167.5	153.1	29.3	*	*
90	1.3	17.8	98.0	201.9	184.5	38.3	0.7	*
87.5	1.5	21.0	115.5	237.8	217.3	47.8	1.6	*
85	1.8	24.8	136.0	280.1	255.9	59.0	2.6	*

Table 8.7: Net Suspended Sediment Transport Rate: Scenario II (Russian River C3 Site)

Diameter (μm)	Fall velocity (m/s)	Conc. gradient $(kg/m^3/m)$	Net transport rate $(g/cm/s)$
2.8	3e-6	2e-6	1e-3
5.5	1.3e-5	3.4e-5	0.013
11	6.4e-5	1.88e-4	0.068
22	2.9e-4	3.87e-4	0.107
44	1.2e-3	3.54e-4	0.029
88	4.2e-3	1.02e-4	3e-4
Total			0.219

Table 8.8: Hydrodynamic Parameters: Scenario III (Russian River C3 Site)

Depth $h\ (m)$	Wave bot. orb. vel. $u_{bm}\ (m/s)$	Max. wave shear vel. $u_{*wm}\ (m/s)$	Max. shear vel. $u_{*m}\ (m/s)$	Current shear vel. $u_{*c}\ (m/s)$
95	0.4337	0.0373	0.0376	0.0052
92.5	0.4467	0.0382	0.0385	0.0053
90	0.4575	0.0389	0.0393	0.0053
87.5	0.469	0.0398	0.0401	0.0053
85	0.4813	0.0406	0.0410	0.0053

Table 8.9: Bottom Reference Concentrations,(cm^3/m^3): Scenario III (Russian River C3 Site)

Depth (m)	Diameter (μm)							
	2.8	5.5	11	22	44	88	180	350
95	9.6	135.3	741.9	1527.5	1396	388.2	32.6	1.5
92.5	10.1	142.7	782.6	1611.3	1472.6	410.3	34.7	1.6
90	10.5	148.6	814.9	1677.9	1533.5	427.8	36.3	1.7
87.5	11.1	156.3	857.4	1765.3	1613.4	450.9	38.4	1.8
85	11.6	163.4	895.9	1844.6	1686	471.9	40.3	1.9

Table 8.10: Net Suspended Sediment Transport Rate: Scenario III (Russian River C3 Site)

Diameter (μm)	Fall velocity (m/s)	Conc. gradient $(kg/m^3/m)$	Net transport rate $(g/cm/s)$
2.8	3e-6	5e-6	2.6e-3
5.5	1.3e-5	7.5e-5	0.036
11	6.4e-5	4.08e-4	0.188
22	2.9e-4	8.45e-4	0.308
44	1.2e-3	7.76e-4	0.105
88	4.2e-3	2.23e-4	1.94e-3
180	1.3e-2	2e-5	2.8e-6
350	3.6e-2	1e-6	6e-10
Total			0.641

Table 8.11: Comparison of the net sediment transport rates: Russian River C3 Site

Authors	Harris and Wiberg	Drake and Cacchione	Present work		
Date	1997	1985			
Time of year	Winter	Summer	Summer (diurnal current)	Summer (semi-diurnal current)	Winter Storm
Sediment Transport Rate	0.082-0.108 $(g/cm/s)$	0.05-0.27 (Mean: 0.24) $(g/cm^2/s)$	0.029 $(g/cm/s)$	0.219 $(g/cm/s)$	0.641 $(g/cm/s)$
Details	Net depth-integrated sediment transport rate averaged over 4 months, based on time series simulation of waves and currents	Sediment transport rate at 1.5 m above bottom, averaged over 3 months, calculated as the product of suspended sediment concentration and current measurements	Net depth-integrated suspended sediment transport rate due to the non-equilibrium effect		

Table 8.12: Net Suspended Sediment Transport: Boston Harbor Navigation Channels

	President Roads	Nantasket Roads
Depth, m	17	12
Width, m	1600	2500
Current, m/s	0.3	0.3
Current location, mab	14	9
Max. wave shear vel., u_{*wm}, m/s	0.0178	0.0221
Current shear vel., u_{*c}, m/s	0.0123	0.0131
Conc. gradient, $kg/m^3/m$	2.17e-5	5.61e-5
Transport rate, $g/cm/s$	0.005	0.008
Sediment Influx, $tons/year$	27,247	63,072

Table 8.13: Net Suspended Sediment Transport Rate: Effect of current velocity profile (Scenario III)

Diameter (μm)	Transport Rate (Uni. vel.) ($g/cm/s$)	Transport Rate (Log. vel.) ($g/cm/s$)	Difference (%)
2.8	2.6e-3	2.4e-3	8
5.5	0.036	0.033	9
11	0.188	0.173	9
22	0.308	0.280	10
44	0.105	0.09	17
88	1.94e-3	1.16e-3	67
180	2.8e-6	1.8e-6	55
350	6e-10	3.5e-10	71
Total	0.641	0.579	11

Table 8.14: Net Suspended Sediment Transport Rate: Effect of current velocity profile; Boston harbor

Channel	Uniform velocity		Log. velocity	
	Rate, $g/cm/s$	Amount, $tons/yr$	Rate, $g/cm/s$	Amount, $tons/yr$
President Roads	0.0054	27,247	0.0044	22,201
Nantasket Roads	0.0080	63,072	0.0063	49,669

Table 8.15: Hydrodynamic Parameters: Effect of current velocity magnitude (Scenario I)

Current vel. (m/s)	Wave bot. orb. vel. (m/s)	Max. wave shear vel. (m/s)	Max. shear vel. (m/s)	Current shear vel. (m/s)
0.03	0.0889	0.0176	0.0176	0.0017
0	0.0889	0.0175	0.0175	0

Table 8.16: Hydrodynamic Parameters: Effect of wave-current orientation (Scenario I)

W-C angle (*degrees*)	Wave bot. orb. vel. (m/s)	Max. wave shear vel. (m/s)	Max. shear vel. (m/s)	Current shear vel. (m/s)
0	0.0889	0.0176	0.0176	0.0017
30	0.0889	0.0175	0.0176	0.0017
60	0.0889	0.0175	0.0176	0.0017
90	0.0889	0.0175	0.0175	0.0017

Table 8.17: Parametric Diffusion Coefficient: Range of variables tested

Variable	Range tested
Fall velocity, w_f	13e-6 - 3.6e-2 (m/s)
Current velocity, u_c	0.03 - 1 (m/s)
Water depth, h	4 - 90 (m)
Oscillation period, T	3 - 24 (hrs)

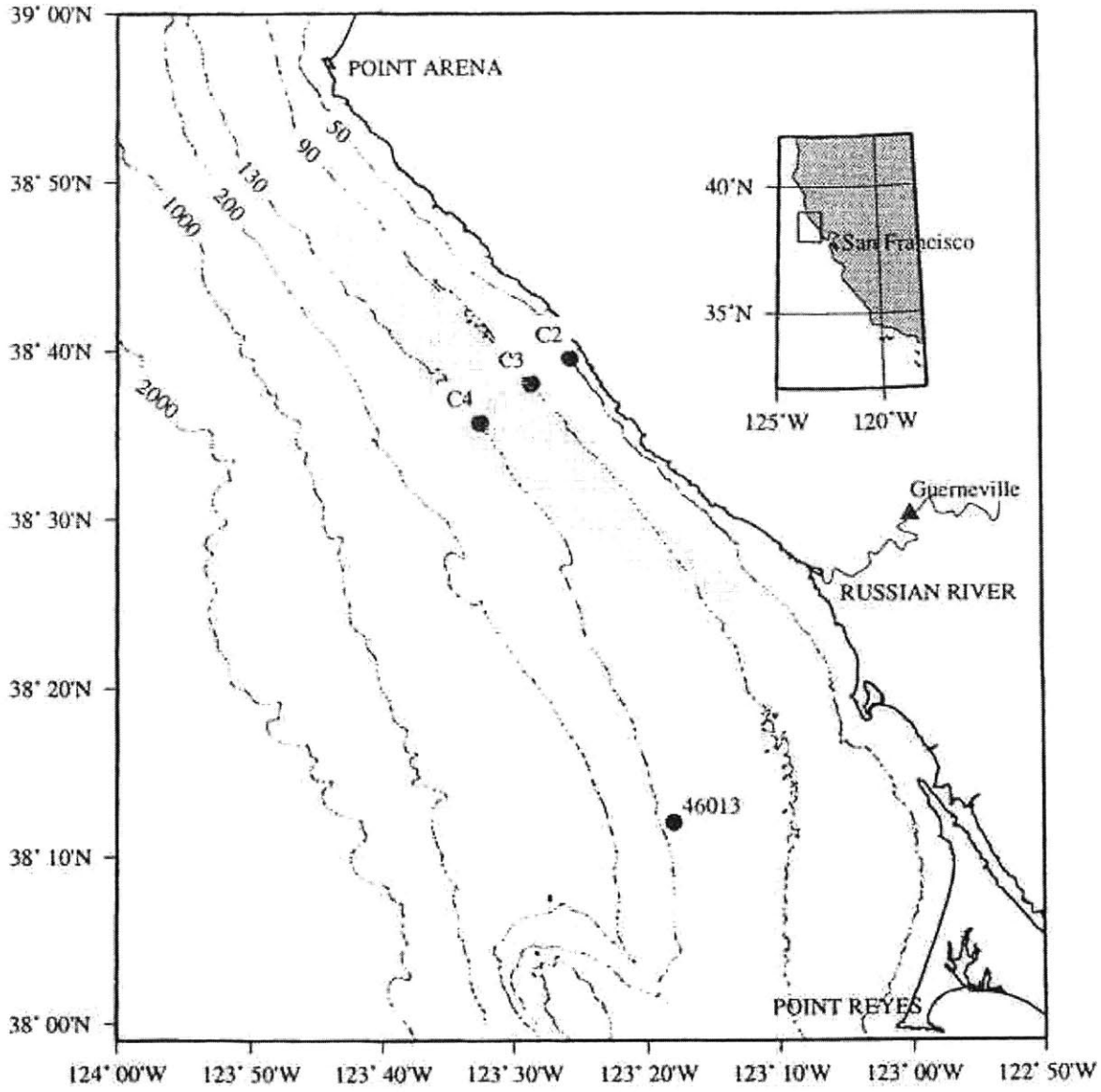

Figure 8-1: Map of the Russian River continental shelf off northern California

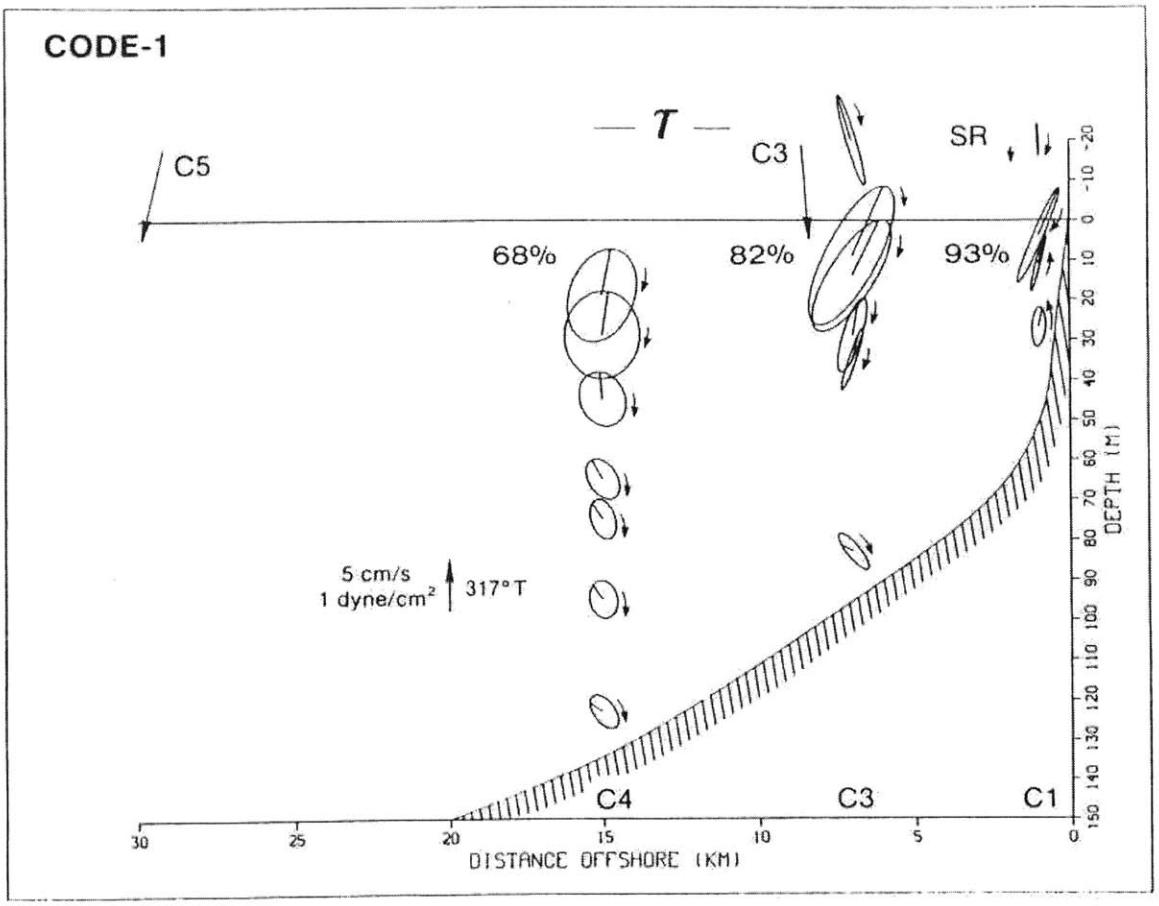

Figure 8-2: Diurnal band horizontal current ellipses at CODE Russian River continental shelf C-line (Rosenfeld, 1986)

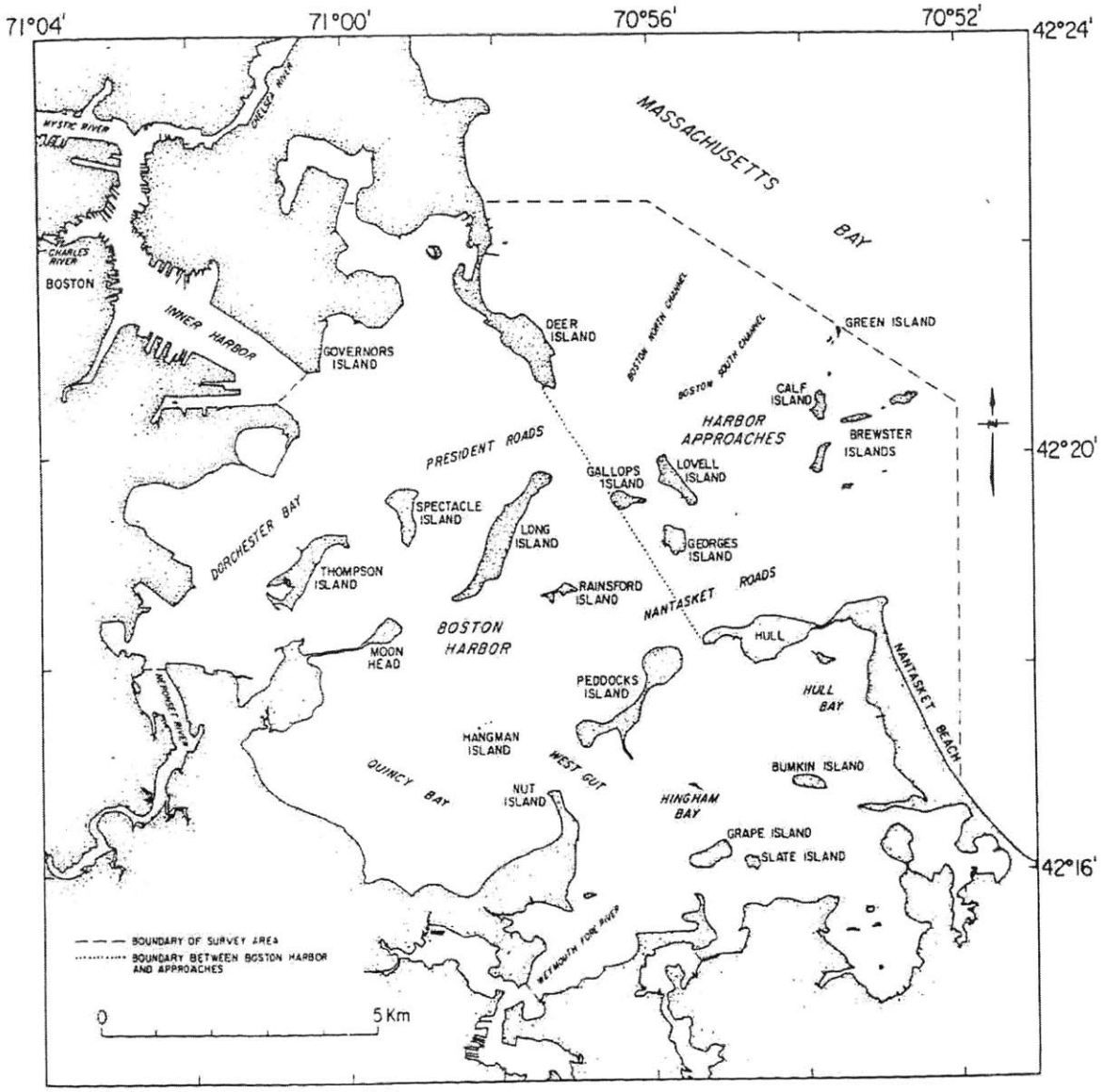

Figure 8-3: Map of Boston Harbor

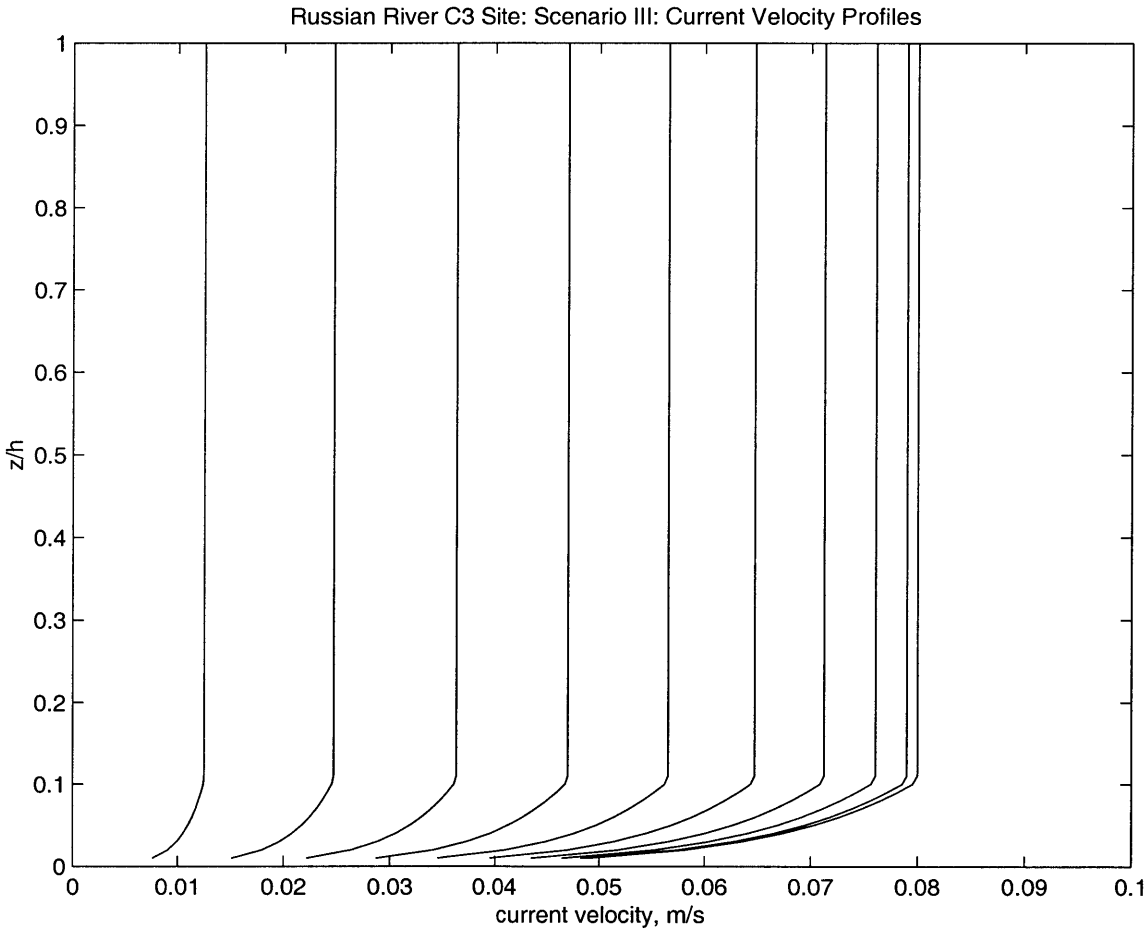

Figure 8-4: Current velocity profiles of different columns as they pass through C3

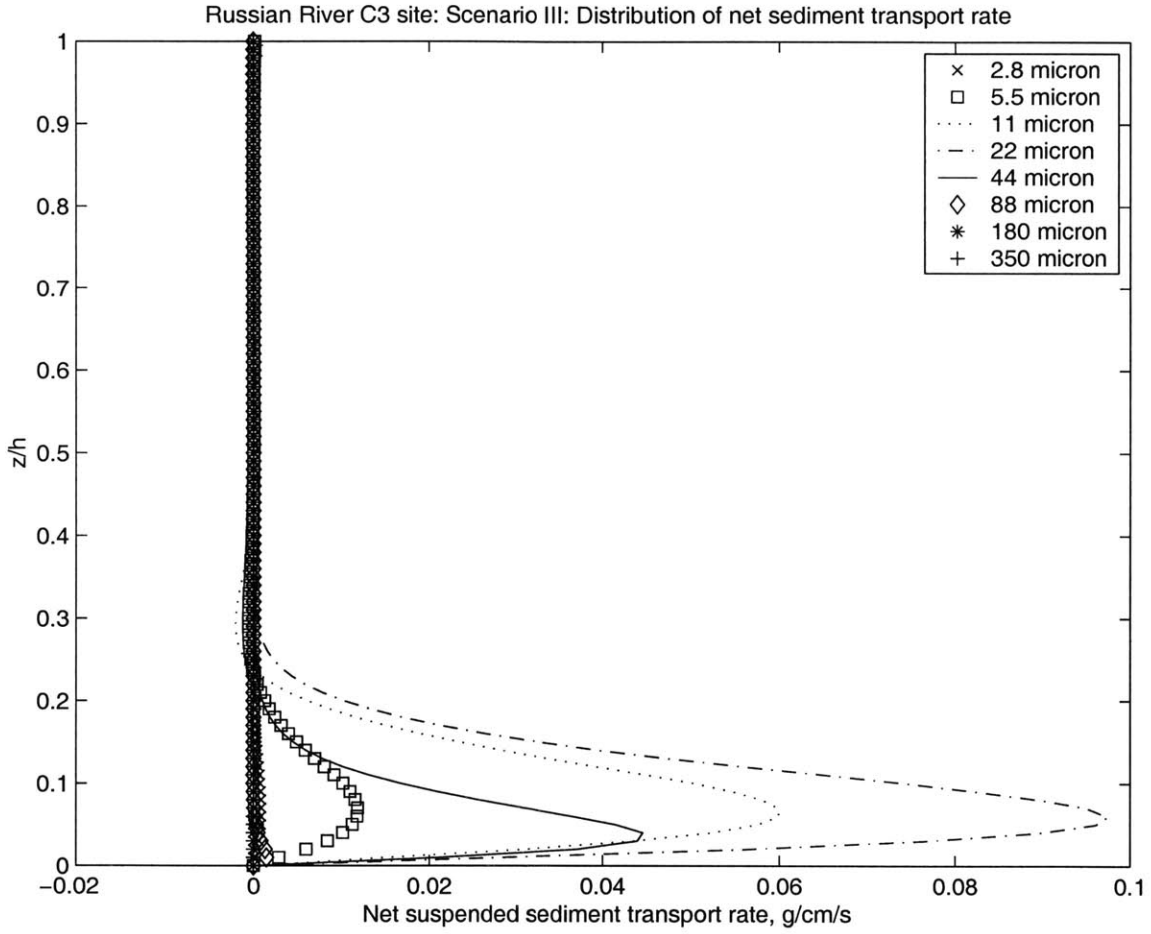

Figure 8-5: Distribution of net suspended sediment transport rate with depth, for different sediment fractions at C3

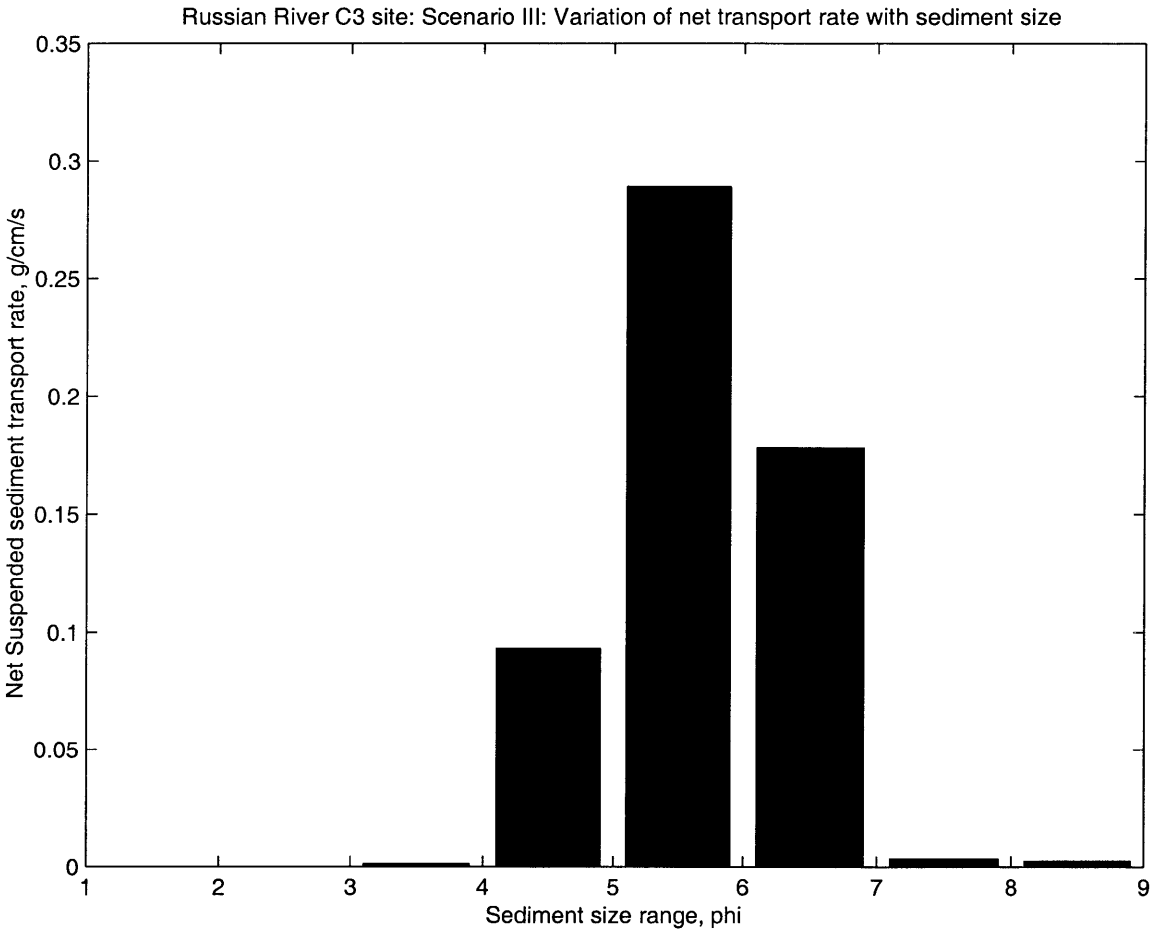

Figure 8-6: Variation of net suspended sediment transport rate with sediment size

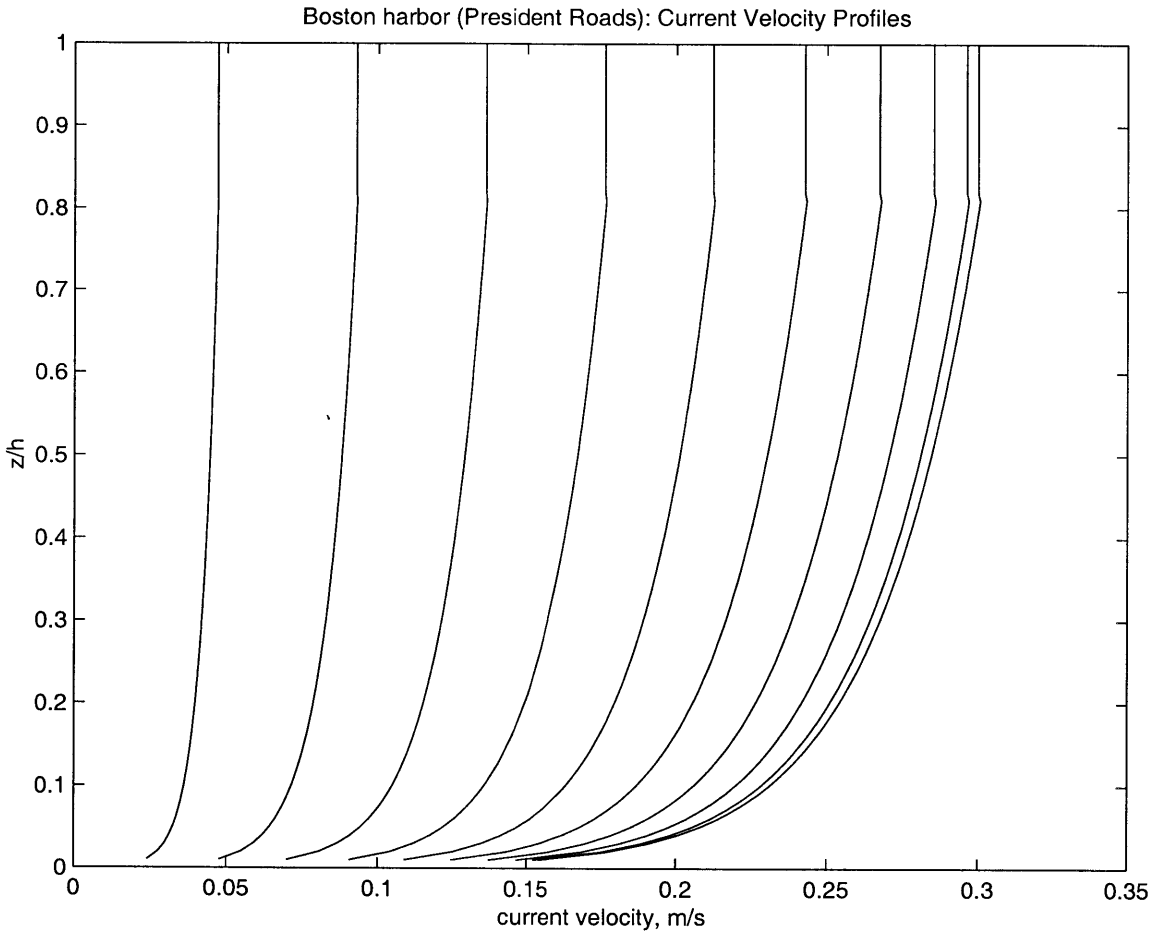

Figure 8-7: Current velocity profiles of different columns; President Roads

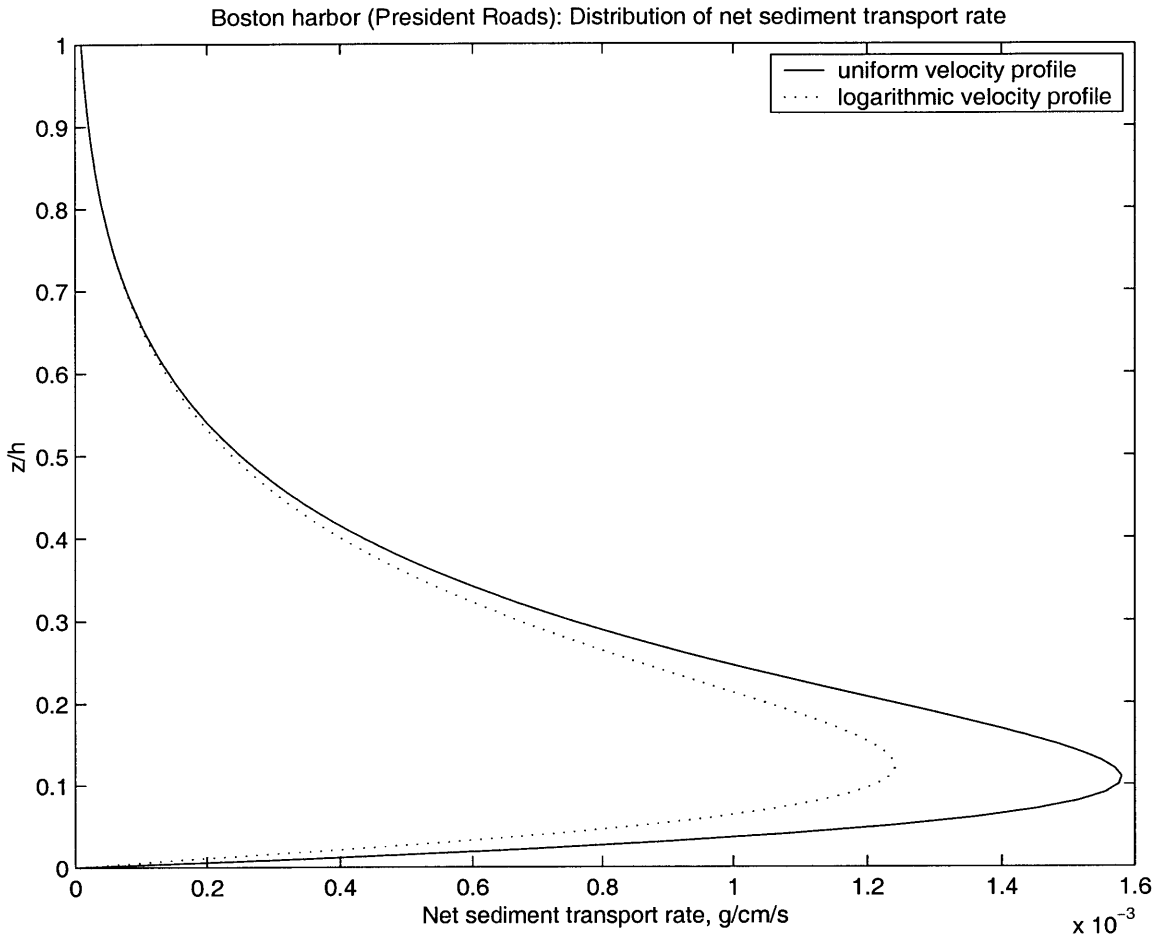

Figure 8-8: Distribution of net suspended sediment transport rate with depth, for different current velocity profiles; President Roads

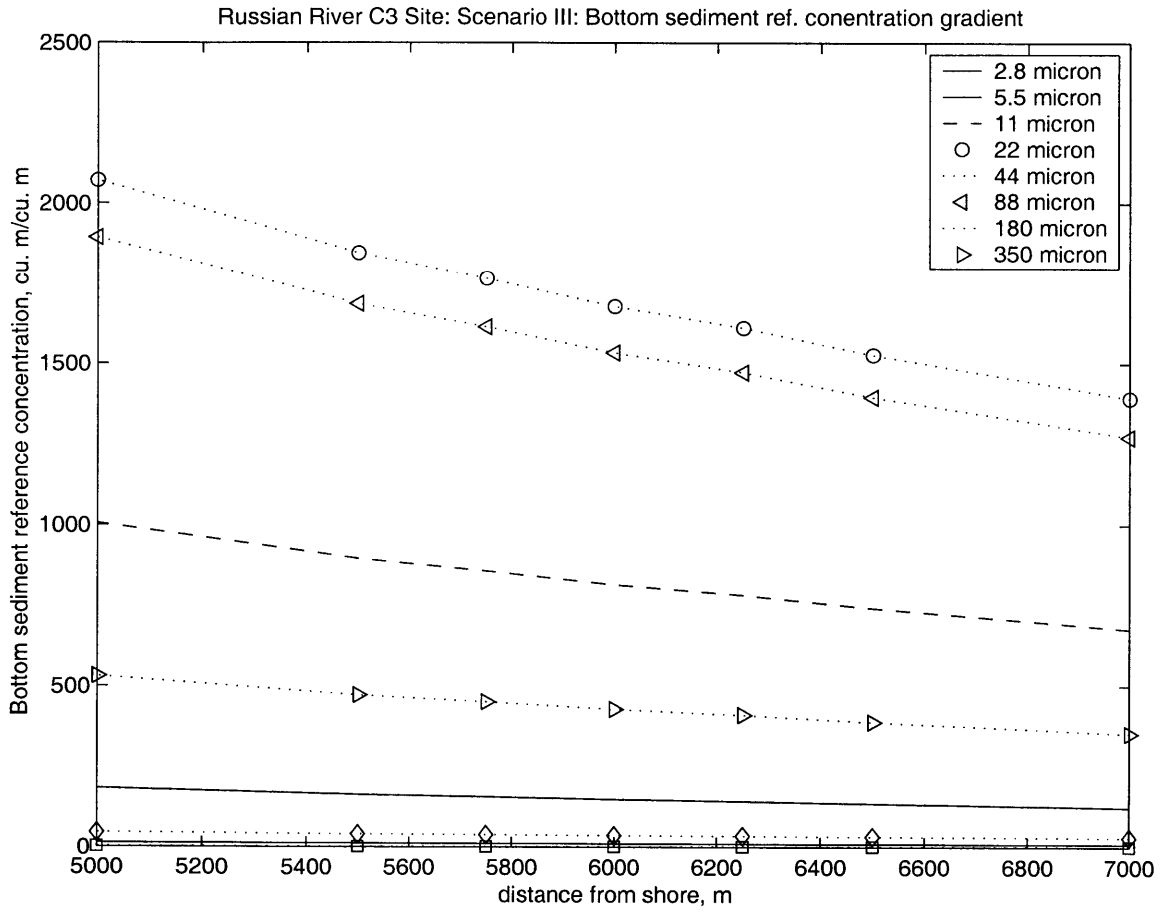

Figure 8-9: Bottom sediment reference concentration gradient in the region around C3

Chapter 9

Conclusions and Suggestions for Future Work

The conclusions of the research program are summarized in this chapter. Avenues are recommended for the pursuit of future research in this field.

9.1 Conclusions

1. We have presented a perturbation solution for the temporal response of suspended sediment concentration in a water column, based on a spatially constant but temporally varying eddy diffusivity. The solution is obtained in Lagrangian formulation, and assumes a linear spatial gradient of bottom reference sediment concentration. The solution can be easily and quickly evaluated to a desired degree of accuracy, and is therefore amenable to be incorporated in common sediment transport models.

2. We have identified a physical system where a net suspended sediment transport is sustained exclusively due to the finite response time of the water column. This system is characterized by the presence of an oscillating current in a region of spatially varying bottom reference sediment concentration.

3. Calculations have been performed to investigate the importance of the proposed

suspended sediment transport mechanism in different scenarios.

The results from a mid-shelf site on the northern California continental shelf indicate that the proposed mechanism may be responsible for a significant cross-shelf sediment transport under certain conditions. This is in contrast to the experimental measurements and the predictions of equilibrium-based models, since their findings always indicate a mainly long-shore transport, due to the dominance of long-shore currents.

The application of the model to the Boston harbor navigation channels points out that the non-equilibrium effect in tidal water columns may cause a significant suspended sediment influx at the harbor-ocean interface.

4. The proposed suspended sediment transport mechanism may not be experimentally identifiable since it is a result of contrasting two large transport rates with reversing flows. Hence, the results are important because the theoretical and numerical methods are the only means of identifying and understanding such sediment transport mechanisms.

5. The proposed mechanism is a non-linear phenomenon, arising out of a distinctly non-linear coupling of multiple effects influencing the particle transport.

6. The transport caused by the proposed mechanism increases with decreasing fall velocity. The mechanism can hence be seen to favor fine sediments. This fact has important implications for the coastal zone issues like beach erosion, dispersal of planktonic larvae, and deposition of particle-reactive chemical species on the shelf. Selective off-shore transport of fines has been abundantly documented in literature, and the proposed mechanism provides one possible explanation for it.

7. The net sediment transport rate is proportional to the gradient of the bottom sediment concentration, and is independent of the absolute value of the concentration. Hence, the transport due to the non-equilibrium effect is purely a gradient-driven mechanism, similar to a diffusion process.

8. The proposed sediment transport mechanism has general applicability and is not limited to tidal environments. It is shown that whenever the residence time of the water column is small compared to the response time of suspended sediment, the presence of a bottom concentration gradient and an oscillatory motion will lead to net transport of sediment.

9.2 Suggestions for future work

On the basis of the results of this research, the author recommends the following directions for future research:

1. The value of the eddy diffusivity in the water column is an important input parameter. Attempt should be made to incorporate a more sophisticated formulation of the eddy diffusivity in the analytical solution.

2. The sediment transport mechanism proposed here should be investigated in the scenarios where the spatial gradient of the reference bottom sediment concentration is non-linear. An interesting case would involve an abrupt change in the bottom boundary condition. This case would have direct relevance to the problem of understanding the sediment transport at the cap edges, for example.

3. The present model assumes bed conditions that are independent of the sediment transport at the site. The theory of the proposed sediment transport mechanism could be significantly advanced by introducing a bed evolution scheme that is coupled with the net sediment transport rate.

4. Since the effect of the proposed sediment transport mechanism is materialized over time scales greater than or equal to the current oscillation period, direct field measurements of sediment transport on the shelf will not be able to provide data for a corroboration of the net sediment transport results. However, the geological parameters are the most promising indicators of net cross-shore sediment transport integrated over long time scales. It would be worthwhile

to search for sites with adequate long-term hydrodynamic and geological evolution data. In combination with an integrated bed-evolution model, this could provide a field validation of the proposed mechanism.

5. Finally, the analytical solution presented in this work could be developed into a modular routine, for possible incorporation into the common sediment transport models. A similar application could be developed for topographical evolution models.

Series Solution

Mathematical Model

The system of governing equations (7.2)-(7.4) can be rewritten in terms of a deficit concentration $c^{'}$, given by

$$c^{'}(z,t) = \frac{c_{ss}(z) - c(z,t)}{c_b} \tag{1}$$

where c_{ss} is the equilibrium concentration corresponding to the bottom concentration c_b. The non-dimensional equation is

$$\theta^2 \frac{\partial c^{'}}{\partial t} = \theta^2 \frac{\partial c^{'}}{\partial z} + \frac{\partial^2 c^{'}}{\partial z^2} \tag{2}$$

where $\theta^2 = 6w_f/ku_*$, $t = \tilde{t}w_f/h$ and $z = \tilde{z}/h$. h and w_f denote water depth and sediment fall velocity respectively.

The initial and boundary conditions become:

$$c^{'}(z,0) = \frac{c_{ss}(z) - g(z)}{c_b} \tag{3}$$

$$c^{'}(z,\infty) = 0 \tag{4}$$

$$c^{'}(0,t) = 0 \tag{5}$$

$$\theta^2 c^{'}(1,t) + \frac{\partial c^{'}}{\partial z}(1,t) = 0 \tag{6}$$

where g(z) is the initial sediment concentration profile, i.e.

$$g(z) = c(z, 0) \tag{7}$$

Using the method of separation of variables, we find the solution to the above system as the following series:

$$c^{'}(z,t) = \sum_{n=1}^{\infty} a_n e^{-\frac{\theta^2 z}{2}} sin(\alpha_n z) e^{-k_n t} \tag{8}$$

where α_n are the eigenvalues of the equation

$$tan\alpha_n = \beta\alpha_n \tag{9}$$

$$\beta = -2/\theta^2 \tag{10}$$

and

$$k_n = \frac{{\alpha_n}^2}{\theta^2} + \frac{\theta^2}{4} \tag{11}$$

The coefficients a_n in the solution are determined from the initial condition, Eq.(A.3), with the equilibrium suspended sediment concentration given by

$$c_{ss}(z) = c_b e^{-\theta^2 z} \tag{12}$$

The initial sediment concentration profile is approximated by a fourth degree polynomial. Using the orthogonality of eigenfunctions, we obtain the amplitudes:

$$a_n = \frac{2}{(1 - \beta cos^2\alpha_n)}[\int_0^1 (\frac{c_{ss}(z) - g(z)}{c_b}) e^{\theta^2 z/2} sin(\alpha_n z) dz] \tag{13}$$

A numerical program evaluates these integrals for a user-specified number of eigenvalues. Thus the sediment concentration profile in the water column can be calculated from Eq.(A.8) at any given instant of time, after one or more parameters like the bot-

tom concentration or shear velocity have changed. The current oscillation period is discretized into infinitesimal timesteps, during each of which the water column is assumed to have constant shear velocity and bottom sediment concentration. For each infinitesimal timestep, we use the mean value of u_* during that timestep in order to develop the sediment concentration profile.The concentration profile obtained at the end of a timestep serves as the initial profile for the next timestep, which is characterized by different values of shear velocity and bottom concentration.

For the very first timestep, at the beginning of the process, a steady-state concentration profile is arbitrarily chosen as the initial condition, and in order to get rid of the effect of this arbitrarily chosen initial condition, the water column is repeatedly passed through current oscillation cycles till periodicity of concentration profiles is achieved. At this stage we find the total sediment load in the water column at the two instances it passes through x=0, once going up-gradient, and once going down-gradient. The difference in the sediment load at these two times multiplied by the velocity of the water column at that point gives the net transport rate across x=0.

The choice of the number of timesteps in the current oscillation period is important. The optimal number is that which allows timesteps small enough to capture the transient response of the water column, while keeping the procedure computationally efficient. Since the response time of the water parcel is dependent on the fall velocity of the sediment, we can expect different resolution requirements for different sediment sizes. As the sediment grain size and its fall velocity increase, the number of timesteps required per current oscillation cycle to accurately simulate the suspension process also increases.

For a current oscillation period of 12 hours, we chose a 6 minute timestep (120 timesteps per period) for fall velocity of 0.01 cm/s, and a 90 second timestep (480 timesteps per period) for fall velocity of 1 cm/s. These values were chosen because the incremental accuracy in results achieved by increasing the resolution was not considered worth the incremental computation expense. The same reason applied to the choice of discretizing the current oscillation motion into 20 water columns.

We performed the calculations for the high and the low end of the sediment fall

velocity range specified in Table 7.1. The transport rate W predicted for the fall velocity w_f = 0.01 m/s is 0.83 tons/meter/period. The value for w_f= 0.0001 m/s is 14.2 tons/meter/period. We see that the results compare well with those obtained from the perturbation solution (Table 7.1). It must be reiterated here that the results of Fourier solution are sensitive to the size of the timestep. The timestep must be appropriately chosen according to the response time of the water column.

The Fourier series solution is computationally more intensive than the analytical solution. At the same time it is more versatile in the sense that any kind of bottom sediment concentration gradient and current velocity can be readily specified by the user. Furthermore, it is well-suited for studying suspended sediment transport during storm events, by virtue of its capability to compute suspended sediment concentration profiles by starting from an arbitrarily defined initial state.

Bibliography

[1] Adams, E.E. and K. D. Stolzenbach (1998), "Transport and Deposition of Contaminated Sediment". In *Contaminated Sediments in Boston Harbor*, K.D. Stolzenbach and E.E. Adams (eds.), Marine Center for Coastal Processes, MIT Sea Grant College Program, Cambridge, MA. pp. 17-44.

[2] Beardsley, R.C. and S.J. Lentz (1987), "The Coastal Ocean Dynamics Experiment Collection: an Introduction," Journal of Geophysical Research 92 (C2), 1455-1463.

[3] Cancino, L. and Neves, R. (1999), "Hydrodynamic and Sediment Suspension Modeling in Estuarine Systems- Part I: Description of the Numerical Models," Journal of Marine Systems, vol. 22, no. 2-3, pp. 105-116.

[4] Celik, I. and W. Rodi (1988), "Modeling Suspended Sediment Transport in Non-equilibrium Situation," Journal of Hydraulic Engineering, vol. 114, no. 10, pp. 1115-1133.

[5] Cohen, A. (1997), "Boston Harbor - Sink for Sediments," Sea Technology, 38 (8): 65-68.

[6] Drake, D.E. and D.A. Cacchione (1985), "Seasonal Variation in Sediment Transport on the Russian River Shelf, California," Continental Shelf Research, vol. 4, no. 5, pp. 495-514.

[7] Eyre, B., Hossain, S., and McKee, L. (1998), "A Suspended Sediment Budget for

the Modified Subtropical Brisbane River Estuary, Australia," Estuarine, Coastal, and Shelf Science, Vol. 47, no. 4, pp. 513-522.

[8] Fang, H.W. and G.Q. Wang (2000), "Three-Dimensional Mathematical Model of Suspended Sediment Transport," Journal of Hydraulic Engineering-ASCE, 126: (8) 578-592.

[9] Glenn S.M. and W.D. Grant (1987), "A Suspended Sediment Stratification Correction for Combined Wave and Current Flows," Journal of Geophysical Research, 92, 8244-8264.

[10] Harris, C.K. and P.L. Wiberg (1997), "Approaches to Quantifying Long-term Continental Shelf Sediment Transport with an Example from the Northern California STRESS Mid-Shelf Site," Continental Shelf Research, vol. 17, no. 11, pp. 1389-1418.

[11] Irie, I. and Y. Kuriyama (1988), "Reproduction of Sedimentation in Harbors by Combined Physical/Mathematical Modeling," In: *Proc. of IAHR Symposium on Mathematical Modeling of Sediment Transport in the Coastal Zone*, IAHR, pp. 79-88.

[12] Jackson, D.R. and K.B. Briggs (1992), "High-Frequency Bottom Backscattering: Roughness versus Sediment Volume Ccattering," Journal of the Acoustical Society of America, 92(2), 962-977.

[13] Jiang, J.H. and Mehta, A.J. (2000), "Fine-Grained Sedimentation in a Shallow Harbor," Journal of Coastal Research, vol. 16, no. 4, pp. 1146-1150.

[14] Kachel N.B. and J.D. Smith (1989), "Sediment Transport and Deposition on the Washington Continental Shelf," In: *Coastal Oceanography of Washington and Oregon*, M.R. Landry and B.M. Hickey, editors, Elsevier, New York, pp. 287-348.

[15] Knebel, H.J., Rendigs, R.R., List, J.H., and R.P. Signell (1996), "Seafloor Environments in Cape Cod Bay, a Large Coastal Embayment," Marine Geology, 133 (1-2): 11-33.

[16] Liden, R. (1999), "A New Approach for Estimating Suspended Sediment Yield," Hydrology and Earth System Sciences, vol. 3, no. 2, pp. 285-294.

[17] Lou, J., Schwab, D.J., Beletsky, D., and Hawley, N. (2000), " A Model of Sediment Resuspension and Transport Dynamics in Southern Lake Michigan," Journal of Geophysical Research-Oceans, vol. 105, no. C3, pp. 6591-6610.

[18] Lyne V.D., B. Butman and W.D. Grant (1990), "Sediment Movement along the U.S. East Coast Continental Shelf-II. Modeling Suspended Sediment Concentrations and Transport Rates during Storms," Continental Shelf Research, 10(5), 429-460.

[19] Madsen, O.S. (1994), "Spectral Wave-Current Bottom Boundary Layer Flows," In *Coastal Engineering 1994, Proceedings of the 24th International Conference* Coastal Engineering Research Council/ASCE, Kobe, Japan, pp. 384-397.

[20] Madsen, O.S. (1993), "Sediment Transport on the Shelf," Lecture Notes, Massachusetts Institute of Technology, Cambridge, MA.

[21] Madsen, O.S. and Wikramanayake, P. (1988), "Respose Characteristics of Suspended Sediment Load," Report no. CR-814240-01-0, prepared for the Environmental Protection Agency, Massachusetts Institute of Technology, Cambridge, MA.

[22] Nicholas, A.P. and D.E. Walling (1998), "Numerical Modeling of Floodplain Hydraulics and Suspended Sediment Transport and Deposition," Hydrological Processes, 12: (8) 1339-1355.

[23] NOAA (1977), "Boston Harbor Tidal Charts," National Oceanographic and Atmospheric Administration, Washington, D.C.

[24] Prandle, D., Hargreaves, J.C., McManus, J.P., Campbell, A.R., Duwe, K., Lane, A., Mahnke, P., Shimwell, S., and Wolf, J. (2000), "Tide, Wave, and Suspended Sediment Modeling on an Open Coast - Holderness," Coastal Engineering, vol. 41, no. 1-3, pp. 237-267.

[25] Rakha, K.A. (1998), "A Quasi-3D Phase-Resolving Hydrodynamic and Sediment Transport Model," Coastal Engineering, vol. 34, no. 3-4, pp. 277-311.

[26] Ravens, T.M. and P.M. Gschwend (1999), "Flume measurements of sediment erodibility in Boston Harbor," Journal of Hydraulic Engineering-ASCE, 125 (10): 998-1005.

[27] Rondeau, B., Cossa, D., Gagnon, P. , and Bilodeau, L. (2000), "Budget and Sources of Suspended Sediment Transported in the St. Lawrence River, Canada," Hydrological Processes, vol. 14, no. 1, pp. 21-36.

[28] Rosenfeld, L.K. (1986), "Tidal Band current Variability over the Northern California Continental Shelf," Ph.D. Thesis, Massachusetts Institute of Technology, Cambridge, and Woods Hole Oceanographic Institute, Woods Hole, MA.

[29] Scheffner, N.W. (1996), "Systematic Analysis of Long-term Fate of Disposed Dredged Material," Journal of Waterway, Port, Coastal, and Ocean Engineering, vol. 122, no. 3, pp. 127.

[30] Styles, R. and S.M. Glenn (2000), "Modeling Stratified Wave and Current Boundary Layers on the Continental Shelf," Journal of Geophysical Research-Oceans, 105: (C10) 24119-24139.

[31] Trawle M.J. and B.H. Johnson (1986), "Alcatraz Disposal Site Investigation," Miscellaneous Paper HL-86-1, US Army Engineer Waterways Experiment Station, Vicksburg, Miss.

[32] Trowbridge, J.H., and Nowell, A.R.M. (1994), "An Introduction to the Sediment Transport Events on Shelves and Slopes (STRESS) Program," Continental Shelf Research, 14, 1057-1061.

[33] U.S. Army Corps of Engineers (1983), "Atlantic Coast Hindcast Shallow-Water Significant Wave Information," WIS Report 9, Washington, D.C.

[34] Wheatcroft, R.A. (1994), "Temporal Variation in Bed Configuration and One-Dimensional Bottom Roughness at the Mid-Shelf STRESS Site," Continental Shelf Research, 14, 1057-1061.

[35] Wheatcroft, R.A. and C.A. Butman (1997), "Spatial and Temporal Variability in Aggregated Grain-Size Distributions with Implications for Sediment Dynamics," Continental Shelf Research, 17, 367-390.

[36] Wiberg, P.L., Drake, D.E., and Cacchione, D.A. (1994), "Sediment Resuspension and Bed Armoring during High Bottom Stress Events on the Northern California Inner Continental Shelf: Measurements and Predictions," Continental Shelf Research, 14, 1191-1219.

[37] Wu, W.M., Rodi, W., and Wenka, T. (2000), "3D Numerical Modeling of Flow and Sediment Transport in Open Channels," Journal of Hydraulic Engineering-ASCE, vol. 126, no. 1, pp. 4-15.

[38] Zhang, Y., Swift, D.J.P., Fan, S.J., Niedoroda, A.W., and C.W. Reed (1999), "Two-Dimensional Numerical Modeling of Storm Deposition on the Northern California shelf," Marine Geology, 154: (1-4) 155-167.